spacial variability of seismic ground motions : arch dams

Eleni Koufoudi

Communauté
UNIVERSITÉ Grenoble Alpes

THÈSE

Pour obtenir le grade de

DOCTEUR DE LA COMMUNAUTE UNIVERSITE GRENOBLE ALPES

Spécialité : **Matériaux, Mécanique, Génie-Civil, Électrochimie**

Arrêté ministériel : 25 mai 2016

Présentée par

Eleni KOUFOUDI

Thèse dirigée par **Frédéric DUFOUR, Professeur, Grenoble INP**,
et
codirigée par **Emmanuel Chaljub, Physicien Adjoint, UGA, Grenoble**

préparée au sein du **du Laboratoire « Sols, Solides, Structures - Risques » (3SR)**
dans **l'École Doctorale « Ingénierie - Matériaux Mécanique Énergétique Environnement Procédés Production » (I-MEP^2)**

Variabilité spatiale des mouvements sismiques : Barrages Voûtes

Thèse soutenue publiquement le **18/09/2017**,
devant le jury composé de :

Mme. Catherine, BERGE-THIERRY
Ingénieur de recherche à CEA, Rapporteur
M. Pierre LÉGER
Professeur à l'École Polytechnique de Montréal, Rapporteur
Mme. Françoise COURBOULEX
Directrice de recherche à Géoazur, President
M. Fabrice COTTON
Professeur à l'Université de Potsdam et au GFZ, Examinateur
M. Pierre-Yves BARD
Ingénieur Général Ponts, Eaux et Forêts, Chercheur ISTerre / IFSTTAR, Examinateur
M. Frédéric DUFOUR
Professeur à Grenoble INP, Directeur de thèse
M. Emmanuel CHALJUB
Physicien Adjoint, UGA, Co-encadrant de thèse
M. Nicolas, HUMBERT
Ingénieur à EDF-CIH, Co-encadrant de thèse

Université Joseph Fourier / Université Pierre Mendès France / Université Stendhal / Université de Savoie / Grenoble INP

To my mom and dad...

Ιθάκη

Σα βγεις στον πηγαιμό για την Ιθάκη,
να εύχεσαι νάναι μακρύς ο δρόμος,
γεμάτος περιπέτειες, γεμάτος γνώσεις.
Τους Λαιστρυγόνας και τους Κύκλωπας,
τον θυμωμένο Ποσειδώνα μη φοβάσαι,
τέτοια στον δρόμο σου ποτέ σου δεν θα βρεις,
αν μέν' η σκέψις σου υψηλή, αν εκλεκτή
συγκίνησις το πνεύμα και το σώμα σου αγγίζει.
Τους Λαιστρυγόνας και τους Κύκλωπας,
τον άγριο Ποσειδώνα δεν θα συναντήσεις,
αν δεν τους κουβανείς μες στην ψυχή σου,
αν η ψυχή σου δεν τους στήνει εμπρός σου.
Να εύχεσαι νάναι μακρύς ο δρόμος.
Πολλά τα καλοκαιρινά πρωιά να είναι
που με τι ευχαρίστησι, με τι χαρά
θα μπαίνεις σε λιμένας πρωτοειδωμένους·
να σταματήσεις σ' εμπορεία Φοινικικά,
και τες καλές πραγμάτειες ν' αποκτήσεις,
σεντέφια και κοράλλια, κεχριμπάρια κ' έβενους,
και ηδονικά μυρωδικά κάθε λογής,
όσο μπορείς πιο άφθονα ηδονικά μυρωδικά·
σε πόλεις Αιγυπτιακές πολλές να πας,
να μάθεις και να μάθεις απ' τους σπουδασμένους.
Πάντα στον νου σου νάχεις την Ιθάκη.
Το φθάσιμον εκεί είν' ο προορισμός σου.
Αλλά μη βιάζεις το ταξείδι διόλου.
Καλλίτερα χρόνια πολλά να διαρκέσει·
και γέρος πια ν' αράξεις στο νησί,
πλούσιος με όσα κέρδισες στον δρόμο,
μη προσδοκώντας πλούτη να σε δώσει η Ιθάκη.
Η Ιθάκη σ' έδωσε τ' ωραίο ταξείδι.
Χωρίς αυτήν δεν θάβγαινες στον δρόμο.
Άλλα δεν έχει να σε δώσει πια.
Κι αν πτωχική την βρεις, η Ιθάκη δεν σε γέλασε.
Έτσι σοφός που έγινες, με τόση πείρα,
ήδη θα το κατάλαβες η Ιθάκες τι σημαίνουν.

Κ.Π. Καβάφης, Ποιήματα (1896-1933)

Ithaka

As you set out for Ithaka
hope your road is a long one,
full of adventure, full of discovery. Laistrygonians,
Cyclops, angry Poseidon—don't be afraid of them:
you'll never find things like that on your way
as long as you keep your thoughts raised high,
as long as a rare excitement
stirs your spirit and your body. Laistrygonians,
Cyclops, wild Poseidon—you won't encounter them
unless you bring them along inside your soul,
unless your soul sets them up in front of you.
Hope your road is a long one.
May there be many summer mornings when,
with what pleasure, what joy,
you enter harbors you're seeing for the first time;
may you stop at Phoenician trading stations
to buy fine things,
mother of pearl and coral, amber and ebony,
sensual perfume of every kind—
as many sensual perfumes as you can;
and may you visit many Egyptian cities
to learn and go on learning from their scholars.
Keep Ithaka always in your mind.
Arriving there is what you're destined for.
But don't hurry the journey at all.
Better if it lasts for years,
so you're old by the time you reach the island,
wealthy with all you've gained on the way,
not expecting Ithaka to make you rich.
Ithaka gave you the marvelous journey.
Without her you wouldn't have set out.
She has nothing left to give you now.
And if you find her poor, Ithaka won't have fooled you.
Wise as you will have become, so full of experience,
you'll have understood by then what these Ithakas mean.

K.P. Kavafis, Poems (1933)
Translated by Edmund Keeley

Abstract

Spatial variability of seismic ground motions (SVGM) denotes the differences between two time histories of the ground motion recorded at different locations, generally at the ground surface. The modeling of SVGM and the understanding of its influence on the dam's response are necessary so as design codes start to incorporate its effects in their provisions. This study presents a measure and a profound investigation of SVGM at the dam-foundation rock interface of an arch dam. In-situ measurements are used to quantify SVGM and numerical simulations to deeper understand the particular physical phenomena that contribute to SVGM at the interface, i.e. local canyon topography and rock-structure interaction. The in-situ data comes from a seismological experimental campaign that has taken place on and around Saint Guérin arch dam over the period of six months. The campaign was held in the framework of the present thesis. The subset of events consists of low to moderate magnitude local and regional earthquakes. Thus, analysis is allowed in the linear range. Firstly, dynamic analysis of the arch dam is conducted; the frequencies of vibration, the damping coefficient and the crest amplification are estimated based on ambient noise and seismic records. Then, SVGM is quantified by means of phase and amplitude variability using coherency estimates and standard deviation of difference of Fourier amplitudes respectively. High variability is observed both in phase and amplitude at the dam-foundation rock interface. Once the estimators of variability are obtained from the data, parametric models are fitted to them. Focus is given on two observations : 1) the ground motions in the free field appear to be slightly less variable with respect to the motions at the dam-foundation rock interface and 2) at the dam-foundation rock interface, there is higher variability around the frequencies of vibration of the dam. These observations suggest that the presence of the structure along with the canyon topography increase SVGM. This increase though seems to be small given that the observations are satisfactory fitted by parametric models based on data coming from flat seismic arrays. Numerical simulations in the SPECFEM3D code, based on the spectral element method are used to deeper investigate the in-situ observations by decoupling the various causes of SVGM and evaluating the impact of each one. A parametric study using a simplified canyon topography attempts to identify the effect of local canyon topography on SVGM while a geometrically accurate model of the Saint Guérin arch dam and its canyon topography gives us a better insight on the dam-foundation rock interaction impact on SVGM. Although both features are found to increase SVGM, their impact remains secondary. The findings of the present research are contributing to enhance our understanding of SVGM at the dam-foundation rock interface and proposing variability models to be used in arch dams' design.

Key-words : *arch dams; spatial variability of ground motions; seismological instrumentation; canyon topography; dam-foundation rock interaction*

Résumé

Le terme variabilité spatiale des mouvements sismiques (SVGM en anglais pour Spatial Variability of Ground Motion) désigne les différences entre deux mesures du mouvement du sol effectuées à différents endroits, généralement en surface. La modélisation de SVGM ainsi que son effet sur la réponse dynamique des barrages est nécessaire pour l'intégration du phénomène dans les codes parasismiques. L'étude actuelle présente une mesure et une enquête approfondie sur SVGM à l'interface barrage voûte - fondation rocher. Des mesures in situ sont utilisées pour sa quantification et des simulations numériques pour la compréhension plus approfondie des phénomènes physiques qui contribuent à SVGM notamment à l'interface, c-à-d la topographie de la voûte et l'interaction sol-structure. Les données in situ proviennent d'une campagne sismologique qui a eu lieu sur et autour du barrage voûte du Saint Guérin pendant six mois. Le sous-ensemble d'événements consiste à des événements de faible à moyenne magnitudes, locaux et régionaux. Ainsi, des analyses linéaires sont permises. Tout d'abord, l'analyse dynamique du barrage voûte est réalisée; les fréquences de vibration, le coefficient d'amortissement et l'amplification de crête sont estimés profitant des mesures continues de bruit ambiant et des enregistrements sismiques. Ensuite, SVGM est quantifiée au moyen de la phase et de la variabilité d'amplitude en utilisant des estimations de cohérence et de l'écart type de la différence des amplitudes des spectres de Fourier respectivement. Une forte variabilité est observée à la fois en phase et en amplitude à l'interface du barrage-fondation rocher. Une fois que les estimateurs de la variabilité sont obtenus à partir des données, les modèles paramétriques existants sont comparés avec eux. L'accent est mis sur deux observations: 1) les mouvements sismiques au champ libre semblent être légèrement moins variable par rapport aux mouvements à l'interface barrage-fondation rocher et 2) à l'interface barrage-fondation rocher, il y a une variabilité plus forte autour des fréquences de vibration du barrage. Ces observations suggèrent que la présence de la structure ainsi que la topographie du canyon augmentent SVGM. Cette hausse semble cependant être faible étant donné que les observations sont déduites par des modèles paramétriques satisfaisants basés sur des données provenant de réseaux sismiques plates (sans topographie et structure). Des simulations numériques dans le code SPECFEM3D, basé sur les éléments spectraux, sont utilisées pour étudier plus profondément les observations in situ par le découplage des différentes causes de SVGM et évaluer l'impact de chacune. Une étude paramétrique en utilisant une topographie du canyon simplifié tente d'identifier l'effet de la topographie du canyon local sur SVGM tandis qu'un modèle géométrique précis du barrage voûte de Saint Guérin et la topographie du canyon nous donne une idée plus précise sur l'impact de l'interaction barrage-fondation rocher sur SVGM. Les résultats de cette recherche contribuent à l'amélioration de notre compréhension de SVGM à l'interface barrage-fondation rocher et proposent des modèles de variabilité à être utilisés dans la conception des barrages voûtes.

Mots-clefs : *barrages voûtes, variabilité spatiale des mouvements sismiques, instrumentation sismologique, topographie de la vallée, interaction barrage-fondation rocheuse*

Acknowledgements

Foremost, I would like to express my warmest gratitude and special appreciation to my advisor and mentor Prof. Frédéric Dufour. Your continuous support during the past five years on a professional and personal level, made the journey to my 'Ithaka' as pleasant as I could wish for. I greatly appreciate your immense knowledge, your priceless advices and your motivating words. All these made my Ph.D study (and all the related or not related research) possible to be completed. You contributed significantly to the research scientist that I have become.

Furthermore, I would like to express my sincere appreciation to my co-advisor, Emmanuel Chaljub. Your continuous guidance, your insightful comments, your endless motivation and our long discussions helped me to widen my scientific horizons and grow as a researcher.

My deep gratitude also goes to Prof. P.Y. Bard. Your valuable comments and suggestions were always offered to me when needed.

I would like to express my warm thanks to Nicolas Humbert. Our constructive discussions helped me to see things from a different point of view. My sincere thanks also go to Emmanuel Robbe and Eric Bourdarot for their helpful advices and guidance throughout my Ph.D thesis.

Moreover, I would like to thank Cécile Cornou, who, although not directly implicated to my thesis, definitely contributed to the final outcome. Your guidance in a professional and personal level, our stimulating discussions, but most importantly your belief in me, encouraged me the past five years.

Besides my advisors, I would like to thank the members of my thesis committee: Dr. Catherine Berge-Thierry, Prof. Pierre Léger, Dr. Francoise Courboulex and Prof. Fabrice Cotton for their insightful comments and suggestions, but also for the questions which leaded me to widen my research from various perspectives. I also want to thank you for letting my defense be an enjoyable moment. My special thanks and gratitude go to Prof. Fabrice Cotton for giving me the opportunity to start a new page in my career through the MEEES master program and, thereafter, supporting me in my small research steps.

Additionally, I would like to thank all the members that contributed to the experimental campaign in Saint Guérin and made it not only successful, but also pleasant (Isabelle, Sandrine, Éric, Marc, Armand, Clèment, Johanes, Maxime, Pauline, Bertrand...). Without your precious support it would not be possible to conduct this successful campaign.

I thank my fellow labmates and friends (Amarylis, Venetia, Zyenep, Olga, Tijan, Nikola, Angelos, Eleni, Timos, Alessandro, Bratislav, Fabio, Claudia, Capucine, Maxime, ...) for the long days and sleepless nights that we spent together during the past five years,

having fun and making life enjoyable in Grenoble or while travelling.
My deepest thanks go to my very good friends, Argyro, Evaggelia, Yolanda, Katerina, Fani and Themis for their presence in my life and their psychological support during my thesis. Alexandre, thank you for your encouragement, support, patience and understanding. Maria, thank you for the numerous discussions and happy moments you gave me, inside and outside our office. Busra and Alexandra, thank you for the endless days and nights we spent together, our discussions and laughs and your support at all levels. We entered harbors we were seeing for the first time, we learned and we go on learning. Last but not least, I would like to thank my family: my parents, Nikos and Polyxeni, and my brother, Sideris (my Iron man). I deeply thank you for supporting me spiritually throughout this thesis, but most importantly, I thank you for being always there in the ups and downs of my life. Your support made my journey to Ithaka possible; a journey that certainly made me rich.

Data and resources

This Ph.D thesis was performed thanks to the support of EDF in the context of Chair PERENITI run by the Fondation Partenariale Grenoble INP. Partners responsibility of the Chair cannot in any circumstances be blamed on the grounds of the content of the publication, which is only binding its author.

For the conduction of the experimental campaign, we thank SISMOB-RESIF that provided the 19 seismological stations.

The spectral element calculations were performed using the Froggy platform from the Calcul Intensif, Modélisation, Expérimentation Numérique et Technologique (CIMENT) HPC center of Grenoble Alpes University, which is supported by the Rhône-Alpes region (Grant CPER07 13 CIRA), the OSUG@2020 labex (reference ANR10 LABX56), and the Equip@Meso project (reference ANR-10-EQPX-29-01) of the Programme Investissements d'Avenir supervised by the Agence Nationale pour la Recherche.

Contents

Abstract iv

Résumé vi

Acknowledgements viii

Contents xi

List of Figures xiv

List of Tables xxvii

General Introduction 1

1 State of the art of spatial variability of the ground motions (SVGM) 7
- 1.1 SVGM . . . 8
  - 1.1.1 Wave passage, extended source and scattering effects . . . 8
  - 1.1.2 Local site effects - Canyon topography . . . 9
- 1.2 Seismological networks . . . 13
  - 1.2.1 Free field seismological networks . . . 13
  - 1.2.2 Dam seismological networks . . . 14
- 1.3 SVGM estimators . . . 14
  - 1.3.1 Phase variability estimator . . . 15
    - 1.3.1.1 Coherency estimator . . . 16
    - 1.3.1.2 Smoothing parameter . . . 21
    - 1.3.1.3 Time window selection . . . 22
    - 1.3.1.4 Statistical properties . . . 23
    - 1.3.1.5 Coherency modeling . . . 24
  - 1.3.2 Amplitude variability estimator . . . 27
    - 1.3.2.1 Difference of natural logarithm of Fourier amplitudes . . . 27
    - 1.3.2.2 Amplitude variability modeling . . . 28
- 1.4 Effect of SVGM on dams . . . 29

2 Seismological campaign in Saint Guérin 32
- 2.1 The Saint Guérin site . . . 33
  - 2.1.1 Seismotectonics and seismicity . . . 33
  - 2.1.2 Local geology . . . 36
  - 2.1.3 Saint Guérin arch dam . . . 37

2.2 Dense seismological array . . . 38
2.3 Data acquisition . . . 42
2.4 Earthquake catalog preparation . . . 46
2.4.1 Selection of subset of seismic events . . . 46
2.4.2 Example waveforms . . . 51
2.5 Dynamic analysis of the arch dam . . . 53
2.5.1 Frequencies of vibration . . . 54
2.5.2 Damping ratio . . . 58
2.5.3 Amplification on the dam crest . . . 60
2.6 Discussion . . . 62

3 SVGM in Saint Guérin 64
3.1 Time window selection . . . 66
3.2 Smoothing parameter . . . 68
3.3 Wave passage effect . . . 69
3.4 Phase variability analysis . . . 73
3.4.1 Lagged coherency estimates . . . 73
3.4.1.1 Sensitivity analysis . . . 80
3.4.1.2 Comparison with the free field motions . . . 89
3.4.2 Unlagged coherency estimates . . . 91
3.4.3 Comparison with existing coherency models . . . 95
3.5 Amplitude variability analysis . . . 100
3.5.1 Standard deviation of difference of Fourier amplitudes . . . 101
3.5.2 Sensitivity analysis . . . 102
3.5.3 Comparison with the free field motions . . . 106
3.5.4 Comparison with existing amplitude variability models . . . 107
3.6 Discussion . . . 110

4 Numerical analysis of the effect of canyon topography and dam-rock interaction on SVGM 114
4.1 Canyon topographic effect on SVGM . . . 115
4.1.1 Numerical modeling of the site . . . 116
4.1.2 Site with sinusoidal surface topography . . . 117
4.1.3 Array of receivers and seismic excitation . . . 119
4.1.4 Ground motions . . . 122
4.1.5 Phase variability analysis . . . 126
4.1.6 Amplitude variability analysis . . . 131
4.2 Arch dam-foundation rock interaction effect on SVGM . . . 134
4.2.1 Numerical modeling of the site and the arch dam . . . 135
4.2.2 Site and arch dam characteristics . . . 136
4.2.3 Ground motions . . . 137
4.2.4 Dynamic analysis of the arch dam . . . 139
4.2.5 Phase variability analysis . . . 140
4.2.6 Amplitude variability analysis . . . 142
4.2.7 Comparison of in-situ and numerical observations . . . 143
4.3 Discussion . . . 149

Conclusions and perspectives **151**

Bibliography **158**

A Appendix A: Array stations in Saint Guérin **176**
A.1 Coordinates of the array stations 176
A.2 Station separation distances 178
A.3 Data availability 180

B Appendix B: Seismological catalog of Saint Guérin events **181**
B.1 Seismological catalog of Saint Guérin events 181
B.2 Signal-to-noise ratio (SNR) of the velocity time series 183
B.3 Peak Ground Velocity values 185
B.4 Reference stations 188

C Appendix C: Dynamic analysis of Saint Guérin arch dam **190**
C.1 Frequencies of vibration 190
C.2 Damping ratio 192
C.3 Crest amplification 193

D Appendix D: Sensitivity analysis of lagged coherency on source characteristics **199**

E Appendix E: Numerical analysis in SPECFEM3D **206**

List of Figures

1 Causes SVGM at the arch dam-foundation rock interface: source, path and local site effects. 4

1.1 Illustration of the physical causes underlying the spatial variation of the seismic ground motion: (a) the wave passage effect, (b) the extended source affect (c) the scattering effect (d) the attenuation effect. The graphic illustrations are presented after Abrahamson [1993]. 8

1.2 Characterization of simple topographic irregularities: (a) notation for a triangular wedge; (b) approximation of actual ground surface (solid line) at trough and crest by wedges (after Faccioli [1991]). 11

1.3 Valley shapes and input wave types for which two-dimensional analyses of wave scattering effects have been reported (Council et al. [1991]). . . . 11

1.4 Example of an 11-point ($M = 3, M = 5, M = 7$) Hamming Window. . . . 22

1.5 5% cosine bell window taper applied at at each end of the earthquake time histories. 23

2.1 Plate tectonics context of Metropolitan France. Relative movements of plates are given with respect to Eurasia (considered as fixed). Zoom in the metropolitan France showing the major extensional faults (Baize et al. [2013]) and location of the arch dam of Saint Guérin. 34

2.2 Sismalp Catalog. Magnitude, M_L, as a function of epicentral distance, R_{epi}, from the dam in Saint Guérin for events recorded between 1989 and 2012. 35

2.3 Seismotectonic settings. The map shows the seismicity of the overall Western Alps from the SISMALP network (Thouvenot et al. [2003]) covering the period from 1986 to 2002. The black rectangle locates the Briançon GPS network area. Yellow stars indicate three published solutions for the emplacements of the Euler pole of the Adriatic microplate rigid counter-clockwise rotation with respect to Eurasia (Walpersdorf et al. [2015]). The location of the arch dam of Saint Guérin is also included. 35

2.4 Location of the arch dam of Saint Guérin on the seismic zonation map of France resulting from the ministerial decree of October 22, 2010. 36

2.5 Geological map of the Saint Guérin region; the location of the two stations on the left (SG05) and right (SG01) abutments of the dam are added. . . 37

2.6 Double curvature, 69 m high and 250 m long arch dam in Saint Guérin. . 38

2.7 Position of seismological stations on and around the dam of Saint Guérin. 39

2.8 Schematic representation of the position of seismological stations on and around the dam of Saint Guérin. 40

2.9 H/V spectral ratios at stations SG13, SG14, SG15, SG17, SG18, SG19 and SG20 based on ambient noise recordings of 1 hour at 06:00:00 the 1^{st} of October 2015. Solid black lines indicate the average value over all time windows and dashed black lines ± 1 standard deviation. 41

2.10 Schematic representation of station configuration: boxes containing the sensor and the digitizer, isolation of the sensor, concrete base and GPS antenna. 43

2.11 Station configuration: boxes containing the sensor and the digitizer, isolation of sensor of type Güralp CMG40T, sensor type Lenhartz 5 sec, Nanometrics Taurus digitizer and GPS antenna. 44

2.12 Power supply of stations: cables supplying stations directly from the dam, batteries inside their box, connected to the dam and solar panels supplying the isolated stations. 44

2.13 Data availability (%) per month recorded from the 19 stations. Numbering from 1 to 13 corresponds to months from June 2015 (1) to June 2016 (13). 46

2.14 Total number of available records for each of the 19 stations and total number of available recordings for each of the 55 selected events. 48

2.15 Map of the subset of 55 events chosen, recorded from the seismological array during the period of six months (July 2015 – December 2015). Green, yellow and red tacks on the map represent event locations with M_L [1.5 2], [2 3] and [3 4.1] respectively. The pink balloon indicates the location of the arch dam. 48

2.16 Local magnitude distribution (M_L) as a function of epicentral distance ($R_{epi}(km)$) (left), hypocentral depth (km) (middle) and back azimuth (BA (°)) (right) for the subset of 55 events. 49

2.17 Peak Ground Veloocity (PGV) distribution (mm/s) as a function of magnitude (M_L) and epicentral distance (R_{epi})(km) for the subset of 55 events (all available recordings) selected for analysis for both horizontal components, NS and EW. 50

2.18 Distribution of the ln of PGV (mm/s) of the 55 events for the NS component recorded at all stations. 50

2.19 Distribution of the ln of PGV (mm/s) of the 55 events for the EW component recorded at all stations. 51

2.20 Map of the example event: Event occurred on September 10, 2015 at UTC 07:32:08 with magnitude M_L 3.3 and epicentral distance 100 km (red point). The yellow tack indicates the location of the arch dam. . . . 52

2.21 Velocity time series for the the NS component recorded at stations SG01, SG02, SG04, SG05, SG06,SG07, SG08, SG09, SG11, SG12, SG13, SG14, SG15, SG17, SG18, SG19 and SG20 for the event that occurred on September 10, 2015 at UTC 07:32:08 with magnitude M_L 3.3 and epicentral distance 100 km. 52

2.22 Velocity response spectra and Fourier amplitude spectra for the the NS component recorded at the dam-foundation rock interface (i.e. SG01, SG05, SG06,SG07, SG08, SG09, SG10, SG11, SG12) for the event that occurred on September 10, 2015 at UTC 07:32:08 with magnitude M_L 3.3 and epicentral distance 100 km. 53

2.23 Fourier velocity spectral amplitudes of individual ambient noise records (grey lines) on the crest and at the dam foundation rock interface (20 minutes-long records two hours before each of the 55 events of Figure 2.15) and median value (black lines) of the three stations on the crest and the nine stations at the dam-foundation rock interface for the two horizontal and the vertical components (NS, EW and Z). 55

2.24 Median value of frequencies of vibration of the Saint Guérin arch dam estimated using 20 minutes-long records of ambient noise two hours before each of the 55 events of Figure 2.15; median value of Fourier velocity spectral amplitudes of the nine stations at the dam-foundation rock interface (right) and median value of Fourier amplitudes of the three stations on the crest (left) for the two horizontal and the vertical components (NS, EW and Z) is presented. 55

2.25 Median value of frequencies of vibration of the Saint Guérin arch dam estimated using 20 minutes-long records of ambient noise two hours before each of the 55 events of Figure 2.15; median value of unsmoothed Fourier velocity spectral amplitudes of the nine stations at the dam-foundation rock interface (right) and median value of unsmoothed Fourier amplitudes of the three stations on the crest (left) for the two horizontal components (NS and EW) is presented; zoom in the frequency range [2.5 10] Hz. . . . 56

2.26 Frequencies of vibration of the Saint Guérin arch dam estimated using 20 minutes-long records of ambient noise two hours before each of the 55 events of Figure 2.15; individual Fourier velocity spectral amplitudes and median value of Fourier amplitudes of the three stations on the crest (left) for the two horizontal and the vertical components (NS, EW and Z) is presented. 57

2.27 Eigen frequencies of the Saint Guérin arch dam estimated using 20 minutes-long records of ambient noise two hours before each of the 55 events of Figure 2.15; median value of Fourier velocity spectral amplitudes of the nine stations at the dam-foundation rock interface and median value of Fourier amplitudes of the three stations on the crest for the two horizontal and the vertical components (NS, EW and Z) is presented. 58

2.28 Amplification of the the crest of the dam (SG02, SG03, SG04 and median value of the motions at the three stations) with respect to the dam - foundation rock interface (median value of stations SG05, SG06, SG07, SG08, SG09, SG10, SG11 and SG12) based on seismic events recordings for the two horizontal and the vertical (NS, EW and Z) components. . . . 61

3.1 Velocity time series for the the NS comp. recorded at the stations of the Saint Guérin array for the event that occurred on September 10^{nth}, 2015 at UTC 07:32:08 with magnitude M_L 3.3 and epicentral distance, R_{epi}, 100 km. $S-$wave window chosen is represented by magenta color. 67

3.2 $S-$wave duration (identified using the method of normalized AI by Abrahamson [2007]) as a function of epicentral distance (R_{epi} in km) and local magnitude (M_L). 67

3.3 Median value of time lag estimations for all station pairs for the NS, EW and Z components. 69

3.4 Standard deviation of time lag for all station pairs for the NS, EW and Z components. 70

3.5 Median value of time lag estimations for all station pairs excluding SG19 and SG20, for the NS, EW and Z components. 70

3.6 Standard deviation of time lag for all station pairs excluding SG19 and SG20 for the NS EW and Z components. 70

3.7 Time lag estimations for all station pairs at the dam-foundation rock interface for a vertical wave propagation. 72

3.8 Cross correlation between the station pairs at the dam-foundation rock interface for the event presented in Figure 2.20; peak cross correlation time lags across the stations as a function of the associated station separation distance. 73

3.9 Total number of station pairs in each distance bin (m) at the dam foundation rock interface (DR) and in the free field (FF stands for free field station pairs SG13-SG14, SG14-SG15 with separation distance 40-80 m) . 74

3.10 Frequency and distance dependence of lagged coherency. 74

3.11 Individual median values of lagged coherency of all pairs along the dam-foundation interface with station separation distances [0 40] m, [40 80] m, [80 120] m, [120 160] m and [160 200] m for each event (gray lines) and median value of all events (black line) as a function of frequency for the NS component. 75

3.12 Individual median values of lagged coherency of all pairs along the dam-foundation interface with station separation distances [0 40] m, [40 80] m, [80 120] m, [120 160] m and [160 200] m for each event (gray lines) and median value of all events (black line) as a function of frequency for the EW component. 76

3.13 Individual median values of lagged coherency of all pairs along the dam-foundation interface with station separation distances [0 40] m, [40 80] m, [80 120] m, [120 160] m and [160 200] m for each event (gry lines) and median value of all events (black line) as a function of frequency for the NS component. 77

3.14 Lagged coherency as a function of frequency for the NS (left), EW (middle) and Z (left) components; median value of all the events within each distance bin along the dam-foundation rock interface (solid and dashed black lines). Frequencies of vibration identified on the Fourier spectra of the dam crest are represented by red lines and at the interface by blue lines. 77

3.15 Individual median values of ATANH(lagged coherency) of all pairs along the dam-foundation interface with station separation distances [0 40] m, [40 80] m, [80 120] m, [120 160] m and [160 200] m for each event (gray lines) and median value of all events (black line) as a function of frequency for the NS component. 78

3.16 Individual median values of ATANH(lagged coherency) of all pairs along the dam-foundation interface with station separation distances [0 40] m, [40 80] m, [80 120] m, [120 160] m and [160 200] m for each event (gray lines) and median value of all events (black line) as a function of frequency for the EW component. 79

3.17 Individual median values of ATANH(lagged coherency) of all pairs along the dam-foundation interface with station separation distances [0 40] m, [40 80] m, [80 120] m, [120 160] m and [160 200] m for each event (gray lines) and median value of all events (black line) as a function of frequency for the Z component. 80

3.18 Coherency residuals of individual median estimates of ATANH(lagged coherency) for each event with respect to the global median (ATANH units) of all the events as a function of magnitude of the NS component for epicentral distance bins of R_{epi} [0 100] km (magenta) and R_{epi} [100 350] km (blue). 82

3.19 Coherency residuals of individual median estimates of ATANH(lagged coherency) for each event with respect to the global median (ATANH units) of all the events as a function of epicentral distance of the NS component for magnitude bins of M_L [1.5 2.5] (magenta) and M_L [2.5 4.1] (blue). 82

3.20 Coherency residuals of individual median estimates of ATANH(lagged coherency) for each event with respect to the global median (ATANH units) of all the events as a function of back azimuth of the NS component. 83

3.21 Comparison of lagged coherency estimates for the NS and EW components on the right and left banks of the dam for station separation distances D [40 80] m and D [80 120] m. 84

3.22 $S-$wave duration chosen based on $0.05 < AI < 0.95$ (red squares) and $0.1 < AI < 0.75$ (black squares) as a function of epicentral distance (km) and magnitude (M_L). 86

3.23 Comparison of lagged coherency estimates for $S-$wave time windows based on $0.05 < AI < 0.95$ (red lines) and $0.10 < AI < 0.75$ (black lines). 86

3.24 Velocity time serie and selected windows for lagged coherency analysis of the the NS component recorded at station SG09, for the event that occurred on September 10, 2015 at UTC 07:32:08 with magnitude M_L 3.3 and epicentral distance, R_{epi} 100 km. 88

3.25 Comparison of lagged coherency estimates for $S-$wave time windows based on $0.10 < AI < 0.75$ (black lines), PGV$\pm$15 sec (red lines), 14 sec of coda waves (green lines) and ambient noise data (purple lines) for the NS component. 88

3.26 Comparison of lagged coherency estimates in the free field (red lines for station pairs SG13-SG14, SG14-SG15 and SG13-SG15 and magenta lines for SG17-SG18) and at the dam-foundation rock interface (black lines) for station separation distances D [40 80] m and D [80 120] m. 91

3.27 Individual median values of unlagged coherency of not aligned time histories of all pairs along the dam-foundation interface with inter-station distances [0 40] m, [40 80] m, [80 120] m, [120 160] m and [160 200] m for each event (gray lines) and median value of all events (black line) as a function of frequency for the NS component. 92

3.28 Individual median values of unlagged coherency of not aligned time histories of all pairs along the dam-foundation interface with inter-station distances [0 40] m, [40 80] m, [80 120] m, [120 160] m and [160 200] m for each event (gray lines) and median value of all events (black line) as a function of frequency for the EW component. 93

3.29 Individual median values of unlagged coherency of not aligned time histories of all pairs along the dam-foundation interface with inter-station distances [0 40] m, [40 80] m, [80 120] m, [120 160] m and [160 200] m for each event (gray lines) and median value of all events (black line) as a function of frequency for the Z component. 94

3.30 Unlagged coherency of not aligned time histories as a function of frequency for the NS (left) and EW (middle) and Z (left) components; median value of all the events within each distance bin along the dam-foundation rock interface (solid and dashed black lines). 94

3.31 Estimated lagged coherency as a function of frequency for the NS (black solid lines) and EW (gray solid lines) component; median value of all the events within each distance bin along the dam-foundation interface. Black dashed lines correspond to coherency estimates of Ancheta et al. [2011] model and black dotted lines to coherency estimates of Menke et al. [1990] coherency model every 10 m within each separation distance bin. . 97

3.32 Estimated lagged and unlagged coherency as a function of frequency for the NS (black solid lines) and EW (gray solid lines) component; median value of all the events within each distance bin along the dam-foundation interface. Dashed red and blue lines correspond to plane-wave and unlagged coherency estimates of Abrahamson [2006] models every 10 m within each separation distance bin. 100

3.33 Standard deviation of the difference of natural logarithm of Fourier spectral velocities of ground motion as a function of frequency for NS (left) and EW (right) component; black solid and dashed lines represent the median value of all the events within each distance bin along the dam-foundation interface, e.g [0 40] m, [40 80] m, [80 120] m, [120 160] m and [160 200] m. Frequencies of vibration identified on the dam crest are represented by red lines and at the interface by blue lines. 101

3.34 Amplitude variability residuals of individual estimates of standard deviation of difference of natural logarithm of Fourier spectral velocities for each event with respect to the global median of all the events as a function of magnitude, M_L of the NS component for epicentral distance bins of D [0 100] km and D [100 350] km. 103

3.35 Amplitude variability residuals of individual estimates of standard deviation of difference of natural logarithm of Fourier spectral velocities for each event with respect to the global median of all the events as a function of epicentral distance of the NS component for magnitude bins of M [1.5 2.5] and M [2.5 4.1]. 104

3.36 Amplitude variability residuals of individual estimates of standard deviation of difference of natural logarithm of Fourier spectral velocities for each event with respect to the global median of all the events as a function of back azimuth of the NS component. 104

3.37 Comparison of amplitude variability estimates for smoothed (Hamming window $M = 5$) and unsmoothed Fourier spectra for the three components (NS, EW and Z) and for all station separation distance bins at the dam-foundation rock interface. 105

3.38 Comparison of standard deviation of difference of natural logarithm of Fourier spectral velocities in the free field (red lines for SG13, SG14 and SG15 and magenta lines for SG17-SG18) and at the dam-foundation rock interface (black lines) for station separation distances D [40 80] m and D [80 120] m. 107

3.39 Standard deviation of difference of natural logarithm of unsmoothed Fourier spectral velocities as a function of frequency; black and gray solid lines represent the median value of all the events within each distance bin along the dam-foundation interface, e.g [0 40] m and [40 80] m, for NS and EW comp. respectively. Black dashed lines represent amplitude variability predictions of the Ancheta et al. [2011] model at each 10 m within the separation distance bins. 109

3.40 Standard deviation of difference of natural logarithm of smoothed Fourier spectral velocities as a function of frequency; black and gray solid lines represent the median value of all the events within each distance bin along the dam-foundation interface, e.g [0 40] m and [40 80] m, for NS and EW components respectively. Black dashed lines represent amplitude variability predictions of the Schneider et al. [1992] model at each 10 m within the separation distance bins. 110

4.1 20x30x15 km^3 site with sinusoidal topography implemented on the free surface, modeled in SPECFEM3D. 118

4.2 Refinement with mesh tripling layer of 1.8 km below the free surface of the model in SPECFEM3D. 118

4.3 Reference bedrock V_S and V_P velocity profile (m/s) proposed by Poggi et al. [2011]. 119

4.4 Location of the array of receivers (red disc) and of the double couple point source (red circle) for a plane ($H/L = 0$) and a sinusoidal ($H/L = 0.1$) topography (left up and down figures). Zoom in to the station array (right up and down figures). 120

4.5 Step time function in the time domain (left) and theoritical far field displacement spectrum radiated in the frequency domain (right) of the double couple point source. 121

4.6 Normalized velocity time series of the X horizontal component as a function of the distance of the station from the source following the free surface; Plane topography $H/L = 0$. $P-$, $S-$ and spurious reflected waves are pointed. 122

4.7 Normalized velocity time series of the X horizontal component as a function of the distance of the station from the source following the free surface; Sinusoidal topography $H/L = 0.1$. $P-$, $S-$ and surface waves are pointed. 123

4.8 Normalized velocity time series of the X horizontal component as a function of the distance of the station from the source following the free surface; Sinusoidal topography $H/L = 0.2$. 123

4.9 Normalized velocity time series of the X horizontal component as a function of the distance of the station from the source following the free surface; Sinusoidal topography $H/L = 0.33$. 124

4.10 Normalized velocity time series of the X horizontal component as a function of the distance of the station from the source following the free surface; Sinusoidal topography $H/L = 0.5$. 124

4.11 Velocity time series (m/s) (X horizontal component) of all receivers for all canyon topographies, i.e. $H/L = 0$, $H/L = 0.1$, $H/L = 0.2$, $H/L = 0.33$ and $H/L = 0.5$. 125

4.12 Aligned velocity time series (m/s) recorded from all receivers for all canyon topographies, i.e. $H/L = 0$, $H/L = 0.1$, $H/L = 0.2$, $H/L = 0.33$ and $H/L = 0.5$. 125

4.13 $S-$wave window selected for all receiver recordings and all canyon topographies, i.e. $H/L = 0$, $H/L = 0.1$, $H/L = 0.2$, $H/L = 0.33$ and $H/L = 0.5$. 128

4.14 Total number of receiver pairs in each distance bin (m) at the canyon walls. 128

4.15 Median lagged coherency estimates for all distance bins along the valley, i.e. [0 400] m, [400 800] m, [800 1200] m, [1200 1600] m and [1600 2000] m, as a function of frequency for each canyon topography, i.e. $H/L = 0$, $H/L = 0.1$, $H/L = 0.2$, $H/L = 0.33$ and $H/L = 0.5$. 129

4.16 Median lagged coherency estimates within each distance bin along the valley, i.e. [0 400] m, [400 800] m, [800 1200] m, [1200 1600] m and [1600 2000] m, as a function of frequency for all canyon topographies, i.e. $H/L = 0$, $H/L = 0.1$, $H/L = 0.2$, $H/L = 0.33$ and $H/L = 0.5$. 129

4.17 Comparison of lagged coherency estimates for $S-$wave time windows (black lines) and entire signal (red lines) for all canyon topographies, i.e. $H/L = 0$, $H/L = 0.1$, $H/L = 0.2$, $H/L = 0.33$ and $H/L = 0.5$. 131

4.18 Standard deviation of the difference of natural logarithm of Fourier velocities of ground motion for all distance bins along the valley, i.e. [0 400] m, [400 800] m, [800 1200] m, [1200 1600] m and [1600 2000] m, as a function of frequency for each canyon topography, i.e. $H/L = 0$, $H/L = 0.1$, $H/L = 0.2$, $H/L = 0.33$ and $H/L = 0.5$. 132

4.19 Standard deviation of the difference of natural logarithm of Fourier velocities of ground motion within each distance bin along the valley, e.g [0 400] m, [400 800] m, [800 1200] m, [1200 1600] m and [1600 2000] m, as a function of frequency for all canyon topographies, i.e. $H/L = 0$, $H/L = 0.1$, $H/L = 0.2$, $H/L = 0.33$ and $H/L = 0.5$. 133

4.20 Comparison of lagged coherency estimates for $S-$wave time windows (black lines) and entire signal (red lines) for all canyon topographies, i.e. $H/L = 0$, $H/L = 0.1$, $H/L = 0.2$, $H/L = 0.33$ and $H/L = 0.5$. 134

4.21 SPECFEM3D model of 20x30x15 km^3 site, Saint Guérin local canyon topography, arch dam and name of nodes at the dam-foundation rock interface and on the crest (up-stream nodes represented by black and down-stream nodes by green color). 136

4.22 Velocity time series recorded from the array along the canyon without and with the arch dam; entire signal and zoom in of the records from 0 to 1 or 2 sec. 138

4.23 Velocity time series recorded from the array along the dam's crest. 138

4.24 Eigen frequencies of the model of Saint Guérin arch dam estimated using a double couple point source; Fourier spectral velocities of the receivers on the crest and at the dam-foundation rock interface for the X component; black lines correspond to the median value of all spectra on the crest and at the dam-foundation rock interface. 140

4.25 Comparison of median value of lagged coherency within each distance bin along canyon walls, i.e. [0 40] m, [40 80] m, [80 120] m, [120 160] m and [160 200] m without and with the presence of the dam (black lines); the blue line represents the frequencies of vibration at the dam-foundation rock interface as estimated on the crest. 141

4.26 Fourier spectrum and phase as a function of frequency for receiver 3D161 at the dam-foundation rock interface (left abutment). 141

4.27 Comparison of median value of standard deviation of natural logarithm of Fourier amplitudes within each distance bin along canyon walls, i.e. [0 40] m, [40 80] m, [80 120] m, [120 160] m and [160 200] m without and with the presence of the dam (black lines); the blue line represents the frequencies of vibration at the dam-foundation rock interface as estimated on the crest. 143

4.28 Comparison of frequencies of vibration of the arch dam between the Saint Guérin NS comp. (black solid lines) and the numerical model of the arch dam X comp. (black dashed lines). 145

4.29 Ratio between the spectra at the crest and at the interface : Fourier spectra (left) and Response spectra (right) of velocity time series. The median spectrum of the crest receivers with respect to the median spectrum of the receivers at the dam-foundation rock interface are presented for the Saint Guérin NS comp. (black solid lines) and numerical model of the arch dam X comp. (black dashed lines). 146

4.30 Comparison of the time lag between each pair of receivers at the dam-foundation rock interface as a function of their receiver separation distance (m) between the Saint Guérin observations, NS comp., (black squares) and the SPECFEM3D model of the arch dam, X comp. (blue squares). . 147

4.31 Comparison of the lagged coherency estimates of the pair of receivers at the dam-foundation rock interface between the Saint Guérin NS comp. (black solid lines) and the SPECFEM3D model of the arch dam X comp. (black dashed lines). 148

4.32 Comparison of the standard deviation of difference of natural logarithm of Fourier amplitudes of the pair of receivers at the dam-foundation rock interface between the Saint Guérin NS comp. (black solid lines) and the SPECFEM3D model of the arch dam X comp. (black dashed lines). . . . 148

List of Tables

2.1 Data availability recorded from the 19 stations. The left column indicates the period between two visits. Green rectangles indicate $95-100\%$ of data availability and red rectangles $\leq 50\%$ of data availability. The gray zones correspond to absence of data due to the removal of a station. 45

2.2 Average signal-to-noise ratio (SNR) of the velocity time series of the two horizontal components for each station for the 55 selected seismic events. 47

2.3 Number of selected events for each magnitude (M_L), epicentral distance ($R_{epi}(km)$) and back-azimuth (BA (°)) group. 49

2.4 Mean value of damping ratio, $\xi\%$, of the available data out of the subset of 55 events for the three crest stations SG02, SG03 and SG04 and median value of all the three stations for NS, EW and Z component. 59

3.1 Plane-wave coherency model coefficients of Abrahamson [2007] model for the horizontal component. 99

4.1 Characteristics of the double couple point source 121

General Introduction

Plainly, these are the causes, and this is how many they are. They are four, and the student of nature should know them all, and it will be his method, when stating on account of what, to get back to them all : the matter, the form, the thing which effects the change, and what the thing is for.

Aristotle, 'Physics'

Earthquake, also known as quake, tremor or seismic (greek: $\sigma\varepsilon\iota\sigma\mu\iota\kappa$o) event, is the perceptible shaking of the surface of the earth (i.e ground motion), resulting from the sudden release of energy due to rock slip in the earth's crust. The rock slip of the earth's crust creates seismic waves. The complexity of the earthquake source, the propagation path of the generated waves and the site effects at a certain location on the earth's surface are the factors that determine the characteristics of the ground motion.

Earthquake is one of the deadliest natural hazards for human civilization. In terms of human and economic lose, seismic shaking is the most significant factor contributing to the overall earthquake hazard. There are no means to prevent such a physical phenomenon yet. The damage caused by an earthquake is a combination of the intensity of the ground motion and the vulnerability of the engineered structures. The inevitable risk due to the location of urban centres near major faults as well as the growing urbanization in such regions combined with the risk due to construction of large and extended structures challenges the engineering and seismological community to better understand the physical processes associated with seismic ground motion. Despite the extensive efforts during the last century, currently there is no possibility to predict short term occurrence of earthquakes with accuracy in terms of location, size and time. Thus, the engineering community has focused its efforts on appropriate planning and construction measures to reduce earthquake damages. Experience from past earthquakes demonstrates that engineered structures built according to modern structural codes, typically later than about 1980, face limited damage.

Dams, a barrier that impounds water or underground streams, constitute an important part of the global infrastructural system. The hazard posed by dams has been detected since the 1920s by the damages experienced from several dams of all types and in many parts of the world. It became evident that the seismic design concepts based on which most existing dams were built at the time, needed to be re evaluated. This, coupled with the continuous expansion of the population at risk in locations downstream of major dams led to extensive research during the last decades. Thankfully, no total failure of a concrete dam has resulted from earthquake excitation to the extent that the reservoir was released, even though more than 100 concrete dams of all types have been subjected to measurable shaking due to earthquakes in many parts of the world. It has to be noted however that in very few of these cases measurements of the intensity of shaking were actually made. The only complete collapses of concrete dams have been occurred due to failures in the foundation rock supporting the dams. The Hsinfengkiang dam in China and Koyna dam in India are the only two significant examples of earthquake damages to concrete dams in 1960s. No flooding damage occurred in any of the two cases; however major repairs and strengthening was required. Other concrete dams have been subjected to significant earthquake motions but have suffered only minor or no damage. Given the risk, such failure examples, even though rare, enhance the effort of the engineering

community to both monitor existing concrete dams in seismic regions and perform more adequate design of new dams planned in such regions.

The definition of the expected seismic excitation and the evaluation of the response of the dam to this input are the major tasks of the engineer. The seismic inputs, as specified in most criteria, are the design basis earthquake (DBE) and the maximum credible earthquake (MCE). The DBE is defined as the greatest earthquake excitation expected to occur at least once during the life of the dam (possibly 100 years) and the MCE is the greatest earthquake excitation that could ever occur at the dam site. First, the linear structural response is calculated assuming that the dam is a linear system in which the displacements are directly proportional to the input excitation. Thereafter, to establish the ultimate resisting capacity of the dam, damage mechanisms and the resulting non-linearities are considered. The evaluation of data from dynamic tests (i.e real earthquake response information, laboratory and field test data) follows. Finally, to ensure the earthquake performance of the dam, suitable performance criteria are established.

The input seismic motion for the seismic evaluation of an existing or newly constructed dam is directly deducted from the dam site. Either according to extensive seismic hazard analysis of the site or following the recommendations of a structural code regarding the type of the soil, the ground motion to be expected at this site is defined. The input motion corresponds to three components, two horizontal and one vertical, at the ground surface in a free field location. In the seismic response analysis, difficulty is faced on defining the transfer function between the free field motions and the motions of the points at which the structure is supported. Thereafter a major question rises concerning how the defined input earthquake motions should be applied to the supports of the dam. In the recent years, analytical procedures have been developed that account for the transfer function between the free-field earthquake motions and the motions at the dam-foundation rock interface. Regarding the application of the motions at the supports, traditionally, the assumption of the input motion applied to a rigid base is made. This assumption can be valid for lightweight relatively small dams, such as earth dams, supported in hard foundation rock, but becomes inadequate for massive stiff concrete dams supported by very broad foundation rock surfaces or irregular topographies, such as arch dams. In the later case, there may be significant variations between the motions at widely spaced points at the dam-foundation interface.

Spatial variability of seismic ground motions (SVGM) denotes the differences between two time histories of the ground motion recorded at different locations, generally at the ground surface. A few such reports of spatially variable motions on dams do exist, mostly for abutment motions. Differential motions have been observed at the two abutments of the Tonoyama arch dam in 1964, of the Tagokura gravity dam and the Kurobe arch dam, all of them in Japan. A number of theoretical studies since the 1990s has

been trying to simulate SVGM at highly idealized dam-canyon interfaces. In this case the free field motion is defined as the motion of the dam-foundation rock interface due to seismic excitation without the presence of the dam. In-situ installation of seismological networks at the canyon sites of existing dams along with installations in free field sites in canyons where dams might be built are very helpful in order to quantify SVGM and define the earthquake input motion within the dimensions of the dam. However, the lack of such experimental campaigns of case-studies delays the better understanding and modeling of this physical phenomenon. Some important questions that still remain without answer are: Is SVGM important at a canyon topography of a stiff rock site? Does the presence of large, mat and rigid foundations, such as this of arch dams, affects SVGM? Our research work attempts to give an answer to these two critical questions.

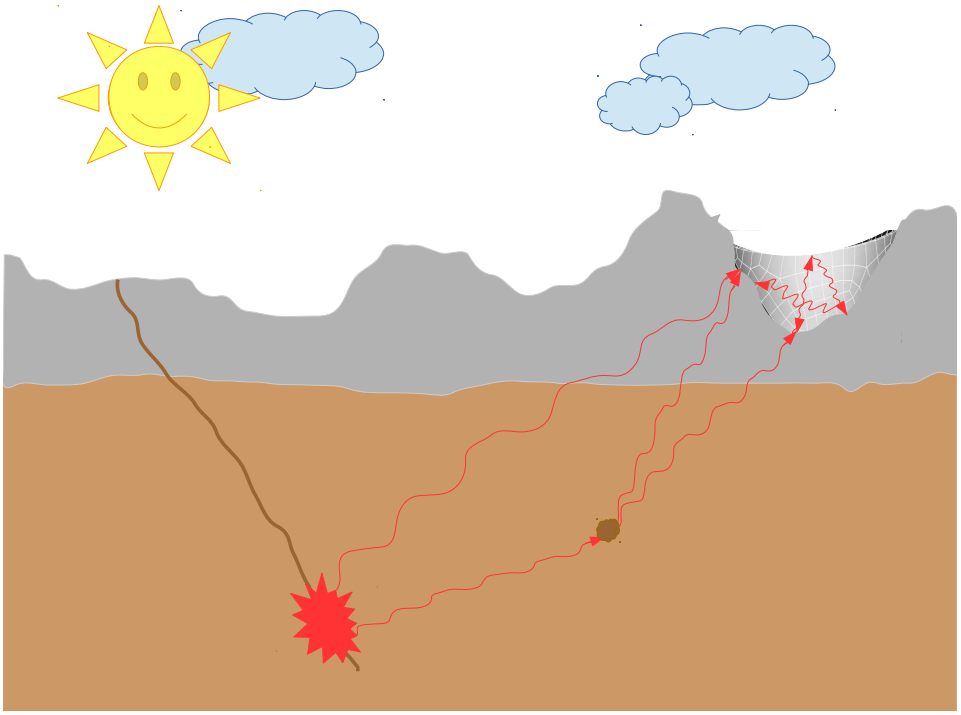

FIGURE 1: Causes SVGM at the arch dam-foundation rock interface: source, path and local site effects.

The main goal of the present thesis is to understand the key parameters that locally control SVGM at dam-canyon interfaces aiming to contribute in the future development and calibration of input motion models accounting for SVGM. It consists of two main parts. The first part is dedicated to the quantification and analysis of SVGM along a dam-foundation rock interface based on in-situ measurements of a case-study of an arch dam. The second part investigates the decoupled contribution of the canyon topographic effect and the soil-dam interaction effect on SVGM using numerical simulations of idealized media and topographies.

The thesis begins (Chapter 1) with a summarized state of the art on the subject of

SVGM. The main causes of the phenomenon are briefly explained and the available seismological networks worldwide, used for better understanding of SVGM, are summarized. Then, the estimators used for its quantification, decoupled in two parts, i.e. phase and amplitude variability, are described. Finally, the effect that this physical phenomenon has on dams is discussed. The literature review helps us summarize the knowledge that has been acquired on the subject as well as identify the research gaps that the scientific community is called to answer.

Having identified the weak points and gaps related to SVGM at the dam-rock interface, we chose two approaches that we consider complementary, experimental campaign and numerical simulations, targeting to answer the open questions that we are called to deal with in the present thesis. The seismological experimental campaign that was performed in the framework of the present thesis in Saint Guérin is extensively presented in Chapter 2. We provide an overview of the seismotectonics, seismicity and geology of the alpine area where the arch dam of our case study is located. The dense array located on and around the arch dam is presented in details along with the catalog of a selected number of recorded earthquakes. This dense network offers a complete catalog of both ambient noise and seismological data. To get a better insight into the structural system, a preliminary analysis of the dynamic behavior of the arch dam (frequencies of vibration, damping ratios and crest amplification) is conducted, taking advantage of the available seismological and ambient noise data.

The quantification of SVGM at the dam-foundation rock interface, which is the first task of our study, is performed in Chapter 3 using the earthquake data recorded from the dense seismological array. The chapter offers a detailed description of the parameters used for phase and amplitude variability analysis. Variability estimates at the dam-foundation rock interface for the subset of events are provided along with their interpretations. Sensitivity analyses of the results on various sources and site characteristics are also conducted. The phase and amplitude variability observations at the dam-foundation rock interface are compared with the free field observations as well as with existing variability models. This comparison allows us to conclude regarding the applicability of conventional SVGM models on the case of arch dams.

The quantification of SVGM using in-situ measurements opens the discussion regarding two particular physical phenomena that are occurring at the canyon topography along the dam-rock interface. The decoupled contribution of 1) the canyon topographic effect and 2) the soil-dam interaction effect on SVGM is examined using numerical simulations of idealized media and topographies in Chapter 4. A parametric study, using an idealized canyon topography, is conducted to get a better insight into the effect of the local canyon topography on the estimation of SVGM. The effect of soil-arch dam interaction is investigated by modeling the Saint Guérin arch dam and a simplified version of its local canyon topography.

The last section wraps up the main findings of this study. Its main contribution is that it enlightens several physical phenomena occurring at the dam-foundation rock interface and defines parametric models of seismic input motion at the interface that account for SVGM. This part gives our answer to the two aforementioned questions. At the same time, numerous perspectives open based on our findings that we are called to further investigate.

Chapter 1

State of the art of spatial variability of the ground motions (SVGM)

Here and elsewhere we shall not obtain the best insigth into things
until we actually see them growing from the beginning.
Aristotle, 'Politics'

1.1 SVGM

Spatial variability of ground motions (SVGM) refers to the similarity between two recorded ground motions of the same event in amplitude and phase content. These two time histories can be recorded either over extended areas on the ground surface or even within the dimensions of an engineered structure over a short distance. The ground motion at a given site is affected by different factors that can be broadly grouped into source (magnitude, slip distribution etc.), path (site-to-source distance, travel path geology, attenuation etc.), and site effects (local geology and topography). In the literature, four main causes of SVGM have been identified (Harichandran [1999], Hao et al. [1989], Abrahamson [1993]), namely, wave passage effect (path and local site effect), extended source effect, scattering effect (path and local site effect) and attenuation effect (path effect).

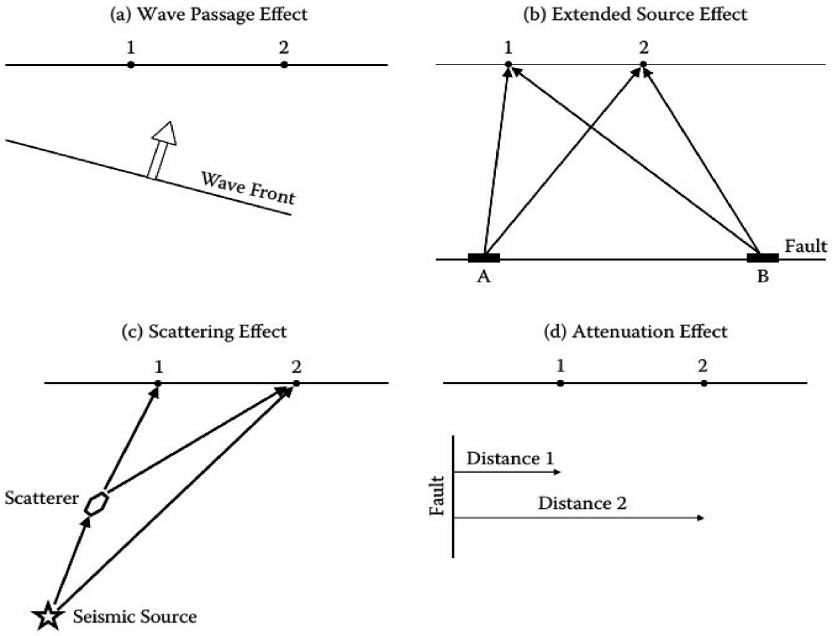

FIGURE 1.1: Illustration of the physical causes underlying the spatial variation of the seismic ground motion: (a) the wave passage effect, (b) the extended source affect (c) the scattering effect (d) the attenuation effect. The graphic illustrations are presented after Abrahamson [1993].

1.1.1 Wave passage, extended source and scattering effects

The wave passage effect is the most commonly recognized cause for SVGM. It is defined as the systematic spatial variation due to difference in arrival times of seismic waves over a short distance due to inclined incidence of propagating plane body waves or horizontally propagating surface waves. Due to the inclined incidence arriving at the site,

seismic waves arrive at different times at different locations on the ground surface. This wave passage time delay between two locations introduces a shift in the Fourier phases of earthquake ground motions, which is possible to be estimated in a deterministic way. The wave passage effect is illustrated in Figure 1.1a (after Abrahamson [1993]).
Differences in the way multiple waves are combined when arriving from an extended source (Figure 1.1b, after Abrahamson [1993]), cause differences particularly in the phase content but in the magnitude as well of the ground motions of two distant points. This is the so called 'extended source effect'. In the case of this phenomenon, as rupture propagates along an extended fault, especially when the rupture kinematics is highly heterogeneous (variable slip, variable rake, rise time, rupture velocity), it transmits energy that arrives delayed on the ground surface, resulting in variability in the waveforms in terms of phase and amplitude at the various locations.
The scattering effect is an additional, very important, cause of variability. This effect is the combination of multiple waves scattered, i.e. refracted or diffracted irregularly, by irregularities and local heterogeneities along their propagation path from the source to the site (Figure 1.1c, after Abrahamson [1993]). When waves are propagating away from the source they encounter scatterers/collisions that modify their waveforms and direction of propagation; they are forced to deviate from a straight trajectory by one or more paths due to localized non-uniformities in the medium through which they pass. Scattering causes random Fourier phase and amplitude variations.
The attenuation effect (Figure 1.1d) of the waves as they travel away from the source to the site contributes to these variations. As a seismic wave propagates through a medium, the elastic energy associated with the wave is gradually absorbed by the medium, eventually ending up as heat energy. This is known as absorption (or anelastic attenuation) and will eventually cause the total disappearance of the seismic wave (Toksoz & Johnston [1981]). The rate of attenuation increases with frequency, i.e. dispersive behavior (dispersion means that waves of different wavelength propagate at different phase velocities). Abrahamson [1992b] proposes that for site conditions being assumed to be homogeneous, SVGM would be caused by the wave passage effect and complex source-site wave scattering. Thus SVGM would be a result of deviations from 1D plane layered velocity models.

1.1.2 Local site effects - Canyon topography

The local site effect, meaning differences in local conditions at each station and its neighborhood, may alter the amplitude, frequency content and duration of the motion. Local site effects refer to physical phenomena arising from the propagation of complex seismic waves in near-surface geological formations (shallow substructures) or in geometrically

irregular configurations on the earth surface. Earthquake ground motion affected by these irregularities tends to increase in amplitude, and often in duration. In case of sedimentary valleys, the seismic waves get trapped within the valley and surface waves develop at the basin edge leading to large amplification on the sediment sites compared to the rock sites (e.g. Graves [1993]).

Topographical irregularities have been recognized as a cause of spatial variations in the intensity and phase content of ground motions (among others Council et al. [1991], Trifunac [1973], Sanchez-Sesma & Rosenbleuth [1979], Wong & Trifunac [1974], Wong [1982], Sanchez-Sesma et al. [1986], Kramer [1996]). A schematic representation of simple topographic irregularities at trough and crest by wedges is presented in Figure 1.2 after Faccioli [1991]. Analysis of topographic irregularities is a complicated problem; the interaction of waves can produce complex patterns of amplification and de-amplification, depending on the geometry of the irregularity and on the types, frequencies and angles of incidence of the incoming waves (Sánchez-Sesma & Campillo [1993]). The scattering and diffraction of the incident seismic waves generated from local topography may generate either large amplifications or reductions of ground motion over short distances (Council et al. [1991]). These phenomena have been studied, under the assumption of elastic behaviour, for different types of waves and surface relief. A canyon with constant cross section for some distance up-stream and down-stream can be represented as a linearly elastic half-plane. Therefore, the free field motion can be evaluated using the canyon as a scatterer. The simplest case involves only horizontal incident shear waves, SH, so that only out-of-plane displacements occur. In more realistic geometries of canyons, other types of incident waves, i.e P (primary compression waves), SH and SV (horizontal and vertical shear waves) and *Rayleigh* (surface) waves, should be considered. Figure 1.3 shows valley shapes and input wave types for which two-dimensional analyses of wave scattering effects have been reported in the literature (Council et al. [1991]).

The three main factors on which the motions at the canyon walls depend on are found to be the ratio of canyon width to wavelength (related to wave frequency), the angle of wave incidence and the wave type (Council et al. [1991]). When the wavelength is of the same order as or smaller than the canyon width then the effect of scattering becomes more significant. The free field motion at the canyon surface can be either amplified or reduced depending on the location of the observation point. Generally, motions near the upper corner of the canyon facing the incident wave are amplified; the amplification increases as the wavelength decreases and as the direction of incidence tends toward the horizontal. Trifunac [1973], Wong & Trifunac [1974] and Wong [1982] studied the scattering of different types of waves from a semi-cylindrical and semi-elliptical canyon and the effect of surface topography on the diffraction of the waves. They found that the surface amplification around and in the canyon changes rapidly from one point to the other and the maximum amplification is 2 for these types of canyons. Wong & Jennings

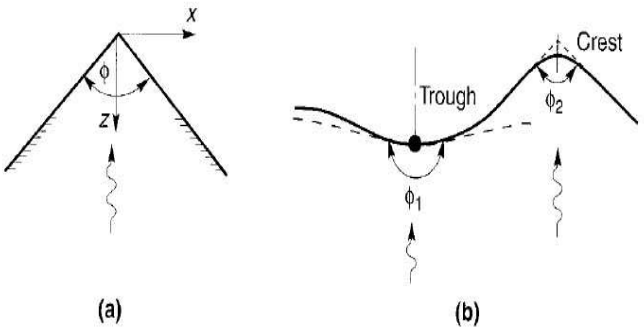

FIGURE 1.2: Characterization of simple topographic irregularities: (a) notation for a triangular wedge; (b) approximation of actual ground surface (solid line) at trough and crest by wedges (after Faccioli [1991]).

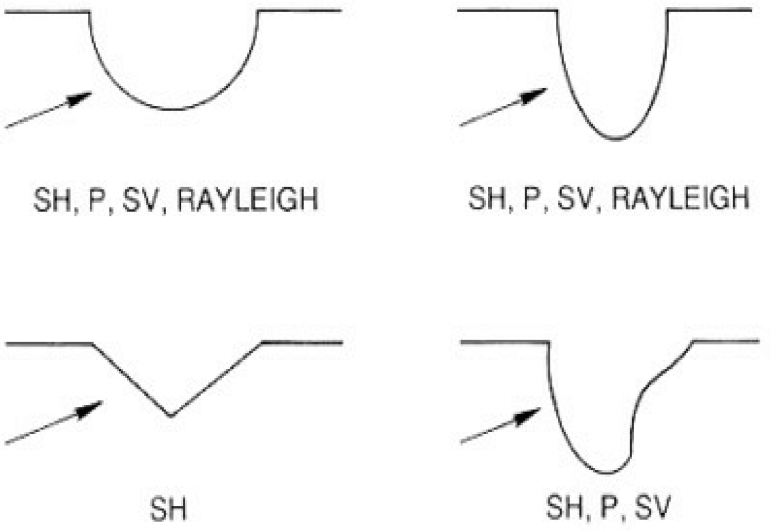

FIGURE 1.3: Valley shapes and input wave types for which two-dimensional analyses of wave scattering effects have been reported (Council et al. [1991]).

[1975] found that this amplification factor can be higher due to the trapped energy if the canyon surface has local convex regions. Motion from SH and *Rayleigh* waves generally is reduced near the bottom of the canyon (Council et al. [1991]). Sanchez-Sesma & Rosenbleuth [1979], analysing the ground motion at canyons of arbitrary shape found that for vertically incident SH waves, the wall slope of a triangular canyon has significant effects on the motion at the wall surface; steeper slopes lead to greater reductions in motion near the bottom of the canyon. An effort to define an averaged index of input motion intensity including the topographic effect based on simple semi-cylindrical topography and SH incident waves was made by Sanchez-Sesma et al. [1986]; this index is dependent on the location and the angle of incidence. More recently, Lee et al. [2009], using digital terrain model (DTM) data, and simulating three-dimensional seismic wave propagation demonstrated that seismic shaking in mountainous areas is strongly affected by topography and source frequency content, i.e. amplification of motions of a factor 2 at the tops of hills and ridges whilst lower levels of ground shaking at the valleys and flat-topped hills; higher amplification was also found in some parts of valleys where brooks eroded the ground surface, resulting in steep topography. Regarding the source frequency content, they found that a higher source frequency results in more small-scale perturbations and larger peak values along the profile, to the contrary of a lower source frequency that results in a smooth distribution of PGA amplification; this result is due to the fact that high-frequency waves interact with small-scale topography, which further amplifies the peak values. Faccioli et al. [2002], investigating the topographic amplification for a historical earthquake in a mountainous region in Italy found out approximatively one intensity degree increase at locations on hilltops, crests and severely sloping ground. The topographic amplification factors specified in the current version of Part 5 of the CEN [2005] range between 1.2 and 1.4, depending on the geometry of the irregularity. Trifunac [1973] analysed the phase variation for SH waves incident to a semi-circular canyon concluding that near the upper corners of the canyon more abrupt variations of phase angle appear.

The majority of the approaches for the estimation of amplification that are mentioned above are based on the assumption of 1-D, $S-$wave propagation through soil columns. This approximation however, although may be valid for ground-surface locations that are far apart from each other and in the absence of surface waves, it cannot capture the complex constructive interference of the waveforms occurring at sites with irregular surface and subsurface topography, nor the generation of additional, types of waves. Moreover, it can be noticed that the scientific community has focused its efforts on the magnitude variability of the motions in terms of amplification using numerical studies and in-situ observations while regarding the phase variation of motions along the canyon walls research is very limited. Complementary analyses are required in order to define phase SVGM along the canyon walls.

1.2 Seismological networks

The seismological recordings coming from dense seismological arrays provide valuable information for completing the understanding and therefore modeling this physical phenomenon. In-situ observations can complete analytical studies, such as the ones presented above, for identifying and deeper understanding SVGM. Several permanent and temporary arrays have been and are being deployed around the world aiming to further promote research on the scientific field of the characteristics of seismic ground motions.

1.2.1 Free field seismological networks

The majority of the installed arrays were/are located in free field uniform ground conditions and mostly at soil sites. The El Centro differential array was one of the first to be installed (Bycroft [1980b]); it was deployed in a soil site. Seismic recordings coming from the Strong Motion Array located in Lotung, in the north-east corner of Taiwan, named SMART-1 (Iwan [1979]), are from the most used ones. Within the SMART-1 array, a smaller scale array was installed, the Lotung Large Scale Seismic Test (LSST) array (Bolt et al. [1982]). These arrays offer the largest set of dense-array strong motion recordings. Among several other soil site arrays that have been widely used for research purposes are the Imperial Valley array (Bycroft [1980b]), the Chiba array (Yamazaki & Shimizu [2000]), the Hollister differential array (Schneider et al. [1992]) and the Stanford temporary array (Schneider et al. [1992]). Rock site arrays, on the other hand, are more limited in number than soil site arrays. Among others are the Coalinga temporary array (Schneider et al. [1992]), the USGS Parkfield array (Abrahamson et al. [1991]), the EPRI Parkfield array (Schneider et al. [1992]) and the Pynion Flat Array (Schneider et al. [1992]). These dense arrays have recorded strong (max M_L 7.8) and weak motions (min M_L 2.0) with minimum station separations varying from 3 m to 1 km. The recorded PGA values reach up to 0.89 g.
The majority of arrays were/are implemented in locations with uniform ground conditions and no particular topographic irregularities; exception is the USGS Parkfield array located over an area with significant topographic variations. Extrapolation of the use of data coming from free field flat arrays to non-uniform site conditions or different configuration of local sites needs to be verified. It would be of great scientific interest to complete the seismic databases with data coming from arrays with non-uniform ground conditions, irregular topographies as well as dense arrays located on and around engineered structures. Such datasets would contribute to further study a wide range of physical phenomena related to seismic ground motions such as soil-structure interaction and local site effetcs.

1.2.2 Dam seismological networks

The topic of strong-motion instrumentation placed at concrete dam sites for the purpose of studying SVGM has not received sufficient attention. Traditionally, for recording the input motion it was considered adequate to have one strong-motion recorder at either the toe of the dam or one of the abutments (Council et al. [1991]). Later on, one of the array types suggested was the "local effect array" that could be used to study the "variation of ground motions across valleys." But in that suggestion the emphasis was clearly on the motion of the overburden soil in a valley rather than that along a canyon wall (Council et al. [1991]). Thus, the number of very dense seismological arrays located on and around dams remains limited.

Seismological networks in Pacoima arch dam have recorded several moderate to strong ground motions. Other networks that have recorded earthquake motions on dams are on the Ambiesta arch dam in Italy (Castoldi [1978]), the Chirkey arch dam in the Soviet Union (Skorik [1981]), the Techi dam site in Taiwan (Clough et al. [1982]), the Nagawado arch dam in Japan (Fujii et al. [1987], Katayama & Tsuzuki [1987]). One of the very first identification of differential motions at the two abutments of dams was made in Tonoyama arch dam in Japan in 1964 (Okamoto et al. [1964a]). Similarly, differential motions have been also observed in the Tagokura gravity dam (Alarcon [1975]) and the Kurobe arch dam in Japan (Nose [1970]). Among the very few dam arrays are the dense accelerometric networks on concrete dams installed in Switzerland in 1990s; the Mauvoisin, Emosson and Punt-dal-Gall arch dams, the Grande-Dixence high gravity dam and the Mattmark high embankment dam (Darbre [1995]) were instrumented with several stations.

The measuring of free-field and interface input motion has been recognized to be as important as that of the dam response (MacDonald & Viksne [1980]). The majority of the aforementioned available seismological instrumentations on dams consist of a limited number of stations on the dams' scale. Arrays consisting of a big number of stations covering the dam-rock interface, the crest and the surrounding area would contribute significantly for the purpose of defining seismic input.

1.3 SVGM estimators

Considering the very limited number of dense array instrumentations covering a dam and its surrounding area and trying to boost this effort, we propose an in-situ campaign that offers such small-scale data on and around a dam (Chapter 2). The question that rises, given that the necessary data are available thanks to the dense array, is to quantify SVGM to define the seismic input for the dam, which in the present study is the structure

of interest. To do so, SVGM has to be decoupled in its two parts, namely phase and amplitude variability.

1.3.1 Phase variability estimator

Coherency is the most widely used estimator of phase variability of ground motions. It allows the estimation of deterministic or 'coherent' and stochastic or 'incoherent' part of the ground motion. The deterministic or 'coherent' part is due to the wave passage effect while the stochastic or 'incoherent' part to the scattering effect. There are three main assumptions to be applied to extract valuable information from the recorded time histories during an earthquake, as identified by Zerva & Zervas [2002].

- Firstly, the ground motion random field is considered to be homogeneous in space. This means that the probability distribution function and joint probability distribution function of two time histories are functions of the separation distance between stations, but independent of absolute location. The assumption implies that the amplitude of the seismic motions at different recording stations does not vary significantly.

- Secondly, the time histories are realizations of stationary random processes, i.e. the probability functions of the random process are independent of absolute time but function of the time lag only. Thirdly, the stationary random processes at the different locations are ergodic meaning that the information contained in each realization is sufficient for the full description of the process. The aforementioned assumptions could easily be adopted for continuous recordings of ambient vibrations but are less applicable for transient high amplitude signals. According to Zerva & Zervas [2002], the aforementioned assumptions, although strong, could be adopted in recordings of seismic signals. Because the majority of the dense instrument arrays are located on fairly uniform soil conditions, the assumption of homogeneity is valid. The assumption of stationarity can be justified in the sense that most characteristics of seismic ground motions for engineering applications are evaluated from the strong motion window, i.e. shear ($S-$) wave, which, in fact, can be viewed as a segment of an infinite time history with uniform characteristics through time.

- Lastly, the assumption of ergodicity is considered as necessary otherwise the description of SVGM would require recordings at the same site from many earthquakes with similar characteristics, so that averages of the ensemble of data can be evaluated. In reality, there is only one set of recorded data at the array for an earthquake with specific characteristics. Making these assumptions, data recorded

at dense seismological arrays during the strong motion, $S-$wave, window may be viewed as homogeneous, stationary, and ergodic in a limited sense.

1.3.1.1 Coherency estimator

By definition, coherency characterizes the variation in Fourier phase and expresses the loss of correlation between two seismic time histories. This stochastic estimator is evaluated by applying signal processing techniques to the recorded time histories which are considered as the realizations of a bivariate stochastic process. The joint descriptors of the bivariate process, i.e cross covariance function in the time domain and cross spectral density in the frequency domain, describe the joint characteristics of the time histories at two discrete locations on the ground surface. Because of its mathematical convenience in random vibration analysis, the frequency domain description, i.e. cross spectral density, is used in most analyses (Matsushima [1977], Abrahamson et al. [1990], Harichandran [1991], Zerva & Zervas [2002]). The coherency of the seismic motions is obtained from the smoothed cross spectrum of the time series between the two locations.
The coherency of the seismic motion between the stations j and k is given by the ratio of the smoothed cross-spectrum of the two time series to the geometric mean of the respective, identically smoothed, auto power spectra. The mathematical formulation of coherency is described, herein, following Abrahamson [2007]. Let $U_j(t)$ be a recorded ground motion at location j. The selected time window is segmented from the original time history by applying a 5% cosine bell window taper, $v(t)$, at each end to envelope the strong shaking. The selected window is assumed to be the segment from infinite time histories with uniform characteristics through time (stationarity assumption). The tapered time window is, then, given by $U_j(t) \cdot v_j(t)$. The Fourier transform, $A_j(\omega)$, of the tapered time series is:

$$A_j(\omega) = \sum_{l=1}^{N_t} v(l) U_j(\omega) exp(-i\omega l) \tag{1.1}$$

where N_t is the number of time samples, l is the time sample, and ω is the pulsation (in radians/sec). The cross-spectrum from recordings at sites j and k is a complex number given by $A_j(\omega) A_k*(\omega)$, where the $*$ operator indicates the complex conjugate. For coherency estimates, the cross-spectrum is smoothed over a constant frequency band. Alternatively, the cross spectral estimation can be evaluated in the frequency domain: let $A_j(\omega) = \Lambda_j(\omega) exp[i\Phi_j(\omega)]$, then the cross spectrum estimator becomes:

$$S_{jk}(\omega) = \frac{2\pi}{T} \Lambda_j(\omega) \Lambda_k(\omega) exp[i(\Phi_k(\omega) - \Phi_j(\omega))] \tag{1.2}$$

The smooth cross-spectrum, S_{jk}, is given by

$$S_{jk}(\omega) = \sum_{m=-M}^{M} \alpha_m A_j(\omega_m) * A_k(\omega_m) \tag{1.3}$$

where $2M+1$ is the number of discrete frequencies smoothed, $\omega_m = \omega + 2/N_t$ and α_m are the weights used in the frequency smoothing.

Complex coherency

Although the cross spectral density estimator describes the joint characteristics of the processes at two locations on the ground surface, it is customary to work with the coherency estimator. The complex coherency, $\gamma_{jk}(\omega)$, is given by the ratio of the smoothed cross spectrum of the time series between the locations j and k, to the geometric mean of the corresponding smoothed auto power spectra:

$$\gamma_{jk}(\omega) = \frac{S_{jk}(\omega)}{\sqrt{S_{jj}(\omega) S_{kk}(\omega)}} \tag{1.4}$$

The smoothed phase spectrum, i.e. phase, $\phi_{jk}(\omega)$, is derived from the ratio of the imaginary part, $\Im\gamma_{jk}(\omega)$, to the real part, $\Re\gamma_{jk}(\omega)$, of the complex coherency. This is equal to the phase spectrum of the smoothed cross spectral estimator as well.

$$\phi_{jk}(\omega) = \tan^{-1}[\frac{\Im\gamma_{jk}(\omega)}{\Re\gamma_{jk}(\omega)}] = \frac{\Im S_{jk}(\omega)}{\Re S_{jk}(\omega)} \tag{1.5}$$

The phase spectrum of the coherency (Equation 1.5) or, equivalently, of the cross spectral density, describes the phase differences between two locations and indicates whether the frequency component of the time history at one station precedes or follows the other time series at that frequency. Thus, it incorporates two effects, the wave propagation between two stations and the random phase variability at each station. The first one signifies the delay in the arrival of the waveforms at the further away location caused solely by the inclined plane wave propagation. The phase spectrum of such motion is a linear function of frequency. Alternatively, the complex function of coherency can be expressed as (Zerva [2009]) (i denotes the complex number $\sqrt{-1}$). :

$$\gamma_{jk}(\omega) = |\gamma_{jk}(\omega)| exp[i\phi_{jk}(\omega)] \tag{1.6}$$

The complex term, $exp[i\phi_{jk}(\omega)]$, includes the wave passage effect, i.e., the delay in the

arrival of the waveforms at the further away station caused by the propagation of the waveforms. Alternatively, Vanmarcke [2010] expressing the vector of the separation distance between the locations by $\xi_{jk} = r_k - r_j$ and the propagation velocity by c gives the analytical coherency expression:

$$\gamma_{jk}(\xi_{jk}, \omega) = exp[-i\frac{\omega(\overrightarrow{c} \cdot \overrightarrow{\xi}_{jk})}{|\overrightarrow{c}|^2}] = exp[-i\frac{\omega\xi_{jk}}{c}] \tag{1.7}$$

where $\xi_{jk} = |\overrightarrow{\xi}_{jk}|, c = |\overrightarrow{c}|$, and it has been implicitly assumed that the waveform propagates from location j to k. Equation 1.7 implies that $|\gamma_{jk}(\xi_{jk}, \omega)| = 1$ and the complex term in the equation describes the wave passage effect, i.e., the delay in the arrival of the waveforms at the further-away location caused solely by their propagation. The phase spectrum of such motions is then a linear function of frequency described by:

$$\theta_{jk}(\xi_{jk}, \omega) = \frac{\omega\xi_{jk}}{c} \tag{1.8}$$

where $\frac{\xi_{jk}}{c}$ reflects, actually, the time lag dt.

The apparent propagation velocity of the seismic motions across an array can be estimated by means of signal processing techniques, such as the conventional method (Abrahamson & Bolt [1987], Capon [1969]), the high resolution method (Capon [1969]), or the multiple signal characterization method Goldstein & Archuleta [1991a], Goldstein & Archuleta [1991b]. These techniques evaluate, in different forms, the frequency-wavenumber (F-K) spectrum of the motions, and identify the propagation characteristics of the waveforms from the locations of the peaks of the F-K spectrum. For a single type of wave dominating the motions during the analyzed time segment, as is, generally, the case for the strong motion, $S-$wave, window used in spatial variability evaluations, a single peak is identified. Its location determines the average apparent velocity and direction of propagation of the impinging wave at that particular frequency. Because body waves are non-dispersive, except in highly attenuated media, the location of the peak varies only slightly over the frequency range where the $S-$wave controls the motions (Spudich & Oppenheimer [1986]). In this case, the phase spectrum caused by the apparent propagation of waveforms can be approximated by Equation 1.8 with constant propagation velocity, c, over frequency. However, as frequency increases, additional wave components, and, essentially, scattered energy, start dominating the motions. In this case, the propagation characteristics of the waveforms fluctuate significantly with frequency, and Equation 1.8 is no longer valid.

Coherency can be described in several ways, namely, lagged coherency, plane-wave coherency, and unlagged coherency. The complex coherency is a complex number and the square of its modulus, termed as coherence, is a real number assuming values

$0 \leqslant |\gamma_{jk}(\omega)|^2 \leqslant 1$ (Zerva [2009]):

$$|\gamma_{jk}(\omega)|^2 = \frac{|S_{jk}(\omega)|^2}{\sqrt{S_{jj}(\omega)S_{kk}(\omega)}} \tag{1.9}$$

Lagged coherency

Lagged coherency is the most commonly cited coherency measure and it indicates the degree of linear correlation between the random processes recorded at two locations. The two time histories may not or may be aligned using the time lag that leads to the largest correlation of the two ground motions. If the ground motion at location k is aligned with respect to the location j by time samples, then the Fourier transform can be expressed, as :

$$A_k(\omega) = \sum_{l=1}^{N_t} v(l + \Delta l)U_{l+dl}(\omega)exp(-i\omega(l + \Delta l)) \tag{1.10}$$

The lagged coherency between the stations j and k is given by the modulus of their complex coherency,

$$|\gamma_{jk}(\omega)| = \frac{|S_{jk}(\omega)|}{S_{jj}(\omega)S_{kk}(\omega)} \tag{1.11}$$

At low frequencies (large wavelengths) and small separation distances, the ground motions between two locations are supposed to be very similar, which results in lagged coherency estimates tending to 1. The motions will become uncorrelated at higher frequencies (small wavelengths) and large separation distances, i.e. coherency tends to 0. Therefore, it is perceived that the value of coherency will decay with increasing frequencies and separation distances from 1 to 0. Coherency analyses from recorded earthquake data have validated this expectation and the functional forms describing the lagged coherency at any site and any event consider exponential decay with separation distance and frequency (Zerva & Zervas [2002]). However, the lagged coherency does not tend to 0 at large separations and high frequencies due to the bias in the estimation. The value of coherency estimate depends strongly on the selected frequency smoothing as well. The lagged coherency is always 1 if no frequency smoothing is used. If lagged coherency is not defined by means of the smoothed spectral estimates but, instead, through the unsmoothed estimators for the power and cross spectral densities, respectively, the absolute value of the coherency estimate corresponding to Equation 1.11 would then be (Zerva [2009]):

$$|\gamma_{jk}(\omega)| = \frac{|S_{jk}(\omega)|}{\sqrt{S_{jj}(\omega)S_{kk}(\omega)}} = \frac{\Lambda_j(\omega)\Lambda_k(\omega)exp[i(\Phi_k(\omega) - \Phi_j(\omega))]}{\sqrt{\Lambda_{jj}^2(\omega)\Lambda_{kk}^2(\omega)}} \equiv 1 \tag{1.12}$$

i.e., the expression becomes identically equal to unity, and no additional information can be extracted from the data. Finally, Spudich [1994] illustrated with an example that the absolute value of the coherency is not sensitive to amplitude variations regardless of whether the motions at the various stations are multiples of each other or not.

Plane-wave coherency

[Abrahamson et al., 1990] and Abrahamson et al. [1991] noted that lagged coherency describes only the deviations of the ground motions from plane wave propagation at each frequency; it does not consider the deviations of the motions from a single plane wave at all frequencies. If the analyzed segment contains wave components in addition to the plane wave, as is most commonly the case at the higher frequencies where scattered energy or noise contribute significantly to the records, the correlation of these additional wave components is reflected in the lagged coherency as if they were part of the plane wave (Zerva [2009]). The plane-wave coherency is estimated after removing a time shift which is constrained to be the same (consistent with a single wave direction and apparent velocity) for each station (Abrahamson [2007]). Plane-wave coherency actually considers the deviations of the motions from a single plane wave at all frequencies where plane-waves are accompanied by other wave components, such as scattered energy or noise. It is estimated by taking the real part of the smoothed cross-spectrum after aligning the ground motions based on the best estimate of plane-wave velocity. To express the departure of the data from that of plane-wave propagation at all frequencies, Abrahamson et al. [1990] and Abrahamson et al. [1991] introduced the concept of the plane-wave coherency. The lagged plane-wave coherency is given by:

$$|\gamma_{jk}^{pw}(\xi_{jk}, \xi_{jk}^{r}, \omega)| = |\gamma_{jk}^{M}(\xi_{jk}, \omega)| h(\xi_{jk}^{r}, \omega) \tag{1.13}$$

where $h(\xi_{jk}^{r}, \omega)$ is the relative power of the coherent wavefield that can be described by a plane wave at all frequencies. Because the real part of the smoothed cross-spectrum will have both positive and negative values, coherency estimates will approach 0 at high frequencies and large separation distances. Because $h(\xi_{jk}^{r}, \omega) \leq 1$, plane-wave coherency is equal or smaller than lagged coherency.

Unlagged coherency

The real part of complex coherency, $\Re[\gamma_{jk}(\omega)]$, is referred to as the unlagged coherency. Unlike lagged coherency, the unlagged coherency estimate does not consider the time lag between the pair of stations, which means, it includes the wave-passage effects. Its values are less than or equal to the plane-wave coherency and can range from -1 to 1. The negative values result from the coherent part of the wave-passage effect and

indicate out of phase ground motions between the pair of stations. For very short separation distances, a few hundreds of meters or less, the wave passage effects will not be significant because of the small travel time among the stations and the unlagged coherency will be similar to the plane-wave coherency (Abrahamson [2007]).

1.3.1.2 Smoothing parameter

The information about the differences in the phases of the motions at different locations is introduced in the estimate of the covariance function through the smoothing process. When no smoothing window is used, the phase difference terms disappear from the covariance spectra and the lagged coherency estimate will be unity for any frequency and any station-pair (Jenkins & Watts [1969]). Smoothing also controls the statistical properties, i.e variance and bias, and the resolution of the coherency estimates. The more the frequencies are smoothed, the larger the decrease in uncertainty in the coherency estimation, but this in turn causes a corresponding loss of resolution in frequency. According to Harichandran [1991], the common smoothing windows of different types yield similar results as long as the equivalent bandwidths of the spectral windows are the same. Therefore, selection of an appropriate equivalent bandwidth of spectral windows is more important than choosing smoothing spectral window types. From the available smoothing windows, the Hamming window is most commonly used for smoothing the seismic spectral estimates [10]. The Hamming window is a smoothed version of a triangle window, resembling to a Gaussian function, as shown in Figure 1.4. Its expression (in samples) is given by:

$$W(m) = 0.54 - 0.46cos(\frac{\pi(m+M)}{M}), m = -M, ..., M \tag{1.14}$$

and its graphical representation for M = 1, 3, 5, 7 and 9 is illustrated in Figure 1.4. Abrahamson et al. [1991], suggests that the selection of optimal smoothing parameters should not only depend on the statistical properties of the coherency, but also on the purpose for which the coherency is estimated. To use coherency estimates in structural analysis, for time windows less than approximately 2000 samples and for structural damping coefficient of 5%, an 11-point Hamming window ($M = 5$ for the a_m) is suggested by Abrahamson et al. [1991]. Averaging the complex cross spectrum over 11 frequencies can provide with a reasonable trade-off between the frequency resolution and the bias and uncertainty. The resolvability threshold of lagged coherency is 0.33 for the frequency smoothing applied (e.g $M = 5$), hence lagged coherency values below 0.33 cannot be interpreted (Abrahamson et al. [1991]).

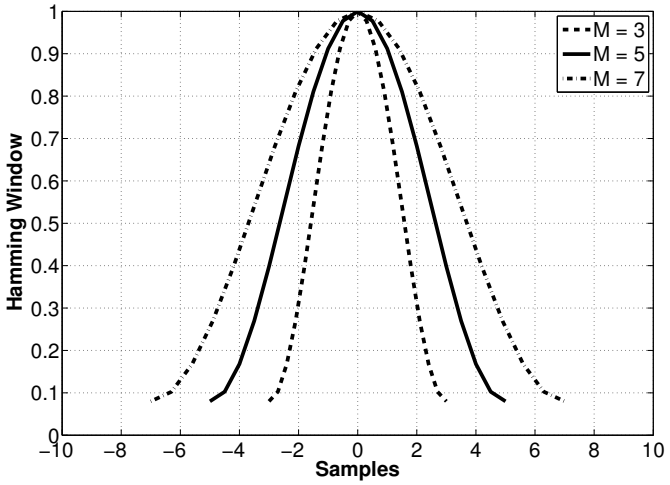

FIGURE 1.4: Example of an 11-point ($M = 3, M = 5, M = 7$) Hamming Window.

1.3.1.3 Time window selection

With the assumption of homogeneity, stationarity and ergodicity, it is a common practice to choose some specific time windows to estimate the coherency function, usually the $S-$wave window. That is because in most cases the $S-$wave part carries the strongest energy in earthquake recordings and, generally, is the most damaging component. There is no standard "rule" available for selecting the time windows given that it is difficult to identify a clear $S-$wave part of the signal which can be often contaminated by other wave components. Different time window lengths have been used in the literature depending on the specific earthquake events and the corresponding recorded time histories. Hao et al. [1989] used 5, 9, 10 and 21 seconds, Schneider et al. [1990] 2 seconds, Harichandran [1991] and Boissieres & Vanmarcke [1995a] 10 seconds. The $S-$wave window could be identified from visual inspection (manual identification). Abrahamson [2007] proposed the selection based on the duration of the normalized Arias Intensity (AI) of the two horizontal components of velocity. To estimate the normalized AI, an initial data window is applied that starts 10 seconds before the peak velocity and ends 10 seconds after the peak velocity. The peak velocity is identified separately for each component, V_1 and V_2.

$$0.1 \leq AI(\tau) = \frac{\int_{T_p}^{\tau}(V_1^2(t) + V_2^2(t))dt}{\int_{T_p-10}^{T_p+10}(V_1^2(t) + V_2^2(t))dt} \leq 0.75 \tag{1.15}$$

where, T_p is the time of the peak velocity, V_1 and V_2 correspond to the velocities of two horizontal components and τ indicates time. The final time window is then estimated based on the time at which the normalized AI reaches a value of 0.10 and 0.75, denoted as $T_{0.1}$ and $T_{0.75}$, respectively. Finally, after their identification, the selected time windows have been segmented from the original time history by applying a 5% cosine

bell window taper at each end (Figure 1.5). Therefore, the windows can be assumed to be the segments from infinite time histories with uniform characteristics through time (stationarity assumption).

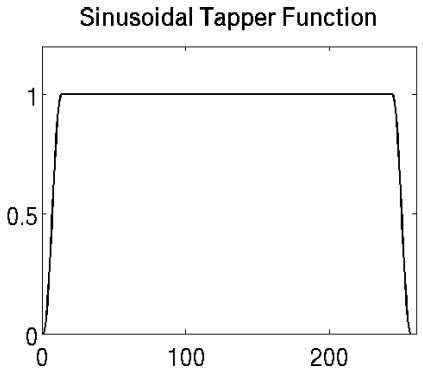

FIGURE 1.5: 5% cosine bell window taper applied at at each end of the earthquake time histories.

1.3.1.4 Statistical properties

Coherency is biased given that its estimation is performed over limited, finite segments of data by using spectral estimators. Bias can be introduced due to the sensitivity characteristics of seismometers and the use of finite length series (Harichandran [1991]). Additional uncertainty is introduced by inaccuracies in recorder synchronization, and by imperfect elimination of time lags caused by wave passage effects (Zerva & Zervas [2002]). As discussed by Abrahamson [1992b], the uncertainty of the estimate increases as the coherency values decrease. When the lagged coherency is not small, its $tanh^{-1}$ (or $ATANH$) transformation produces an approximately normal distribution with a bias that can be estimated and removed (Enochson & Goodman [1965]); this makes the uncertainty nearly constant. That is why, the statistical analyses of coherency are suggested to be performed on the $tanh^{-1}|\gamma_{jk}(\omega)|$ instead of $|\gamma_{jk}(\omega)|$ (Harichandran [1991]; Abrahamson et al. [1991]). However, the assumption of normal distribution of $tanh^{-1}|\gamma_{jk}(\omega)|$ is a poor approximation when the coherency values are small. The statistical properties of coherency are dependent on the selection of frequency smoothing. The expected value and variance of the estimated coherency are given by (Abrahamson [1992b], Abrahamson [1992c]):

$$E[tanh^{-1}|\gamma_{jk}(\omega)|] \simeq tanh^{-1}|\gamma_{jk}(\omega)| + \frac{g^2}{2(1-g^2)} \tag{1.16}$$

$$VAR[tanh^{-1}|\gamma_{jk}(\omega)|] \simeq \frac{g^2}{2} \tag{1.17}$$

where $|\gamma_{jk}(\omega)|$ is the estimate of the 'true' coherency $|\gamma_{jk}(\omega)|$, g^2 includes mainly the effects of the frequency smoothing (Abrahamson [1992c]):

$$g^2 = \sum_{m=-M}^{M} \alpha_m^2 \tag{1.18}$$

When the chosen frequency smoothing is a Hamming window with $M = 5$, the bias and standard deviation of $tanh^{-1}|\gamma_{jk}(\omega)|$ are 0.08 and 0.26, respectively. The 50% and 90% confidence levels for "noise" (the coherency resolvability threshold) are 0.34 and 0.63, respectively for $tanh^{-1}|\gamma_{jk}(\omega)|$ while 0.33 and 0.57, respectively for $|\gamma_{jk}(\omega)|$. However, in the statistics of $tanh^{-1}$ transformation it is required that the spectra of the processes, $U_j(\omega)$ and $U_k(\omega)$, have approximately constant amplitude over the bandwidth of the frequency window; if this is not the case, then a second source of bias is introduced in the estimates. This bias is not easily quantifiable and it increases as the frequency band increases. Abrahamson [1992a] mentions that this second source of bias can be reduced by using a triangular shaped smoothing window where the frequency weight, a_m, is subjective towards the central frequency of the window; but this essentially increases the first bias. Therefore, smoothing window type and sufficient number of frequencies are the key aspects in the statistical analysis of coherency.

1.3.1.5 Coherency modeling

The stochastic approach of coherency estimation, described above, is the most commonly used in the literature to model the phase variability of the motions during the strong motion $S-$wave window. A purely stochastic approach, however, does not allow an association of SVGM with its physical causes; experimental campaigns are necessary to complete the effort. It is difficult, though, to compare observations coming from different in-situ campaigns, because of the various experimental set-ups, different site conditions, source mechanisms and data analyses procedures. Consequently, a wide range of experiments, covering different cases, is necessary to make robust conclusions.

The availability of data coming from dense seismological arrays contributed to the development of a large number of empirical functions for modeling of SVGM. The majority of them are using lagged coherency as estimator. Liao [2006] lists a large number of these coherency models. Coherency is generally modeled as exponential function decaying with increasing frequency and station separation distance (e.g., Luco & Wong [1986], Somerville et al. [1988]) or a double exponential decay (e.g. Harichandran & Vanmarcke [1986]). For frequencies lower than a specific distance dependent value, lagged coherency

is observed to be approximately constant, while it decays with increasing frequency beyond a specific value, which can be treated as a 'corner' frequency (Harichandran & Vanmarcke [1986]). Hao et al. [1989], presented an empirical coherency model incorporating non-stationarity and response spectrum compatibility in the generated time series as well as Oliveira et al. [1991] did. One of the most widely used empirical models (calibrated on one seismic event coming from in-situ measurements) is the one introduced by Harichandran [1987] and re-evaluated by Harichandran [1991], assuming isotropy, with functional form:

$$|\gamma(\xi,\omega)| = Aexp(-\frac{2B\xi}{\alpha v(f)}) + (1-A)exp(2B\xi v(f)) \tag{1.19}$$

$$v(f) = k[1+\frac{f}{f_0}^{b}]^{-1/2} \tag{1.20}$$

$$B = (1-A+\alpha A) \tag{1.21}$$

where $A = 0.736$, $a = 0.147$, $k = 5210$ m, $f_0 = 1.09$ Hz and $b = 2.78$ for the radial direction.

The majority of the empirical models obtained by purely statistical approaches do not account for the physical causes of SVGM, thus, they cannot be reliably extrapolated to different sites and earthquake ranges. Analytical or semi-empirical models were attempted in the literature. Abrahamson et al. [1990] and Abrahamson et al. [1991] presented a parametric coherency model for short separation distances ($R \leq 100m$) based on many seismic events, following the idea that coherency is independent of earthquake magnitude and source-site distance. Abrahamson [1993], proposed single functional forms for the horizontal and vertical lagged and plane-wave coherency using an extensive set of data recorded at various sites, mainly soil but also rock sites. The model of Luco & Wong [1986] is one of the most quoted coherency models in the literature. Its functional form is:

$$|\gamma(\xi,\omega)| = exp(-(\frac{v\omega\xi}{V_s})^2) = exp(-\alpha^2\omega^2\xi^2) \tag{1.22}$$

$$v = \mu(\frac{R}{r_0})^{1/2}; \alpha = \frac{v}{V_s} \tag{1.23}$$

where V_s is an estimate for the elastic $S-$wave velocity in the random medium, R the distance in the random medium travelled by the wave, r_0 the scale length of random inhomogeneities along the path and μ^2 a measure of the relative variation of the elastic properties of the medium. The coherency drop parameter, α, controls the exponential decay of the function: the higher the value of α, the more significant the loss of coherency

as separation distance and frequency increase ($\alpha = 2.5*10^4$ sec/m suggested as a median value).

The practise of mixing seismic data recorded at different types of sites, soil and rock, can be questionable for the derivation of a single coherency model. In the case of records coming from rock sites, the exponential decay of parametric model is slower with respect to soil sites. The majority of the coherency expressions were developed for alluvial sites while models at rock sites are limited due to limited in-situ measurements. One of the few rock site lagged coherency models was developed by Menke et al. [1990].

$$|\gamma(\xi,\omega)| = exp(-\alpha f \xi) \tag{1.24}$$

where f is frequency in Hz, ξ is the separation distance in m and α ranges from $0.4*10^{-3}$ to $0.7*10^{-3}$ sec/m and is valid for all three ground motion components (vertical, radial and tangential) and all epicentral azimuth and distance ranges. Abrahamson [2007] presented a lagged and plane-wave coherency model also based on rock site data only. The formulation of the lagged coherency model for horizontal motion is:

$$tanh^{-1}|\gamma(\xi,\omega)| = \frac{c_3(\xi)}{1 + c_4(\xi)f + c_7(\xi)f^2} + (4.80 - c_3(\xi))expc_6(\xi)f + 0.35) \tag{1.25}$$

where

$$c_3(\xi) = \frac{3.95}{1 + 0.0077\xi + 0.000023\xi^2} + 0.85exp(-1.00013\xi) \tag{1.26}$$

$$c_4(\xi) = \frac{0.4[1 - \frac{1}{1+(\xi/5)^3}]}{[1 + (\xi/190)^8] + [1 + (\xi/180)^3]} \tag{1.27}$$

$$c_6(\xi) = 3(exp(-\xi/20) - 1) - 0.0018\xi) \tag{1.28}$$

$$c_7(\xi) = -0.598 + 0.106ln(\xi + 325) - 0.0151exp(-0.6\xi) \tag{1.29}$$

Comparison of coherency models evaluated from the same data by different investigators show different picture of the exponential decay of the coherency at a site. This is due to the complexity of wave propagation but also the inherent variance in the spectral estimation procedure adopted by different investigators and different functional forms for the coherency models. Additional attention should be paid on the extrapolation of the models' application to different separation distances and frequency ranges because the extrapolating empirically adjusted models may not produce reliable results. As Abrahamson [1988] showed, coherencies predicted by extrapolated models based on arrays with longer separation distances between stations were larger than the coherencies

measured from shorter distance arrays. Some analytical approaches of coherency modeling were also attempted (among others Kausel & Pais [1987], Somerville et al. [1991], Liao & Li [2002]). Although analytical studies can enlighten several physical aspects of SVGM, the analytical modeling will remain limited because of the assumptions that are necessarily made to simplify the problem (Zerva [2009]).

1.3.2 Amplitude variability estimator

Lagged coherency, although the modulus of a complex number, is attributed more to the phase variability in the motions rather than their amplitude variability. Early studies show that coherency is only minimally affected by the amplitude variability between the motions at two locations. Even though, through coherency, the phase variability has been widely investigated, the amplitude variability of the seismic motions has not attracted significant attention. There is no widely used estimator characterizing amplitude variability, like there is coherency for phase variability.

1.3.2.1 Difference of natural logarithm of Fourier amplitudes

The amplitude variability can be reflected directly using the difference of natural logarithm of the Fourier amplitudes between the motions at two locations. Either smoothed (using the same smoothing as the one applied for the coherency estimation) or unsmoothed spectra can be used for the estimation of this indicator. Abrahamson et al. [1990] and Schneider et al. [1992] proposed as amplitude variability estimator the standard deviation of differences of the natural logarithm of the Fourier amplitudes of the motions. Let $A_j(\omega)$ be the Fourier amplitude spectrum for j location and $A_k(\omega)$ of k location and $\Delta A_{jk}(\omega)$ the difference between the log normal Fourier amplitude of the j^{th} and k^{th} locations. Then :

$$\Delta A_{jk}(\omega) = ln[A_j(\omega)] - ln[A_k(\omega)] \tag{1.30}$$

Let $\sigma(\omega, \xi)$ be the standard deviation of $\Delta A_{jk}(\omega)$. It is assumed that $\sigma(\omega, \xi)$ is independent of the event. As the separation distance ξ goes to zero, by definition $\sigma(, \xi)$ goes to zero as well. $\sigma(\omega, \xi)$ is expected to increasing with increasing frequency. Both smoothed and not smoothed spectra can be used for the estimation of this indicator. Schneider et al. [1992], to be consistent with the phase variability procedure, used the same frequency smoothing, i.e. Hamming window, $M = 5$. Ancheta et al. [2011] used no smoothing parameter for the estimation of the Fourier amplitudes. Alternatively, Goda

& Atkinson [2010] used the standard deviation of difference of residuals of response spectral amplitudes. They came to similar conclusions as the previously mentioned authors regarding the dependence of amplitude variability on frequency and inter-station separation distance.

1.3.2.2 Amplitude variability modeling

Abrahamson et al. [1990] and Schneider et al. [1992], analysing data recorded at LSST array and subsequently at various arrays both at rock and soil sites, estimated the amplitude variability using as estimator the standard deviation of differences of the natural logarithm of the Fourier amplitudes of the motions. To be consistent with the coherency analysis, a Hamming window with $M = 5$ was used.

$$\sigma_{\Delta A}(\xi, f) = 0.93[1 - exp(-0.16f - 0.0019f\xi)] \tag{1.31}$$

where $\Delta A_{jk}(f)$ is the difference of the natural logarithm of the Fourier amplitudes at two locations, $A_j(f)$ and $A_k(f)$, and $\sigma_{\Delta A}(\xi, f)$ their standard deviation. In this model, the standard deviation is not forced to tend to zero when separation distance tends to zero. They observed that amplitude variability increases with station separation distance and frequency, and tends to a constant value at higher frequencies. More recently, Ancheta et al. [2011] adapted the model using in the expression unsmoothed Fourier spectral ordinates. Based on their data, the frequency dependency was found to be stronger than the station separation distance dependency thus the functional form of the model is:

$$\sigma(f) = A(1 - exp(Bf)) \tag{1.32}$$

where $A = 0.93$, $B = b_1 + b_2\xi$ and $b_1 = -0.1005$ and $b_2 = -0.0025$. The range of applicability of the model, as proposed by the authors, is from 5 to 100 m station separation distance and frequencies from 0.25 to 25 Hz.

Goda & Atkinson [2010] investigated the amplitude variability of SK-net dataset. They developed a spatial correlation model based on the observed data. As estimator of the amplitude SVGM they used the standard deviation of difference of residuals of response spectral amplitudes, instead of directly the Fourier amplitudes adopted by the two aforementioned studies. They pointed out that at short separation distances (less than 1 km), wherein empirical data are limited and estimates are uncertain, discretion is required in adopting such models for seismic hazard and risk assessment of spatially distributed structures.

1.4 Effect of SVGM on dams

Sites with inhomogeneity in surface geology and geometry and irregularities in surface topography complicate the wave field to an extent that amplifications or de-amplifications, loss of coherency and significant ground strains may be observed on the ground surface. These local site effects, combined with path and source effects, may lead to significant spatially variable ground motions within a a small distance scale. Thus, different supports of long structures or continuous points along their foundations may undergo differential motions during an earthquake.

Since the 1960s, studies analyze the influence of SVGM on above-ground (e.g. dams, suspension bridges, nuclear power plants, offshore structures, symmetrical and asymmetrical conventional structures) and buried structures (e.g. pipelines, tunnels). Initially, the differential motions at the structures' supports were attributed to the wave passage effect, i.e., it was considered that the ground motions propagate with a constant velocity on the ground surface without any change in their shape. SVGM was, then, described by the deterministic time delay required for the waveforms to reach the further-away supports of the structures.

In the 1980s, the response of large, mat, rigid foundations, such as those of nuclear power plants, induced by spatially variable seismic ground motions started being investigated (e.g. Smith et al. [1982], Hoshiya & Ishii [1983], Luco & Wong [1986], Mita & Luco [1986], Harichandran [1987], Luco & Mita [1987], Veletsos & Prasad [1989], Pais & Kausel [1990], Veletsos et al. [1997], Kim & Stewart [2003]). Large, mat, rigid foundations, such as those of power plants or dams, tend to average the seismic excitation (Yamahara [1970], Scanlan [1976], Matsushima [1977], Newmark et al. [1977], Tamura et al. [1977], Bycroft [1980a], Harichandran [1987] etc.). In these early studies, it was found that the interaction of the soil with the massless foundation tends to decrease the foundation's translational response as the frequency of the excitation and the foundation size increase. The effect of loss of coherency and wave passage on the response of large, mat, rigid rectangular and circular foundations was extensively examined by Luco & Wong [1986] and Mita & Luco [1986]. Therein, it was concluded that there is a reduction of the translational response and that the loss of coherency in the seismic ground motions produces effects that are comparable, perhaps slightly stronger, to the deterministic effects of wave passage.

In the 1990s started an extended research of the effect of SVGM on the response of dams. In the case of arch dams, the non-uniform reservoir geometry of the dam and the irregular local topography cause scattering of the incident waves and result in a ground motion field that is different from what would have resulted in a half-space (e.g., Szczesiak et al. [1999], Zhang & Chopra [1991a] and Zhang & Chopra [1991b]). Lin & Wang [1996] concluded that taking into account SVGM for seismic design is very important because the

traditional uniform input models ignore the high stress concentrations at the two abutments of the dam. The significance of complex topographic effects on the 3D response of arch dams is underlined by several studies (Zhang & Chopra [1991a] and Zhang & Chopra [1991b], Kojic & Trifunac [1991] and Kojić & Trifunac [1991], Szczesiak et al. [1999], Maeso et al. [2002], Alves & Hall [2006a] and Alves & Hall [2006b]). The complex topography of their location introduces significant spatial variability in the incident seismic ground motion field. To account for topographic effects, Szczesiak et al. [1999], Zhang & Chopra [1991a] and Zhang & Chopra [1991b] evaluated first the response of the canyon, in the absence of the dam, to incident plane waves; the canyon can have an arbitrary cross section, which is, generally, assumed to extend uniformly in an infinite half-space. The resulting ground motions are then applied as input excitations in the evaluation of the response of arch dams (e.g., Camara [2000], Kojic & Trifunac [1991] and Kojić & Trifunac [1991] and Nowak & Hall [1990]). The results of these studies show the significance of the consideration of both the angle of incidence of the waves and the wave type in the evaluation of the dam response. Alves & Hall [2006a] and Alves & Hall [2006b] made a comparison of the response due to non-uniform input with the response due to uniform input on the Pacoima dam, by studing the topographic amplification and time delay of ground motions. Their analysis revealed that if the motion recorded at the base of the dam is used as uniform input, the responses will be less severe compared to the non-uniform input. Using the same case study, i.e. the Pacoima dam, Ghaemian & Sohrabi-Gilani [2012] also concluded that applying the base motions as the uniform excitations, underestimate the crest displacements and developed stresses in the dam body. Alves & Hall [2006b] further demonstrated the significance of the pseudo-static component of the response due to to non-uniform input. The significance of the pseudo-static effects on the dam response was also observed earlier by Kojic & Trifunac [1991] and Kojić & Trifunac [1991]. On the other hand, Nowak & Hall [1990] showed that the inclusion of non-uniformity in the stream component of the excitation reduces the dam response, and the effect of the non-uniformity in the cross-stream and vertical component of the excitation varies, with the potential for a significant increase. Similar observation was made by Chen & Harichandran [2001] in their evaluation of the response of the Santa Felicia rolled-fill earth dam. Generally, the more advanced the numerical models developed, the more the conclusion that SVGM plays a significant role on the seismic response becomes (e.g. Proulx & Darbre [2008], Chopra [2012], Oliveira et al. [2012]). The aforementioned studies show that some qualitative conclusions can be drawn, e.g. different response patterns emerge when the excitation is uniform or nonuniform, the importance of pseudo-static response which is induced by the non-uniform excitations, the importance of the angle of incidence of body and surface waves on the complex topography. However, given that the results remain qualitative, it is obvious that further research in this scientific field is necessary to make concrete conclusions regarding the

effect that SVGM has on the seismic response of dams.

Taking into consideration the current state of knowledge on this scientific field, continuous efforts are made so as the phenomenon of SVGM to be incorporated in the design provisions. Regarding large and rigid foundations, Seismic Analysis of Safety-Related Nuclear Structures and Commentary, ASCE [2000] Standard 4-98 takes into account the reduction of the free-field motions due to the soil-structure interaction. According to ASCE [2000] Standard, the assumption of vertically propagating shear and compressional waves in soil-structure interaction evaluations results, usually, in conservative estimates for in-structure responses. It is suggested that, in the absence of analyses to establish the reduction of the response due to the loss of coherency in the seismic excitations, a conservative estimate would be to reduce the values of the ground response spectra. Response spectra incorporating spatial variability in the excitations were developed by Zembaty & Krenk [1993], Trifunac & Todorovska [1997], and Zembaty & Rutenberg [2002] and Trifunac & Gicev [2006]. Council et al. [1991] although it proposes as necessary the consideration of spatial variation of the input earthquake motions in dams' design, it points out that reliable descriptions of the earthquake motions to be expected at the dam-foundation rock interface are not available at present. Barrages-Séismes [2014] defines the characteristic dimension D as $D = min(L, 3H)$, L being the peak length of the dam, and H the height on foundations. The latter provision aims to decreasing the high frequency content to take into account the effect of spatial variability of seismic movement when the structures have a certain hold on the ground: this effect is higher as the wavelength is shorter, i.e. the period is shorter. However, according to Barrages-Séismes [2014], it must be ensured that the dimensions of the structure are sufficiently large to permit this 'arrangement'.

The choice of the coherency model is controlling factor in the estimation of the seismic input. Zerva [2009] argues that the variability in the seismic motions resulting from complex topographic effects cannot be approximated by the conventional coherency models. Till recently, no in-situ data were available to confirm or controversy this argument. Additionally, uniform and non-uniform excitation provokes different response patterns of dams. The major differences in the patterns are caused by the pseudo-static response, which is induced only by non-uniform excitations, and the significance of which depends, for each structure, on the characteristics of the spatially variable ground motions (Zerva [2009]). Although the scientific community has accelerated the recent years its efforts, further research is needed in enhancing the understanding of SVGM within the dimensions of dams such that the seismic input to be defined and, thereafter, robustly evaluating its seismic response. The present study focuses on the definition of the seismic input at the dam's base, using experimental and numerical tools.

Chapter 2

Seismological campaign in Saint Guérin

Chapter 2 presents a brief description of the Saint Guérin site, where our seismological campaign took place from mid of June 2015 to end of June 2016. The chapter starts with an overview of the seismotectonics, seismicity and local geology of the alpine area where the arch dam is located in. Thereafter follows an overview of the seismological campaign. The catalog of a selected number of recorded earthquakes and the quality of the acquired data used for analyses are also discussed. Finally, a preliminary analysis of the dynamic behavior of the arch dam in Saint Guérin based on the available seismological and ambient noise data is provided by means of frequencies of vibration, damping ratios and crest amplification.

For the things we have to learn before we can do, we learn by doing.
Aristotle, 'Nicomachean Ethics'

2.1 The Saint Guérin site

The spatial variability of seismic ground motions (SVGM) was recognized as a potentially important component of the seismic wave field since the early 20th century. However, this scientific field started being investigated about four-five decades ago with the installation of several strong motion instrument arrays. The seismological data recorded at dense seismograph arrays have provided valuable information in understanding and modeling SVGM. Nowadays, many permanent and temporary dense arrays have been installed at different types of sites around the world. Most of these arrays are (or have been) located at uniform ground conditions, mostly at soil sites. Dense seismological arrays that could provide a better insight in SVGM in the case of arch dams (irregular local topography, rock site, soil-structure interaction etc.) are very limited. Worldwide, there is a lack of very densely instrumented (with seismological arrays) arch dams that could provide the necessary density of recordings. To fill this gap, in the framework of the present thesis, a seismological campaign of the instrumentation of an arch dam and its surrounding area was held in Saint Guérin. Saint Guérin is located in the Savoie department of the Auvergne-Rhône-Alpes region. This alpine region is one of the most seismically active regions in metropolitan France. Three french research unities, Institut des Sciences de la Terre (ISTerre), Laboratoire Sol, Solides, Structures, Risques (3SR) and Centre d'Ingénierie Hydraulique, Electricité de France (CIH-EDF) participated in the instrumental set-up which lasted from mid June 2015 till end of June 2016. The present thesis analyzes the SVGM in the Saint Guérin site based on the data acquired from this temporary seismological network.

2.1.1 Seismotectonics and seismicity

The ongoing collision between the tectonic plates of Africa and Europe is the most probable cause of seismicity induced in the southern part of France. Figure 2.1 presents the plate tectonics context of Metropolitan France (Baize et al. [2013]). Most of metropolitan France territory lies in a zone with little crustal strain; baselines within France change by no more than 2 mm/yr as shown from geodetic measurements (Vigny et al. [2002]). This is consistent with the very low slip rates, of the order of 0.1 mm/yr at most, on the few recognized active faults (Schlupp et al. [2001]).
The experimental campaign is taking place in the region south of Beaufort village, Savoie, northern French Alps, in France, where the dam of Saint Guérin is located in. The earthquake activity along the Alpine chain is confined within two arcs, namely the Briançonnais and the Piemont seismic arc. As estimated in Walpersdorf et al. [2015], the seismic rate of the Briançon area, which covers the southern tip of Briançonnais arc

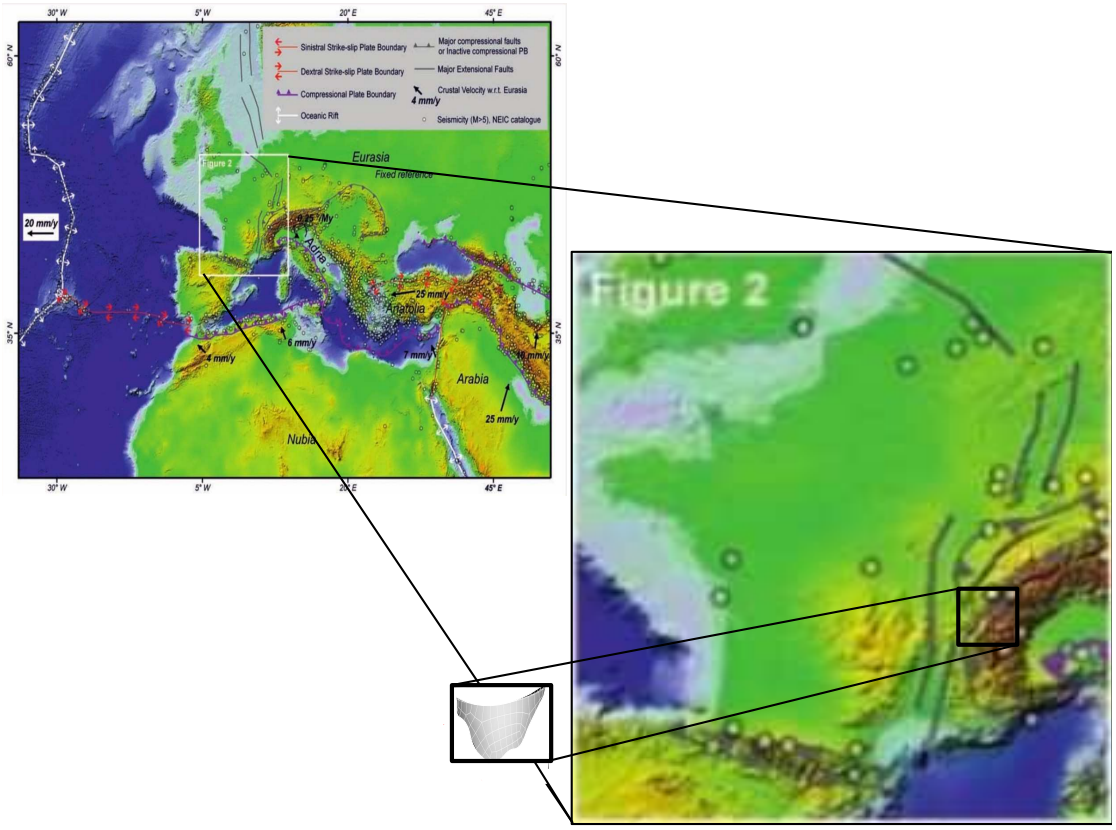

FIGURE 2.1: Plate tectonics context of Metropolitan France. Relative movements of plates are given with respect to Eurasia (considered as fixed). Zoom in the metropolitan France showing the major extensional faults (Baize et al. [2013]) and location of the arch dam of Saint Guérin.

and it is its most active part, is low (1 earthquake of magnitude 5 with return period of 10 years). The geodetic displacement of the region, estimated by GPS measurements by the aforementioned authors, is of the order of 1 mm/yr.

Figure 2.2 shows the seismicity of the area according to the catalog of SISMALP (i.e. the alpine seismicity observation network, https://sismalp.osug.fr), for a period of 23 years, from 1989 to 2012. Events with magnitude $M_L \geq 2$ and maximum epicentral distance, $R_{epi} \leq 150$ km, from the arch dam in Saint Guérin are shown. As identified, during 23 years of recordings, around 56 events with magnitude $M_w \geq 3$ and epicentral distance from the dam $R_{epi} \leq 150$ km have occurred. Therefore, the rate of occurrence of an event with magnitude higher than 3 is around 3 per year. The recent M_w 5 earthquake, which occurred in the study area on the 7th of April 2014 (Ubaye Valley), is one of the strongest events in the western Alps during the last 50 years. The map of Figure 2.3 represents the seismicity ($M_L \geq 0$) of the overall western Alps from the SISMALP network (which is also included in the same figure) covering the period from 1986 to 2002 (Thouvenot et al. [2003]).

The map of seismic zonation of France is given in Figure 2.4; the location of the arch dam of Saint Guérin is also added on the map. The arch dam of our case study is located

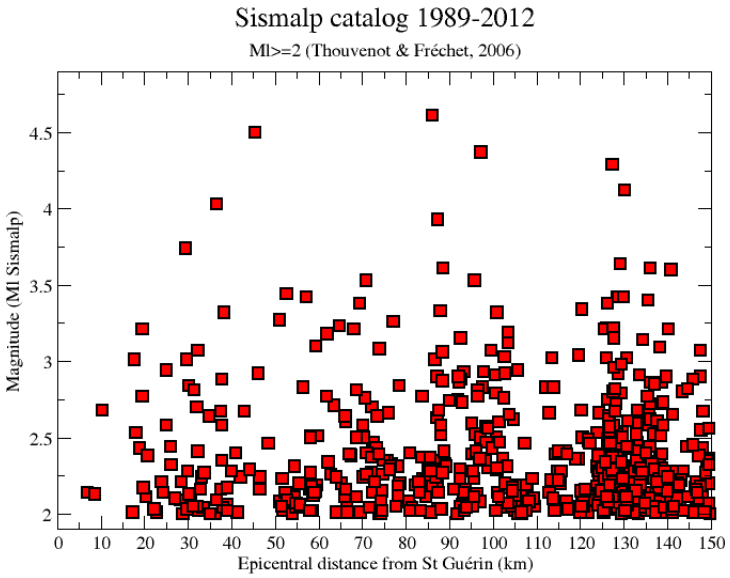

FIGURE 2.2: Sismalp Catalog. Magnitude, M_L, as a function of epicentral distance, R_{epi}, from the dam in Saint Guérin for events recorded between 1989 and 2012.

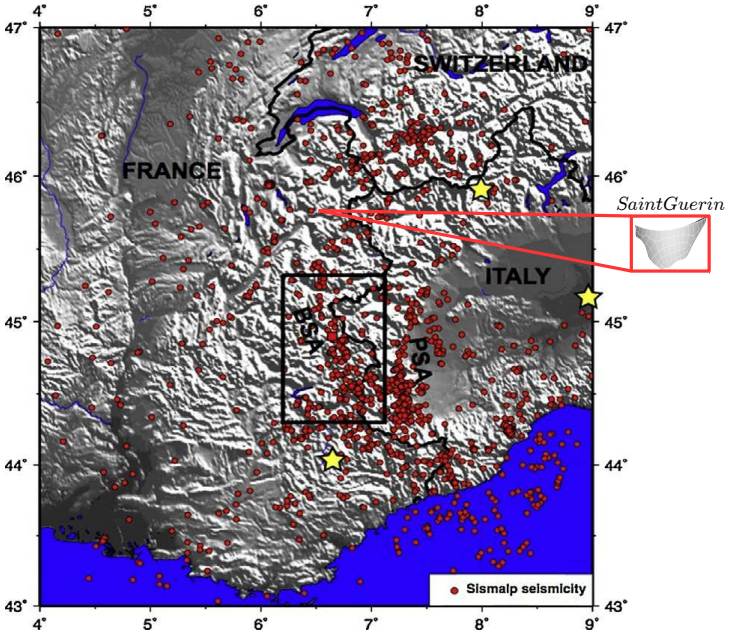

FIGURE 2.3: Seismotectonic settings. The map shows the seismicity of the overall Western Alps from the SISMALP network (Thouvenot et al. [2003]) covering the period from 1986 to 2002. The black rectangle locates the Briançon GPS network area. Yellow stars indicate three published solutions for the emplacements of the Euler pole of the Adriatic micro-plate rigid counter-clockwise rotation with respect to Eurasia (Walpersdorf et al. [2015]). The location of the arch dam of Saint Guérin is also included.

in one of the three most seismically active regions of metropolitan France. The values of horizontal accelerations at a rock site (as they are defined from the ministerial decree of October 22, 2010) for categories of structures II, III and IV are 1.6, 1.92 and 2.24 m/s^2 respectively at the location of the dam (i.e. zone 4). According to the aforementioned seismotectonic situation and the sismicity of the recent years, the region of Saint Guérin is one of the french regions that offer the possibility to collect a sufficient number of seismological data in a relatively short period of time.

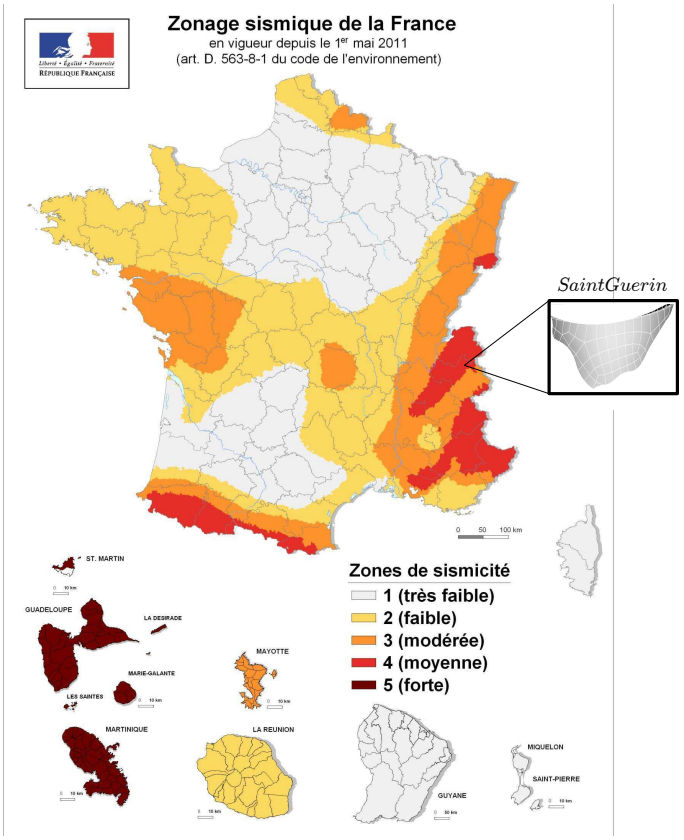

FIGURE 2.4: Location of the arch dam of Saint Guérin on the seismic zonation map of France resulting from the ministerial decree of October 22, 2010.

2.1.2 Local geology

The geological map of the region of Saint Guérin is provided in Figure 2.5. The available geological and geophysical description of the area points to high compression and shear wave velocities layers, covered by a shallow layer of scree or alluvial deposits. The dam is located on the eastern border of the inner branch of the crystalline massif of Belledone. It is implanted on a glacial lock constituted by biotite gneisses (V_S [2700 3500] and V_P [4400 5200] m/s) which is characterized by a well-marked foliation, generally oriented north-south (upstream-downstream) with a dip between 25° and 50° towards the East. The foliation presents varying dips below the foundation of the dam, e.g. at mid-height

of the left bank it tends to rise upright vertically while at the right bank several fractures can be found. The basin is largely covered by scree (V_S [100 300] and V_P [300 700] m/s) at the edges and moraines and alluvial deposits in the bottom (V_S [800 1800] and V_P [2000 3500] m/s), all of which are permeable. Beneath these covers there is a strip of trias (dolomite and cargneules, i.e V_S [1900 3600] and V_P [3500 6500] m/s) which forms the basis of the secondary cover of the crystalline massif of Belledone. The general dip of this trias is oriented towards the south-east. Everything that is to the west of this band of trias is crystalline, everything that is to the east is marls and schists of lias, watertight terrains (V_S [750 1500] and V_P [2000 3000] m/s).

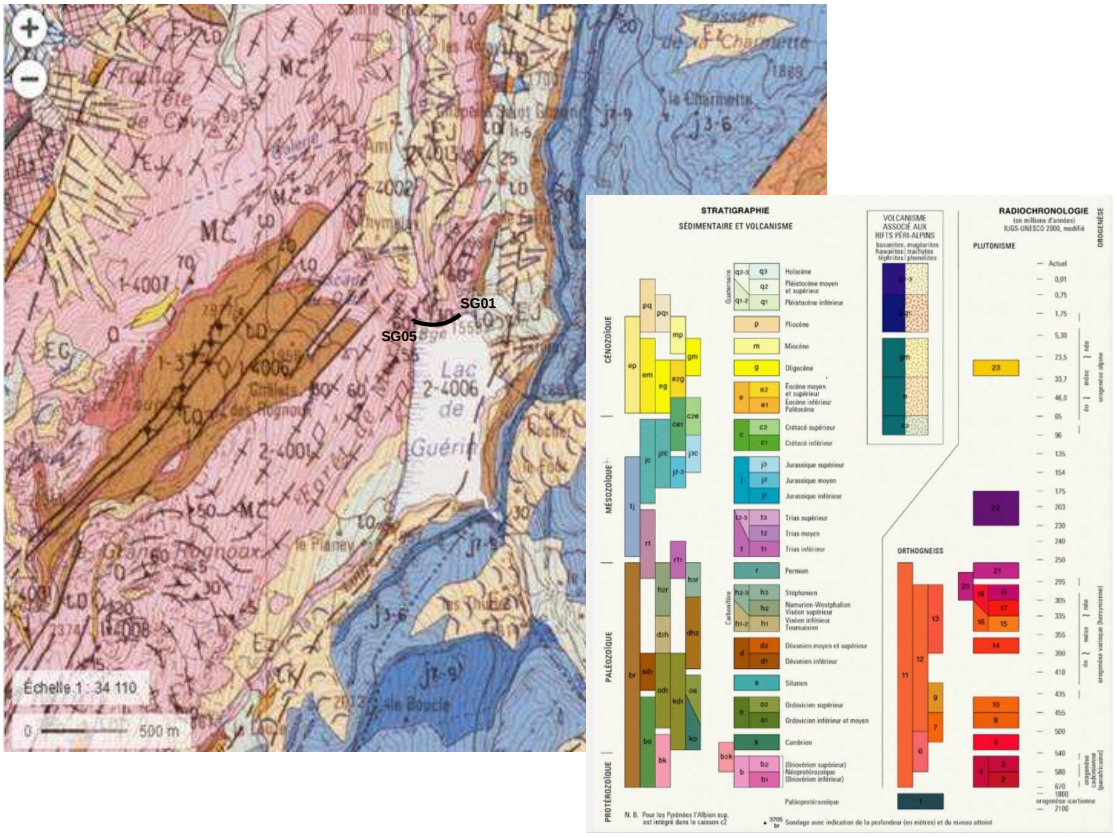

FIGURE 2.5: Geological map of the Saint Guérin region; the location of the two stations on the left (SG05) and right (SG01) abutments of the dam are added.

2.1.3 Saint Guérin arch dam

Saint Guérin, patron saint of herds, gave his name to the valley and, thereafter, the valley to the dam. The latitude and longitude of the dam are $45°39'0.55"N$ and $06°34'45.52"E$ respectively. The owner of the dam is the Électricité de France (EDF). Its construction started in 1957 and it was completed in 1961. Saint Guérin dam is a double curvature arch dam (i.e. its radius varies with heigh / curved in plan and elevation), made of concrete, of 69 m height and its arched-gravity structure measures length of 250 m. The

thickness of the crest is 3.10 m and of the base 12 m. Except the double curvature shape, that is optimised for the specific topography of the Saint Guérin valley, the dam has a pretty simple design with no intake power station. It has a total volume of 65000 m^3 and its retained water volume is 13.5 km^3; its water surface area (the Saint Guérin lake) is 500000 m^2 (50 hectares) with a maximum depth of 69 m. The dam contributes to feeding the Roselend lake through a connecting pipe between the reservoirs that operate in the manner of communicating vessels. Its behavior has been monitored since its start of use by a regular inspection of its displacements. A panoramic view of the arch dam is presented in Figure 2.6.

FIGURE 2.6: Double curvature, 69 m high and 250 m long arch dam in Saint Guérin.

2.2 Dense seismological array

On the double curvature arch dam of Saint Guérin as well as on its surrounding area we deployed a very dense seismological array, consisting of 19 three-component velocimeters. The configuration as well as a schematic representation of all the stations of the seismological array at the Saint Guérin site is shown in Figures 2.7 and 2.8. The deployed array aims primarily to capture the SVGM at the dam-foundation rock interface, therefore 9 stations were installed along the interface, SG01, SG09, SG10, SG11 and

SG12 on the right bank and SG05, SG06, SG07, SG08 on the left bank. To get an idea of the response of the dam, 3 stations were installed on the crest, i.e. SG02, SG03 and SG04. Due to the irregular alpine topography, difficulties were faced on identifying adequate and easily accessible locations that could be used as free field sources of data, with 'free field' signifying rock sites on a flat area. Thus, the term 'free field' is used herein for a location away from the dam, but not necessarily sufficiently far away to provide data totally uninfluenced from the presence of the structure and/or the local topography. 3 free field stations were located along the path that leads to the bottom of the dam, along the axis of the valley, i.e. SG13, SG14 and SG15. Free field data are also provided by stations SG17 and SG18, located towards the east of the dam on rock sites (SG17 installed inside a small-size cave and SG18 on a hill) and stations SG19 and SG20, installed around the dam reservoir (SG19 on a scree layer east of the reservoir and SG20 on a rather rock site in the west of the reservoir). Table A.1 in APPENDIX A includes the station coordinates (Latitude, Longitude, Northing, Easting) and Table A.2 shows the station separation distances for all station pairs in the array.

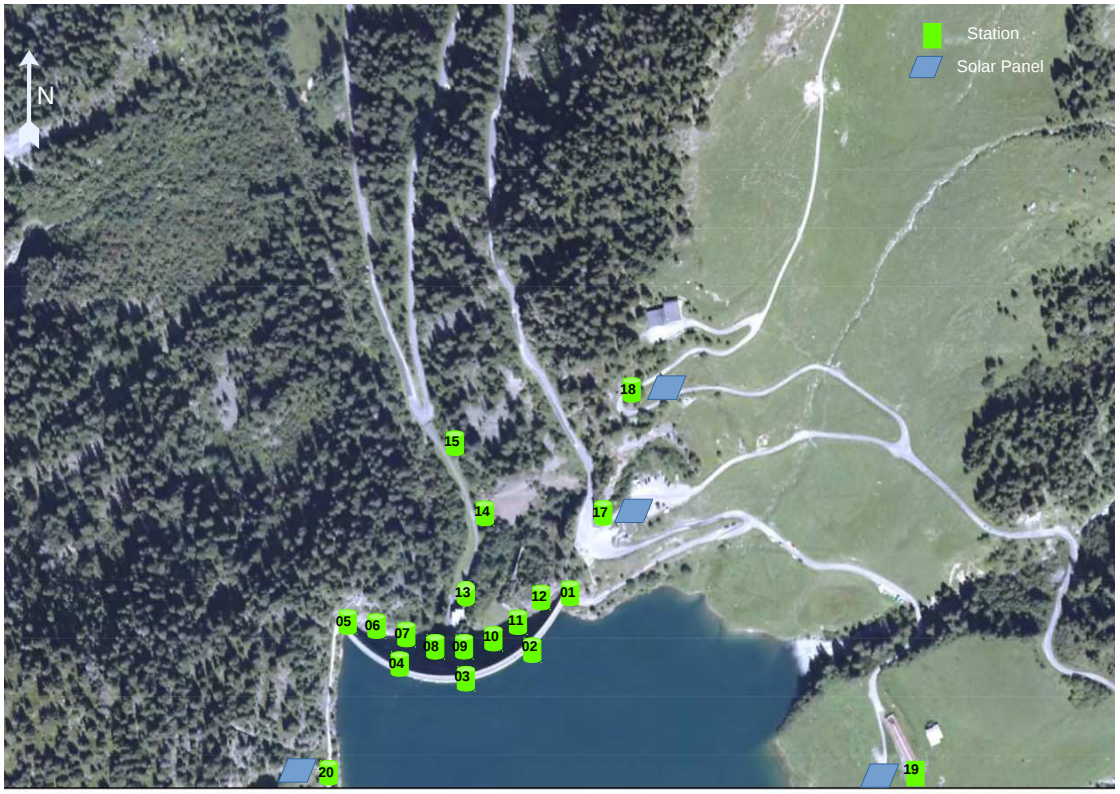

FIGURE 2.7: Position of seismological stations on and around the dam of Saint Guérin.

The seven free field stations, i.e. SG13, SG14, SG15, SG17, SG18, SG19 and SG20, are not located on the same geological unit. Hence, Horizontal to Vertical (H/V) analysis was performed to obtain information for the individual sites chosen around the dam. A preliminary study is performed to be used as guideline for the SVGM analysis that

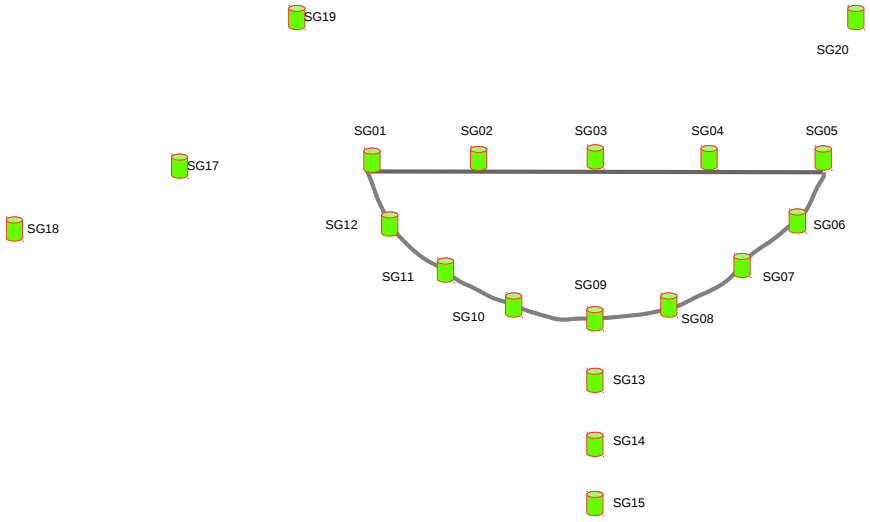

FIGURE 2.8: Schematic representation of the position of seismological stations on and around the dam of Saint Guérin.

follows in Chapter 3. The H/V spectral ratio is calculated based on one hour ambient noise recorded by the acquisition units at the free field positions. The ambient noise record used is the 1^{st} of October 2015, at 06:00:00; early in the morning the Saint Guérin site is generally very calm, i.e. ambient noise is composed mainly of physical sources while human activity nearby is avoided.

The H/V curves are calculated by averaging over time windows with length of 160 s (Hanning tapered) superposed at 5% (which gives a frequency accuracy of $f = 1/160 = 0.00625$ Hz) based on one hour of recordings (velocity records of 3600 s are used, originally with a sample frequency of 200 Hz). The H/V curves are presented in Figure 2.9. The study outlined the fundamental frequencies of the different sites around the dam (considered as free field locations). As observed in Figure 2.9, the sites where SG15, SG17 and SG20 are located appear to be very good reference points since no particular site effects are identified (relatively horizontal H/V curves). The site of SG13 is contaminated from the signature of the dam; a clear amplification is observed at the frequencies of vibration of the dam (as they are presented later on in Chapter 2). The site of SG14 is also contaminated, although less than the site of SG13. At the sites where SG18 and SG19 are located clear site effects are observed around 2 Hz for the first one and all along the frequency range for the second one. In the first case, the

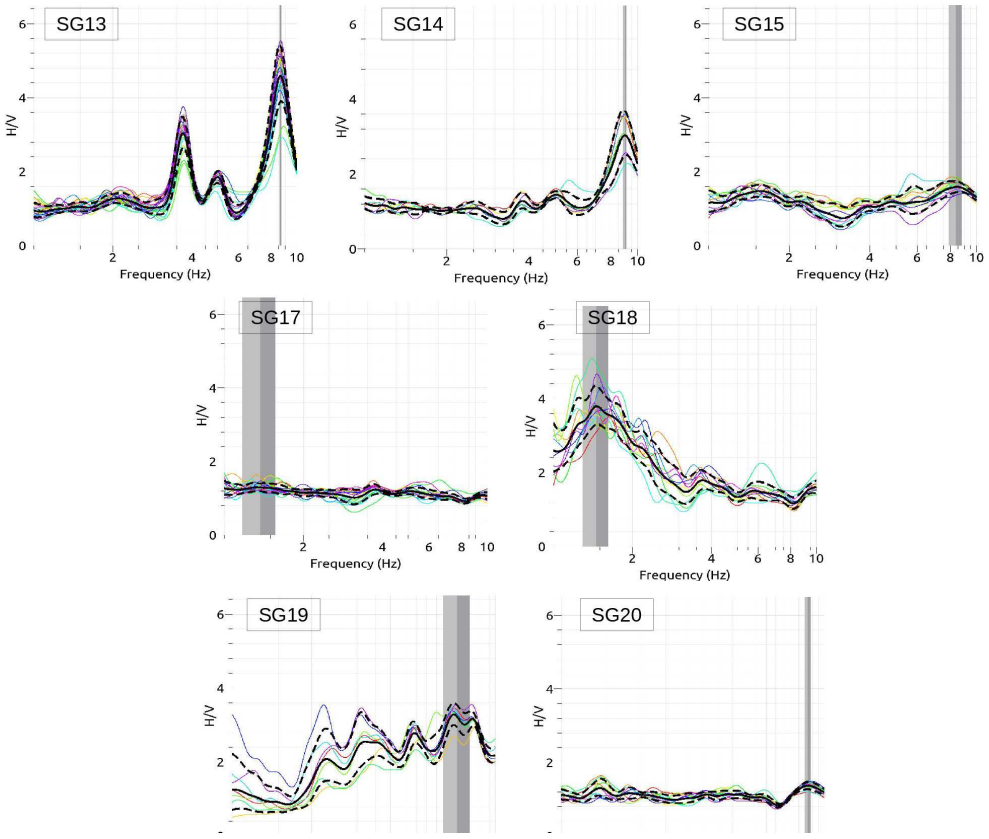

FIGURE 2.9: H/V spectral ratios at stations SG13, SG14, SG15, SG17, SG18, SG19 and SG20 based on ambient noise recordings of 1 hour at 06:00:00 the 1^{st} of October 2015. Solid black lines indicate the average value over all time windows and dashed black lines ±1 standard deviation.

peak of the spectrum around 2 Hz is most probably explained by a topographic effect, given that the station is located on a hill, while in the case of SG19, the presence of the scree layer laying on stiff rock evidently creates an amplification at several frequencies. The non existence of any H/V peaks at the sites of the stations SG17 (located in a rock cave) and SG20 (west side of the dam reservoir) reveal that their locations are good free field references without local site effects. The fat spectrum of SG20 station shows that, unlike to the east side of the reservoir, in this location of the west side no scree layer covers the dolomite/cargneules layer,letting the station to lay on stiff rock.

The H/V curves of the free field stations reveal the difficulties faced finding good rock references. The alpine area where the dam is located in addition to the low velocity shallow layers around the Saint Guérin lake and the presence of the structure itself, made it hard to avoid site effects on the records of the free field stations. Despite the aforementioned though, the chosen free field locations offer data that could be of great interest when compared with the data at the dam-foundation rock interface. The 3 stations located along the path that leads to the bottom of the dam, i.e. SG13, SG14 and SG15, unlikely to the stations at the interface, do not incorporate canyon topographic

effects. On the other hand the two stations on the rock sites, i.e. SG17 and SG18 do not incorporate the signature of the dam.

2.3 Data acquisition

Continuous records from all stations were acquired during the entire period of the seismological campaign offering a complete database that could eventually be of great use for numerous quantitative analyses. Continuous records allow the monitoring and analysis of global earthquakes in addition to the local and regional ones. The continuous records of non-earthquake, additionally to earthquake activity, have been proved to be a useful tool. They allow spatio-temporal correlations of other sources of activity to be analyzed, e.g. ambient noise which can be local noise from wind or anthropogenic activities, to incessant signals generated at the ocean floor and coasts induced by ocean waves (the global microseism), to cryospheric events associated with large icebergs and glaciers. Continuous data can also be used to extract the key dynamic properties of the dam-reservoir-foundation system (e.g frequencies of vibration, mode shapes, damping, crest amplification). The continuous records cover different periods of the reservoir filling cycle allowing also to investigate water level effects on the dynamic properties of the dam-reservoir-foundation system.

The type of the all sensors was chosen to be Güralp CMG40T, with eigen periods between 30 and 60 s. However, the three sensors deployed on the crest of the dam are of type Lenhartz 5s, a choice guided both from the limited available space of installation on the crest (the size of Lenhartz 5s is smaller than of the Güralp CMG40T) and by the fact that since the motions on the crest are more amplified with respect to these at the bottom of the dam, less precise sensor is accepted. All stations are connected to 24 bit Nanometrics Taurus digitizers. Both sensors and digitizers belong to the French mobile national seismological pool INSU/SISMOB (https://sismob.resif.fr). The quality of the records highly depend on the deployment of the station itself. Three main factors congregate: the level of isolation from environmental influence, such as wind or solar radiation, the coupling to solid ground and the vertical levelling of the seismometer (Lott [2017]). The stations in Saint Guérin are installed as described above. Figure 2.11 illustrates a typical instrumentation consisting of a sensor connected to a digitizer. An example of the configuration in a schematic representation in the free field and on the dam-rock interface is presented in Figure 2.10. The sensor and the digitizer are positioned in two different plastic boxes; the box that contains the sensor is thermally isolated from the environment by an isolation layer aiming to maintain the conditions in the inside of the box stable. Great attention was also paid during the installation process to the vertical levelling of the velocimeters. GPS antennas ensure the synchronization

of all stations.

Regarding the energy supply, fifteen out of nineteen stations are directly powered by the dam (i.e. SG01, SG02, SG03, SG04, SG05, SG06, SG07, SG08, SG09, SG10, SG11, SG12, SG13, SG14 and SG15) while the four remaining (SG17, SG18, SG19, SG20) are powered using solar panels. Additionally, batteries were connected to the dam and the solar panels respectively for the energy emergency cases. This was the case particularly for the stations SG19 and SG20, around the dam reservoir, where the batteries supplied the stations several times due to insufficient supply from the solar panels. Figure 2.12 illustrates schematically the power supply of the stations.

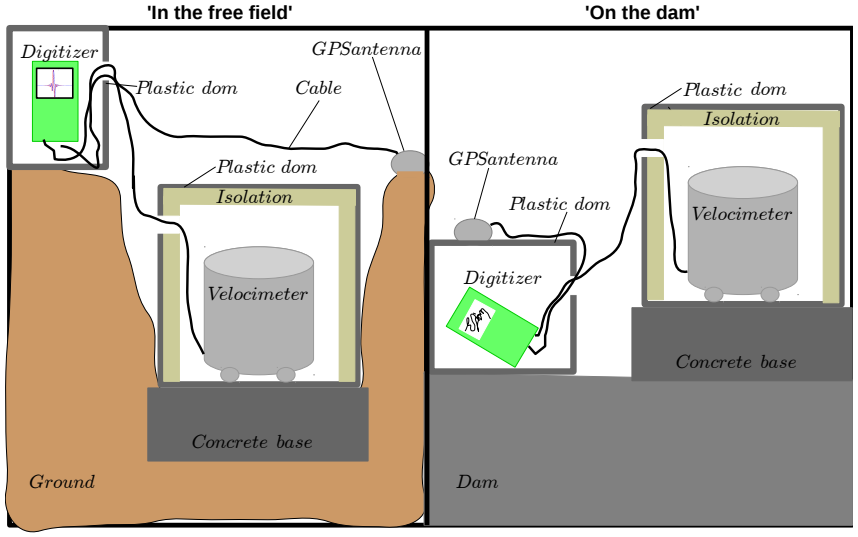

FIGURE 2.10: Schematic representation of station configuration: boxes containing the sensor and the digitizer, isolation of the sensor, concrete base and GPS antenna.

The stations were well maintained throughout the entire duration of the experiment. A routine-maintenance was performed; during the first month every two weeks and then once per month to recover the seismological data as well as to ensure the better functioning of the stations. Although continuous good quality data has been acquired by all stations, there are still data gaps due to some difficulties faced at the site. Issues of malfunctioning of either sensors or digitizers were faced and resolved during the regular monthly visit. Some of those problems where resolved with relative delay since the site that the dam is located is in high altitude which made it difficult to access during the winter because of bad weather conditions (snow and ice). Therefore, the visits were sometimes postponed for some days. According to analyses performed after the acquisition of the first recordings, the position of the GPS antennas for six stations (SG08, SG09, SG10, SG11, SG12, SG17) was adjusted to have better satellite exposure. The signal-to-noise ratio (SNR) of the station SG11 at the interface of the dam with the

FIGURE 2.11: Station configuration: boxes containing the sensor and the digitizer, isolation of sensor of type Güralp CMG40T, sensor type Lenhartz 5 sec, Nanometrics Taurus digitizer and GPS antenna.

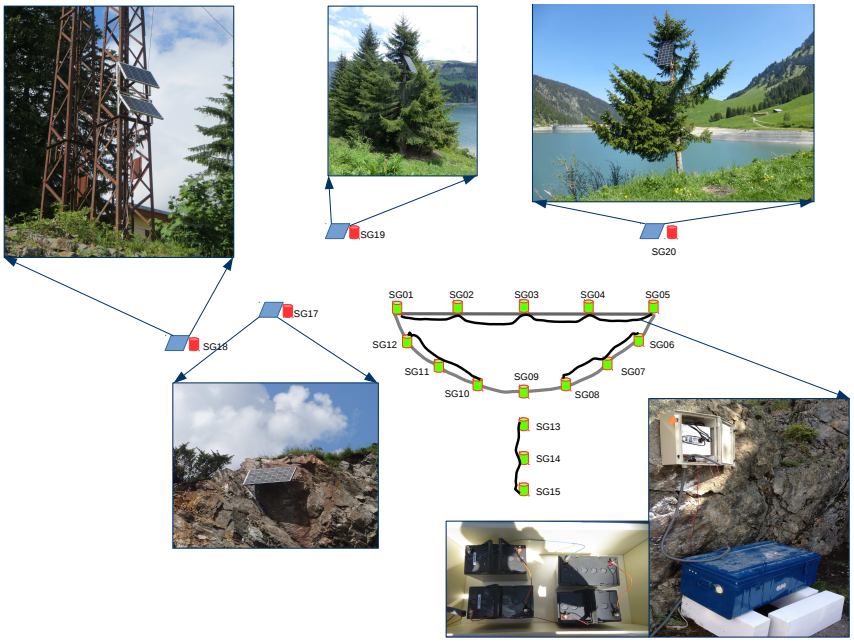

FIGURE 2.12: Power supply of stations: cables supplying stations directly from the dam, batteries inside their box, connected to the dam and solar panels supplying the isolated stations.

TABLE 2.1: Data availability recorded from the 19 stations. The left column indicates the period between two visits. Green rectangles indicate $95-100\%$ of data availability and red rectangles $\leq 50\%$ of data availability. The gray zones correspond to absence of data due to the removal of a station.

Station/ Period	SG01	SG02	SG03	SG04	SG05	SG06	SG07	SG08	SG09	SG10	SG11	SG12	SG13	SG14	SG15	SG17	SG18	SG19	SG20
18/06/15-01/07/15																			
01/07/15-21/07/15																			
21/07/15-28/08/15																			
28/08/15-25/09/15																			
25/09/15-20/10/15																			
20/10/15-03/12/15																			
03/12/15-16/12/15																			
16/12/15-05/01/16																			
05/01/16-12/01/16																			
12/01/16-21/01/16																			
21/01/16-09/02/16																			
09/02/16-08/03/16																			
08/03/16-08/04/16																			
08/04/16-13/05/16																			
13/05/16-30/06/16																			

rock was identified as low after the first few visits and the sensor was replaced. In few cases, malfunctioning of the system leaded to loss of one of the three components of the records for a limited time (up to several minutes). Table 2.1 shows the data status for the duration of the experimental campaign organized in periods between two maintenance visits. Except for SG01 and SG20 that were installed two weeks later than the other stations, data are not acquired in between two dates of maintenance in most of the cases due to malfunctioning of the digitizers. Figure A.1 in APPENDIX A presents the detailed data availability organized by day recordings for the period from June to December 2015 that the totality of the 19 stations were deployed in-situ. A few-minute malfunctioning of the seismograph system is not represented in the tables. A summary of this table is given in Figure 2.13 where the percentage of monthly data availability is provided. Overall, the data acquisition was successful throughout the entire campaign and the data losses remained limited.

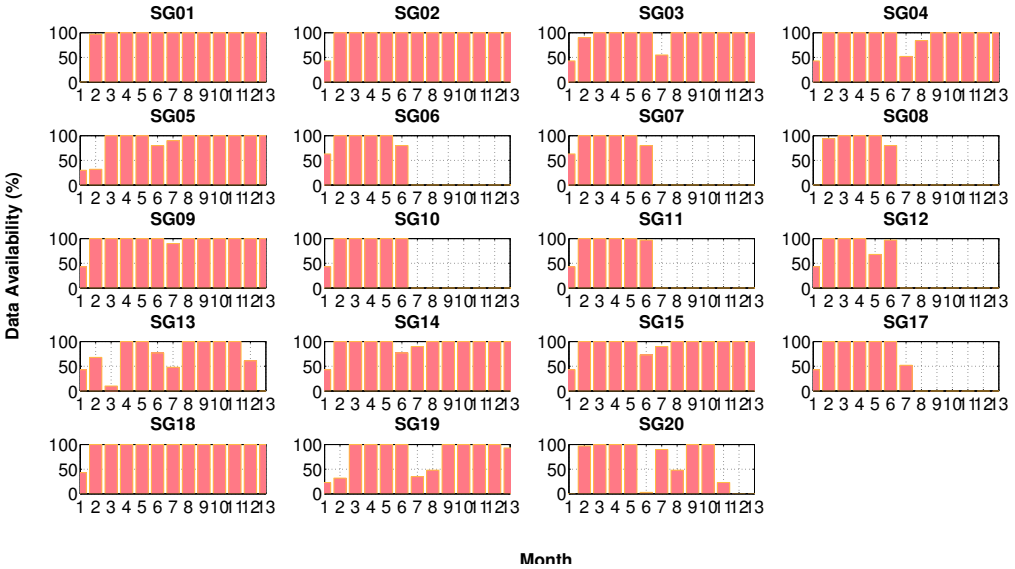

FIGURE 2.13: Data availability (%) per month recorded from the 19 stations. Numbering from 1 to 13 corresponds to months from June 2015 (1) to June 2016 (13).

2.4 Earthquake catalog preparation

Because we are interested in performing SVGM analysis, only records from mid June 2015 till beginning of December 2015 are considered for earthquake catalog preparation, when data of all station at the dam-foundation rock interface are available. Le Réseau National de Surveillance Sismique (RéNaSS) is a federation of networks under the responsibility of various Observatoires des Sciences de l'Univers (OSU) and partner Universities. Based on the existing catalog of RéNaSS, probable seismic events are first identified from the continuous records through visual inspection. This catalog is used to identify the origin time and characteristics of the events. Over the first six months of the deployment of the seismological array in Saint Guérin, more than 100 local and regional events, with $M_L \geq 1.5$, occurred in the broader Alpine area, i.e. $R_{epi} \leq 350km$.

2.4.1 Selection of subset of seismic events

A subset of events with very good signal-to-noise ratio (SNR), recorded by the stations of the dense network, was selected for SVGM analysis in terms of amplitude and phase. The SNR of each recording at one station is estimated by computing the ratio of its summed squared magnitude to that of the noise recorded at the same station 5 minutes before the occurrence of the event. For the seismic and the noise signals a 20 sec window is defined (10 sec before and 10 sec after the PGV for the seismic events) to compute the ratio. After careful inspection, 55 events with recordings having high SNR (generally $SNR \geq 3$ in the frequency band of interest, i.e. [1 20] Hz) and all the three

TABLE 2.2: Average signal-to-noise ratio (SNR) of the velocity time series of the two horizontal components for each station for the 55 selected seismic events.

Average SNR										
	SG01	**SG02**	**SG03**	**SG04**	**SG05**	**SG06**	**SG07**	**SG08**	**SG09**	**SG10**
NS comp.	13,73	11,97	13,00	12,09	13,75	13,02	11,99	11,90	12,26	12,49
EW comp.	13,66	11,88	12,15	11,90	12,66	12,55	12,38	13,26	13,19	13,06
	SG11	**SG12**	**SG13**	**SG14**	**SG15**	**SG17**	**SG18**	**SG19**	**SG20**	
NS comp.	11,78	13,28	13,41	13,16	13,36	12,94	14,68	13,63	13,21	
EW comp.	12,90	10,95	13,83	13,36	13,86	13,16	12,70	13,37	13,53	

components of motion acquired were selected for earthquake catalog preparation. The metadata of the 55 events are presented in Table B.1 in APPENDIX B. The SNR of each recording for the frequency band [1 20] Hz, is presented in Table B.1 in APPENDIX B. The average value of SNR of the 55 events for each station is given in Table 2.2 for both horizontal components. Additionally, the percentage of records missing because of either malfunctioning/absence of a station and because of low SNR are shown in Figure B.2 in APPENDIX B. 8% of the records are missing due to malfunctioning/absence of a station. SNR has an important impact on the choice of the final dataset; 43 % of the records for the 55 events (457 out of 1045 that could be obtained) is not used because of low SNR. This is because of the combined effect of low magnitude and distant events that produce very small ground shaking. However, the number of available records (588) is largely sufficient for an accurate statistical analysis and the average SNR value for all records that are considered is more than 10, showing data of excellent quality. The number of available records for each one of the events as well as for each one of the 19 stations is shown in Figure 2.14. For 24 events more than 10 station recordings are available while only for very few events (11) less than 5 are available. The lowest number of available seismic recordings corresponds to the 3 stations on the crest of the dam, i.e. SG02, SG03 and SG04; 15, 8 and 11 recordings respectively. This is due to the vibrations of the structure itself that are strong on the crest combined with the low magnitude and distant events that provoke very small shaking. The two aforementioned factors lead to low SNR ratio of the recordings of the three stations on the crest.

A total of 55 local and regional events, within 320 km distance from the array having magnitude from 1.5 to more than 4, was selected. Most of the events are shallow crustal (hypocentral depth $\leq$ 25 km). As identified in Figure 2.15, which shows the location of the subset of selected events, an homogeneous distribution in terms of azimuthal coverage cannot be achieved due to locations of the earthquakes; the vast majority of the events occurred in the north-east and south-east of the dam, were the main faults that dominate the seismicity of the region are found. Figure 2.16 shows the distribution of the magnitude (M_L) of the events as a function of their epicentral distance R_{epi} (km) from the dam, their hypocentral depth (km) and azimuth, BA (°). Table 2.3 shows the number of selected events for each magnitude, epicentral distance and azimuth group

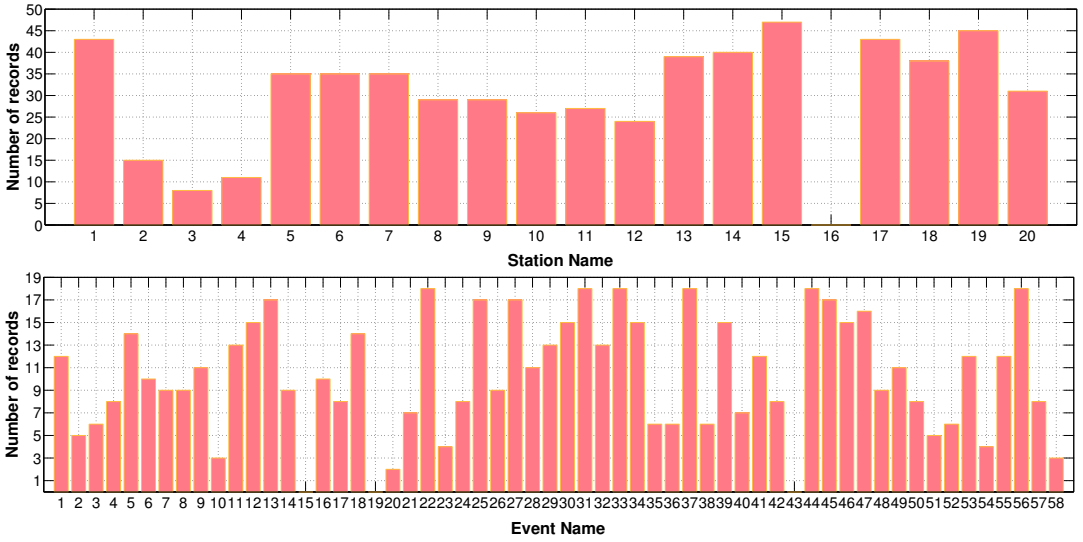

FIGURE 2.14: Total number of available records for each of the 19 stations and total number of available recordings for each of the 55 selected events.

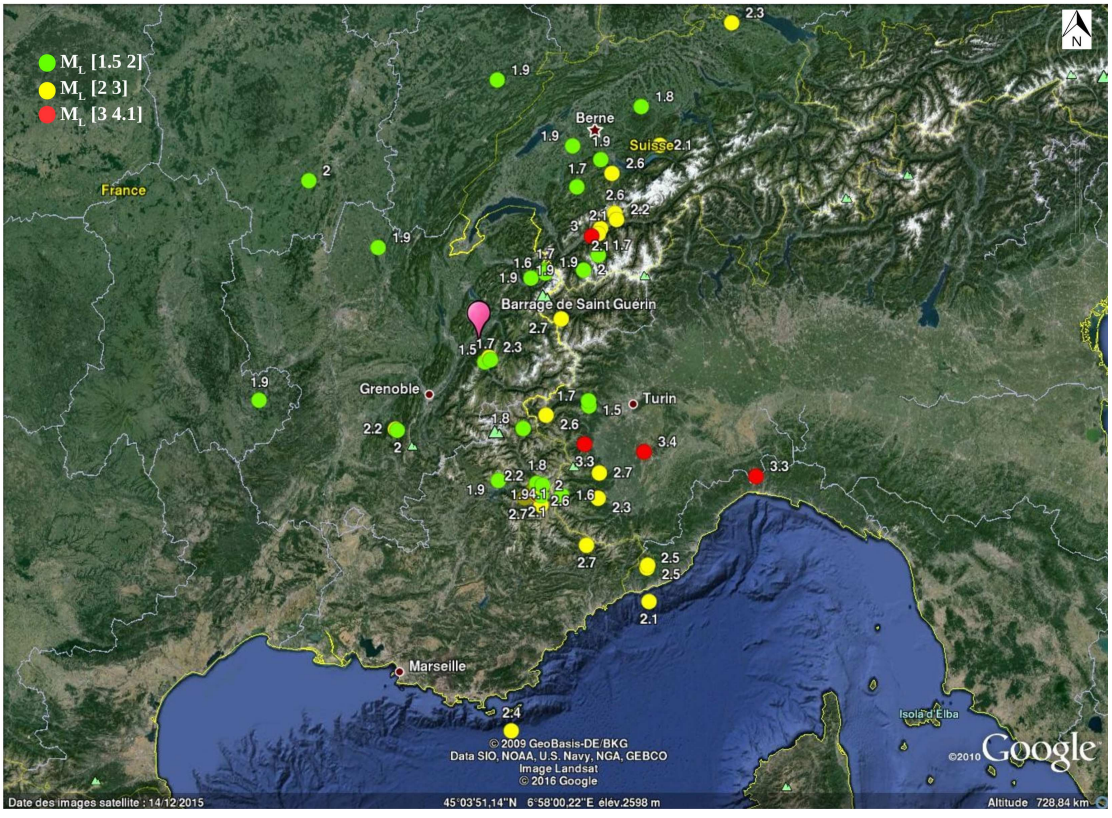

FIGURE 2.15: Map of the subset of 55 events chosen, recorded from the seismological array during the period of six months (July 2015 – December 2015). Green, yellow and red tacks on the map represent event locations with M_L [1.5 2], [2 3] and [3 4.1] respectively. The pink balloon indicates the location of the arch dam.

TABLE 2.3: Number of selected events for each magnitude (M_L), epicentral distance ($R_{epi}(km)$) and back-azimuth (BA (°)) group.

M_L			$R_{epi}(km)$			BA (°)	
[1.5 2.0]	[2.0 3.0]	[3.0 4.5]	[0 100]	[100 200]	[200 350]	[0 180]	[180 360]
22	28	5	17	32	6	44	11

analyzed. The majority of the events are of low magnitude, ranging from 2 to 3, and epicentral distance from 100 to 200 km. Very few events have magnitude that is higher than 3 and epicentral distance from the dam lower than 100 km. Origin date and time, latitude, longitude, magnitude (M_L), epicentral distance (R_{epi}) and hypocentral depth for the subset of events are given in Table B.1 in APPENDIX B. Figure 2.17 illustrates the Peak Ground Velocity (PGV) distribution with both magnitude (M_L) and epicentral distance (R_{epi}) (km) for each one of the recordings for each event for the two horizontal components. PGV values of most of the recorded events range from 0.0001 to 0.1 mm/s with the highest value to be 0.2 mm/s. The highest PGA value observed on the crest is 0.12 mm/s^2 (0.0012 m/s^2). The NS component appears to be more energetic than the EW component, which is to be expected because the first one is parallel to the valley. It has to be noted that the highest value of PGA, equal to 0.0012 m/s^2, is very low with respect to the design values of the dam's area, that are in the order of 1.6 m/s^2 or more (Figure 2.4).

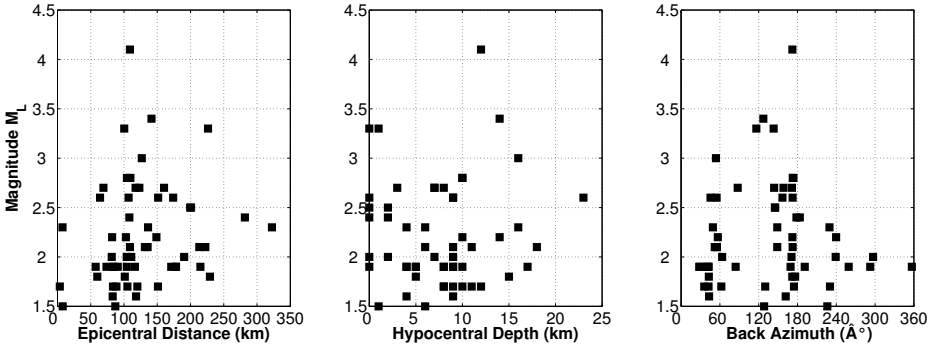

FIGURE 2.16: Local magnitude distribution (M_L) as a function of epicentral distance ($R_{epi}(km)$) (left), hypocentral depth (km) (middle) and back azimuth (BA (°)) (right) for the subset of 55 events.

When implementing PSHA, the logarithmic spectral acceleration at a site due to an earthquake is usually assumed to be well represented by the normal distribution marginally (e.g., Kramer [1996]). Abrahamson [1988] performed rigorous statistical studies to verify the assumption that logarithmic PGA values follow the normal distribution marginally. To verify that the PGV values recorded from the Saint Guérin array, have this same characteristic, the distribution of logarithmic PGV values of the 55 events for both horizontal components recorded at all stations are shown in Figures 2.18 and 2.19. The logarithmic PGV for most of the stations (with the exception of the three stations on the

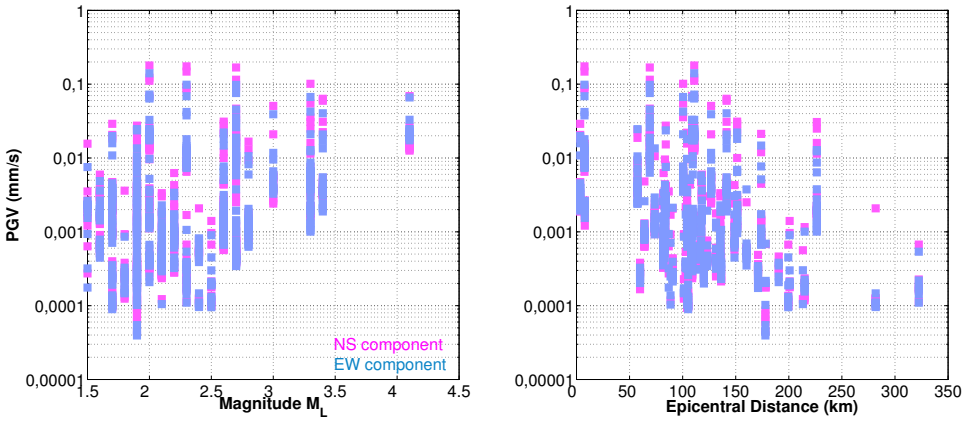

FIGURE 2.17: Peak Ground Veloocity (PGV) distribution (mm/s) as a function of magnitude (M_L) and epicentral distance (R_{epi})(km) for the subset of 55 events (all available recordings) selected for analysis for both horizontal components, NS and EW.

crest of the dam) seem to follow a normal (Gaussian) distribution marginally, confirming the above statements.

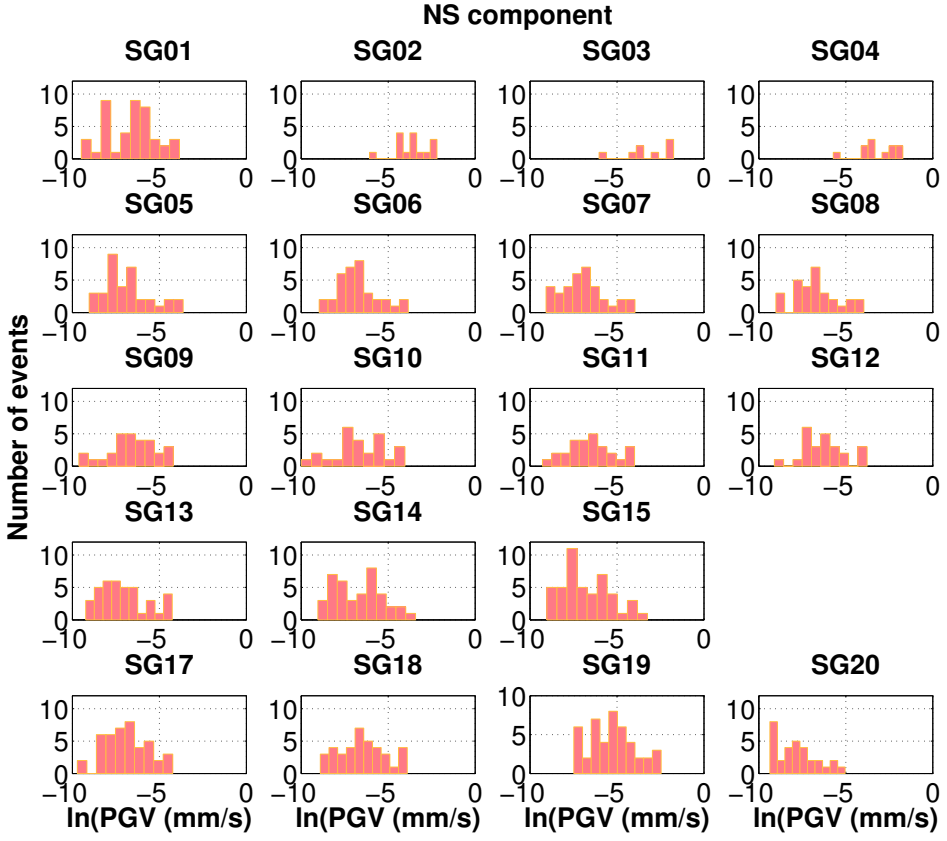

FIGURE 2.18: Distribution of the ln of PGV (mm/s) of the 55 events for the NS component recorded at all stations.

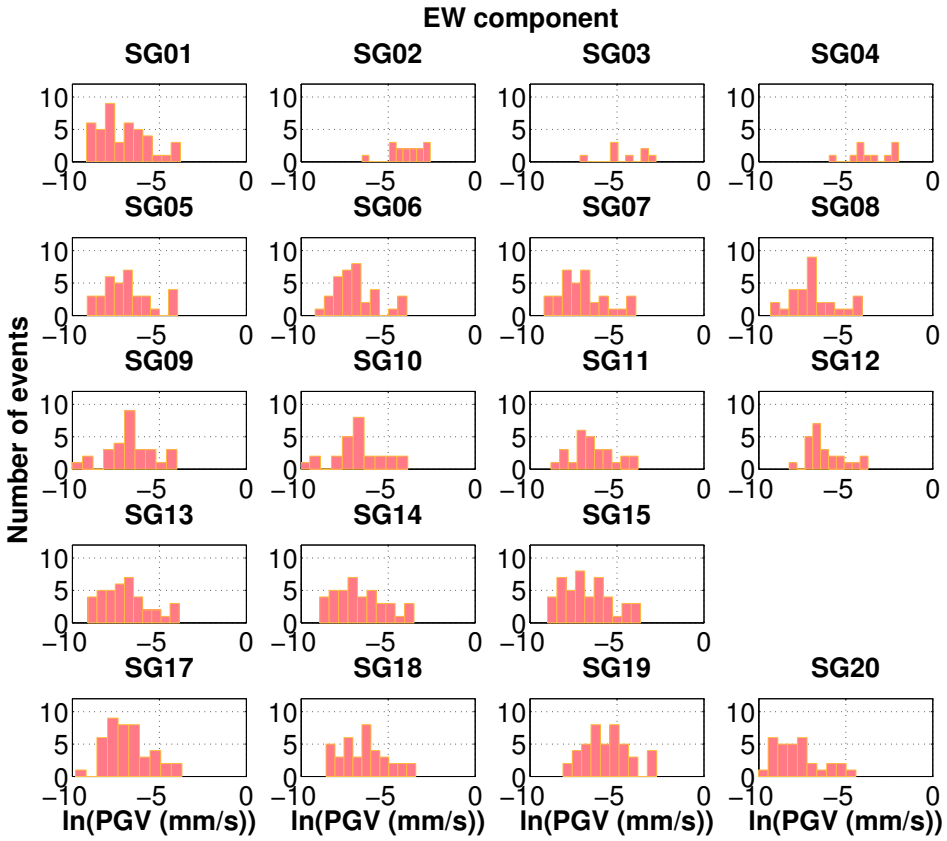

FIGURE 2.19: Distribution of the ln of PGV (mm/s) of the 55 events for the EW component recorded at all stations.

2.4.2 Example waveforms

Example waveforms from a local event that occurred the September 10^{th} at UTC 07:32:08 are included in this section. Its local magnitude, M_L, is 3.3 at epicentral distance, R_{epi}, of 100 km from the dam of Saint Guérin. The hypocentral depth is 1 km, according to ReNass catalog. Figure 2.20 shows the location of the event with respect to the location of the dam. The velocity time series of the NS component recorded from 18 of the stations are presented in Figure 2.21. The record of SG03 station on the crest of the dam is not included because of saturation of the NS component. The amplification of the motions on the crest (recordings of SG02 and SG04) with respect to the motions at the base of the dam is obvious; it is demonstrated on the figure by red color of the frame. Similarly, the motions are amplified at the station SG19 since the station is located by the lake, on a low velocity scree layer laying above the rock.

To get a better idea (visually) of the variability among the records at the dam-foundation rock interface both in amplitude and frequency content, the Response and the Fourier spectral amplitudes (no smoothing applied to either of the two), of the stations at the interface (i.e. SG01, SG05, SG06, SG07, SG08, SG09, SG10, SG11 and SG12) are given

in Figure 2.22. The variability of the motions can be easily identified in the Response and Fourier spectra of the time histories; it can be noticed though that the amplitude differences among the records are stronger than the phase variations. Several peaks are observed on the spectra along the frequency range; these peaks could be linked either to the frequency content of this particular earthquake (signature of this seismic event) or to the frequencies of vibration of the dam (signature of the dam). Coupling of the two phenomena results in strong peaks on the spectra.

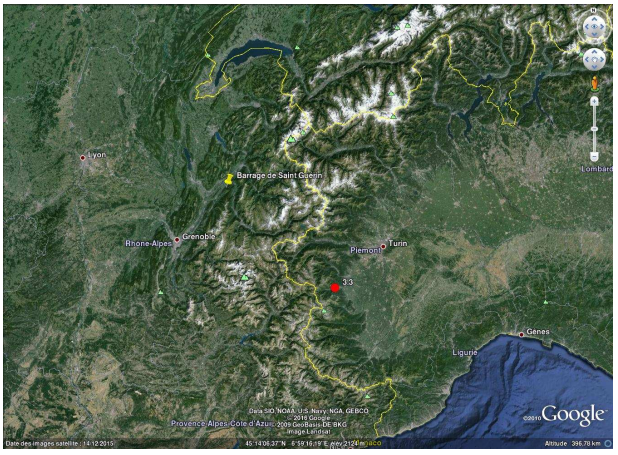

FIGURE 2.20: Map of the example event: Event occurred on September 10, 2015 at UTC 07:32:08 with magnitude M_L 3.3 and epicentral distance 100 km (red point). The yellow tack indicates the location of the arch dam.

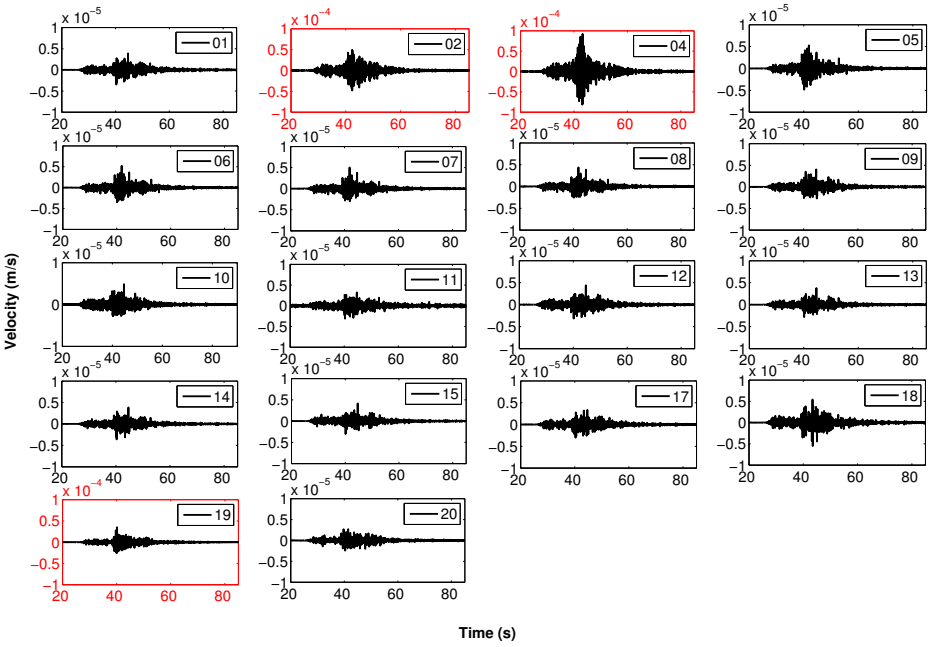

FIGURE 2.21: Velocity time series for the the NS component recorded at stations SG01, SG02, SG04, SG05, SG06,SG07, SG08, SG09, SG11, SG12, SG13, SG14, SG15, SG17, SG18, SG19 and SG20 for the event that occurred on September 10, 2015 at UTC 07:32:08 with magnitude M_L 3.3 and epicentral distance 100 km.

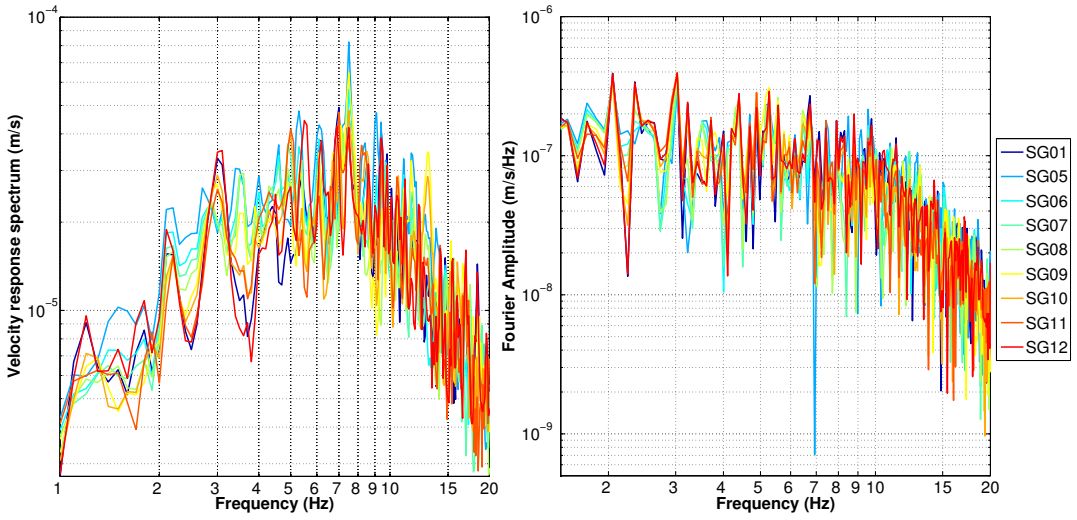

FIGURE 2.22: Velocity response spectra and Fourier amplitude spectra for the the NS component recorded at the dam-foundation rock interface (i.e. SG01, SG05, SG06,SG07, SG08, SG09, SG10, SG11, SG12) for the event that occurred on September 10, 2015 at UTC 07:32:08 with magnitude M_L 3.3 and epicentral distance 100 km.

2.5 Dynamic analysis of the arch dam

The earthquake and ambient noise data are valuable for the calibration of numerical procedures used to carry out earthquake analysis and seismic safety evaluation. The main objective of the seismological campaign held in Saint Guérin is to collect data to identify the effective input motions as well as the free field motions at specific sites and to establish a set of records covering dam excitation and response. The seismic data of the dense network allow to monitor the overall dam behavior during seismic events and to identify the response patterns and governing effects during earthquakes. The key dynamic properties of the dam-reservoir-foundation system (e.g frequencies of vibration, damping) and its response in terms of crest amplification can be extracted. Complementing this effort, ambient vibration data could also be of great use because they offer a fast as well as inexpensive way to obtain the dynamic characteristics of a civil engineering structure. The continuous recordings cover different periods of the reservoir filling cycle allowing to, also, investigate water level effects on the dynamic properties of the dam-reservoir-foundation system. Ambient noise's causes include nearby human activities (such as traffic or heavy machinery), winds and other atmospheric phenomena, and ocean waves. In Saint Guérin site, given the location, nearby human activities are very limited thus the main sources of ambient vibrations are due to various atmospheric phenomena (principally wind and reservoir motion) and the waves of the Atlantic ocean and the Mediterranean sea.

2.5.1 Frequencies of vibration

Herein, a simple approach aiming to identify the frequencies of vibration of the arch dam in Saint Guérin is adopted taking advantage of the in-situ ambient vibration records. Analyzing ambient noise recorded at the 3 stations located on the crest of the dam and the 9 stations at the dam-foundation rock interface, several eigen frequencies of the dam are identified within the broader frequency range from 1 to 20 Hz. 20 minute-long recordings, 2 hours before the occurrence of each seismic event (selected subset of 55 events presented earlier in Chapter 2), are used. The choice of the time of the recordings is made to identify the frequencies of vibration of the structure during the occurrence of the seismic events that will be used for the spatial variability analysis that follows in Chapter 3. The recorded velocity time histories are used. For each one of the velocity time histories, the Fourier spectrum is estimated in the frequency range of interest. The Fourier spectra without smoothing and then smoothed are estimated. For the smoothing procedure, the Konno-Ohmachi smoothing window (Konno & Ohmachi [1998]) with a coefficient of 90, i.e. very light smoothing coefficient, is chosen because it allows the necessary resolution for clear peak identification.

The smoothed Fourier velocity spectral amplitudes of individual ambient noise records (gray lines) on the crest and at the dam foundation rock interface as well as the median value (black line) of the three stations on the crest and the nine stations at the dam-foundation rock interface for the two horizontal (NS and EW) and the vertical (Z) components are illustrated in Figure 2.23. The median values for the three components on the crest and at the dam-foundation rock are plotted together in Figure 2.24. The results of the unsmoothed Fourier spectra are provided in APPENDIX C (Figures C.1 and C.2). A zoom in the frequency range [2.5 10] Hz of the unsmoothed Fourier spectra is presented in Figure 2.25. In the aforementioned figures, the frequencies of vibration of the dam can be clearly identified on the crest and they are still easily observable at the dam-foundation rock interface. According to the smoothed spectra, the first vibrational frequency is at 3.8 Hz. However, the unsmoothed spectra in Figure 2.25 reveal two vibrational frequencies with values very close to each other, $\sim$ 3.8 and $\sim$ 3.9 Hz. The next frequency peak is at 5.2 followed by a smaller amplitude peak at 5.75 Hz. In the broader frequency range between 6.5 and 11 Hz there are four peaks, at around 7.2, 8.5, 9 and 11 Hz. A last, clear, peak is identified at around 18 Hz. The same frequency peaks are observed in all three components of motion (NS, EW and Z) with the NS component to be slightly more energetic than the EW component indicating a relatively stronger motion of the dam parallel to the valley. The vertical amplitudes are lower than the two horizontal ones, however the frequencies of vibration are still identified clearly.

Given the complexity of the mode shapes of an arch dam, instead of combining the three stations on the crest to find their median value, each station is studied independently.

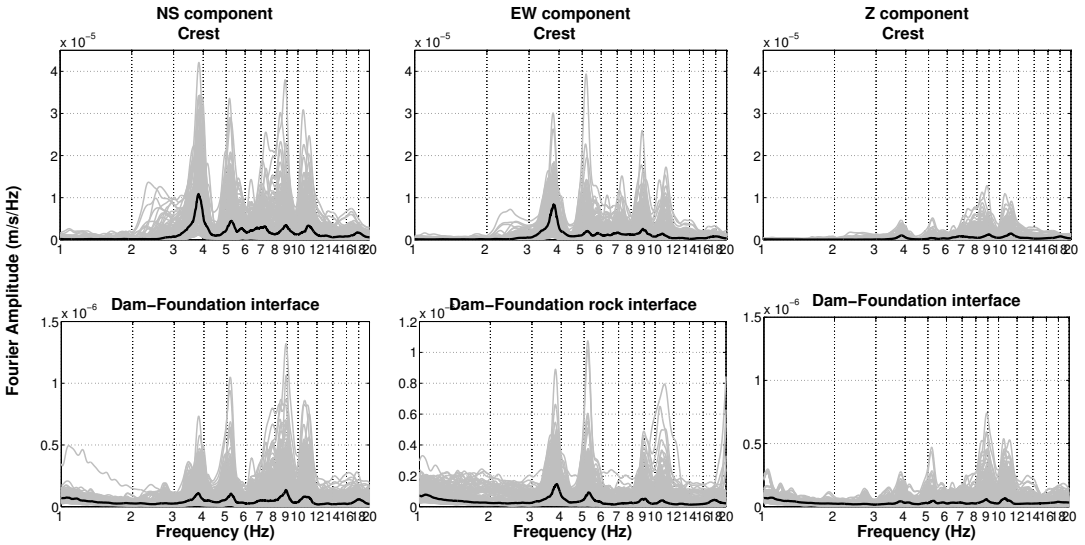

FIGURE 2.23: Fourier velocity spectral amplitudes of individual ambient noise records (grey lines) on the crest and at the dam foundation rock interface (20 minutes-long records two hours before each of the 55 events of Figure 2.15) and median value (black lines) of the three stations on the crest and the nine stations at the dam-foundation rock interface for the two horizontal and the vertical components (NS, EW and Z).

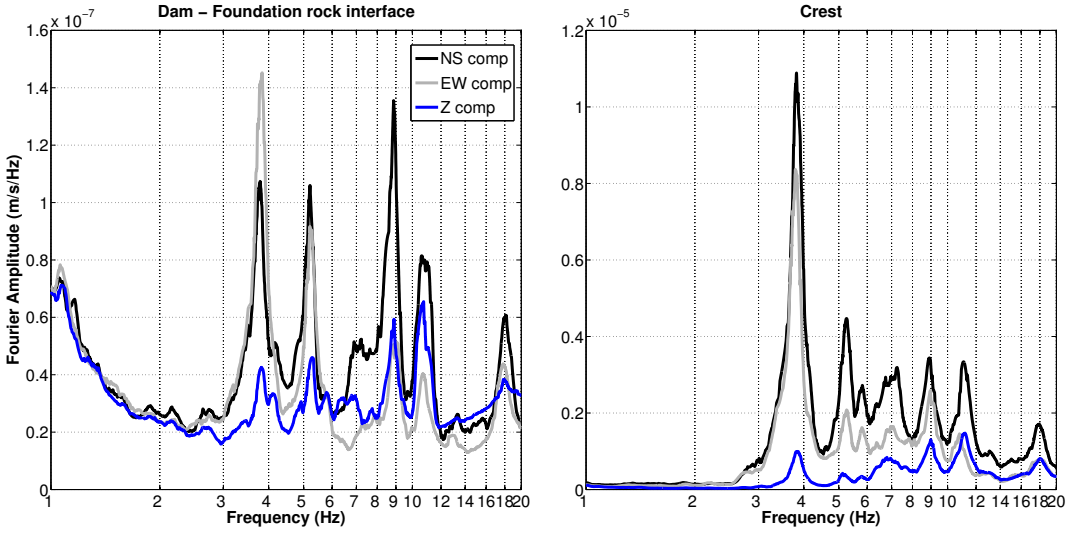

FIGURE 2.24: Median value of frequencies of vibration of the Saint Guérin arch dam estimated using 20 minutes-long records of ambient noise two hours before each of the 55 events of Figure 2.15; median value of Fourier velocity spectral amplitudes of the nine stations at the dam-foundation rock interface (right) and median value of Fourier amplitudes of the three stations on the crest (left) for the two horizontal and the vertical components (NS, EW and Z) is presented.

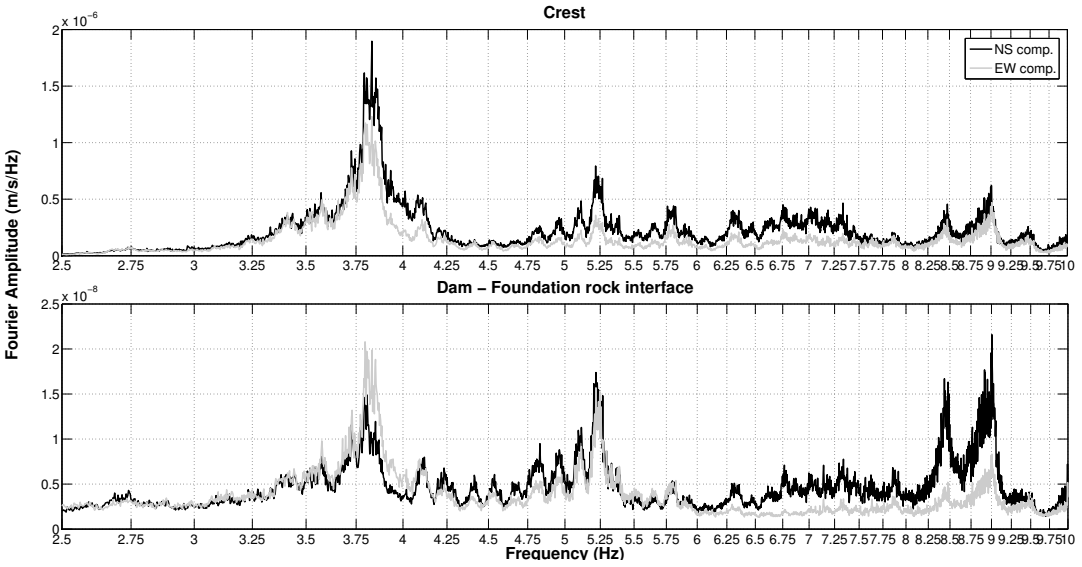

FIGURE 2.25: Median value of frequencies of vibration of the Saint Guérin arch dam estimated using 20 minutes-long records of ambient noise two hours before each of the 55 events of Figure 2.15; median value of unsmoothed Fourier velocity spectral amplitudes of the nine stations at the dam-foundation rock interface (right) and median value of unsmoothed Fourier amplitudes of the three stations on the crest (left) for the two horizontal components (NS and EW) is presented; zoom in the frequency range [2.5 10] Hz.

The Fourier velocity amplitudes of the SG02 (magenta lines), SG03 (blue lines) and SG04 (gray lines) as well as the median value of each station are shown in Figure 2.26 for the three components (NS, EW and Z)(the results using the ansmoothed spectra are provided in APPENDIX C, Figure C.3). We notice that not all frequencies of vibration are identified from all the three stations on the dam crest as well as that the various frequency peaks are differently amplified at the three locations on the crest. This phenomena point to different mode shapes. Further analysis is required for the identification of the mode shapes corresponding to the first eigen frequencies, that would show us with precision the frequencies of vibration. Such detailed analysis is beyond the scope of the present thesis, thus it is not performed. The rough identification of the frequencies of vibration of the dam is useful for the spatial variability analysis that follows because it gives a better insight in the dam's state. The analysis presented herein is neither a sufficient nor a very accurate method of frequency vibration estimation for the case of such a complicated structure. Nonetheless, the rough estimation of the frequency peaks using all the stations on the crest and at the base allows us to use them later on when needed in Chapters 3 and Chapter 4.

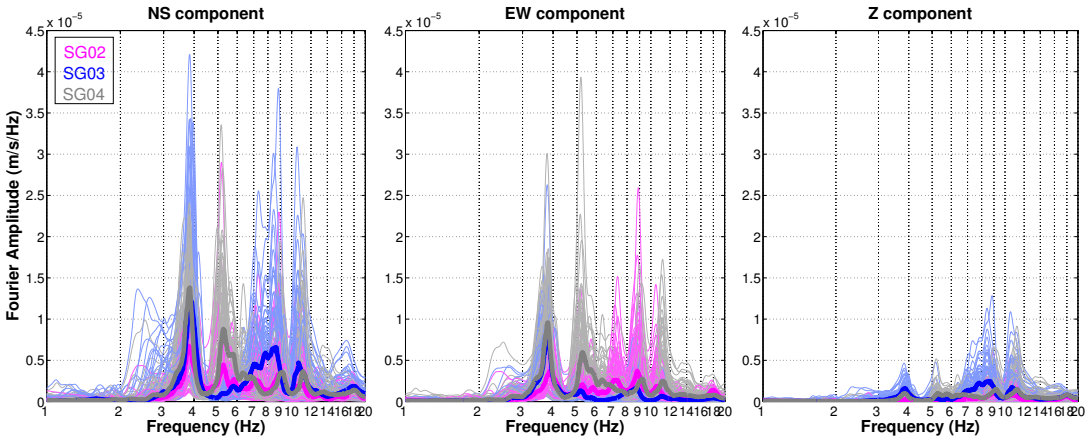

FIGURE 2.26: Frequencies of vibration of the Saint Guérin arch dam estimated using 20 minutes-long records of ambient noise two hours before each of the 55 events of Figure 2.15; individual Fourier velocity spectral amplitudes and median value of Fourier amplitudes of the three stations on the crest (left) for the two horizontal and the vertical components (NS, EW and Z) is presented.

Sensitivity analysis on water level

Generally the frequencies of vibration vary with the evolution of the water level of the reservoir of the dam. With the increase of water level, the mass is increasing while the rigidity of the system remains constant. Thus, changes are expected on the vibrational frequencies of the structure. A decrease in the main peak frequencies occurs when the water level is increasing (Oliveira et al. [2012]). A sensitivity test of the observed frequencies of vibration on the water level is performed. The water level in the Saint Guérin reservoir is constant up until the end of October while afterwards it starts to decrease (several meters). Half of the subset of events (30 earthquakes) occurred from June 2015 till October 2015 when the water level was stable. Figure 2.27 shows the identified frequencies of vibration on the crest and at the base for the three components (median values) firstly considering records up to the end of October and then the totality of the records during the six-month period, till December. As it is observed, the identified peaks for the two cases of water level, constant and variable, are almost identical. The Fourier spectral peaks are slightly shifted to lower frequencies in the case of constant water level with respect to the variable water lever, i.e. decreasing water level, which is in accordance to the statement that when the water level is increasing there is a decrease in the main peak frequencies. The frequency shifts are very slight with values generally ≤ 0.1 Hz. Significant difference is observed, however, of the amplitudes, particularly for the higher frequencies of vibration. This is explained by higher damping coefficients in the case of higher water mass. Given that the identified frequencies are almost identical, the evolution of frequencies of vibration with the water level is not further investigated.

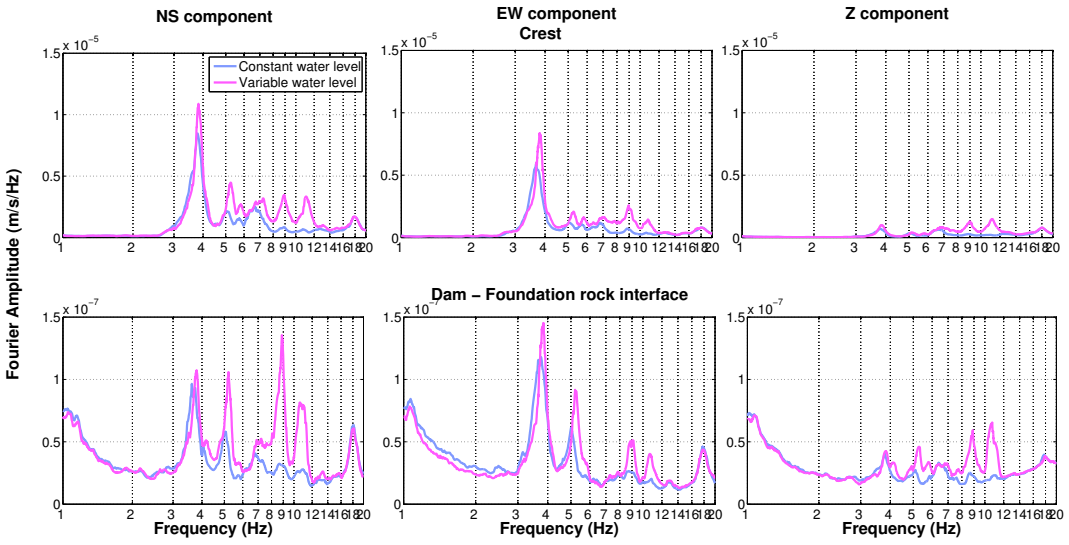

FIGURE 2.27: Eigen frequencies of the Saint Guérin arch dam estimated using 20 minutes-long records of ambient noise two hours before each of the 55 events of Figure 2.15; median value of Fourier velocity spectral amplitudes of the nine stations at the dam-foundation rock interface and median value of Fourier amplitudes of the three stations on the crest for the two horizontal and the vertical components (NS, EW and Z) is presented.

2.5.2 Damping ratio

Viscous damping ratio represents the energy loss of an oscillating system. The loss can be either internal (material damping) or to another system (radiated damping). The computation of the viscous damping assumes the friction forces (energy loss) are proportional to the velocity of the system. For a single degree-of-freedom system, the solution of the differential equation in time (impulse response function) is then an exponentially decreasing sinusoidal function of the form:

$$h(t) = \alpha e^{-\xi\omega t} sin(\omega' t) \tag{2.1}$$

with

$$\omega' = \omega\sqrt{(1-\xi)^2} \tag{2.2}$$

where ξ is the damping ratio and ω the angular resonance frequency of the system. The Random Decrement technique is based on the assumption that at each time step, the signal is the sum of a random signal and the impulse response function of the study-system. Stacking many time windows with the same initial condition results in enhancing the impulse response function component with respect to the zero-mean random part. The algorithm selects all the windows of the given length starting with a 0 amplitude and a positive derivative and averages them. Then, the Impulse response function is fitted by an exponentially decreasing sine function (starting at 0) depending on an amplitude,

α, the resonance frequency, $f = \frac{\omega}{2\pi}$ and the damping ratio, ξ (Cole [1973], Rodrigues & Brincker [2005]).

For the damping analysis herein, the 'Damping' Geopsy Tool is used which aims at computing the viscous damping ratio of an identified oscillating structure using the Random Decrement technique. The three stations on the crest are used, i.e. SG02, SG03 and SG04, to estimate the damping ratio during earthquakes, ξ, at the first identified frequency of vibration of the structure, i.e. around 3.8 Hz (Figure 2.24). The velocity time series of the available recordings of the 3 stations for the subset of 55 events are filtered around 3.8 Hz. The estimated damping ratios for each component and each station for all the available records are given in Tables C.1, C.2 and C.3 in APPENDIX C. The mean values of damping ratio for the NS, EW and Z for the three stations are summed up in Table 2.4. It needs to be underlined that the number of available records for the stations SG02, SG03 and SG04 is relatively limited for a very accurate statistical analysis (15, 8 and 11 records respectively as shown in Figure 2.14. To this end, the conclusions should be made with caution.

TABLE 2.4: Mean value of damping ratio, $\xi\%$, of the available data out of the subset of 55 events for the three crest stations SG02, SG03 and SG04 and median value of all the three stations for NS, EW and Z component.

	$\xi\%$		
	NS	**EW**	**Z**
SG02	2.53	1.53	1.16
SG03	1.71	1.01	1.48
SG04	1.92	1.46	2.15
Mean	**2.06**	**1.33**	**1.60**

The analysis reveals that the damping ratio, $\xi\%$, of the first vibrational frequency, ranges between 1 and 2 % for the three components with the NS component to be twice as damped as the EW. The detected values are consistent with modal damping values ranging from 1 to 3 or 4 % in the literature (Council et al. [1991] and references therein). These damping ratios are due to the large potential for radiation of energy that exists within a concrete dam because it is fully embedded in foundation rock that often has material properties similar to concrete (as is the case in Saint Guérin) and with the impounded water completely covering one face. During strong shaking, however, the material component of the damping would be expected to increase due to a larger activation of micro-crack sliding which provides loss of energy by friction. As proved from the sensitivity analysis performed in the section above (Figure 2.27), lower water level leads to lower damping values.

2.5.3 Amplification on the dam crest

Due to the response of the structure, on the crest of the dam the motions are stronger than at the base. By the 1950s the importance of the dynamic earthquake response of typical structures such as buildings and bridges was recognized. However, it was still commonly assumed that, concrete dams were stiff enough that amplification of earthquake ground motions through structural response was insignificant (U.S. Army [1958]); this would most probably refer to gravity dams. At the time earthquake effects were still being characterized by equivalent static forces. Despite that, it was recognized that, given the relatively infrequent occurrence and short duration of earthquakes, it was appropriate to apply criteria having less conservatism for loading conditions that included earthquakes than for loading conditions without earthquakes (U.S. Army [1958]). Large amplification of motions on the crest with respect to the foundation rock has been detected in several cases (Ambiesta (Castoldi [1978]), Hsinfengkiang (Tsung-Ho et al. [1976]), Kurobe (Nose [1970]), Nagawado (Fujii et al. [1987]), Shintoyone (arch) Dam (Kuroda & Baba [1985]), Techi (Chang et al. [1987]), Tonoyama (arch) Dam (Okamoto & Takahashi [1960], Okamoto et al. [1964a]), and Yuda (Iida et al. [1983]). In the late 1960s, it was accepted that, although concrete dams are relatively stiff structures, substantial amplitudes of earthquake ground motions could indeed occur at frequencies well within the frequency range of response for concrete dams. Therefore, it was concluded that the resulting response amplification should not be ignored. The aforementioned large amplifications were estimated based on a number of measurements during small to very small shaking (distant and small earthquakes) in which case a small damping is expected. These observations, though, may not characterize the crest amplification due to strong motions when the material component of the damping would be higher.

The amplification phenomenon is observed in the arch dam of Saint Guérin. The amplification of the crest with respect to the base may differ significantly though depending on the source of the motions, i.e. ambient noise or earthquakes, hence, it is estimated in both cases. It needs to be underlined that the seismic motions recorded are small, indicating a damping coefficient of 1% as estimated in the previous section, thus the conclusions cannot be extrapolated to stronger shaking when the damping would be higher. At the base of the dam, the records coming from the stations all along the dam-foundation rock interface are considered, i.e. SG01, SG05, SG06, SG07, SG08, SG09, SG10, SG11 and SG12. The Fourier spectra are estimated from the velocity time histories. The amplification of the Fourier spectra of the time histories recorded at the stations on the crest, i.e. SG02, SG03 and SG04, are found with respect to median spectral value at the dam-foundation rock interface.

Although it is interesting to estimate the amplification of the crest based on ambient noise (the analysis is conducted and included in Appendix C), it is more important

from the structural safety point of view to perform this analysis during earthquakes. Contrary to the large number of available data when using ambient noise, in the case of seismic events, the available number of data is more limited. As illustrated in Figure 2.14, the total number of records for the stations SG02, SG03 and SG04 is 15, 8 and 11 respectively, making the statistical analysis delicate. The analysis is performed for each station location on the crest independently and thereafter the median value of the amplification of the three stations is found. The ratio of the unsmoothed Fourier amplitudes of each station on the crest to the median value of the Fourier amplitudes of the stations at the base along with the median of the 3 crest stations are presented in Figures 2.28 for the three components.

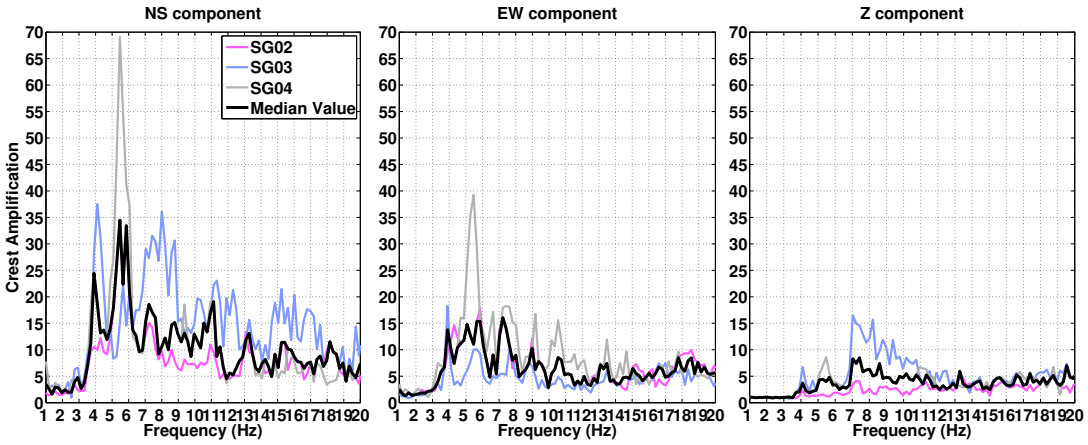

FIGURE 2.28: Amplification of the the crest of the dam (SG02, SG03, SG04 and median value of the motions at the three stations) with respect to the dam - foundation rock interface (median value of stations SG05, SG06, SG07, SG08, SG09, SG10, SG11 and SG12) based on seismic events recordings for the two horizontal and the vertical (NS, EW and Z) components.

The amplification of the Fourier spectra on the crest is frequency dependent. It appears to be much stronger around the frequencies of vibration of the arch dam (as they were identified previously) for all the three components and it stabilizes for higher frequencies (after $\sim$ 12 Hz). Higher amplification indicates lower damping coefficient at these frequencies with respect to the rest of the frequency range of interest. The currently considered amplification for dam design is about 7 and it corresponds to stronger earthquakes when the damping coefficient is higher. The Saint Guérin amplification is relatively higher because of the small earthquakes. This is consistent with the small damping values of 1-2% estimated, using the same data, in Table 2.4. A extensive sensitivity analysis on source parameters (APPENDIX C) shows no clear dependency of the amplification on PGV, magnitude or epicentral distance of the events. Given the limited number of records used for analysis, an interesting verification would be to use seismic data of one year that are available for the three stations on the crest and estimate the amplification with respect to the stations SG01 (right abutment), SG05 (left abutment)

and SG09 (bottom). During the occurrence of earthquakes, the Fourier spectral ratio is much lower with respect to the observed one based on ambient vibrations (APPENDIX C). This points to higher damping values during earthquakes, which is to be expected given that the stronger the motions the higher the material component of damping. However, the main patterns are observed for both analyses.

2.6 Discussion

In this chapter, information is given on the Saint Guérin site where our dense seismological network was deployed from mid June 2015 till end June 2016. The combination of a seismically active French region and of a dam in excellent state with simple structure made the location ideal for the deployment of a seismological network which could provide the necessary data for SVGM analysis. 19 stations (velocimeters) were deployed in the area around and on the dam; 12 stations on the dam and 7 stations in the free field. Continuous recordings during the period of one year (June 2015 - June 2016) are available as a successful outcome of the experimental campaign. The density of the network allows to study extensively SVGM at the dam-foundation interface as well as to extract further information regarding the topographic and rock-structure interaction effects by comparison with the free field motions. During the period of the first six months of acquisition, excellent quality data were recorded for 55 events. The magnitude range (M_L) is between 1.5 and 4.1 and the maximum epicentral distance from the dam, R_{epi}, 320 km. Given the regional seismotectonics context, the azimuthal coverage of the earthquakes is poor, with the majority of them to occur in the East of the dam. However, the number and the magnitude/epicentral distance range of recorded earthquakes is sufficient for a robust statistical analysis covering the linear behavior of the dam.

The dynamic analysis of the arch dam is conducted taking advantage of the continuous ambient noise data and the seismic recordings during the first six months. Using ambient noise records, the first few frequencies of vibration of the structure are found. The estimated peaks seem to be only minor affected by the change of the water level, with a small shift (of the order of 0.1 Hz) of the peak frequencies to lower values when the water level is increasing. The damping coefficients appear to be higher with the higher water level although no detailed analysis of this effect was conducted; a quantification of this effect would be of great interest. The damping ratio for the first identified frequency of vibration of the dam is estimated to range between 1 and 2% during the seismic events. These low values of damping are to be expected given that the earthquakes used for analysis are mostly distant and of small magnitude leading to low solicitation at the base of the dam (PGV under 0.2 mm/s). The damping analysis, although performed only for the first frequency of vibration, should not be interpreted as suggestion that the

damping coefficient is the same for all vibrational frequencies. To complete this effort, similar analysis should be performed on the higher frequencies as well. The Fourier spectral ratio of the crest to the base of the dam is calculated during the earthquake events. The frequency dependent Fourier spectral ratio of the crest with respect to the foundation rock ranges from approximately from 5 to 35 with an average value of 10. The ratio is significantly higher around the frequencies of vibration of the structure, explained by lower damping coefficients at these frequencies. The crest amplification estimations of Saint Guérin arch dam during earthquakes confirm the value of amplification that is currently considered for dam design. Although an extensive modal analysis is not conducted because it is beyond the scope of the present study, the aforementioned analyses provide the necessary information for a good understanding of the dam linear behavior that will be helpful for the SVGM analysis that follows in Chapters 3 and 4.

Chapter 3

SVGM in Saint Guérin

This chapter presents the analysis of spatial variability of ground motions (SVGM) using the earthquake data from the dense seismological array in Saint Guérin site, recorded during the period of 6 months. The wave passage effect is calculated and discussed. Then, spatial coherency estimates, i.e lagged and unlagged coherency, and amplitude variability estimates, i.e standard deviation of difference of natural logarithm of Fourier amplitudes, are used to quantify phase and amplitude variability of the strong ground motion respectively. Lagged and unlagged coherency and amplitude variability estimates at the dam-foundation rock interface for the subset of events are provided along with their interpretations. A detailed description of the time window selection and smoothing procedure for SVGM is given. Various sensitivity analyses are conducted to investigate our assumptions regarding the smoothing parameters, the length of the $S-$wave window and the choice of the wave type (i.e. $P-$, $S-$, surface, coda waves or ambient noise). Sensitivity analyses of the results on source (i.e. magnitude, epicentral distance and azimuth) and site parameters (local topography) are also conducted. The coherency and amplitude variability observations at the dam-foundation rock interface are compared with the free field observations as well as with existing variability models.

For ourselves, we may take as a basic assumption, clear from a survey of particular cases, that natural things are some or all of them subject to change.

Aristotle, 'Physics'

The wave passage effect is the most commonly recognized cause for SVGM. It is defined as the systematic spatial variation due to difference in arrival times of seismic waves over a short distance due to inclined incidence of propagating plane body waves or horizontally propagating surface waves. Due to the inclined incidence arriving at the site, seismic waves arrive at different times at different locations on the ground surface. Coherency characterizes the variation in Fourier phase and expresses the loss of correlation between two seismic time histories. The joint stochastic characteristics of the motions between two stations, considering that the records are realizations of a bivariate (vector) process, are, generally, described by their second moments, i.e. the cross spectral density in the frequency domain (Equation 1.3). The frequency domain is the most commonly used. Signal processing techniques are applied to the time histories to evaluate their stochastic estimators. In the present study, the cross spectral density and the auto spectral densities of each station are estimated by applying the Conventional Spectral Analysis method, which has the necessary resolution for practical engineering applications (Harichandran & Vanmarcke [1986], Harichandran [1991]). Complex coherency of the seismic motions is obtained from the smoothed cross spectrum of the time series between two stations normalized with respect to the corresponding power spectra (Equation 1.4). Lagged coherency is the modulus of complex coherency and it measures the similarity between two ground motions for a given frequency band (Abrahamson [1992a]), namely the coherent motion (Equation 1.11). Unlagged coherency is the real part of coherency. The unlagged coherency estimate does not consider the time lag between the pair of stations, which means, it includes the wave-passage effects. Plane-wave coherency differs from the lagged coherency in that the time shift for each station is constrained to be the same (consistent with a single wave direction (azimuth) and apparent velocity (incidence)). It is found by taking the real part of the smoothed cross spectrum after aligning the ground motions based on the best plane-wave speed (Equation 1.13). Coherency is attributed to the phase variability in the motions and early studies show that it is only minimally affected by the amplitude variability between the motions at two locations. The amplitude variability can be reflected directly using the difference of natural logarithm of the (unsmoothed or smoothed) Fourier amplitudes between the motions at two locations.

In the present study, firstly the wave passage effect is estimated. Then, the different coherency types are used for the characterization of differences in the Fourier phases between two ground motions. Finally, the difference of natural logarithm of the Fourier amplitudes are calculated so as to quantify the amplitude variability.

3.1 Time window selection

Velocity time histories are used for the analysis. Before estimating the various variability estimators, we need to define the velocity time window which we will use for analysis. In most cases, the shear wave carries the strongest energy in earthquake recordings and, generally, is the most damaging component from the engineering point of view. For the selected subset of events (presented in Chapter 2) the time window to be used for our analysis is chosen to be only the $S-$wave part which can be seen as a segment of a stationary process with limited duration. The $S-$wave window is identified based on the duration of the normalized Arias Intensity (AI) of the two horizontal components of velocity (Abrahamson [2007]). Verified by visual inspection, this methodology appears to be robust for recordings on rock sites, where the $S-$wave part is not very contaminated by other types of waves. To estimate the normalized AI, an initial window is applied that starts 10 sec before and ends 10 sec after the peak ground velocity (PGV). PGV is identified separately for each component. The final time window is then estimated based on the time at which the normalized AI has a value in between 0.10 and 0.75, denoted as $T_{0.1}$ and $T_{0.75}$, respectively (Equation 1.15). The robustness of the hypothesis of $0.1 < AI < 0.75$ will be evaluated later on.

Reference station data are used to perform the AI-based time window estimation. All stations located in the free field can be used as reference stations; however, some are more appropriate than others. The reference station SG17 has a flat spectrum while a small site effect is observed in the site of station SG18 at around 2 Hz (Figure 2.9). Station SG15 can also be used as reference station because no local site effects are observed (flat spectrum as shown in Figure 2.9). The $S-$wave part of the signals is defined based on the $S-$wave arrivals at the reference rock station SG17 while for the events that SG17 is missing, the reference rock station SG18 is used. When both SG17 and SG18 are missing, one of the three stations on the road perpendicular to the dam, i.e. SG13, SG14 and SG15, is used as reference station. The reference station used per event is presented in Table B.4 in APPENDIX B. The selected time windows have been segmented from the original time history by applying a 5% cosine bell window taper at each end (Figure 1.5). These windows are assumed to be the segments from infinite time histories with uniform characteristics through time (stationarity assumption).

Example waveforms (velocity times histories of the NS component) from the local event with magnitude M_L 3.3 and epicentral distance, R_{epi}, 100 km, that occurred on September 10^{nth} at UTC 07:32:08 (Figures 2.20 and 2.21) are included in Figure 3.1 along with the chosen $S-$wave window, estimated according to the normalized AI method as 9.5 sec. Figure 3.2 represents the distribution of $S-$wave duration for each of the 55 selected events, identified as described above, with magnitude (M_L) and epicentral distance (R_{epi}). The $S-$wave duration appears to vary from 1.8 to 11 sec, duration that is

sufficient for the performance of coherency analysis (similar durations have been used in previous studies using data on rock sites, e.g Abrahamson [2007], [Abrahamson, 2006]). The choice of the length of the $S-$wave window will be questioned and compared with other time windows in a following section.

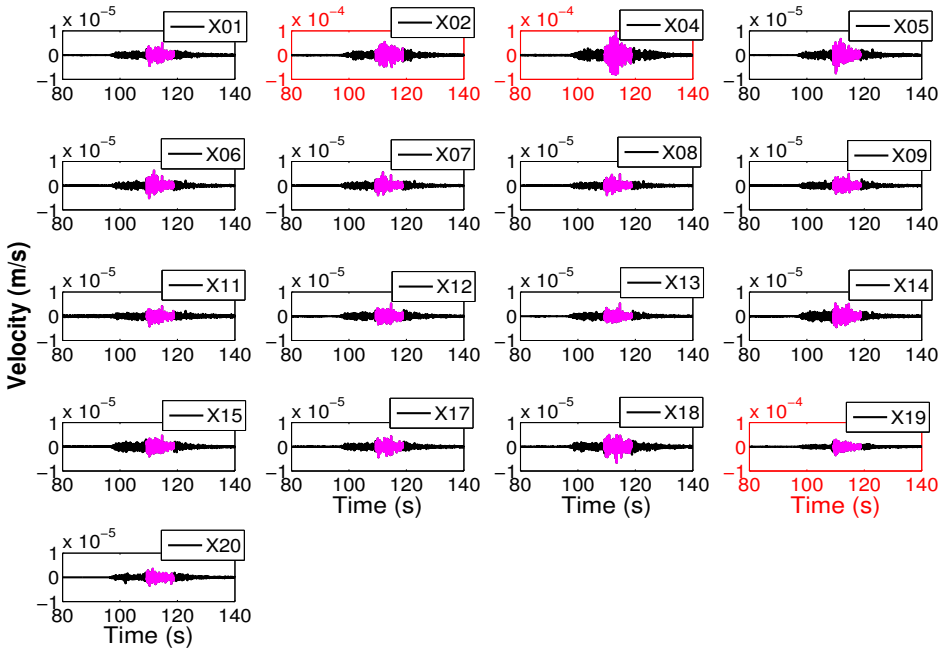

FIGURE 3.1: Velocity time series for the the NS comp. recorded at the stations of the Saint Guérin array for the event that occurred on September 10^{nth}, 2015 at UTC 07:32:08 with magnitude M_L 3.3 and epicentral distance, R_{epi}, 100 km. $S-$wave window chosen is represented by magenta color.

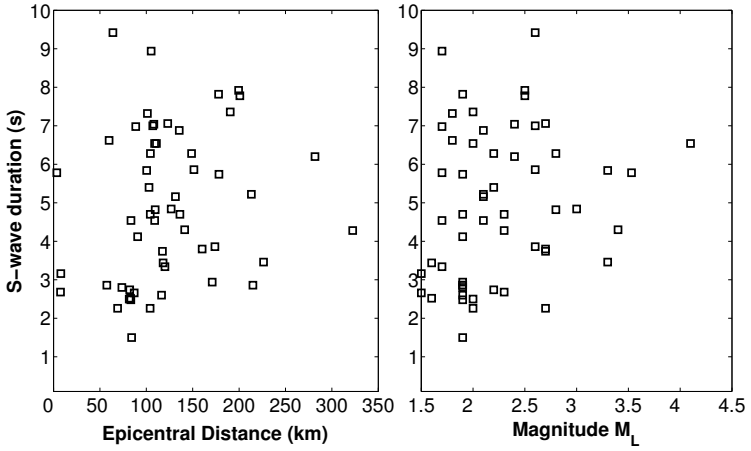

FIGURE 3.2: $S-$wave duration (identified using the method of normalized AI by Abrahamson [2007]) as a function of epicentral distance (R_{epi} in km) and local magnitude (M_L).

3.2 Smoothing parameter

The information about the differences in the phases of the motions (coherency estimation) at two locations is introduced through the smoothing process. If lagged coherency is not defined by means of the smoothed spectral estimates but, instead, through the unsmoothed estimators for the power and cross spectral densities, respectively, the absolute value of the coherency estimate corresponding to Equation 1.11 would then be unity (Zerva [2009]). No additional information can be extracted from the data. The more the Fourier spectra are smoothed, the larger the decrease in variance of coherency estimates, but this in turn causes a corresponding loss of resolution in frequency. Hence, the issue of smoothing of the spectral estimators is not only important for the reduction of their variance, but, also, for extracting meaningful information regarding the coherency of the signals (Zerva [2009]). To use coherency estimates in structural analysis, Abrahamson et al. [1991] argue that averaging the complex cross spectrum over 11 frequencies can provide a reasonable trade-off between the frequency resolution and the bias and uncertainty of coherency estimates. The Hamming window is a smoothed version of a triangle window, as it is presented in Figure 1.4. The power spectral and cross spectral densities have, therefore, been smoothed before being used in the coherency estimation. The frequency band smoothed is calculated as in Equation 3.1:

$$f_{smoothed} = 2 * M * \frac{f_s}{N_f} \tag{3.1}$$

where f_s is the sampling frequency and N_f is the number of frequency points for the signal duration. The original time step of the time series recorded from the Saint Guérin array, ΔT, is 0.005 sec so for 1 sec $S-$wave duration, frequency sampling, f_s, is $1/0.005 = 200Hz$. Decimation of 4 is applied to the velocity time series, thus f_s becomes $1/0.02 = 50Hz$ and therefore the band of frequency smoothing is $f_{smoothed} = 2 * 5 * 50/256 = 1.95Hz$. Equivalent number of smoothing points has been used for the longer durations of time windows so that the band of frequency smoothed remains constant. At high frequencies, especially for the longer separation distances, the theoretical value of the lagged coherency of the $S-$wave should tend to zero. However, the lagged coherency evaluated from the data will not tend to zero but, rather, to the value of the coherency of noise smoothed with the particular window used in the evaluation, which, for $M = 5$ Hamming spectral window, is equal to 0.33 (Abrahamson et al. [1991]). Hence, lagged coherency values below 0.33 should not be interpreted.

3.3 Wave passage effect

Wave passage results from delays in arrival times of seismic waves at different locations across a site due to varying site-source distances and inclined incidence of propagating plane body waves or horizontally propagating surface waves. For stations belonging to a horizontally placed array, the critical controlling parameter is the apparent wave propagation velocity of shear waves ($V_{app,\theta}$) across the array (Ancheta et al. [2011]). The $V_{app,\theta}$ depends on the apparent wave speed in the underlying rock, V_{app}, and azimuth angle, θ, (Ancheta et al. [2011]) :

$$V_{app,\theta} = \frac{V_{app}}{sin(\theta)} \tag{3.2}$$

Using the $S-$wave windows as estimated in section 3.1, the time lag, dt, between two stations is determined by estimating the cross-correlation function between the two station records and, then, evaluating the positive maximum correlation coefficients (Boissieres & Vanmarcke [1995a]). The median value of time delay for each station pair for the subset of events as well as the standard deviation are calculated and presented in Figures 3.3 and 3.4 respectively. A zoom in the stations closer to the dam, by excluding SG19 and SG20, is given in Figures 3.5 and 3.6; it helps to better identify the values at the interface. The reference station is the station with lower numbering, e.g if the time lag of the station pair SG01-SG09 is 0.01 sec, it indicates that the arrival time of the $S-$wave of station SG09 is 0.01 sec later than the $S-$wave arrival of SG01.

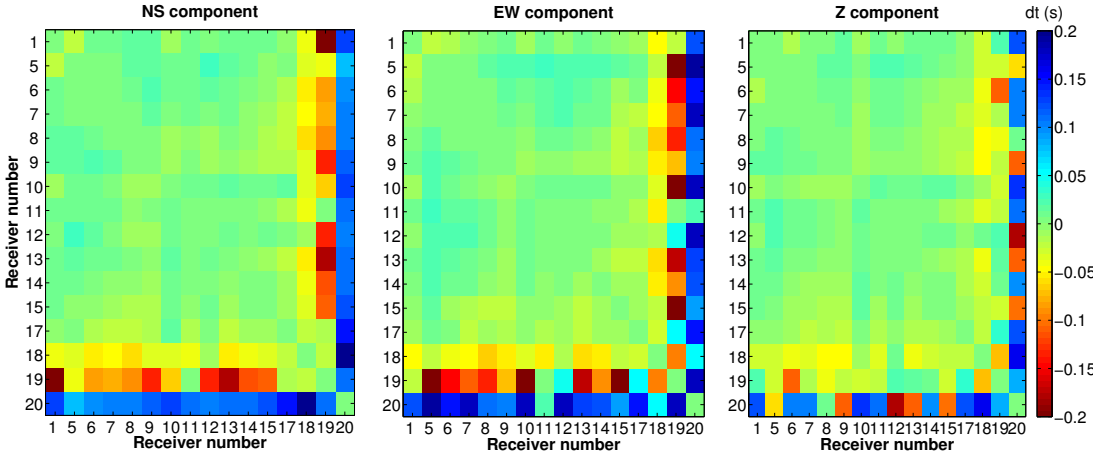

FIGURE 3.3: Median value of time lag estimations for all station pairs for the NS, EW and Z components.

The median value of time lag varies from 0 to 0.06 sec as it can be seen in Figure 3.5, except for stations SG19 and SG20 that the values are up to 0.2 sec. The time lag estimations are robust among the different events with a standard deviation that is about

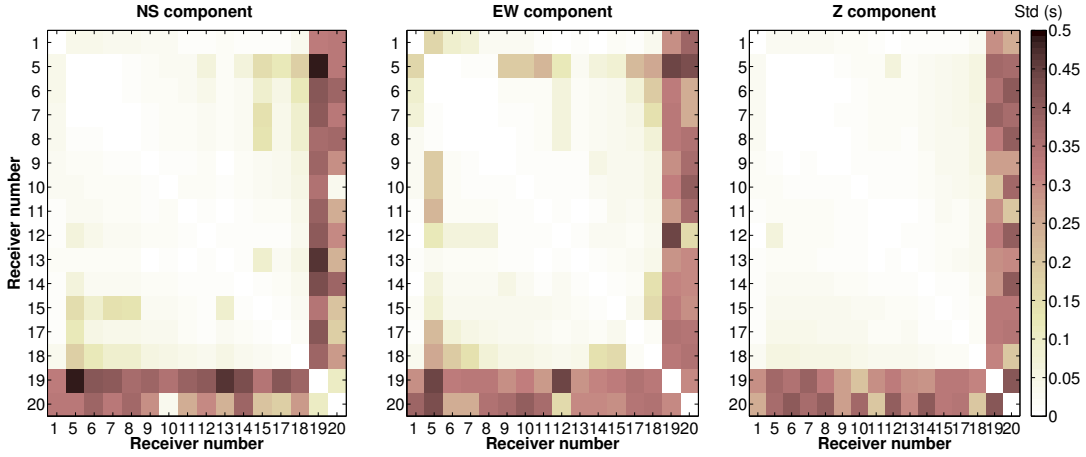

FIGURE 3.4: Standard deviation of time lag for all station pairs for the NS, EW and Z components.

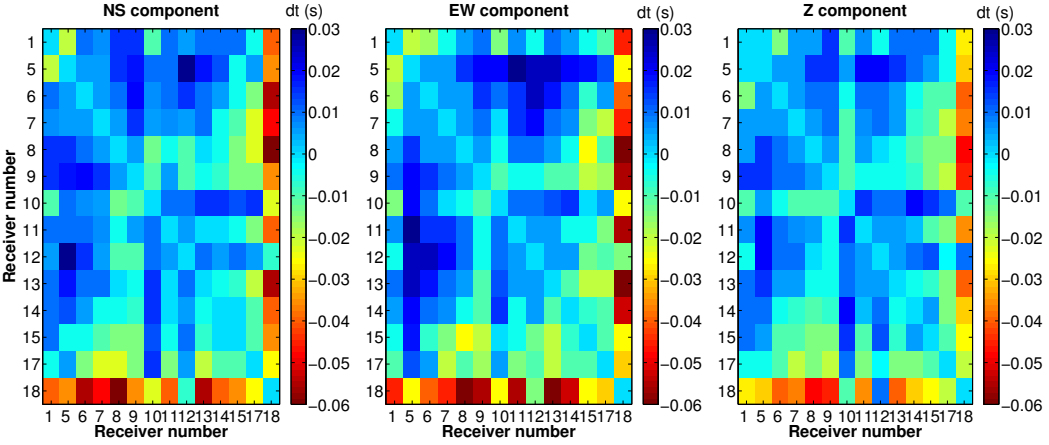

FIGURE 3.5: Median value of time lag estimations for all station pairs excluding SG19 and SG20, for the NS, EW and Z components.

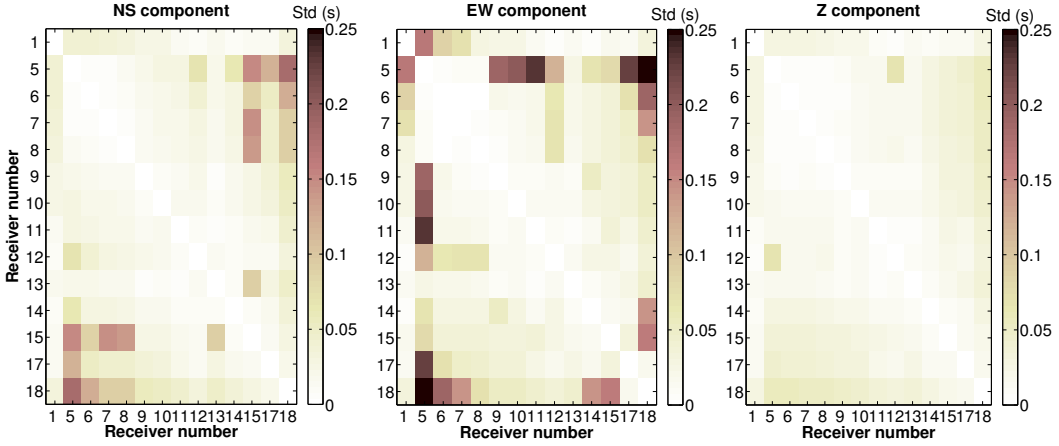

FIGURE 3.6: Standard deviation of time lag for all station pairs excluding SG19 and SG20 for the NS EW and Z components.

0.05 sec for the majority of station pairs. However higher standard deviations can be observed, which is not abnormal, given, firstly, the relative variety in azimuthal coverage that leads to arrival of the waves from various angles and, secondly, the soil-structure interaction that perturbates the wave field. Nevertheless, it becomes apparent that there is a preferential backazimuth; the $S-$waves appear to arrive firstly in the station SG18 ($-0.06 \leq dt \leq -0.01$), then, almost simultaneously to SG17 and SG19 (east bank of the reservoir) and finally, clearly later to SG20 which is on the west bank of the reservoir, indicating a preferential backazimuth in the East (Figure 2.7). This observation is in accordance with the fact that the majority of the subset of events used for the analysis are occurring in two azimuthal branches as shown in Figure 2.15, both branches in the East of the dam. Regarding the stations at the dam foundation rock interface, it is not easy to draw any conclusions since the values of time lag are very small (from 0 to 0.03 sec). It seems that the soil-structure interaction perturbates the incidence and no particular directionality can be identified.

To get a closer look in what happens at the dam-foundation rock interface, we compare the Saint Guérin wave passage observations with a vertical wave propagation. In the case of a vertical wave propagation, which is the most commonly used for structural analysis, in a medium with constant propagation velocity, which is considered as $V_S = 1400m/s$, the time lag, dt, between two stations, j and k, can be easily identified as:

$$dt = \frac{(z_j - z_k)}{V_S} \tag{3.3}$$

The time lags between all the station pairs at the dam-foundation rock interface are shown in Figure 3.7. Evidently, the waves would reach firstly the SG09 at the base of the dam, then propagate along the two banks, i.e. from SG08 towards SG07 and then SG06 for the left bank and from SG10 towards SG11 and then SG12 for the right bank reaching finally the two abutments, SG05 and SG01 for the left and right bank accordingly. Comparing the time lags resulting from a vertical propagation with the time lags identified from the in situ earthquake recordings, we conclude that the actual propagation cannot be considered as vertical.

A constant propagation velocity would produce time lags that increase linearly with station separation distance. Boissieres & Vanmarcke [1995a] analyzed arrival time perturbations at the Lotung SMART1 array and their observations indicated a nearly linear increase of lag with distance and significant scatter of the data, which they quantified as a distance-dependent standard deviation term. At distances less than 400 m, this standard deviation in time lag was approximately 0.02-0.03 sec. Although Ancheta et al. [2011] showed some non linearity in this relationship (constant propagation velocity does not produce time lags that increase perfectly linearly with station separation

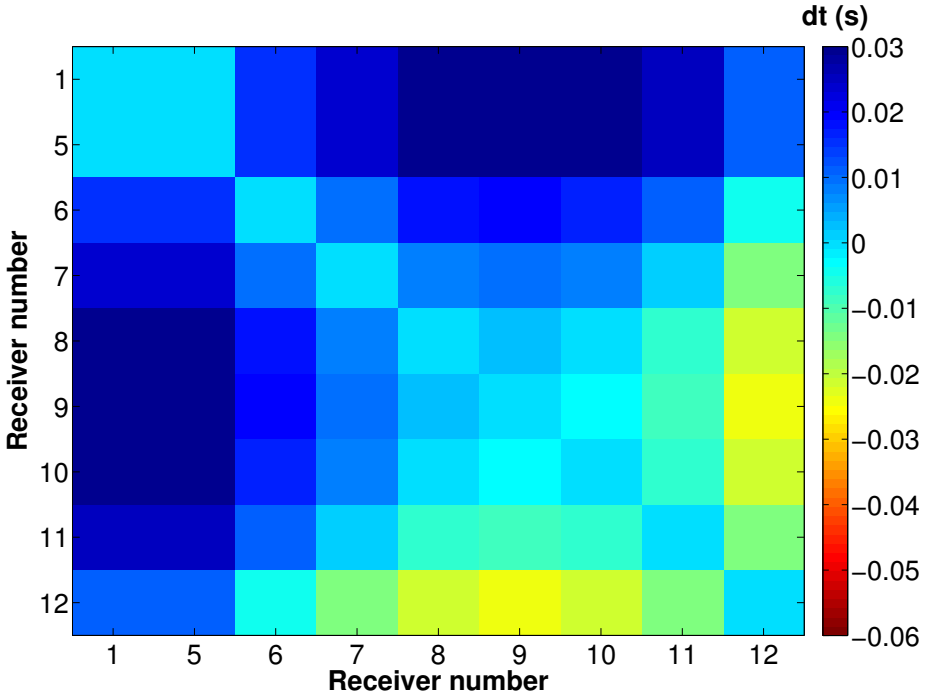

FIGURE 3.7: Time lag estimations for all station pairs at the dam-foundation rock interface for a vertical wave propagation.

distance), they, as well, concluded that a mean relationship could be derived for a given event. Both studies showed that there is a low level of scatter at low station separation distances that suggests that arrival time perturbations are likely negligible relative to epistemic uncertainty on $V_{app,\theta}$ for this distance range. Following the rational of the previous studies, using as example the event that occurred on the September 10^{th}, 2015 at UTC 07:32:08 with magnitude M_L 3.3 and epicentral distance 100 km (Figure 2.20) the cross correlation coefficient is estimated between the pairs at the dam foundation rock interface (SG01 is used as reference station). Figure 3.8 shows that in the case of Saint Guérin due to the particular local (canyon) topography the results cannot indicate a nearly linear increase of lag with station separation distance. In Figure 3.8 we follow the propagation of the $S-$wave from the left bank of the dam (stations SG05, SG06, SG07, SG08) towards the right bank (SG09, SG11, SG12). The event occurred in the North East of the dam (azimuth equal to 143°) which does not clearly confirm the preferential propagation from the left to the right bank. The explanation for this phenomenon is the effect of the regional alpine and local canyon topography along with the presence of an engineered structure that influences the seismic wave field. The assumption made in the aforementioned studies that a single wave direction (azimuth) and apparent velocity (incidence) can be defined along an array is not easily applicable in the case of an array located in irregular topography and where soil-structure interaction is also present, such as the one in Saint Guérin.

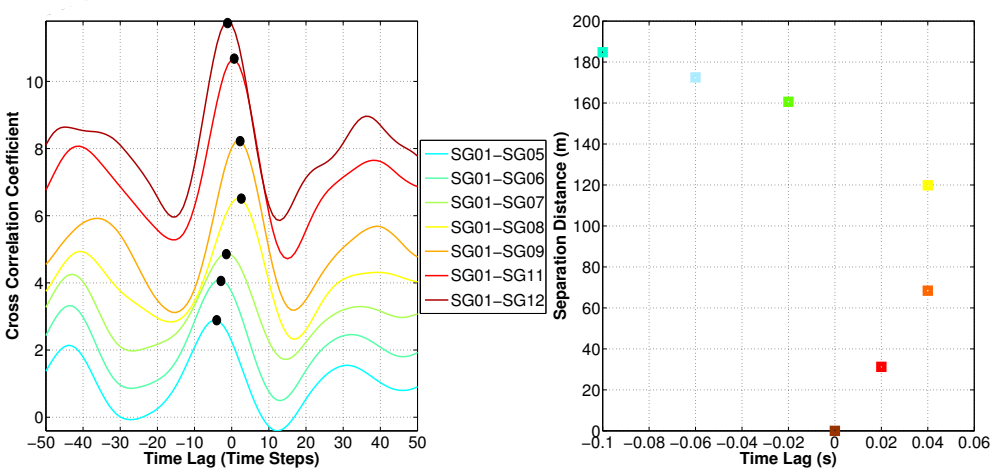

FIGURE 3.8: Cross correlation between the station pairs at the dam-foundation rock interface for the event presented in Figure 2.20; peak cross correlation time lags across the stations as a function of the associated station separation distance.

3.4 Phase variability analysis

3.4.1 Lagged coherency estimates

To determine the Fourier phase variabilities between each pair of stations, we, firstly, calculate the lagged coherency. Arrival time perturbations are removed from the data by aligning the two velocity time histories of each pair of stations (the time lags in the alignment are determined by estimating the cross-correlation between stations and evaluating the positive maximum correlation coefficients, as explained in the previous section). Lagged coherency is estimated for all the station pairs at the dam-foundation rock interface. Firstly, for each event, the median estimates of lagged coherency of all the available pairs of stations within a distance bin are computed. Then the global median estimate of all the events is calculated. Given that the dam is about 200 m long, five distance ranges are considered, i.e. [0 40] m, [40 80] m, [80 120] m, [120 160] m and [160 200] m. The number of station pairs considered in each distance bin at the dam-foundation rock interface and in the free field, depending on the data availability, are presented in Figure 3.9. For all distance bins, the number of available station pairs is at least 38, so the statistical analysis is robust. The analysis is performed for the two horizontal (NS and EW) and the vertical (Z) components. The lagged coherency estimates for each pair along with the median value of all station pairs in each selected distance bin are given in Figures 3.11, 3.12 and 3.13 for each component respectively. The median values of lagged coherency in each distance bin for each one of the three components are grouped in Figure 3.14.

Generally, lagged coherency is large for low frequencies (large wavelengths) and short

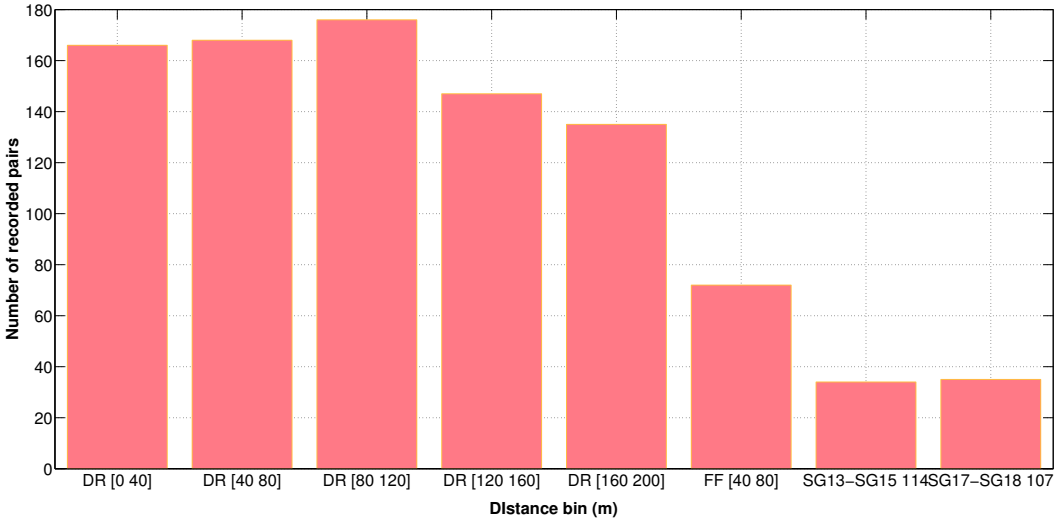

FIGURE 3.9: Total number of station pairs in each distance bin (m) at the dam foundation rock interface (DR) and in the free field (FF stands for free field station pairs SG13-SG14, SG14-SG15 with separation distance 40-80 m)

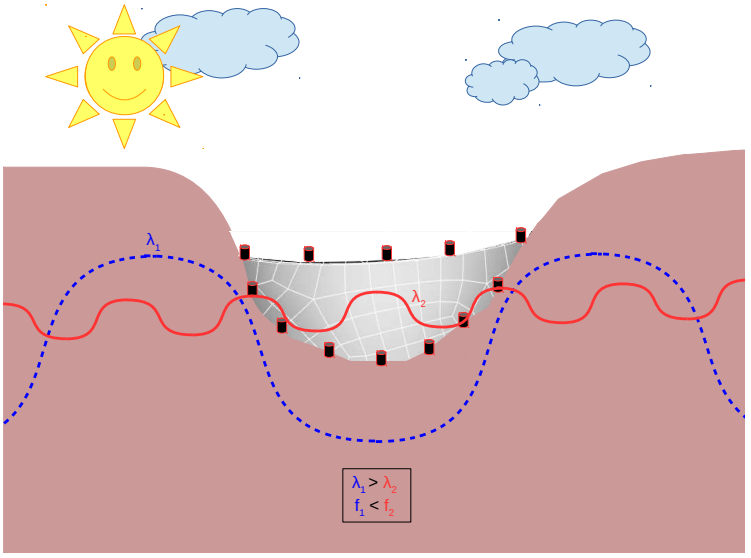

FIGURE 3.10: Frequency and distance dependence of lagged coherency.

separation distances and small for higher frequencies (shorter wavelengths) and longer distances meaning that coherency is frequency and distance dependent. The reasoning is demonstrated with the schematic representation in Figure 3.10. The decay of lagged coherency with increasing station separation distance and frequency is evident for all three components. The median lagged coherency estimate starts from 1 at very short separation distances and very low frequencies while at the frequency of 20 Hz for the longer station separation distances, i.e. 160-200 m, it reaches values less than 0.4, pointing out a high variability. The two horizontal components show very similar trends both

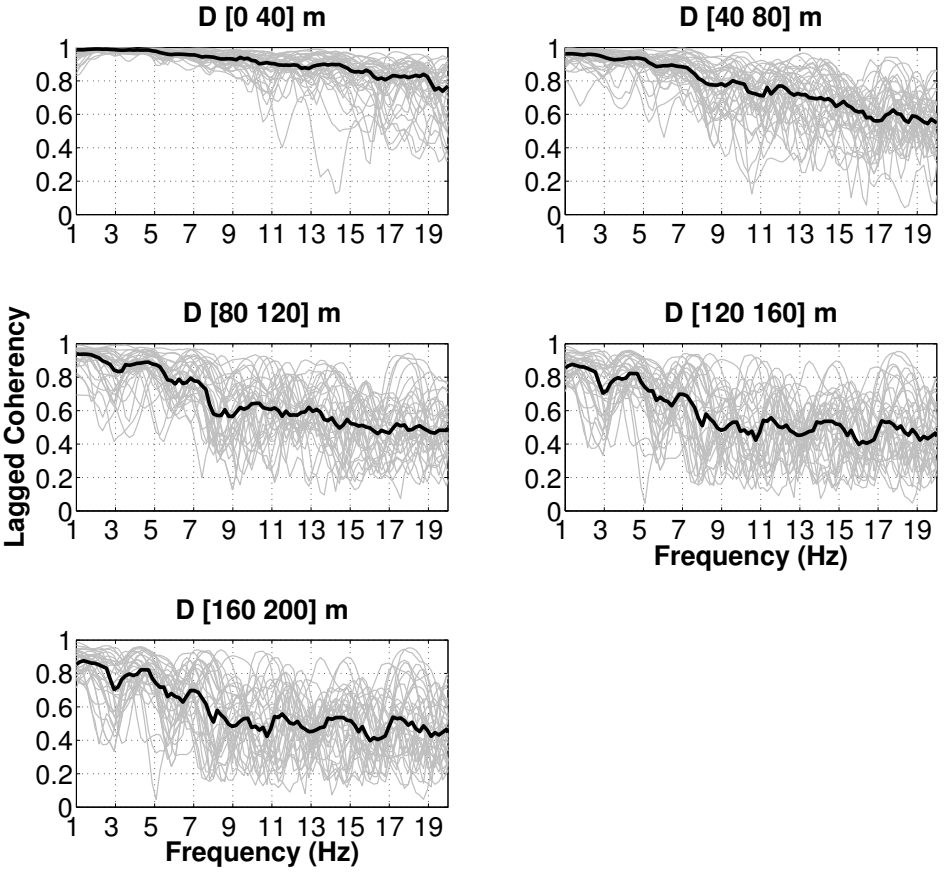

FIGURE 3.11: Individual median values of lagged coherency of all pairs along the dam-foundation interface with station separation distances [0 40] m, [40 80] m, [80 120] m, [120 160] m and [160 200] m for each event (gray lines) and median value of all events (black line) as a function of frequency for the NS component.

with frequency and station separation distance while the vertical component looks somewhat different; the motions on the vertical component are more coherent especially for higher station separation distances. According to Abrahamson [2007], while the horizontal component is dominated by the $S-$waves, the vertical component will include both $P-$waves and SVwaves. At high frequencies, the coherency for the vertical component is greater than the coherency for the horizontal component. This increase is due to the larger coherencies at high frequencies from $P-$waves than from $S-$waves. The coherency resolvability threshold of lagged coherency estimation is 0.33 for $M = 5$, not allowing the lower values to be interpreted. However, the estimated median curves are observed to be well above the coherency resolvability threshold. Regarding the scatter of the independent coherency curves around the median value, we note that it increases both with frequency and station separation distance. For such an averaging process among all the

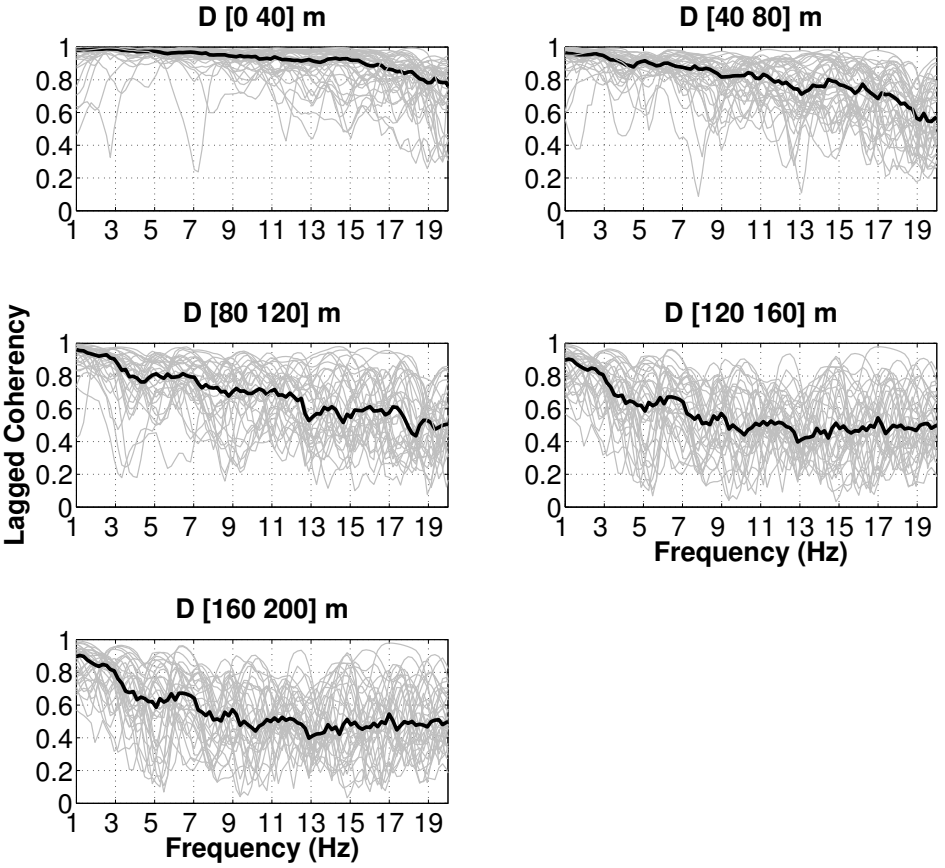

FIGURE 3.12: Individual median values of lagged coherency of all pairs along the dam-foundation interface with station separation distances [0 40] m, [40 80] m, [80 120] m, [120 160] m and [160 200] m for each event (gray lines) and median value of all events (black line) as a function of frequency for the EW component.

earthquakes, as for any kind of statistical analysis, normally distributed data is preferable. Therefore, a $tanh^{-1}$ (or, ATANH) transformation is applied to the coherency to produce approximately normally distributed data about the median (Enochson & Goodman [1965], Abrahamson [2007]). Abrahamson [2007] shows through an example how scatter of the coherency becomes independent of frequency (homoscedastic) with such a transformation. Normally distributed data allow median coherency to be used as an estimate instead of mean values. The estimated ATANH(lagged coherency) values for the three components are presented in Figures 3.15, 3.16 and 3.17. As observed, the independent coherencies appear to be more symmetrical about the median value. The frequency interdependency of the ATANH(lagged coherency) estimates is verified in the section 3.4.1.1.

In Figure 3.14, a slightly higher phase variability in between narrow frequency bands can be roughly observed for the two horizontal components. This higher variability seems to

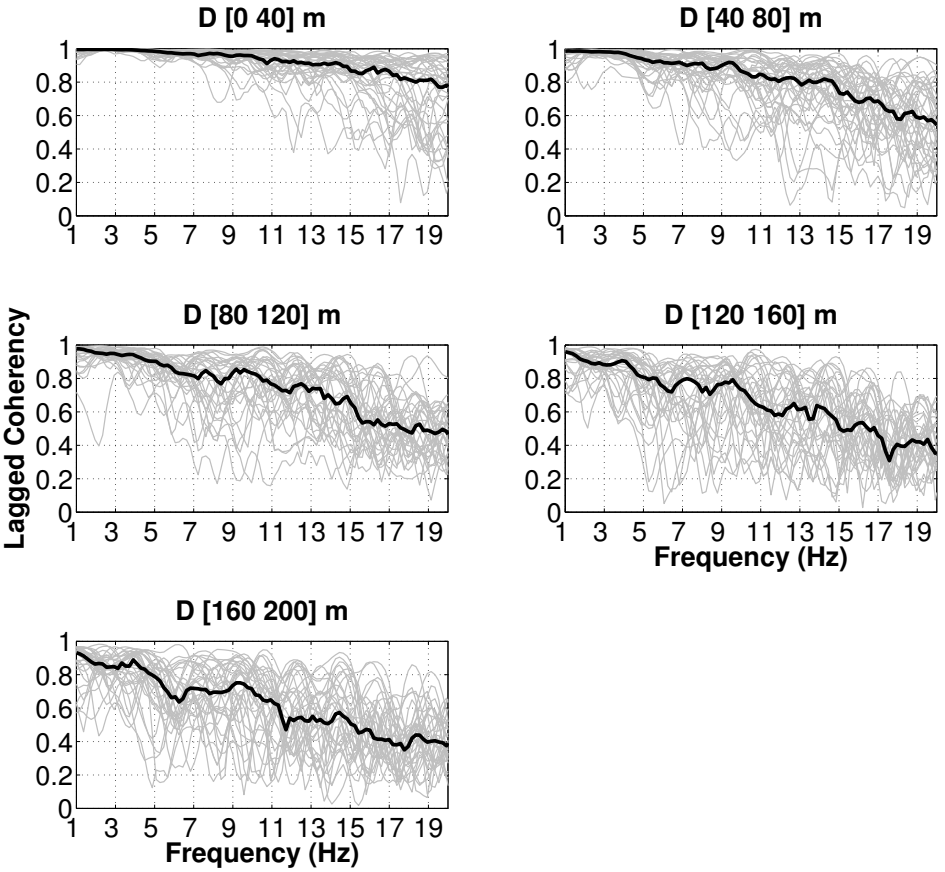

FIGURE 3.13: Individual median values of lagged coherency of all pairs along the dam-foundation interface with station separation distances [0 40] m, [40 80] m, [80 120] m, [120 160] m and [160 200] m for each event (gry lines) and median value of all events (black line) as a function of frequency for the NS component.

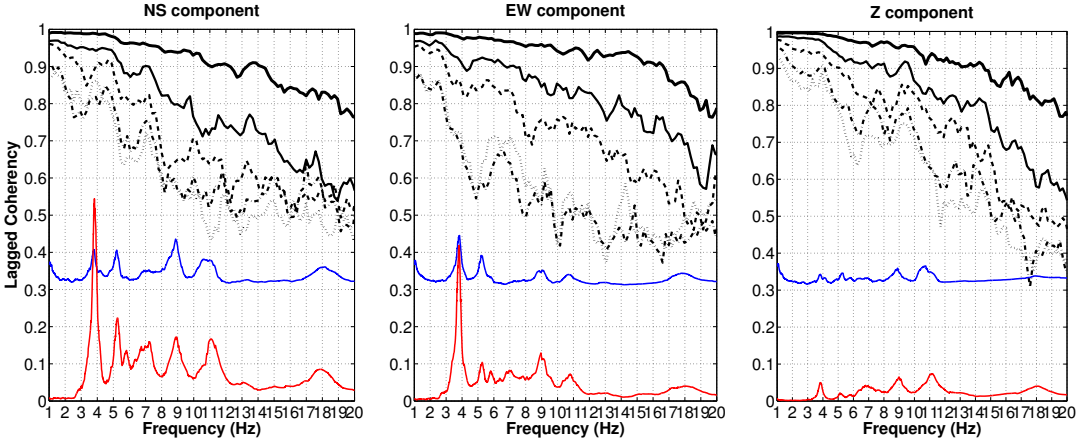

FIGURE 3.14: Lagged coherency as a function of frequency for the NS (left), EW (middle) and Z (left) components; median value of all the events within each distance bin along the dam-foundation rock interface (solid and dashed black lines). Frequencies of vibration identified on the Fourier spectra of the dam crest are represented by red lines and at the interface by blue lines.

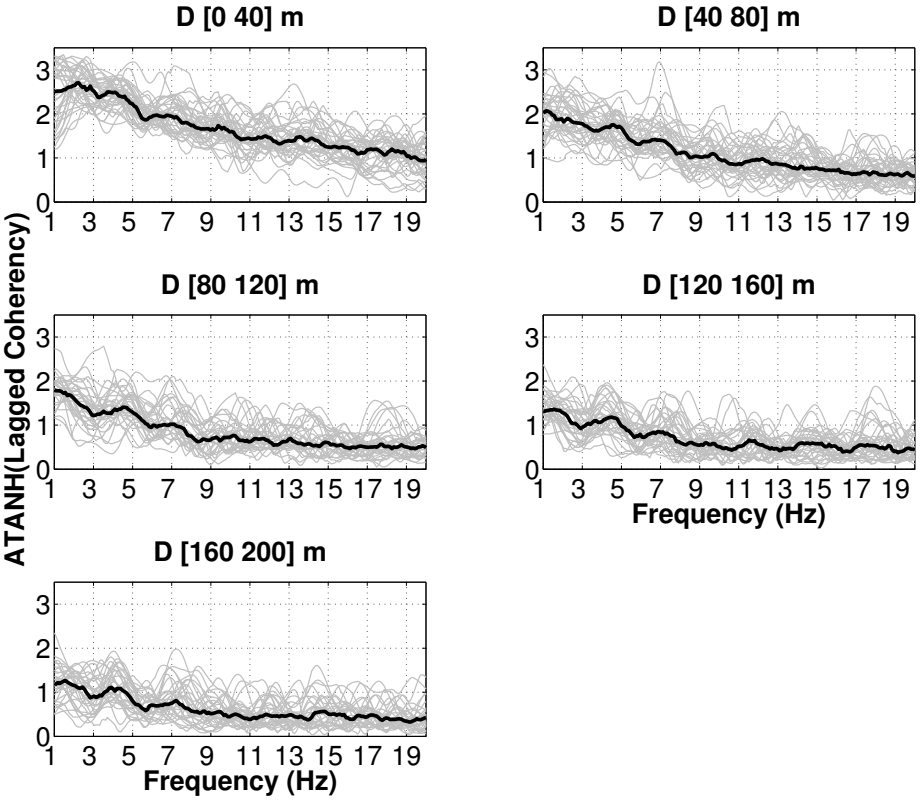

FIGURE 3.15: Individual median values of ATANH(lagged coherency) of all pairs along the dam-foundation interface with station separation distances [0 40] m, [40 80] m, [80 120] m, [120 160] m and [160 200] m for each event (gray lines) and median value of all events (black line) as a function of frequency for the NS component.

occur around the first few frequencies of vibration of the dam identified by ambient noise analyses (Figure 2.24) suggesting that the presence of the structure modifies the phase content of the motions. The Fourier spectra on the dam crest and at the interface where the frequencies of vibration for the three components are identified and also represented in Figure 3.14. Similarly, in the vertical component a higher loss of coherency seems to occur around 5 to 6, 8, 11 and 18 Hz. Again, the frequency ranges within which there is higher variability appear to be around the frequencies of vibration of the dam. Several studies (e.g Zerva & Harada [1997],Bi & Hao [2009], Liao & Li [2002]) have shown that there is a decrease of the coherency function at the vicinity of the frequencies where the spectra are amplified. According to Imtiaz [2015a], 'bumps' in the lagged coherency values appear when the spectra for the motions of two stations exhibit a simultaneous peak at one frequency range. These peaks may be dominated by coherent energy coming from direct waves. On the contrary, 'troughs' in the coherency estimates correspond to incoherent energy coming from either the scattered waves or destructive interference between two waves of comparable amplitude. Herein, it is observed that there is a loss of

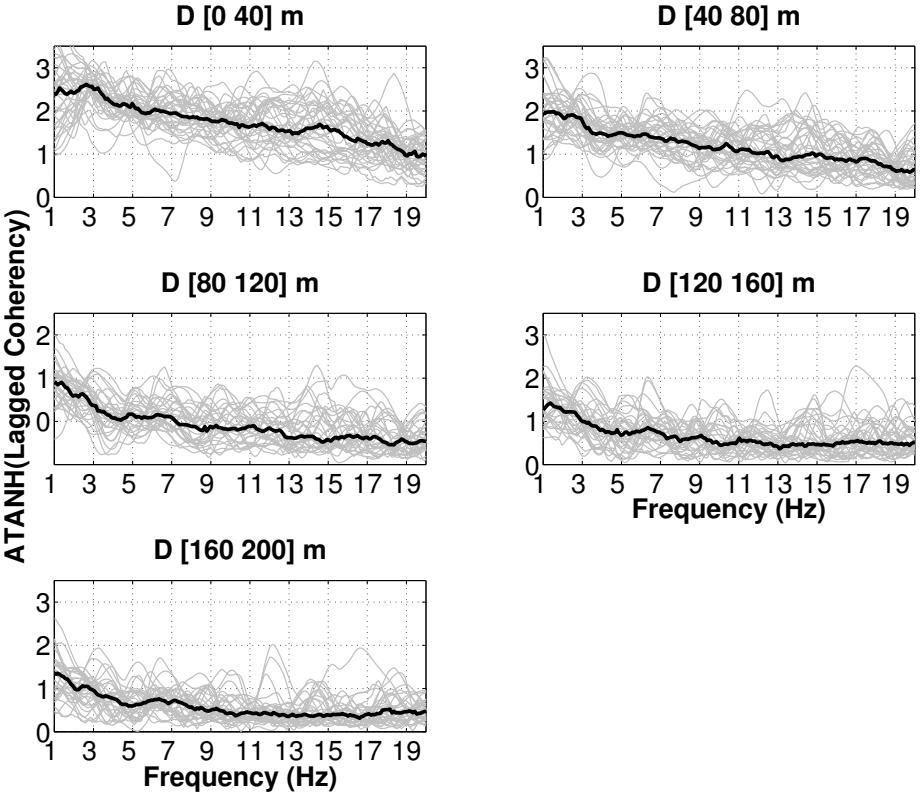

FIGURE 3.16: Individual median values of ATANH(lagged coherency) of all pairs along the dam-foundation interface with station separation distances [0 40] m, [40 80] m, [80 120] m, [120 160] m and [160 200] m for each event (gray lines) and median value of all events (black line) as a function of frequency for the EW component.

coherency in the frequency ranges where there is a stronger amplification of the spectra (i.e. frequencies of vibration of the dam). This observation suggest that the presence of the structure contributes to additional loss of coherency (higher variability). However, this hypothesis is not perfectly demonstrated by the confrontation of decrease in the lagged coherency estimates and the peaks in Fourier spectra at the crest of the dam; therefore in Chapter 4 this observation will be studied more profoundly.

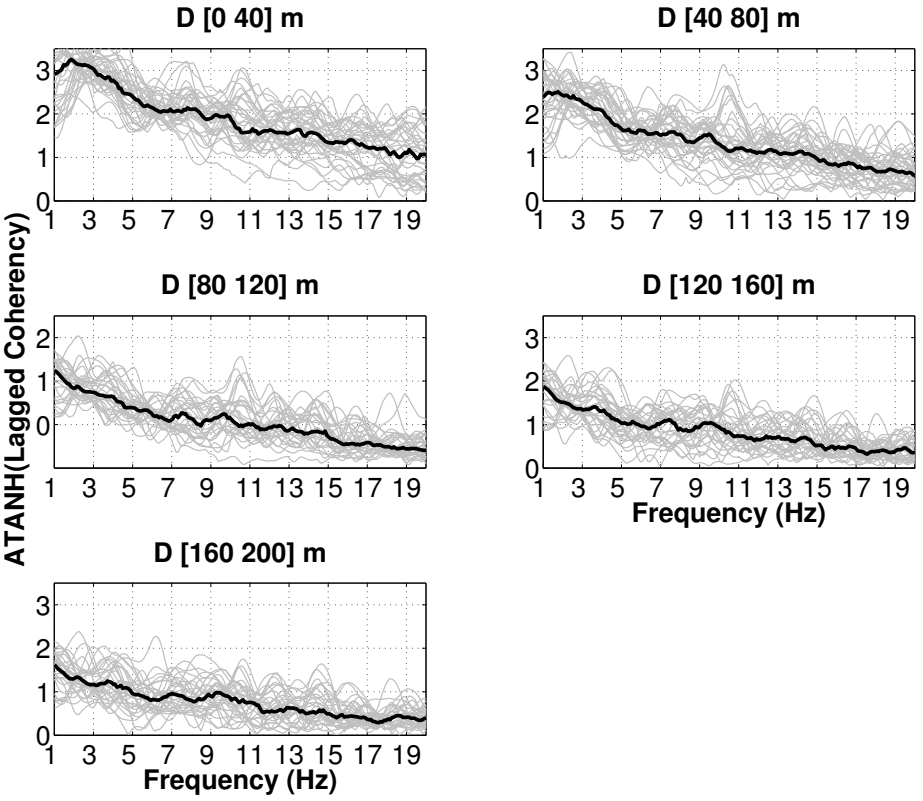

FIGURE 3.17: Individual median values of ATANH(lagged coherency) of all pairs along the dam-foundation interface with station separation distances [0 40] m, [40 80] m, [80 120] m, [120 160] m and [160 200] m for each event (gray lines) and median value of all events (black line) as a function of frequency for the Z component.

3.4.1.1 Sensitivity analysis

It is evident from the figures above, that lagged coherency is small for low frequencies and short separation distances and large for higher frequencies and longer distances, indicating that coherency variability is frequency and distance dependent. Moreover, the observed variability may be significant from earthquake to earthquake, and it is difficult and dangerous to draw conclusions from observations on single earthquake. It is necessary to investigate the dependency of coherency on various site and source characteristics on the basis of averaged values derived from a large and representative set of events. For such an averaging process, as for any kind of statistical analysis on the coherency estimates, normally distributed data is preferable. Therefore, firstly, a $tanh^{-}1$ (or, ATANH) transformation is applied to the coherency to produce approximately normally distributed data, as shown in Figures 3.15, 3.16 and 3.17. Because normally distributed data are produced, median coherency can be used as an estimate instead of

mean coherency. Thereafter, given that no 'rule' exists for the $S-$wave window identification, the dependency on the choice is argued by applying different window lengths and different smoothing parameters accordingly. Different wave types, additionally to the strong motion $S-$ wave, are also considered for analysis. Finally, comparison of the observations at the dam-foundation rock interface with the free field motions is required to give a better insight on the contribution of the local topography on the SVGM. Irregular local topography causes scattering of the incident waves that could result in a ground motion field that is more variable from the one in the free field.

ATANH(lagged coherency) values are used for statistical analysis to investigate the dependence of coherency on different source and site parameters. Five inter-station distance ranges (0-40, 40-80, 80-120, 120-160 and 160-200 m) are chosen and the coherency estimates of the pairs available for each distance range are used to derive the 'individual median' curve for a single event. The 'global median' of all the events at a given inter-station distance range are also derived by combining all the pairs available from 55 events. The residuals for each event are computed from the difference between 'individual median' and 'global median'. Distribution of the ATANH(lagged coherency) values at different station separation distances and frequency ranges are also evaluated.

Source characteristics

The observed variability may be significant from earthquake to earthquake, and it is difficult to draw conclusions from observations on single events. Thus it is important to investigate the dependency of coherency analysis on various source characteristics (magnitude, source to site distance and azimuth) based on averaged values derived from a sufficiently large and representative set of events. The residuals of each 'individual median' value of ATANH lagged coherency from the 'global median' value are estimated. To seek the magnitude dependence, the subset of events is divided into two epicentral distance groups, local events with epicentral distance R_{epi} of [0 100] km (17 events) and regional events with epicentral distance R_{epi} of [100 350] km (41 events); the number of available events in each bin is given in Table 2.3. Figures 3.18, D.1 (APPENDIX D) and D.2 (APPENDIX D) show the residual plots of the ATANH(lagged coherency) estimations of the NS, EW and Z components respectively as a function of magnitude, for different station separation distance groups and frequency ranges. Similarly, the events are grouped into two magnitude ranges, M_L [1.5 2.5] (41 events) and M_L [2.5 4.1] (17 events) to examine the distance dependence. Residuals of ATANH(lagged coherency) values (NS, EW and Z components) of the two magnitude groups of events are presented in Figures 3.19, D.3 (APPENDIX D) and D.4 (APPENDIX D) as a function of the corresponding epicentral distances for increasing inter-station distances and frequency ranges. Finally the azimuth dependence is examined for increasing station

separation distances and frequency ranges for the two horizontal and the vertical components in Figures 3.20, D.5 (APPENDIX D) and D.6 (APPENDIX D).

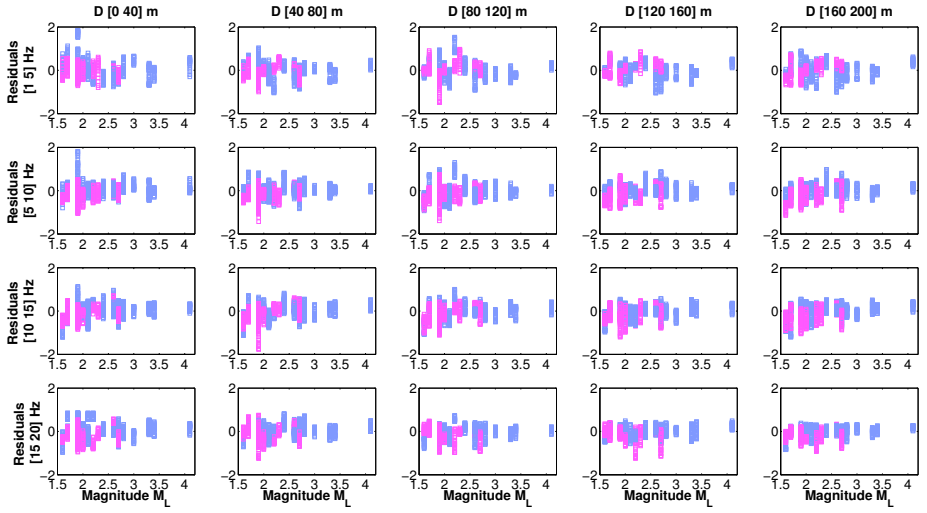

FIGURE 3.18: Coherency residuals of individual median estimates of ATANH(lagged coherency) for each event with respect to the global median (ATANH units) of all the events as a function of magnitude of the NS component for epicentral distance bins of R_{epi} [0 100] km (magenta) and R_{epi} [100 350] km (blue).

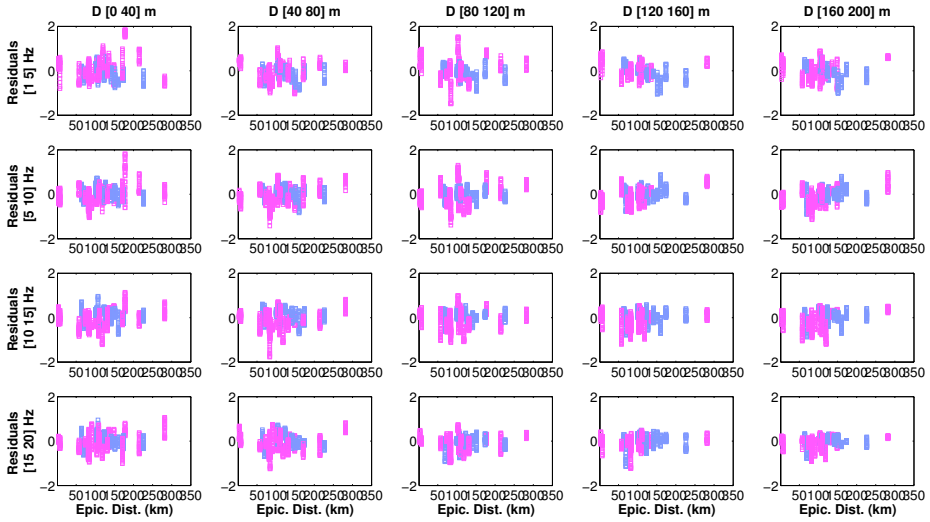

FIGURE 3.19: Coherency residuals of individual median estimates of ATANH(lagged coherency) for each event with respect to the global median (ATANH units) of all the events as a function of epicentral distance of the NS component for magnitude bins of M_L [1.5 2.5] (magenta) and M_L [2.5 4.1] (blue).

No clear magnitude, source to site distance or azimuth dependence is identified. No systematic difference is observed between the ATANH(lagged coherency) estimates of the two horizontal and the vertical components either. However, the residuals of the distant events, i.e. R_{epi} of [100 350] km (Figures 3.19, D.3 and D.4) seem to have slightly

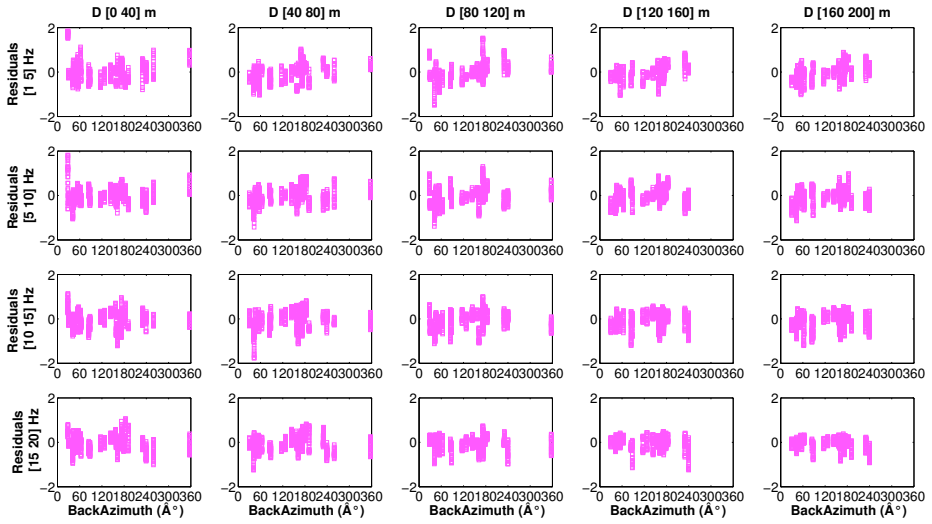

FIGURE 3.20: Coherency residuals of individual median estimates of ATANH(lagged coherency) for each event with respect to the global median (ATANH units) of all the events as a function of back azimuth of the NS component.

smaller scatter compared to those of local events, i.e. R_{epi} of [0 100] km. A slight decrease of the scatter with increasing separation distance can also be identified. Similar observations have been done in the Argostoli seismological array by Imtiaz [2015a]. The aforementioned authors found as possible explanation for this phenomenon that at greater distances the extended source effects diminish and the variability in coherency estimates among different events are mainly caused by the local site properties. In near source, the spatial incoherence can be caused by a combined effect of nearby extended seismic source, source-site complex wave propagation and local soil properties, which in turn may cause larger scatter of the coherency estimates.

The observation of the present study that no particular dependency on source characteristics exist is in accordance with the conclusions in Abrahamson [2007] that, when larger data sets are used, dependence on source characteristics does not remain. It is important though to underline that both the magnitude range and the azimuth range of our dataset are relatively limited given that only low to moderate earthquakes in terms of magnitude have been recorded (M_L of [1.5 4.1]) and the vast majority of them have two preferential azimuths, both of them from the East (Figure 2.15).

Righ and left bank of the dam

The arch dam of Saint Guérin has a particular, non symmetrical, geometry. As identified in Figure 2.8 the left (east) bank is steeper than the right (west) one. A more abrupt inclination may lead to higher phase variability. The left bank consists of the stations SG05, SG06, SG07, SG08 and SG09 and the right of the stations SG01, SG12, SG11, SG10 and SG09. There are three station separation distance bins, [0 40] m, [40 80] m

and [80 120] m (the station separation distances are given in Table A.2 in APPENDIX A). The lagged coherency estimates on the right and the left bank are estimated and compared aiming to better investigate the sensitivity on the topography. The results are compared in Figure 3.21 for the two horizontal components. The left bank seems to have a somewhat higher variability for longer station separation distances, i.e. $D \geq 40$ m. For shorter station separation distances, the right bank appears to have higher phase variability. It is rather difficult, based on this analysis, to conclude if higher inclination of the canyon walls leads to higher phase variability of the motions. Thus, a numerical approach will be adopted in Chapter 4, aiming to get a better understanding of this phenomenon.

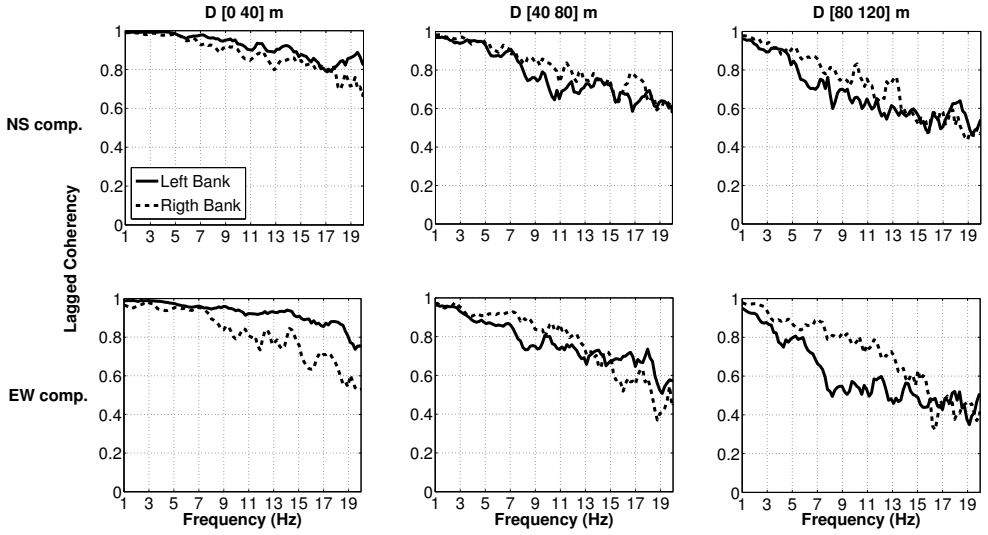

FIGURE 3.21: Comparison of lagged coherency estimates for the NS and EW components on the right and left banks of the dam for station separation distances D [40 80] m and D [80 120] m.

Time window and smoothing parameter

Coherency can be influenced by several parameters of the analysis, such as the window length and the wave types included in the window or the frequency range which is considered. A complete and robust analyses and interpretation of the coherency, especially for engineering applications, should include not only signals from different events, but also different wave phases and different time windows, to avoid a precipitate interpretation. Riepl et al. [1997] showed that at short inter-station distances, the coherence is more sensitive to the choice of the time window ($S-$wave, coda wave or noise) than at large distances. The site effects become minor and similarities within the signals arising from source or path contributions are at least of the same order than the local site effects, provoking significant variations due to different wave types. Consequently, they conclude that at this distance range, a general application of noise recordings to

study the coherence is not justified.

To perform a sensitivity analysis on the duration of $S-$wave time window, a different range of normalized Arias Intensity, AI, is used. An alternative time window is estimated based on the time at which the normalized AI has value between 0.05 and 0.95. The same rock-station data are used again for the identification of $S-$waves, i.e. SG17, SG18 and in the case of absence of both recordings the SG15, SG14 or SG13 (Table B.4 in APPENDIX B). $S-$wave duration chosen based on $0.05 < AI < 0.95$ and $0.1 < AI < 0.75$ as a function of epicentral distance, R_{epi} (km), and magnitude, M_L, is presented in Figure 3.22. When AI is chosen between 0.1 and 0.75, the $S-$wave duration ranges between 1.5 and 11 sec while choosing AI between 0.05 and 0.95 leads to longer durations of time windows; from a minimum length of more than 6 up to 17 sec. Therefore, in some cases, a part of $P-$waves and/or a contaminated part of $S-$waves is included due to surface waves, diffracted waves etc. The smoothing window used is adapted accordingly leading to 'less smoothed' estimations (higher resolution).

The coherency estimates of the NS, EW and Z components for the two different time windows, according to different AI ranges, are compared in Figure 3.23. The same separation distance bins as for the previous analyses are used for the comparison, i.e. [0 40] m, [40 80] m, [120 160] m and [160 200] m. With the increase of the duration of the $S-$wave window there is no effect on the trends of the coherency estimates. As expected, the resolution of the estimates is higher, resulting to more abrupt coherency losses. The comparison shows that, although for some distance bins for the vertical component there is a slight decrease of coherency, the two time windows result in nearly the same median values at all distances along the frequency range. This means either that the $S-$wave window is not highly contaminated by other types of waves (which is usually the case in rock sites) or that if the strong motion part is included in the time window that results are robust. In any case, although no absolute 'rule' of window selection is available, the small sensitivity test on the $S-$ window selection allows us to conclude that the coherency estimates are robust. The observation made in Figures 3.14 that there is a possible higher variability around the frequencies of vibration of the dam becomes more clear with the use of longer $S-$wave windows and higher resolution. The confirmation and physical explanation of this observation is attempted in Chapter 4.

Going a step further, time windows of different wave types are also considered for lagged coherency calculation. In Figure 3.25, lagged coherency estimates of the commonly used in the literature $S-$wave window, are compared with estimates based on three different/longer time windows : a symmetrical 15 sec window around the PGV, which includes the $S-$wave part along with $P-$, surface and scattered waves, a 14 sec window of coda waves contaminated with other scattered or surface wave phases as well as a window of ambient noise data.

According to Abrahamson [2007], while the horizontal component is dominated by the

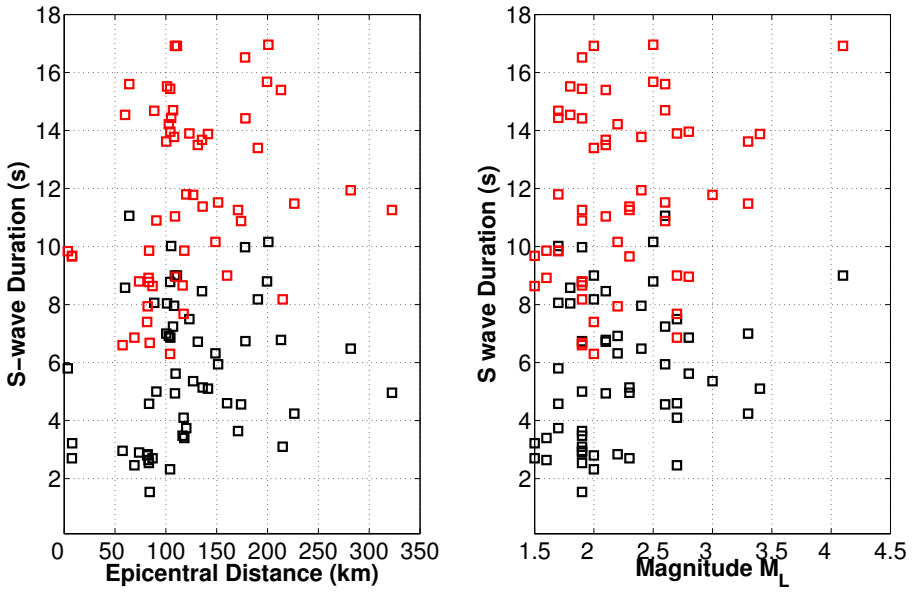

FIGURE 3.22: $S-$wave duration chosen based on $0.05 < AI < 0.95$ (red squares) and $0.1 < AI < 0.75$ (black squares) as a function of epicentral distance (km) and magnitude (M_L).

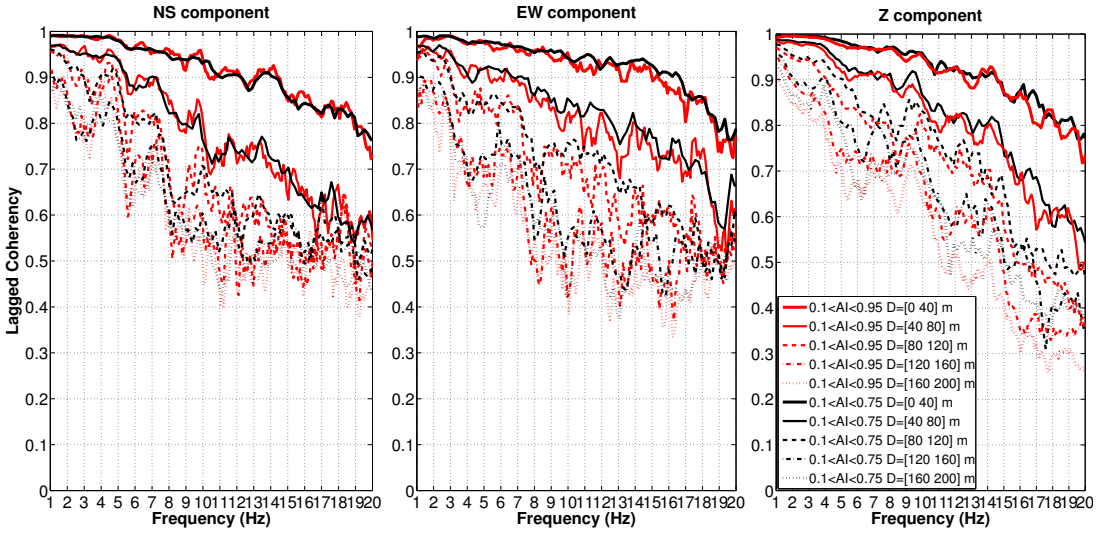

FIGURE 3.23: Comparison of lagged coherency estimates for $S-$wave time windows based on $0.05 < AI < 0.95$ (red lines) and $0.10 < AI < 0.75$ (black lines).

$S-$waves, the vertical component will include both $P-$waves and SVwaves. At high frequencies, the coherency for the vertical component is greater than the coherency for the horizontal component. This increase is due to the larger coherencies at high frequencies from $P-$waves than from $S-$waves. In addition to the $P-$ and $S-$waves, the wave field may also include surface waves. The surface waves will be low frequency waves for which the coherency model is already near unity (Abrahamson [2007]). We could assume that adding these wave components would result to different coherency estimates.

On the other hand, it is interesting to see what would be the effect on lagged coherency, if the strong motion part would not be included in the window of analysis. Coda waves are interpreted as back-scattering waves from numerous heterogeneities distributed uniformly in the earth, named as the 'tail' part of the seismogram of an earthquake. After Rautian & Khalturin [1978], the basic procedure is to place the coda-start where the time measured from the earthquake origin time is twice the $S-$wave travel time. If this rule becomes too demanding, the coda-start can be placed closer to the $S-$wave time of arrival. In any case it is necessary to avoid contamination with the contribution made by direct S phases. The end of coda is usually placed where the SNR reaches a chosen, low value. This rule of thumb was approximately followed for the definition of the coda window herein, leading to the choice of a 14 sec long window, avoiding to include the pure $S-$waves, but including other wave types that follow such as surface and scattered waves. An example waveform of all three windows is shown in Figure 3.24. The smoothing window used is imposed to be the same for all three cases so as to have the same resolution. The lagged coherency analysis is performed for the NS component for the 55 events.

As a final step to the sensitivity of coherency on the selection of wave types, based on the ambient noise records from the Saint Guérin array, the lagged coherency at the dam-foundation rock interface is estimated to be compared with the observations made based on earthquake data. Ambient noise data 2 hours before the occurrence of the 55 seismic events are used; the same recordings were used in Chapter 2 to identify the frequencies of vibration of the arch dam. No 'rule' exists in the literature for the choice of the length of the time window to be analyzed when calculating coherency based on ambient noise. After a short sensitivity analysis, a 5 second-long window is chosen in the present study and the median value of all the independent lagged coherency estimates is estimated.

When using earthquake wave types, the comparison reveals that lagged coherency has similar trends in all three cases with the $S-$wave phases to be more coherent than the combined $P-$, $S-$, and other wave phases and these last ones to be more coherent than the contaminated coda wave phases. In the case of multiple wave types considered for coherency calculation, the phase content is expected to be more variable than in the

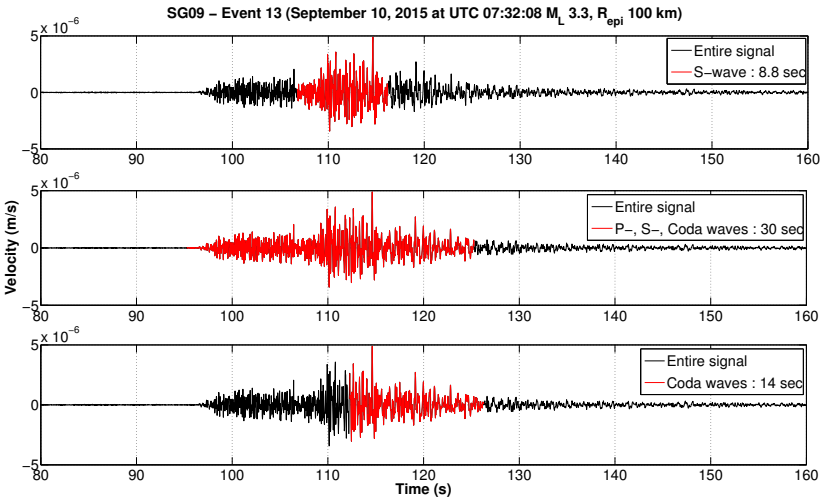

FIGURE 3.24: Velocity time serie and selected windows for lagged coherency analysis of the the NS component recorded at station SG09, for the event that occurred on September 10, 2015 at UTC 07:32:08 with magnitude M_L 3.3 and epicentral distance, R_{epi} 100 km.

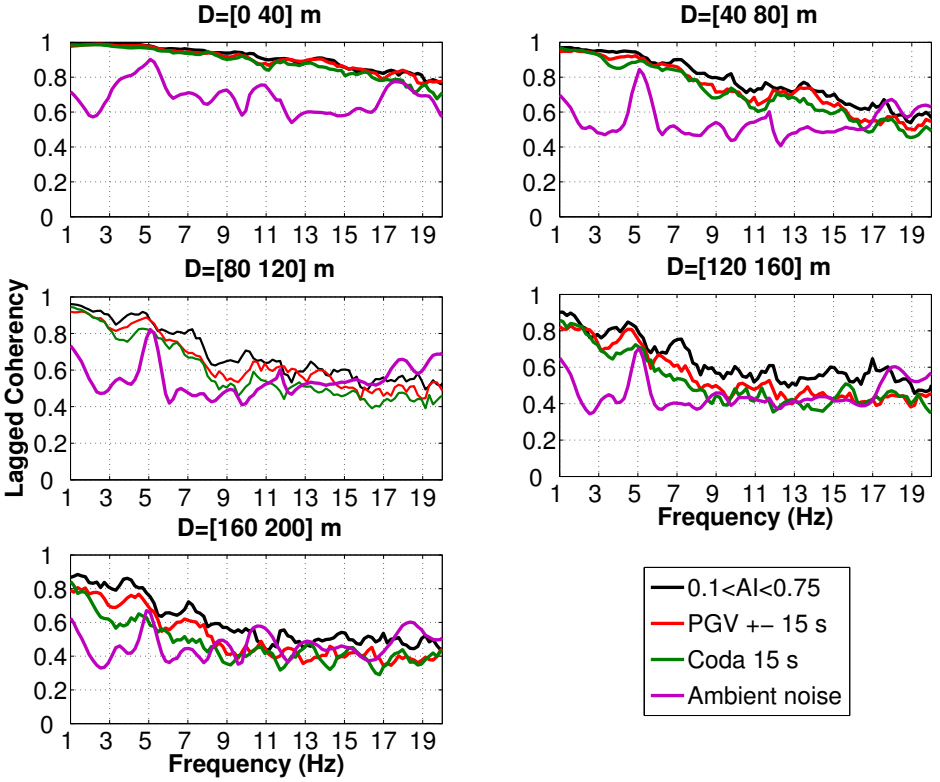

FIGURE 3.25: Comparison of lagged coherency estimates for $S-$wave time windows based on $0.10 < AI < 0.75$ (black lines), PGV$\pm$15 sec (red lines), 14 sec of coda waves (green lines) and ambient noise data (purple lines) for the NS component.

case of a 'relatively pure'/single $S-$wave. The trends though are very similar, showing that when the strong phase of the motion is included, the analysis yields to very similar results. Regarding the coda waves, the contribution of many different sources of scattered wave generation makes the phase content even more variable than in the other two cases (only $S-$ and $S-$ combined with other wave types). The differences in lagged coherency among the three windows remain, however, less than 20%. On the other hand, the lagged coherencies based on ambient noise are not comparable with the observations based on earthquakes. The coherency estimations are not dependent on frequency and the dependency on station separation distance decreases rapidly for longer distances. Interestingly, we note lower variability around the frequency of vibration of the dam at 5.2 Hz, which is contradictory to the observation of higher variability around this frequency of vibration when using earthquake data. The physical causes of ambient noise in the Saint Guérin site include various atmospheric phenomena (principally wind and reservoir motion) while, given the location, nearby human activity of any kind is very limited. Thus, given the various sources of ambient noise, there is no physical explanation for correlation of the motions in terms of phase even for low frequencies (i.e. coherency does not tend to 1 when frequency goes to 0 Hz).
The current analysis on the time window used for coherency estimation shows that, in rock sites, as long as the strong motion $S-$wave part is included in the selected window, the coherency results are robust. Using coda waves could also provide reasonably similar lagged coherency values, which however would be lower. Although the ambient vibration records are a fast as well as inexpensive way to obtain interesting conclusions, the results based on them are not similar to the ones of earthquake data. The observations on ambient noise data demand deeper analyses and further tests to be better understood. This, however, is beyond the scope of the present study. It can be concluded from these preliminary results that at this distance range, a general application of noise recordings to study the phase variability is not justified.

3.4.1.2 Comparison with the free field motions

The dense seismological array in Saint Guérin provides data that cover both the motions at the dam-foundation rock interface and the free field. However, it has its limitations regarding the number of free field stations. The local weather conditions (high altitude thus difficulty in access) as well as the particular alpine topography limited the choices of possible free field deployment of seismological stations. The free field stations SG13, SG14, SG15 are located along the road that leads to the dam with negligible altitude difference (APPENDIX A Table A.1). The signature of the dam (frequencies of vibration), although relatively damped, is found in the recordings of the stations SG13 and SG14

(Figure 2.9). Despite that, these three stations can be considered as free field motions that do not incorporate any topographic effects as in the case of the irregular canyon topography of the stations at the dam-foundation rock interface. Consequently, a comparison of the two groups may provide a conclusion regarding the topography effect on the SVGM. On the other hand, stations SG17 and SG18, both located on rock sites, have an elevation difference of, approximately, 44 m and linear distance of, approximately, 105 m that can be considered as a reason for topographic effects. However the possible topographic effect would remain small with respect to the topographic effect due to the canyon shape at the dam-foundation rock interface. This, combined with the fact that no dam signature (in terms of frequencies of vibration) is identified in the recordings of station SG17 and SG18, make them good reference free field stations. The station pair SG19-SG20 was not considered for comparison due to the strong site effects along the entire frequency range at the location of SG19 which is on the east bank of the reservoir. Taking advantage of the these data, the comparison between the base of the dam and the free field allows to get a better insight on the contribution of the local topography as well as the soil-structure interaction on the SVGM. It has to be noted that, in the free field, there are only two station pairs in each distance bin, i.e in the range of [40 80] m the pairs are SG13 - SG14 and SG14 - SG15 and in the range of [80 120] m SG13 - SG15 and SG17 - SG18. In the first distance bin, i.e. from 40 to 80 m, the two available pairs can be combined and one median value can be estimated while in the second distance bin, i.e from 80 to 120 m, the station pairs SG13-SG15 and SG17-SG18 should be studied separately given their different geological-topographical locations. For a robust statistical analysis, 2 pairs in each distance bin may not be sufficient. Despite that, given the sufficient number of available recordings for the total of the data set (Figure 3.9), preliminary conclusions can be drawn that should be confirmed with future studies. The comparison of the lagged coherencies for the two distance bins for the three components of motion at the dam-foundation rock interface and in the free field is presented in Figure 3.26.

The overall trends of lagged coherency in the free field are comparable to the ones observed at the dam-foundation rock for the three components of motion (NS, EW, Z). In the free field, the values of coherency start from 1 at frequencies around 1 Hz and station separation distances 40-80 m and reaches down to less than 0.5 at station separation distances 80-120 m. The motions at the dam-foundation rock interface are slightly more variable in terms of phase. Irregular local topography causes scattering of the incident waves that could result in a ground motion field that is more variable from the one in the free field, although, as shown from the observations, this effect is not significant. The frequency ranges within which there is higher variability at the dam-foundation rock interface suggests that the presence of the structure contributes to additional loss of coherency which is not observed in the free field. The slightly higher variability at

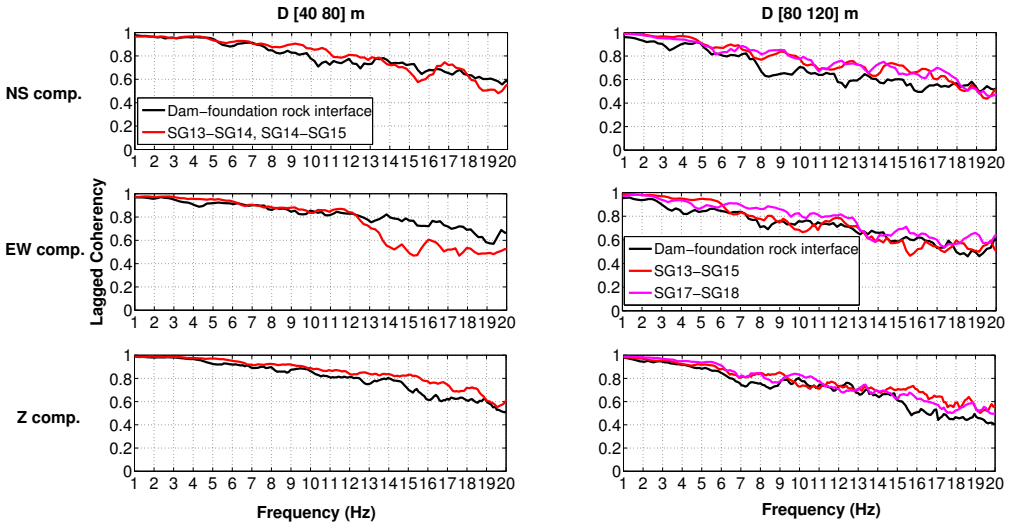

FIGURE 3.26: Comparison of lagged coherency estimates in the free field (red lines for station pairs SG13-SG14, SG14-SG15 and SG13-SG15 and magenta lines for SG17-SG18) and at the dam-foundation rock interface (black lines) for station separation distances D [40 80] m and D [80 120] m.

the dam-foundation rock interface with respect to the free field suggests that the presence of the structure along with the irregular local topography may influence the loss of coherency. Higher phase variability is also observed in the EW component for the pairs with inter-station distances [40 80] m. The trend of coherency appears to increase after 11 Hz, reaching values as low as the ones of pairs with higher inter-station distances, i.e. [80 120] m. A possible explanation for this behavior could be the geological site where the stations SG13, SG14 and SG15, i.e. shallow sedimentary layer laying over a stiff rock; however no particular reason for this phenomenon to occur only on the EW comp is found. From this preliminary analysis, performed based on the limited number of pairs in the free field in Saint Guérin, we can conclude that the topographic and the soil-structure interaction effects have only a minor/secondary on SVGM. Further analysis is necessary to confirm the observations made in Saint Guérin site.

3.4.2 Unlagged coherency estimates

The real part of the complex coherency, $\Re[\gamma_{jk}(\omega)]$, is referred to as the unlagged coherency. The unlagged coherency estimates (including the wave passage effect: not aligned records) for each pair at the dam-foundation rock interface along with the median value of all station pairs in the selected distance bins are presented in Figures 3.27, 3.28 and 3.29 for each component respectively. The median values for each distance bin for each component are grouped in Figure 3.30. The unlagged coherency values start from 1 at low separation distances and low frequencies and reaches down to -0.25 at higher frequencies and longer station separation distances. As aforementioned, negative

values result from the coherent part of the wave-passage effect and indicate out of phase ground motions between the pair of stations. The rest of the conclusions remain the same as in the lagged coherency, i.e. the results are similar for the two horizontal while in the vertical component the unlagged coherency values are somewhat higher. Higher loss of coherency around some frequencies, are easily identified for longer station separation distances, i.e $\geq 120m$. Unlagged coherency is frequency dependent thus ATANH values are used for analysis, however, the results are presented in terms of the untransformed coherency because it is easier to be understood.

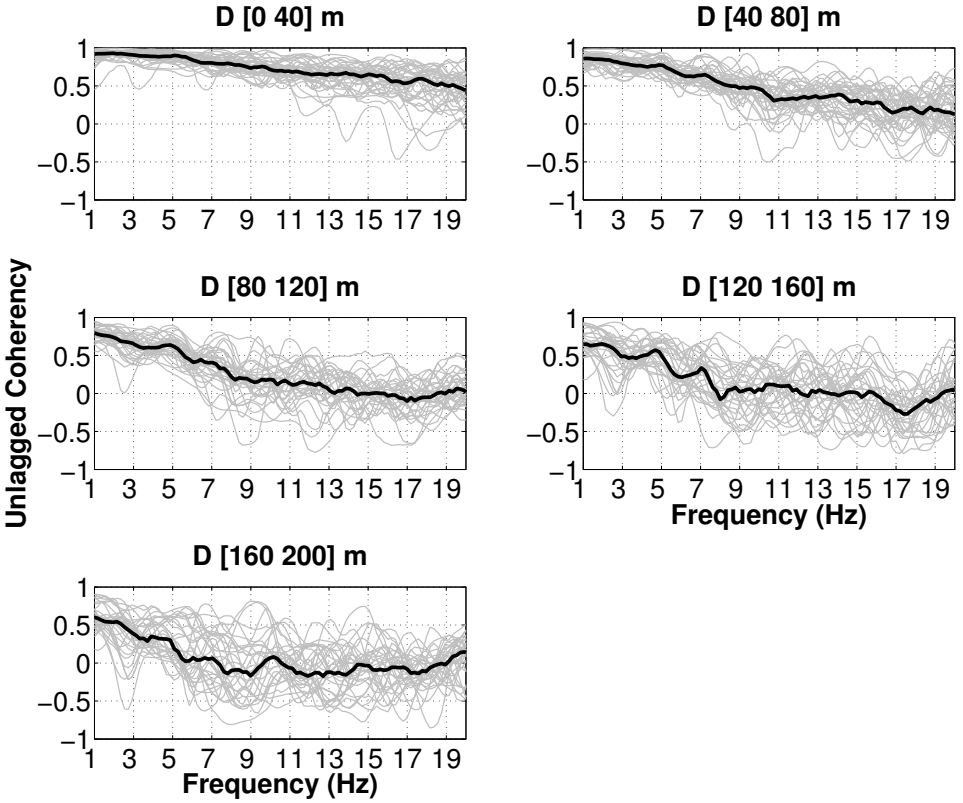

FIGURE 3.27: Individual median values of unlagged coherency of not aligned time histories of all pairs along the dam-foundation interface with inter-station distances [0 40] m, [40 80] m, [80 120] m, [120 160] m and [160 200] m for each event (gray lines) and median value of all events (black line) as a function of frequency for the NS component.

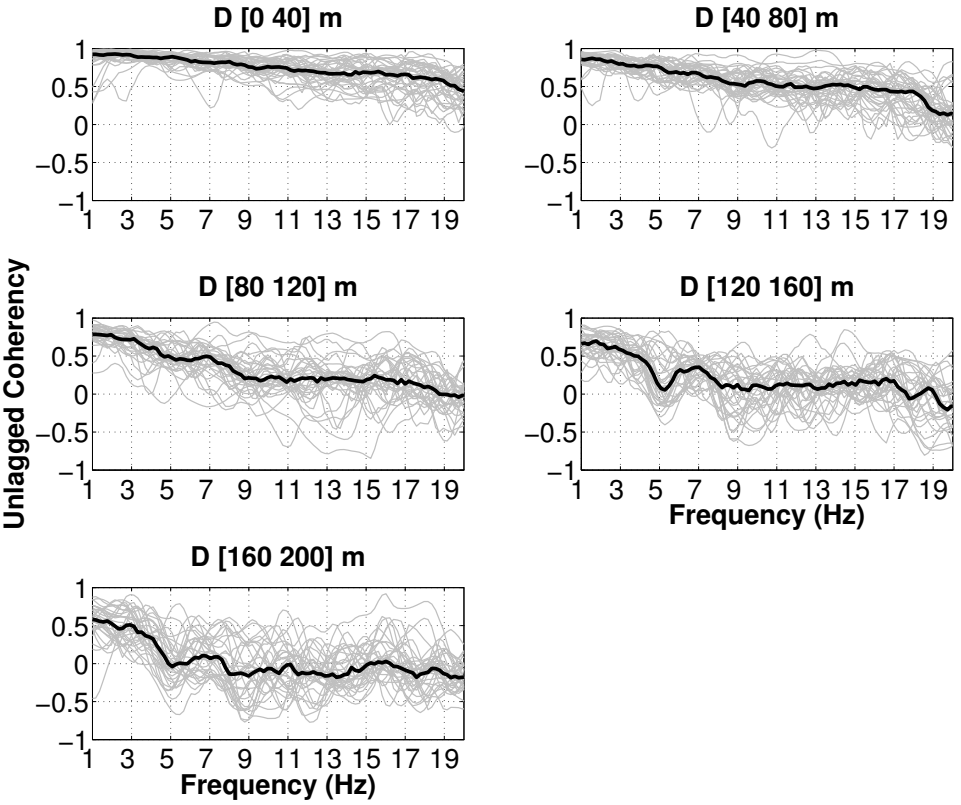

FIGURE 3.28: Individual median values of unlagged coherency of not aligned time histories of all pairs along the dam-foundation interface with inter-station distances [0 40] m, [40 80] m, [80 120] m, [120 160] m and [160 200] m for each event (gray lines) and median value of all events (black line) as a function of frequency for the EW component.

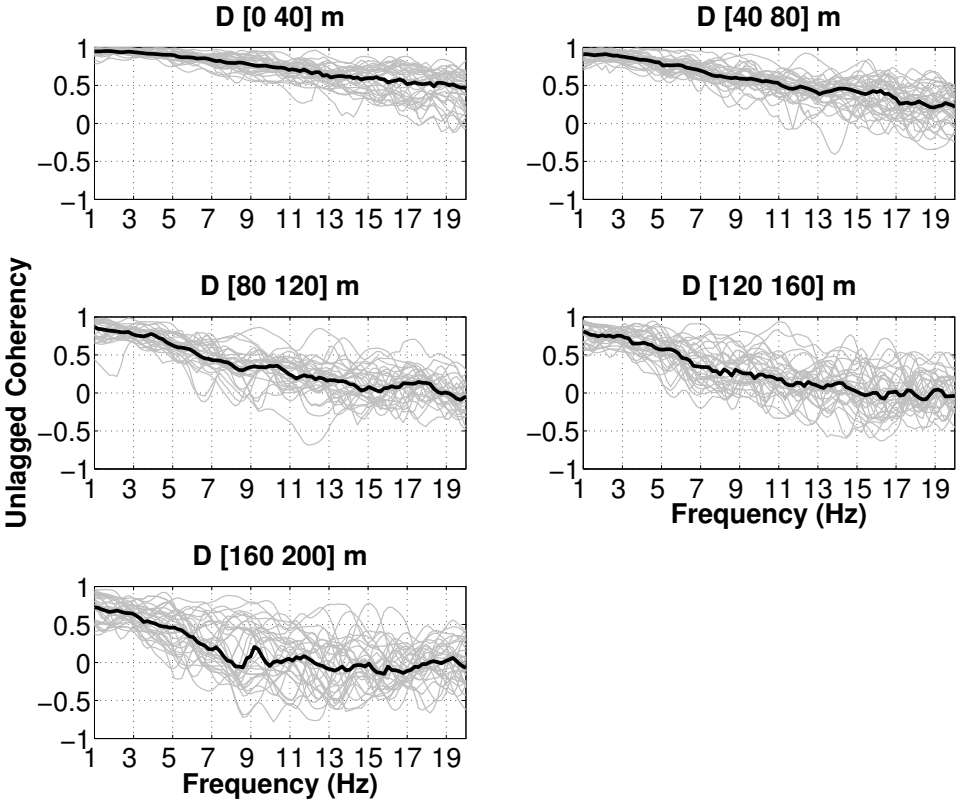

FIGURE 3.29: Individual median values of unlagged coherency of not aligned time histories of all pairs along the dam-foundation interface with inter-station distances [0 40] m, [40 80] m, [80 120] m, [120 160] m and [160 200] m for each event (gray lines) and median value of all events (black line) as a function of frequency for the Z component.

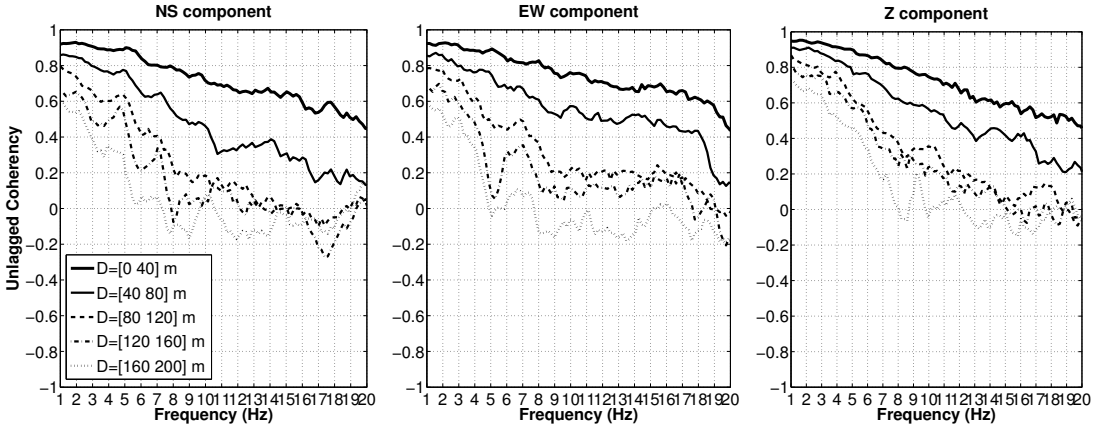

FIGURE 3.30: Unlagged coherency of not aligned time histories as a function of frequency for the NS (left) and EW (middle) and Z (left) components; median value of all the events within each distance bin along the dam-foundation rock interface (solid and dashed black lines).

3.4.3 Comparison with existing coherency models

Once the estimators of phase variability, namely lagged or unlagged coherency, at the dam-foundation rock interface are obtained from the Saint Guérin data, parametric models can be fitted to them. In case the observations are found to be fitted by existing models, there is no need for derivation of new models for the particular case of the interface between a canyon rock topographic site and an arch dam. This would, indirectly, signify that the two additional parameters (local site effects) in the case of Saint Guérin, namely canyon topography and presence of an arch dam, are only secondary causes of phase spatial variability of ground motions. Therefore, they could be disregarded. In the next step of the analysis, these parametric models that fit the measures, may be used either directly in random vibration analyses of the structures or in Monte Carlo simulations for the generation of spatially variable motions to be applied as input excitations at the supports of structures.

Comparison with existing lagged coherency models

Coherency models derived from arrays on rock sites are limited while there is a lack of models based on seismological arrays located on sites with topographical irregularities and/or the presence of an engineered structure. One of the few lagged coherency models based on rock site arrays reported in the literature was developed by Menke et al. [1990]. This model is based on 4 earthquakes (epicentral distances 5, 40, 140 and 170 km, respectively) recorded from two arrays, i.e. the ECO array, a six-element linear seismic array, and the DBM array, a seven-element linear array. Both arrays are located on hard rock sites with high V_s values (2000-3000 m/s), similar to the Saint Guérin site. It is valid for all three ground motion components (vertical, radial and tangential) and all epicentral azimuth and distance ranges. The model has the form of Equation 3.4.

$$\gamma(\xi, f) = exp(-\alpha f \xi) \tag{3.4}$$

with α being in the range of $(0.4 - 0.7)10^{-3}$.

One of the most commonly used lagged coherency models in practice nowadays is the one of Abrahamson [1992a], which is derived based on the Lotung, Taiwan array (LSST) soil site array. Schneider et al. [1992] compared the predictions of this model with the observations on rock site arrays (EPRI Parkfield, USGS Parkfield, ZAYA and Pinyon Flat). Coherencies from the EPRI Parkfield and Pinyon Flat arrays were found to be compatible with the model while coherencies from USGS Parkfield and ZAYA arrays were much lower. Their explanation for the incompatibility of the model with observations from the USGS Parkfield array was that the data are strongly affected by significant topographic variations that would reduce the coherency. Ancheta et al. [2011] adapted the model

using data from the Borrego Valley Differential Array (BVDA) soil site array as well. The underlying soils for the two arrays consist of medium to very dense sands ($S-$wave velocities of 400 to 600 m/s). The soils overlie granitic basements ($S-$wave velocity of 3000 m/s) (Kato et al. [1998], Olson et al. [2000]). Earthquakes with recordings having a high signal to noise ratio and minimum 1 sec window length for $S-$waves were selected to optimize bandwidth. The selected earthquakes are, for the BVDA array, events with $M_L > 2.5$ and for the LSST array, events with $M_L > 6$, typically with epicentral distances $< 80km$ (peak ground accelerations, PGA, $> 0.005g$). The formulation of the lagged coherency model for horizontal motions is:

$$tanh^{-1}(\gamma(f,\xi)) = (a_1 + a_2 ln(\xi))exp(b_1 + b_2\xi)f + d(\xi)f^{c(\xi)} + k \tag{3.5}$$

where f is frequency in Hz, ξ is the separation distance in m and $a_1 = 3.79$, $a_2 = -0.499$, $b_1 = -0.115$, $b_2 = -0.00084$, $c = -0.878$.

Due to the absence of coherency models proposed for the dam-foundation rock interface, or at least at site with irregular topography and the presence of an engineered structure, a comparative study is performed between the coherency observations at the dam-foundation rock interface in Saint Guérin site and the two aforementioned empirical coherency models, i.e Menke et al. [1990] and Ancheta et al. [2011]. The α value chosen for the Menke et al. [1990] model is $0.4 * 10^{-3}$ sec/m; this is the lowest value of α recomended by the authors for stiff rock sites. Despite their distance and frequency range limitations, for the sake of comparison, the predictions of the two models in the frequency range of [1 20] Hz and within the five separation distance bins are presented in Figure 3.31. The median coherency estimation at the dam-foundation rock interface in Saint Guérin for both horizontal components, NS and EW, for each distance bin is also presented.

As observed in Figure 3.31, the coherency model proposed by Menke et al. [1990] overall fits well the observations in Saint Guérin along the frequency range and for all distance bins with the exception of station separation distances higher than 120 m and frequencies higher than 15 Hz. For these longer station separation distances and higher frequencies the model overestimates the loss of coherency. Given that it is calibrated for station separation distances up to 100 m, the observed misfit is to be expected. However, the overall predictions can be considered satisfactory despite the simplicity of the model. The coherency model proposed by Ancheta et al. [2011] captures the saturation towards an asymptote for distances higher than 120 m (although its application range is up to 100 m) and frequencies higher than 15 Hz. On the other hand, for station separation distances shorter than 120 m and frequencies higher than 8 Hz it underestimates the loss of coherency. As noted by its authors, the model underestimates coherency for $\xi < 30$

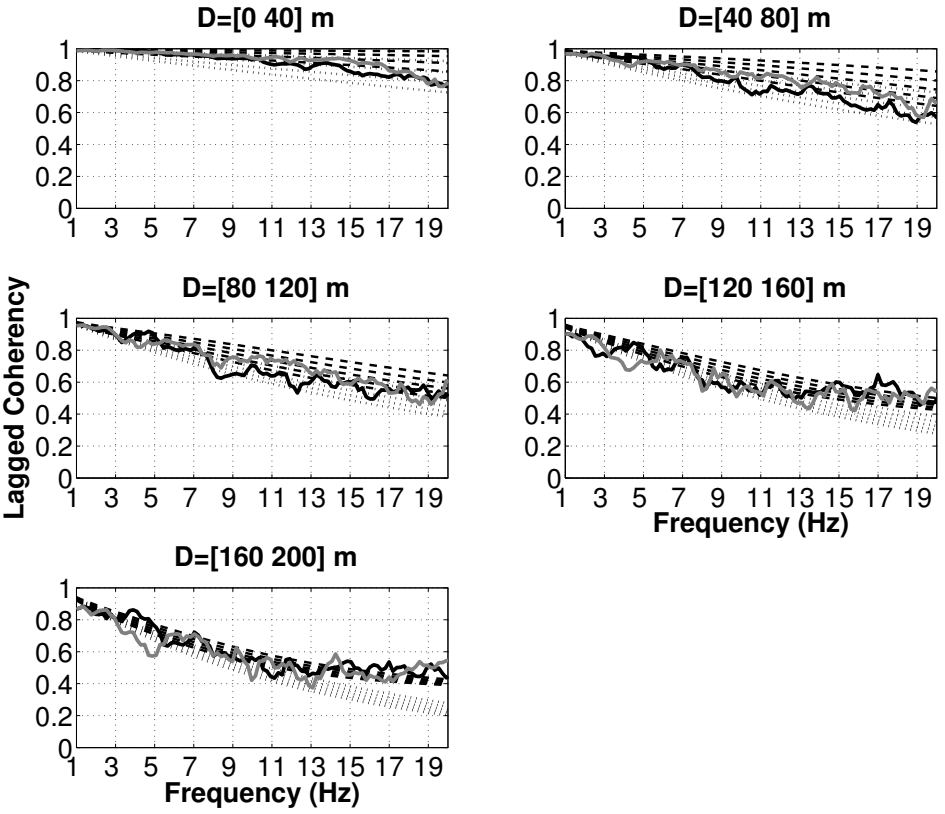

FIGURE 3.31: Estimated lagged coherency as a function of frequency for the NS (black solid lines) and EW (gray solid lines) component; median value of all the events within each distance bin along the dam-foundation interface. Black dashed lines correspond to coherency estimates of Ancheta et al. [2011] model and black dotted lines to coherency estimates of Menke et al. [1990] coherency model every 10 m within each separation distance bin.

m and $f < 10$ Hz, which could partially explain the underestimation of the coherency loss of the observations in Saint Guérin. Despite that the model is calibrated based on soil site arrays, that generally have higher loss of coherency than the rock sites, it slightly underestimates the phase variability at the dam-foundation rock interface implying that the local conditions (presence of the dam, canyon topography and local geology) contribute to further increase of the phase variability. This underestimation of the coherency was observed by the authors of the original model (Schneider et al. [1992]) when compared with the rock site data coming from USGS Parkfield and ZAYA arrays as well. For the first rock array, they also concluded that a possible explanation of the underestimation was the significant topographic variations that could reduce the coherency. An interesting point that needs to be underlined is that the re calibrated model was derived using events with PGA $> 0.005g$ while in the Saint Guérin data the PGA values are much lower with the highest to be 0.00012 g ($0.0012\ m/s^2$).

It can be concluded that, although no irregular topography or engineered structure are

present in the location of the arrays used for the derivation of both models, they fit in an overall satisfactory way the coherency observations of the present study indicating that the effect of the soil-structure interaction and the local canyon topography are secondary causes of phase variability of the ground motions. This observation is in accordance to Riepl et al. [1997] who showed that at short inter-station distances the site effects become minor and similarities within the signals arising from source or path contributions are at least of the same order than the local site effects. Furthermore, the fact that similar results yield from a lower intensity database, such as the one in Saint Guérin, may allow extrapolation of the application of these models in all ranges, confirming once again Abrahamson [2007] that, when larger data sets are used, dependence on source characteristics does not remain. The aforementioned conclusions open the discussion for the applicability of lagged coherency models calibrated in plane free field seismological arrays for the estimation of phase variability of input motions in case of arch dams located in particular canyon topographies. Although this argument should further be investigated and confirmed, it remains a first proof for application of these models in seismic analysis of arch dams.

Comparison with existing plane-wave and unlagged coherency models

The plane wave coherency is given from the Equation 1.13, thus it is equal or smaller than the lagged coherency. Abrahamson [2007] argues that for very short separation distances, a few hundreds of meters or less, the wave passage effects will not be significant because of the small travel time among the stations and the unlagged coherency will be similar to the plane-wave coherency. It is difficult to estimate the plane-wave coherency in the case of the seismic data coming from the Saint Guérin site since a single wave direction (azimuth) and apparent velocity (incidence) cannot be easily defined along an the array which is located in irregular topography and where soil-structure interaction is also present (the reasoning was extensively presented in section 3.3). It is of great interest though to compare the unlagged and lagged coherencies with the plane-wave and unlagged coherency models, to investigate the two aforementioned arguments. Such models for plane wave coherency are proposed by Svay et al. [2017] and for unlagged and plane wave coherency by Abrahamson [2006]. The coefficients of the plane-wave coherency model proposed by Abrahamson [2006] were derived using data from 74, in total, earthquakes with magnitudes ranging from 3 to 7.8, epicentral distances lower than 105 km and PGA values from 0.007 to 0.89 g. The earthquakes were recorded from several soil and rock site arrays (EPRI LSST, EPRI Parkfield, Chiba, Imperial Valley Differential, Hollister Differential, Stanford, Coallinga, Pinyon Flat, SMART-1 and -2). The $S-$wave window duration ranges from 2 to 10 sec (similar to the values of the Saint

Guérin earthquake data).

$$\gamma_{pw}(f,\xi) = [1 + (\frac{fTanh(a_3\xi)}{a_1 f_c(\xi)})^{n_1(\xi)}]^{-\frac{1}{2}}[1 + (\frac{fTanh(a_3\xi)}{a_2})^{n_2}]^{-\frac{1}{2}} \tag{3.6}$$

TABLE 3.1: Plane-wave coherency model coefficients of Abrahamson [2007] model for the horizontal component.

Coefficient	**Horizontal Coefficient**
a_1	1.674
a_2	1.01
a_3	0.4
n_1	7.02
n_2(ξ)	5.1-0.51ln($\xi + 10$)
$f_c(\xi)$	-1.886+2.221ln({4000}{$\xi + 1$} + 1.5)

The separation distance ranges from 6-7 to 240 m, almost identical distance range to the Saint Guérin array. The authors note that since most of the data were from small magnitude earthquakes with small amplitudes at the low frequencies, the computed coherencies are used only for $f > 5Hz$ and up to 50 Hz. The plane-wave coherency is modeled by the functional form described in Equation 3.6 with the coefficients given in Table 3.1. The unlagged coherency model is given from the Equation 3.7:

$$\gamma_{UN}(f,\xi) = |\gamma_{pw}(f,\xi)|cos(2\pi f \xi_R s) \tag{3.7}$$

where s is the slowness in s/m, varying from 0.0005 to 0.00025 s/m, and ξ_R the separation distance in the radial direction in m which for a generic application will have a median value of $\xi_R = \frac{\xi}{\sqrt{2}}$. For the present comparison a slowness equal to 0.00025 s/m (or 4000 m/s) is chosen. Despite its frequency range limitations, for the sake of comparison, the predictions of the model in the frequency range of [1 20] Hz within the five separation distance bins are presented in Figure 3.31. The median unlagged and lagged coherency estimates at the dam-foundation rock interface in Saint Guérin for both horizontal components, NS and EW, for each distance bin are compared in Figure 3.32.

The comparison reveals that the empirical model of plane-wave coherency, indeed, fits well the unlagged coherency estimates of Saint Guérin in the frequency range [5 20] Hz. An underestimation of the phase variability of the motions is observed for frequencies up to 5 Hz. The incompatibility of the model for lower frequencies is expected because of the recorded data in Saint Guérin of small magnitude earthquakes with small amplitudes at the low frequencies. Regarding the trend of the lagged and the plane-wave coherencies, it can be seen that, at the lower frequencies, where the plane wave dominates the motions,

the lagged and plane-wave coherencies are essentially identical for the distance range of applicability of the model. As concluded Zerva [2009] when comparing the lagged and plane-wave coherency models of Abrahamson et al. [1990] and Abrahamson et al. [1991] (older versions of the models used herein), as frequency increases, the lagged coherency, which incorporates the additional, scattered energy contained in the time series, tends to the median value of noise, whereas the plane-wave coherency tends to zero. Finally, from the comparison we can conclude that even within a few hundreds of meters the wave passage is not negligible since the three types of coherency do not coincide.

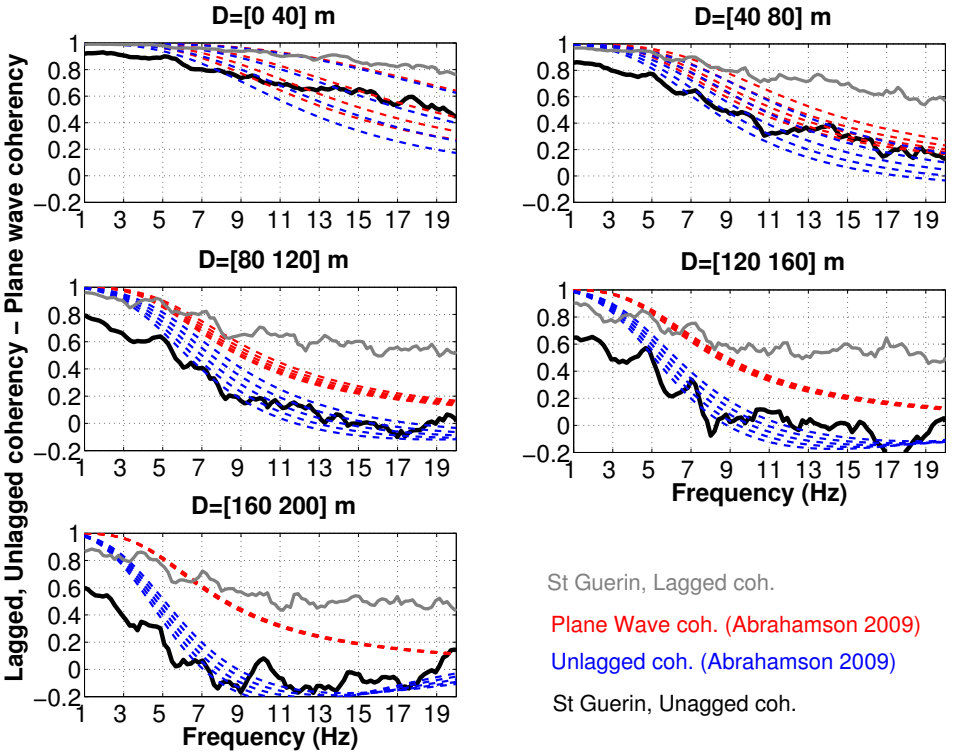

FIGURE 3.32: Estimated lagged and unlagged coherency as a function of frequency for the NS (black solid lines) and EW (gray solid lines) component; median value of all the events within each distance bin along the dam-foundation interface. Dashed red and blue lines correspond to plane-wave and unlagged coherency estimates of Abrahamson [2006] models every 10 m within each separation distance bin.

3.5 Amplitude variability analysis

The consideration of only the phase is not sufficient to account entirely for the spatial variability (e.g. Zerva & Zhang [1997], Schneider et al. [1990]). Lagged coherency is only minimally affected by the amplitude variability between the motions at the two stations. Although the phase variability of the seismic ground motions have been widely studied through the coherency estimates, literature on amplitude variability remains

limited. The amplitude variability can be reflected directly using the difference of natural logarithm of the Fourier amplitudes between the motions at two stations. Velocity time histories are used for the analysis. Either smoothed (using the same smoothing as the one applied for the coherency estimation) or unsmoothed spectra can be used for the estimation of this indicator.

3.5.1 Standard deviation of difference of Fourier amplitudes

The quantification of the amplitude spatial variability of ground motion is conducted using the station pairs at the dam-foundation rock interface. Initially, the unsmoothed Fourier amplitude spectral ordinates in terms of velocity of the $S-$window (as identified earlier in Chapter 3) are considered. The difference of the natural logarithms of the Fourier amplitudes for a given frequency and station separation distance is calculated. The amplitude variability estimates are grouped in separation distance bins as for the coherency analysis, e.g [0 40], [40 80], [80 120], [120 160] and [160 200] m. The standard deviation of all station pairs within each distance bin, using the whole set of events (considering that the standard deviation is independent of the event) is calculated and presented in Figure 3.33. In the same figure are plotted the Fourier spectra at the interface and on the crest as they were estimated in 2.24.

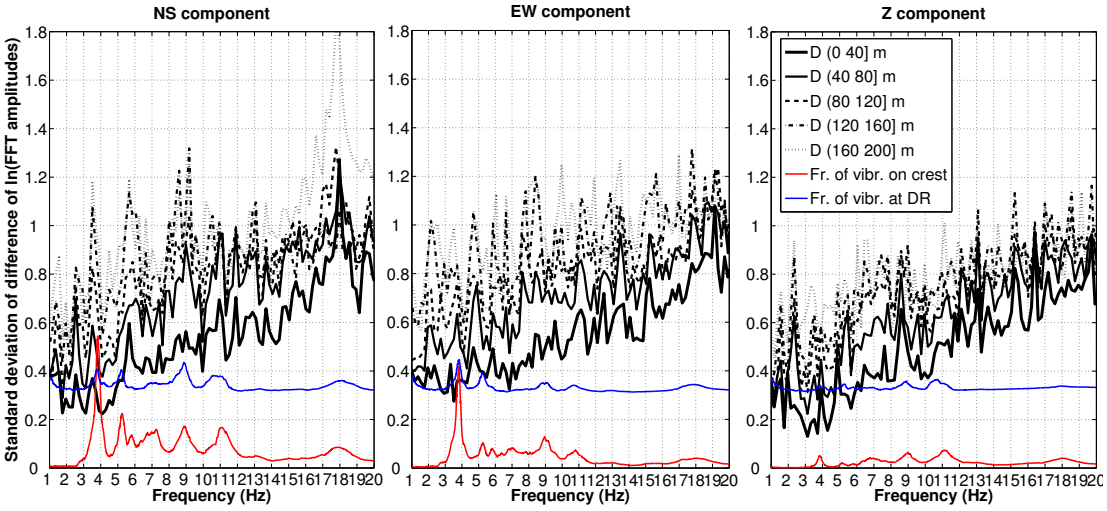

FIGURE 3.33: Standard deviation of the difference of natural logarithm of Fourier spectral velocities of ground motion as a function of frequency for NS (left) and EW (right) component; black solid and dashed lines represent the median value of all the events within each distance bin along the dam-foundation interface, e.g [0 40] m, [40 80] m, [80 120] m, [120 160] m and [160 200] m. Frequencies of vibration identified on the dam crest are represented by red lines and at the interface by blue lines.

In Figure 3.33 it is observed that the amplitude variability has an increasing trend with the increase of station separation distance and frequency, as expected. The frequency

dependency appears to be stronger than the distance dependency with the second one to get saturated after the first 80 m of station separation distance. The stronger frequency with respect to the distance dependency is also made from data coming from other seismological arrays (e.g. Schneider et al. [1992]). The amplitude variability of both horizontal components appears to have very similar trends with values varying from 0.25 to 1.3 while the vertical component is somewhat lower reaching values up to 1.1. Transforming the values in percentages, the amplitude variability reaches values as high as 260% ($= e^{1.3}$) in the NS comp. Although it is difficult to directly compare amplitude with phase variability, Schneider et al. [1992] indicates that the range of amplitude variability is greater than the range of phase variabilities. Such conclusion suggests that amplitude variability is more sensitive to local site conditions than is coherency. Their conclusion using data coming from both soil and rock site arrays, e.g. rock sites as EPRI Parkfield, USGS Parkfield, PynionFlat, Coalinga and in soil sites as Imperial Valley, Stanford, Hollister and Chiba array. Their explanation for this phenomenon is the site resonance, meaning that a slight shift in resonance across a site can easily generate large variations in amplitude (at a given frequency) but have little or no effect on coherency. In this regard, small changes in layer thickness can produce more predominant shifts in resonance for shallow layers; thus shallow soil sites and rock sites with complex geology would tend to experience the largest amplitude variations.

It can be noticed, although not very clearly, that the amplitude variability is locally increased around the frequencies of vibration of the dam, an observation more evident in the NS component. Because of the high resolution (absence of smoothing in the Fourier spectra), the phenomenon cannot be clearly observed; however, more abrupt peaks may be identified around 3.7, 5.5, 9 and 18 Hz (around the frequencies of vibration of the structure as they have been shown in Figure 2.24). Similarly, slight increase of phase variability was also observed around the frequencies of vibration. Thus, according to our observations, a slight shift in resonance across a site can easily generate large variations in amplitude (at a given frequency) but has also an effect on coherency; this will be further discussed in Chapter 4.

3.5.2 Sensitivity analysis

A detailed sensitivity test is conducted on source characteristics (i.e, magnitude, epicentral distance and azimuth) and the choice of smoothing parameter. This would enhance the robustness of the estimated values of amplitude variability.

Source characteristics

The residuals of each individual standard deviation from the global median value are estimated according to the procedure of sensitivity analysis performed for the lagged

coherency. To seek the magnitude dependence, the subset of events is divided into two epicentral distance groups, local events with epicentral distance of [0 100] km (17 events) and regional events with epicentral distance of [100 350] km (41 events). Figures 3.34, D.7 (APPENDIX D) and D.8 (APPENDIX D) show the residual plots of the amplitude variability estimations of the NS, EW and Z components respectively as a function of magnitude, for different inter-station distance groups and frequency ranges. Similarly, the events have been grouped into two magnitude ranges, M_L [1.5 2.5] (41 events) and M_L [2.5 4.1] (17 events) to examine the distance dependence. Residuals of amplitude variability values (NS, EW and Z components) of the two magnitude groups of events are presented in Figures 3.35, D.9 (APPENDIX D) and D.10 (APPENDIX D) as a function of the epicentral distances for increasing inter-station distances and frequency ranges. Finally, the back azimuth dependence is examined for increasing inter-station distances and frequency ranges for the two horizontal and the vertical components in Figures 3.36, D.11 (APPENDIX D) and D.12 (APPENDIX D). No magnitude, source to site distance or back azimuth dependence of the amplitude variability is identified for all the three components of motion. Nonetheless, residuals, generally, appear to be more scattered for higher frequencies ($f \geq 10$ Hz) and higher station separation distances ($D \geq 100$ m).

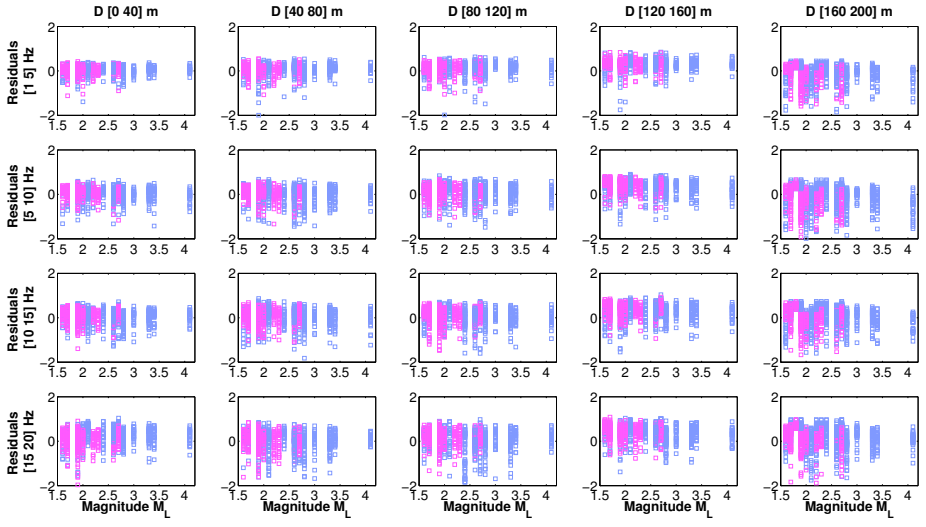

FIGURE 3.34: Amplitude variability residuals of individual estimates of standard deviation of difference of natural logarithm of Fourier spectral velocities for each event with respect to the global median of all the events as a function of magnitude, M_L of the NS component for epicentral distance bins of D [0 100] km and D [100 350] km.

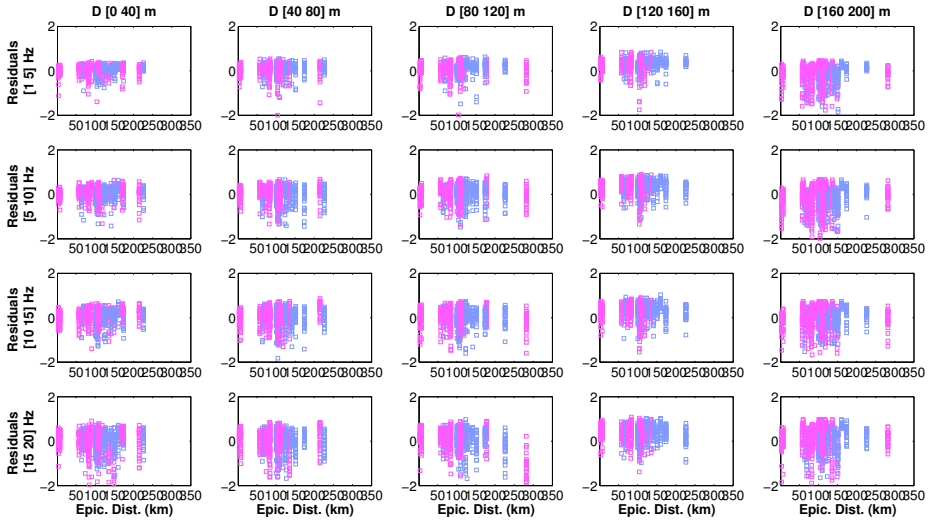

FIGURE 3.35: Amplitude variability residuals of individual estimates of standard deviation of difference of natural logarithm of Fourier spectral velocities for each event with respect to the global median of all the events as a function of epicentral distance of the NS component for magnitude bins of M [1.5 2.5] and M [2.5 4.1].

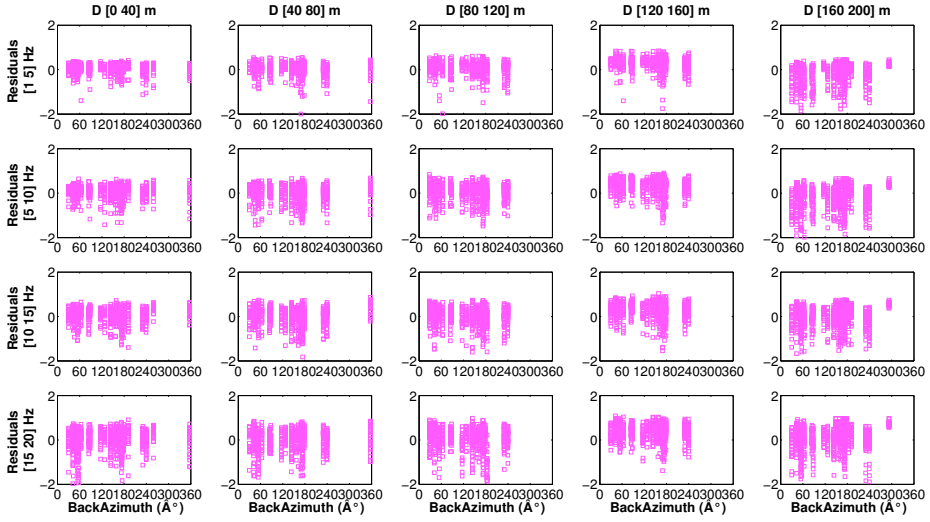

FIGURE 3.36: Amplitude variability residuals of individual estimates of standard deviation of difference of natural logarithm of Fourier spectral velocities for each event with respect to the global median of all the events as a function of back azimuth of the NS component.

Smoothing parameter

For amplitude variability analysis, smoothing is an important parameter that can influence significantly the outcome. To be coherent with previous recent studies (Ancheta et al. [2011]) and allow comparisons, no smoothing was applied to the Fourier spectra for the estimation of the standard deviation of difference in ln(Fourier amplitudes). A sensitivity analysis was performed to give an idea of the importance of smoothing on the evaluation of the indicator. The smoothing parameters were chosen to be the same as the ones for the phase variability analysis, i.e. Hamming window with $M = 5$, for the sake of coherency between the amplitude and phase variability results. Moreover, in past studies (i.e. Schneider et al. [1992]) the same smoothing parameters have been used for the evaluation of amplitude variability and a model was derived based on in situ observations that could be compared with the observations in Saint Guérin.

The results of the standard deviation of difference of ln(Fourier velocity spectra) estimates without and with smoothing are pictured in Figure 3.37. The comparison reveals the importance of smoothing in the analysis; the amplitude variability is strongly damped due to smoothing. Its values, when smoothing is applied, vary from 0.1 to less than 0.8 (120%) while when no smoothing is applied they vary from 0.25 to 1.3 (260%). Nonetheless, the trends of increasing variability with frequency and station separation distance are almost identical. The peaks of variability around the frequencies of vibration of the dam are still identified for the longer station separation distances, despite the damping due to smoothing.

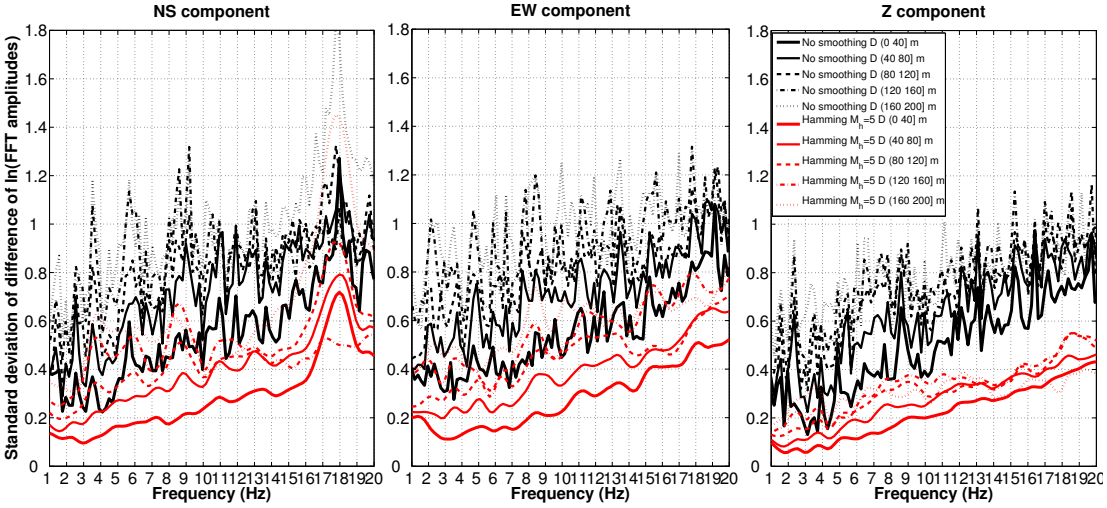

FIGURE 3.37: Comparison of amplitude variability estimates for smoothed (Hamming window $M = 5$) and unsmoothed Fourier spectra for the three components (NS, EW and Z) and for all station separation distance bins at the dam-foundation rock interface.

3.5.3 Comparison with the free field motions

The dense seismological array in Saint Guérin offers the possibility to compare the variability of the motions at the dam-foundation rock interface and in the free field. Similarly to the comparison realized for the lagged coherency estimations, standard deviation of the difference of ln(Fourier velocity spectral amplitudes) are estimated for the free field stations SG13, SG14, SG15, SG17 and SG18. The first three stations can be considered as free field motions that do not incorporate any topographic effects as in the case of the irregular canyon topography of the stations at the dam-foundation rock interface, providing a conclusion regarding the topography effect on SVGM. On the other hand, stations SG17 and SG18, although they may incorporate a small topographic effect due to their small elevation difference, they offer good free field stations without the signature of the dam. In this regard, they can lead to interesting conclusions regarding the soil-structure effect on SVGM.

Only two station pairs are available in each distance bin, i.e in the range of [40 80] m the pairs are SG13-SG14 and SG14-SG15 and in the range of [80 120] m SG13-SG15 and SG17-SG18. In the first distance bin, i.e. [40 80] m, the two available pairs can be combined and one median value can be estimated while in the second distance bin, i.e [80 120] m, the station pairs SG13-SG15 and SG17-SG18 should be studied separately given their different geological locations. Although two pairs in each distance bin may not be sufficient for a robust statistical analysis, the sufficient number of available recordings for the total of the data set (Figure 3.9) allows preliminary conclusions to be drawn that should be confirmed with future studies. The amplitude variability for the two distance bins for the three components of motion at the dam-foundation rock interface and in the free field are compared in Figure 3.38.

The overall trends of the median values of amplitude variability in the free field are comparable to the ones observed at the dam-foundation rock for the three components of motion (NS, EW, Z). In the station separation distance bin [80 120] m, the two station pairs, i.e. SG13-SG15 and SG17-SG18, show almost identical amplitude variability. The motions at the dam-foundation rock interface are slightly more variable in terms of amplitude in both station separation distance bins with respect to free field motions. The difference is more evident for station separation distances longer than 80 m in the whole frequency range studied. From this preliminary analysis, performed based on the limited number of pairs in the free field in Saint Guérin, the slightly higher variability at the dam-foundation rock interface with respect to the free field suggests that the presence of the structure along with the irregular local topography influences SVGM. Nonetheless, further analysis is necessary to confirm this observations.

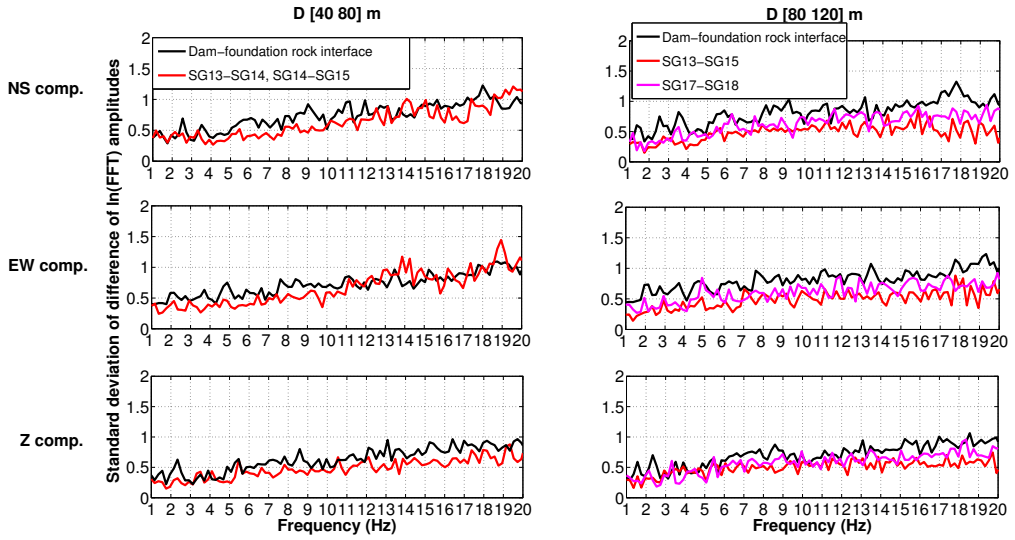

FIGURE 3.38: Comparison of standard deviation of difference of natural logarithm of Fourier spectral velocities in the free field (red lines for SG13, SG14 and SG15 and magenta lines for SG17-SG18) and at the dam-foundation rock interface (black lines) for station separation distances D [40 80] m and D [80 120] m.

3.5.4 Comparison with existing amplitude variability models

Since the amplitude variability of ground motions is not as widely addressed in the literature as phase variability (through coherency), a very limited number of empirical functions for its modeling is available. Due to lack of amplitude variability models calibrated at rock sites, the results based on the data of Saint Guérin dense array are compared with the expression for the standard deviation of difference of natural logarithm of unsmoothed Fourier spectral ordinates (from the $S-$window) proposed by Schneider et al. [1992] and adapted by Ancheta et al. [2011] which is derived based on the LSST and BVDA soil site arrays. Based on the data recorded from the two arrays, the frequency dependency is found to be stronger than the station separation distance dependency. The range of applicability of the model, as proposed by the authors, is from 5 to 100 m station separation distance and frequencies from 0.25 to 25 Hz; same applicability ranges as for the lagged coherency model proposed by tha same authors. The functional form of the model is:

$$\sigma(f) = A(1 - e^{Bf}) \tag{3.8}$$

where $A = 0.93$, $B = b_1 + b_2\xi$ and $b_1 = -0.1005$ and $b_2 = -0.0025$

Figure 3.39 presents predictions of the variation of $\sigma(\xi, f)$ with frequency at each 10 m within the separation distance bins that the model is applicable but also for higher station separation distances, i.e. [0 40], [40 80], [80 120], [120 160] and [160 200] m.

The Saint Guérin amplitude variabilities are also included. As observed, when compared with the observations in Saint Guérin, the model captures the overall variability for all station separation distances (even longer than 100 m that is the limit distance of applicability of the model) and along the whole frequency range for both horizontal components. Within the first 40 m of station separation distances an over-prediction of the amplitude variability is noticed up to 15 Hz; this over-prediction of the variability is underlined by the authors for the LSST and BVDA arrays as well within the first 30 m of station separation distance. Although the model is calibrated based on data coming from soil sites, its predictions are satisfactory for the Saint Guérin observations which consist of hard rock. Schneider et al. [1992] argue that the dependency of amplitude variability on the site conditions is very important. The observation that the amplitude variability in this rock site is comparable to this of soil sites suggests that local topography contributes to a slight increase of the amplitude variability. The presence of a structure with several resonant frequencies with complicated mode shapes, such as the arch dam in Saint Guérin, is possibly the source of additional amplitude variability in the narrow frequency bands around the frequencies of vibration of the dam. This effect becomes more significant for higher station separation distances. However, the fit of the model derived by soil sites to the Saint Guérin observations confirm the conclusion of Schneider et al. [1992] that for the amplitude variability model to be applied on a site specific basis for engineering design, additional research is required.

The standard deviation of difference of the natural logarithm of the smoothed Fourier velocities, as they were estimated and presented in Figure 3.37, are compared with the expression proposed by Schneider et al. [1992]. The original model, that was adapted by Ancheta et al. [2011] as presented above, was derived based on 18 events of the LSST soil site array (station separation distances from 3 to 85 m). The magnitude ranges from 3.7 to 7.8 and the epicentral distance from 4 to 70 km. Based on the LSST data, the frequency dependency is found to be stronger than the station separation distance dependency. The range of applicability of the model is from 6 to 85 m separation distance and frequencies higher than 1 Hz. As underlined, extrapolations to station separations larger than 100 m will result in underestimation of the amplitude variability. Equation 3.9 shows the functional form of the model.

$$\sigma(\xi, f) = 0.93[1 - e^{(-0.16f - 0.0019f\xi)}] \tag{3.9}$$

Predictions of the variation of $\sigma(\xi, f)$ with frequency at each 10 m within the separation distance bins that the model is applicable, e.g [0 40] and [40 80]m, and the measured in Saint Guérin site amplitude variabilities on these distances bins are presented in Figure 3.40. As observed when comparing the observations at Saint Guérin, the model

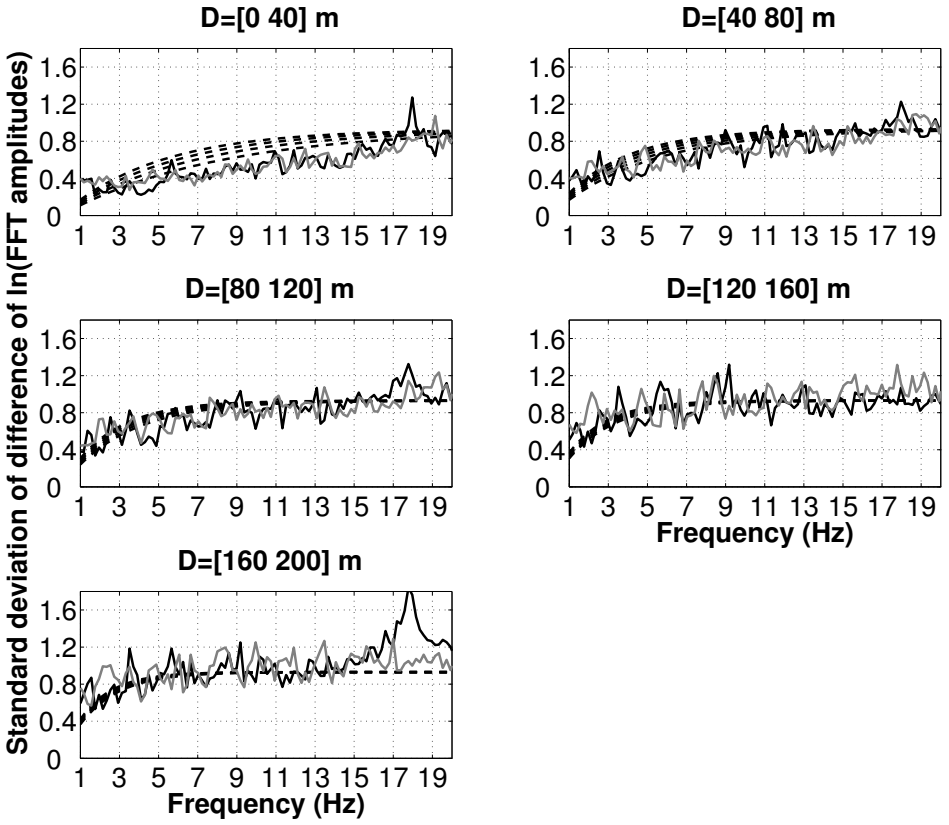

FIGURE 3.39: Standard deviation of difference of natural logarithm of unsmoothed Fourier spectral velocities as a function of frequency; black and gray solid lines represent the median value of all the events within each distance bin along the dam-foundation interface, e.g [0 40] m and [40 80] m, for NS and EW comp. respectively. Black dashed lines represent amplitude variability predictions of the Ancheta et al. [2011] model at each 10 m within the separation distance bins.

captures the overall variability for short separation distances ([0 40] m) up to 15 Hz while it underestimates the amplitude variability with the increase of frequency above 15 Hz for both horizontal components. Although the model's applicability frequency range is up to very high frequencies, it is calibrated based on data up to 15 Hz, thus this could be a possible explanation of the underestimation. The non-dependency of the model on the separation distance becomes evident since there is superposition of the predictions with different separation distances in each distance bin; a slight exponential dependency is imposed by the authors but only from 0 to 5 m thus it cannot be seen herein where predictions after 10 m of separation distance are used. Therefore, the model fails to capture the amplitude variability for station separation distances larger than 40 m.

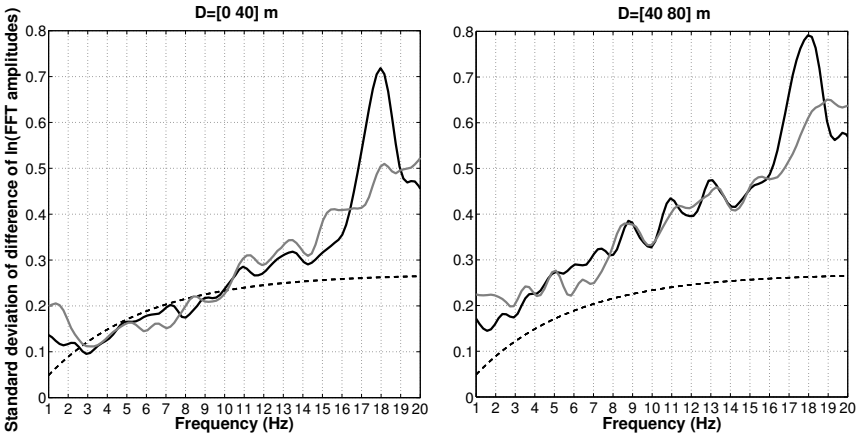

FIGURE 3.40: Standard deviation of difference of natural logarithm of smoothed Fourier spectral velocities as a function of frequency; black and gray solid lines represent the median value of all the events within each distance bin along the dam-foundation interface, e.g [0 40] m and [40 80] m, for NS and EW components respectively. Black dashed lines represent amplitude variability predictions of the Schneider et al. [1992] model at each 10 m within the separation distance bins.

3.6 Discussion

The temporary dense seismological network in Saint Guérin, offers the necessary data (a total of 55 events that are presented in Chapter 2) for a complete SVGM study. This chapter presents an extended spatial variability analysis in the Saint Guérin site based on the in situ seismic recordings. Firstly, the wave passage effect is investigated, by means of time delay between the two time histories of each station pair. Averaging the results of the 55 events, the seismic waves appear to have a preferential backazimuth from the East. This may be explained by the fact that the majority of the events are occurring in the North-East, East and South-East of the dam. Regarding the stations at the dam-foundation rock interface, the observed time delays, varying between 0 and 0.06 sec ([0 16] Hz), do not clearly confirm the preferential propagation from the East to the West bank. The explanation for this phenomenon is the effect of the local canyon topography along with the presence of an engineered structure that complicates the seismic wave field and creates complex time delay patterns. A comparison with the time delays resulting from a vertical propagation, shows that the wave field at the dam-foundation rock is complicated and does not approach a vertical incidence. Vertical incidence is, currently, widely used in engineering applications. Based on our observations, the hypothesis of a single wave direction (azimuth) and apparent velocity (incidence) along an array is not easily applicable in the case of an array located in irregular topography and where soil-structure interaction is also present, such as the one in Saint Guérin.

The phase variability at the dam-foundation rock interface is found by estimating lagged coherency of all possible pairs among stations with separation distances ranging from 13 to 200 m. The $S-$wave part of the seismograms of the 55 events, defined according to the AI, is considered for the variability analysis. Lagged coherency estimates decay with increasing frequency as well as with station separation distance. They start from 1 at very short separation distances and very low frequencies while at the frequency of 20 Hz for the longer station separation distances, i.e. 160-200 m, they reach down to values less than 0.4, pointing out a high aleatory phase variability. The two horizontal components show very similar trends both with frequency and station separation distance while the variability of the vertical component is relatively smaller. Higher phase variability in certain narrow frequency bands is observed which could correspond to the frequencies of vibration of the dam. The observation that the motions are more variable around the frequencies of vibration of the structure suggests that the presence of the structure itself contributes to further loss of coherency. No particular dependency of lagged coherency on source characteristics, i.e. magnitude, epicentral distance and azimuth of the earthquakes, is observed in the available ranges. Comparison of coherencies calculated using different lengths of $S-$wave windows shows that different time windows result in nearly the same averaged values at all distances along the frequency range meaning that when the strong motion part is included in the analysis, the results are robust. This argument is further boosted by the similar coherency values yielding from time windows that include different types of waves in addition to the strong motion $S-$ waves. According to our analysis, coda waves could eventually be used for lagged coherency estimation, leading, however, to an overestimation of the phase variability, while the use of ambient noise is not justified since the estimated variability is not similar to the one of earthquake data. This is because of the difference in the physical causes of ambient noise (atmospheric phenomena such as wind and reservoir motion) with respect to the earthquakes as physical phenomenon.

In the free field the ground motions appear to be slightly more coherent in terms of phase along the frequency range compared to the motions at the interface of the foundation rock with the dam. Around the frequencies of vibration of the dam, there is higher variability at the dam-foundation rock interface which is not observed in the free field. Although the aforementioned two observations suggest that the presence of the structure along with the irregular local topography influence phase variability, the two parameters seem to have only a secondary effect on SVGM, in the examined frequency range, since the overall trends are very similar to the ones of the free field. The majority of the events used for analysis are regional and not local, implying that extended source effects are also not significant. Therefore, it can be suggested that the main cause of spatial variability in Saint Guérin is the scattering effect along the path of the waves while the local site conditions and the source effect are secondary. This conclusion is in

accordance with previous studies regarding small scale sites. The topographic effect is further investigated by separating the two banks of the dam, left and right, that have different inclination. No clear conclusions can be drawn from this analysis, confirming the aforementioned minor effect of the local topography.

Additionally to the lagged coherency, unlagged coherency estimates are provided for not aligned time histories at the dam-foundation rock interface including the wave passage effect. As shown from the time delay analysis, a single wave direction (azimuth) and one apparent velocity (incidence) along the array of Saint Guérin are not easily identified given the irregular topography and the soil-structure interaction. Therefore, plane wave is not calculated. Due to lack of models derived from similar rock sites with canyon topography and the presence of a structure, the lagged and unlagged coherency estimations at the Saint Guérin dam-foundation rock interface are compared with literature models derived from flat arrays. The lagged coherency models proposed by Menke et al. [1990] and Ancheta et al. [2011], the unlagged and the plane-wave coherency model of Abrahamson [2006] are compared with our observations. When the time delay is very small, the plane wave coherency should be very close to the lagged coherency. Regarding the comparison of lagged and plane-wave coherencies, when the plane wave dominates the motions (i.e. lower frequencies), the lagged and plane-wave coherencies are essentially identical for this short distance range. On the other hand, as frequency increases, the lagged coherency, which incorporates also the scattered energy, tends to the median value of noise, whereas the plane-wave coherency tends to zero. Furthermore, we can deduct from the comparison of all the three measures of coherency that, even within a few hundreds of meters, the wave passage effect is not negligible since the three types are not identical. Although no irregular topography or engineered structure are present in the location of the arrays used for the derivation of the literature models used for comparison, they fit in an overall satisfactory way the coherency observations in Saint Guérin. This, further confirms that the effect of the soil-structure interaction and the local canyon topography are secondary causes of SVGM. Based on this study, we argue that lagged coherency models calibrated in plane (flat) free field seismological arrays may be used for the estimation of phase variability of input motions in case of arch dams located in canyon topographies. However, we underline that this conclusion must be confirmed by more, similar experimental campaigns.

The amplitude variability of the motions is evaluated with the standard deviation of the difference of the natural logarithm of unsmoothed Fourier spectra of ground velocities. Similarly to the phase variability, the amplitude variability is higher with the increase of frequency and station separation distance. The amplitude variability of both horizontal components appears to have very similar trends with values varying from 0.25 to 1.3 (indicating higher amplitudes between 20% and 260%) while the vertical component is somewhat lower. No magnitude, source to site distance or azimuth dependence of the

amplitude variability is identified. The importance of the smoothing parameter on the amplitude variability shows that when smoothing is applied, the values of amplitude variability are lower. The comparison of the amplitude variability at the interface and in the free field is also conducted. Slightly higher variability is observed at the dam-foundation rock interface with respect to the free field. The amplitude variability of the unsmoothed Fourier spectra at the dam-foundation rock in Saint Guérin is well represented by the model proposed by Ancheta et al. [2011]. On the other hand, the model of Schneider et al. [1992] for smoothed Fourier spectra fits the Saint Guérin observations only for small separation distances and frequencies lower than 15 Hz due to its non dependency on separation distance. The slightly higher variability observed at the dam-foundation rock interface with respect to the free field along with the acceptable fit of existing amplitude variability models based on flat arrays indicate that, although the presence of the structure along with the irregular local topography influences SVGM, the effect remains limited. The same conclusion was made based on coherency analysis.

Chapter 4

Numerical analysis of the effect of canyon topography and dam-rock interaction on SVGM

This chapter investigates the effect of canyon topography and dam-foundation rock interaction on the spatial variability of the ground motions. To enhance our understanding we use numerical simulations; modeling is necessary in order to break down and investigate each phenomenon independently. A sinusoidal surface topography is implemented in a several kilometre-long site and a parametric study is conducted to get a better insight into the effect of the local canyon topography on the estimation of SVGM. Thereafter, the effect of the presence of an arch dam is attempted to be understood by modeling the Saint Guérin arch dam and a simplified version of its local topography. The results are, then, compared with the in-situ observations of the experimental campaign held in Saint Guérin, as presented in Chapter 3.

We do not know a truth without knowing its cause.
Aristotle, 'Nicomachian Ethics'

4.1 Canyon topographic effect on SVGM

Local site effects is one of the main causes of SVGM (Zerva [2009]). Topographical irregularities (e.g. steep slopes, deep valleys, irregular canyon walls) may perturbate the intensity, the phase content and the duration of ground motions. Complex topography 'works' as a scatterer that may cause either amplifications or reductions of ground motion over short distances. This is the case for canyon topographies that lead to mode conversion, e.g. body-to-surface waves, reflection or diffraction of incident waves and therefore perturbating/complicating the wave field. This physical phenomenon has been attempted to be understood under the hypothesis of elastic behaviour of the soil medium, for different types of incident waves (i.e. SH, SV, P, Rayleigh and Love waves) and shapes of surface topography (i.e. triangular, semi-circular, semi-cylindrical, semi-elliptical and other arbitrary valley shapes). Several studies estimated the effect of topography on amplitude variability of the ground motions (particularly in terms of amplification) (among others Trifunac [1973], Wong & Trifunac [1974], Wong & Jennings [1975], Sanchez-Sesma & Rosenbleuth [1979], Wong [1982], Lee et al. [2009]). The motions at the canyon walls are found to depend on the ratio of canyon width to wavelength, the angle of wave incidence and the wave type. When the wavelength is of the same order as or smaller than the canyon width then the effect of scattering becomes more significant. As a result, the motions at the canyon surface may be either amplified or reduced, depending on the location of the observation point. Generally, motions near the upper corner of the canyon facing the incident wave are found to be amplified and the amplification increases as the wavelength decreases and as the direction of incidence tends toward the horizontal. A schematic representation of the effect of the wavelength with a horizontal angle of incidence is given in Figure 3.10. On the other hand, the amplitude of motions near the bottom of the canyon are reduced with the reduction to be greater when the slopes are steeper. Phase variability is found to be larger near the upper corners of the canyon; however, research on this last topic remains very limited. The motion along canyons with height to length ratio equal or higher than 1 is spatially variable, with a strong frequency (wavelength) dependency. An effort to define an averaged index of input motion variability, due to the topographic effect, based on a simplified representative canyon topography and a realistic incident wave field is presented in this chapter. To this end, a several kilometre-long site with a sinusoidal topography implemented on the free surface is modeled in SPECFEM3D code, which is based on the spectral element method. A seismic excitation, represented by a double-couple point source, is implemented in depth and the variable ground motions, due to the complex wave field, caused by the local topography, are recorded at the canyon walls. A parametric study of different width to length ratios of the canyon is conducted and the spatial variability in terms of amplitude and phase is estimated. Based on this numerical

study, several conclusions can be made regarding the effect of the canyon topography on SVGM.

4.1.1 Numerical modeling of the site

The spectral element method (SEM) is able to simulate elastic-wave propagation in realistic geological structures involving complex free surface topography and material interfaces for two and three dimensional geometries (Komatitsch & Vilotte [1998], Komatitsch & Tromp [1999], Komatitsch et al. [2004], Komatitsch et al. [2005], Chaljub et al. [2007], Peter et al. [2011] etc). SEM is a grid-based method, i.e. a method where the solution of the wave equation is approximated on a fixed grid of points at discrete time steps (Chaljub [2015]). It is a high-order (usually $N \geq 4$) variational method for the spatial approximation of elastic-wave equations that reduces the computational cost, allows an efficient parallel implementation, accounts for topography of the interfaces (mesh adaptivity) while it maintains a low numerical dispersion with only a few number of grid points per wavelength. Its application is based on the Legendre SEM, which has the advantage of leading to a diagonal mass matrix.
The wave equation on a grid point should be solved for all discrete times. The SEM method works on the weak form of the wave equation which is obtained by dotting the wave equation with an arbitrary displacement field and then integrating over the computational domain. First, the computational domain is split into elements, then a polynomial basis on each element to approximate the elastic parameters and the solution of the wave equation is defined followed by a numerical rule to compute the integrals present in the weak form of the wave equation. The choice of elements with tensorized geometries such as hexahedra in 3D is a characteristic of SEM (Chaljub et al. [2007]). The displacement field must be continuous throughout the domain. In regional applications, non-reflecting conditions must be defined at the boundaries of the computational domain to mimic an unbounded medium. To impose the free-surface condition, the surface traction term is canceled and similarly, at the bottom boundary, the traction is replaced by an absorbing condition. The numerical dispersion in the SEM can be maintained at a very low level with 4 to 5 grid points per wavelength. The Spectral Element discretization only applies to the spatial dimension. The way the SEM solution is extrapolated in time is based on a Finite Difference (FD) scheme, where there is an upper limitation in the polynomial.
SPECFEM3D Version 2.0 'Sesame' (Peter et al. [2011]) is an open source software package for local simulations, which implements the SEM method in space and a finite difference method in time. It is freely available via the Computational Infrastructure

for Geodynamics (CIG). SPECFEM3D Version 2.0 'Sesame' can include powerful external meshers, such as CUBIT (Blacker et al. [1994], White et al. [1995], Mitchell [1996], Casarotti et al. [2008]). This tool allows coupled acoustic/(an)elastic simulations.
The model of a rectangular site, having dimensions of 20x30x15 km^3, is developed. Meshing is performed automatically by CUBIT (Blacker et al. [1994]). The size of each hexaedral element is 300 m. The resolution of the mesh enables seismic wave simulations with frequencies up to $\simeq$ 10 Hz. In the near surface, i.e. from 0 to 1.8 km depth, the mesh employs a mesh tripling layer to increase resolution, hence, the size of the elements is reduced to $\simeq$ 100 m. A sensitivity analysis of the results due to the size of the elements was performed. The size of the elements was reduced to 200 m in depth and refined by a factor of 3 near the surface. No influence was identified on the recorded ground motions (visual comparison of the recorded motions in APPENDIX E). Aiming to preserve reasonable computational time, the first model is used, i.e. element size of 300 m.

4.1.2 Site with sinusoidal surface topography

A sinusoidal surface topography is implemented along one horizontal direction (Figure 4.1). In some extents, this approach can be seen as a very simplified representation of a mountain area with parallel valleys. The length of the sinusoidal topography, L, is constant and equal to 2 km. The ratio of height to length, H/L, of the sinusoidal site varies between 0 and 0.5 ($H/L = 0$, $H/L = 0.1$, $H/L = 0.2$, $H/L = 0.33$ and $H/L = 0.5$), i.e. starting from a plane topography towards a canyon topography with steep walls. Therefore, the canyon depth is 0, 200, 400, 660 and 1000 m for the five cases respectively. An example of the simulated model for $H/L = 0.1$ is given in Figure 4.1. Figure 4.2 illustrates the refinement of the mesh at the top layer near the free surface.
Because of lack of information regarding intrinsic attenuation, we use a constant shear quality factor, Q_μ, equal to 100 in the model, which is translated to a damping of 0.5% (Lee et al. [2009] found that synthetic waveforms are not very sensitive to the presence of a low shear Q zone underneath the ground surface). Regarding the velocity profile of the site, the reference bedrock velocity model proposed by Poggi et al. [2011] is implemented in the model. The reference profile is a simplified gradient model with monotonically increasing velocity (i.e. horizontally layered model). This model is representative of the alpine region since it was derived after comparison of velocity profiles from seismic station locations in Switzerland with spectral modeling. citeRefPoggi2011 examined the influence of subsurface structure by considering different wave-speed models (homogeneous, layered and 3D model) concluding that the amplification patterns in all three of

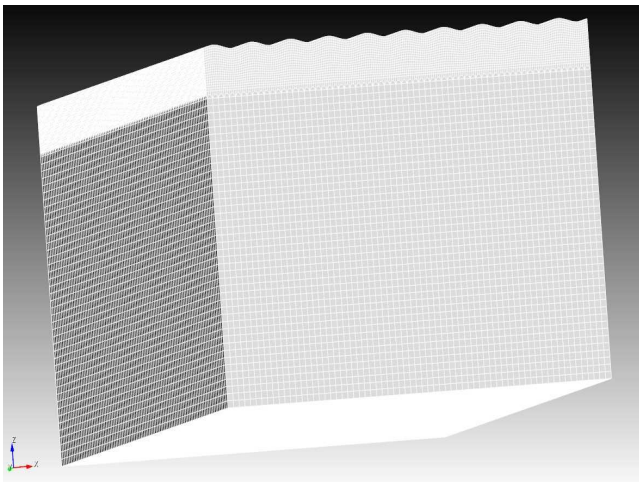

FIGURE 4.1: 20x30x15 km^3 site with sinusoidal topography implemented on the free surface, modeled in SPECFEM3D.

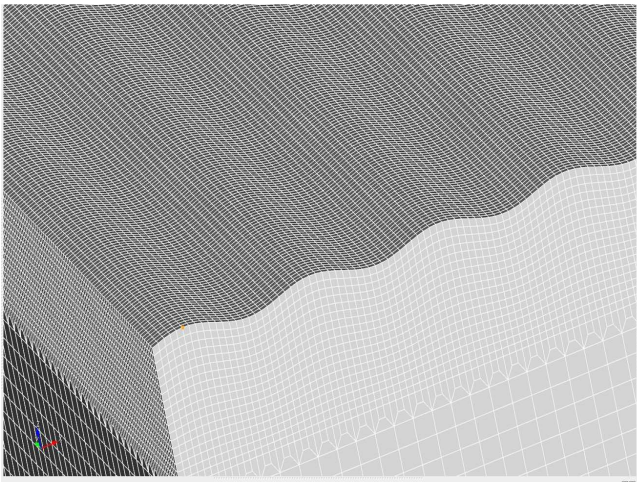

FIGURE 4.2: Refinement with mesh tripling layer of 1.8 km below the free surface of the model in SPECFEM3D.

them are comparable. The functional form of the profile is described in Equation 4.1:

$$V_s(z) = (V_{S,max} - V_{S,min}) * [1 - a^{\frac{z_{top}-z}{b}}] + V_{S,min} \tag{4.1}$$

with $a = 1.30$, $b = 78.16$ and $z_{top} = 0$. The V_P is given as $1.73 * V_S$. Applying the model's functional form, the $S-$wave velocity, V_S, increases with depth from 1000 to 3200 m/s and the $P-$wave velocity, V_P, from 1730 m/s to 5540 m/s in the first 1.5 km below the free surface. In higher depths, V_S remains constant to 3200 m/s and V_P to 5540 m/s. The primary and shear wave velocities as a function of depth are illustrated in Figure 4.3.

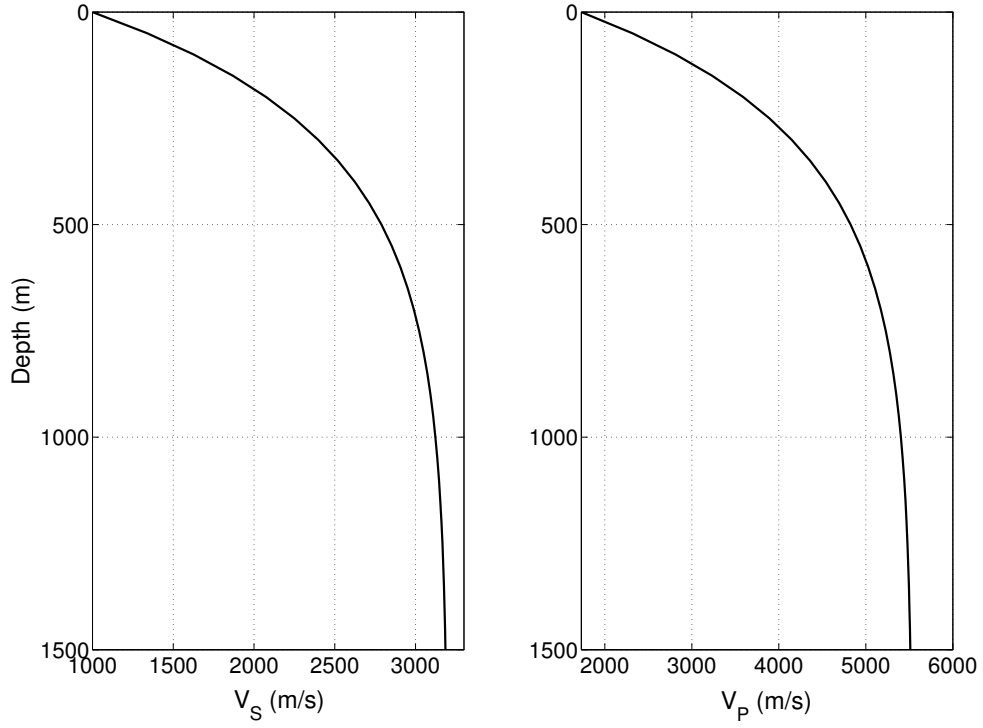

FIGURE 4.3: Reference bedrock V_S and V_P velocity profile (m/s) proposed by Poggi et al. [2011].

4.1.3 Array of receivers and seismic excitation

A dense array of receivers, with inter-station spacing of 25 m, is located linearly along the free surface of the site to record the motions at the canyon walls. The station separation distance of 25 m corresponds to the curvilinear distance along the free surface between two receivers. This means that for each topography, from $H/L = 0$ to $H/L = 0.5$, the total number of receivers is different (increases with increasing H/L). Consequently, in the case of plane topography, i.e. $H/L = 0$, the total number of receivers is 81, in the case of sinusoidal topography of $H/L = 0.1$, 84 receivers, of $H/L = 0.2$, 89 receivers, of $H/L = 0.33$, 98 receivers and of $H/L = 0.5$, 119 receivers. The location of the array of receivers in the case of plane topography ($H/L = 0$) is shown in Figure 4.4 up-left and a zoom in the array of receivers is shown in Figure 4.4 up-right. Similarly, Figure 4.4 down-left and right show an example of the array located in the valley of the sinusoidal topography with $H/L = 0.1$.

The seismic excitation corresponds to a double couple point source with step function time dependence that is located at 10 km depth. It represents a double couple with 22.5 ° strike, 90 ° dip and 0 ° rake angles of a magnitude 2.7 event with a Gaussian source-time function with a half duration of 0.01 sec. The moment magnitude M_0 is

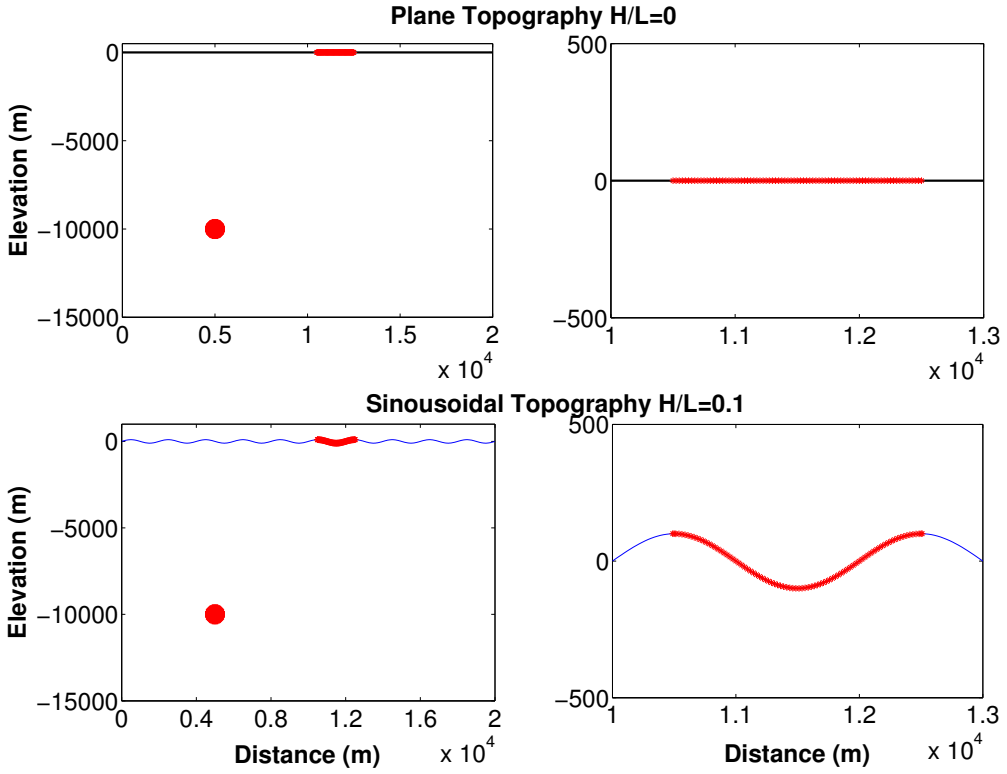

FIGURE 4.4: Location of the array of receivers (red disc) and of the double couple point source (red circle) for a plane ($H/L = 0$) and a sinusoidal ($H/L = 0.1$) topography (left up and down figures). Zoom in to the station array (right up and down figures).

estimated in $N.m$ (Aki & Richards [2002] p.48) as in Equation 4.2.

$$log(M_0) = 1.5M_W + 9.1 \tag{4.2}$$

Then the components of the moment tensor from the strike , dip and rake are computed according to Aki & Richards [2002] p.112.

In Table 4.1 are summed up the characteristics of the point source. The step time function of the source is presented in Figure 4.5. The seismic excitation is situated in 10 km depth and 5 km on the left of the first station of the seismological array. The location of the source in the computational domain is presented in Figure 4.4. Parametric analysis performed by Lee et al. [2009] showed that source depth does not have a significant influence on the amplification observed in a topographic site. A simple parametric study performed herein, showed that modeling sources close to the free surface results to a wave-field very different from this of a deeper source; the P and the S waves are not easily distinguished due to very short arrival time and there is a strong generation of surface (dispersive) waves that can be identified in APPENDIX E, Figure E.2. We consider as more realistic a deeper source, thus we proceed with this

TABLE 4.1: Characteristics of the double couple point source

Strike (°)	22.5
Dip (°)	90.0
Rake (°)	0.0
Magnitude	2.7
Mxx	9.988E12
Myy	-9.988E12
Mzz	0.000
Mxy	9.988E12
Mxz	3.310E-4
Myz	7.991E-4

choice. The displacement field of the source, as it is projected in the far field, has a flat spectrum from 1 to 10 Hz indicating no particular frequency signature of the earthquake; its flat spectrum is presented in Figure 4.5.

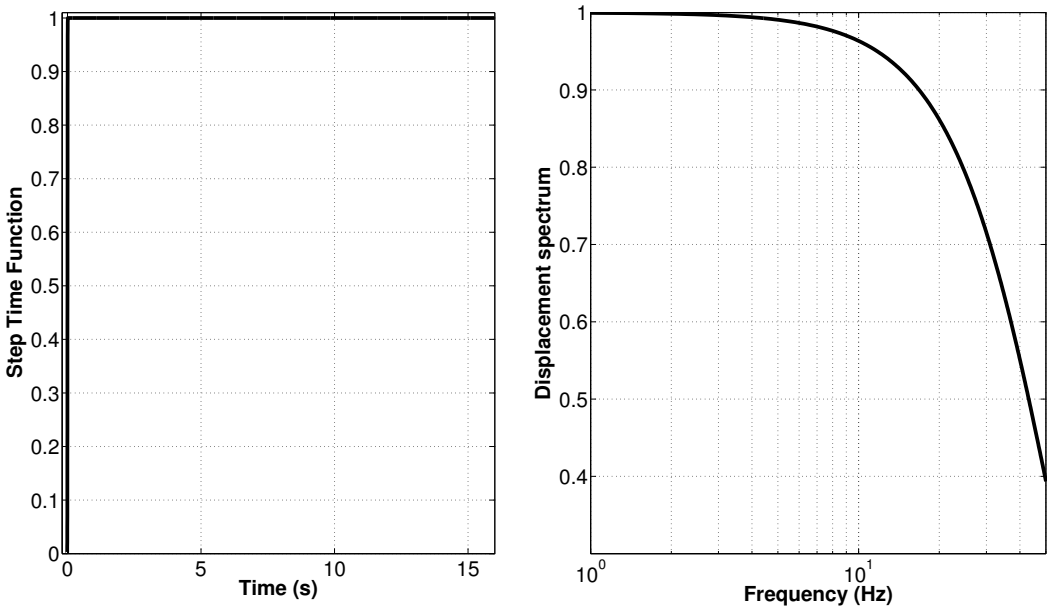

FIGURE 4.5: Step time function in the time domain (left) and theoritical far field displacement spectrum radiated in the frequency domain (right) of the double couple point source.

Since no heterogeneities are introduced in the velocity model, the scattering effect is neglected as a cause of SVGM. Moreover, given that the seismic source is a point and it has a flat spectrum, the extended source effect as a cause of SVGM and the effect of the source frequency content are also absent. Due to the aforementioned, any ground motion variability observed in the free surface should be provoked only by the local surface topography helping up to deeper understand this phenomenon. The use of the flat topography, i.e. $H/L = 0$, could be used as a reference case to verify this assumption.

4.1.4 Ground motions

The velocity time series are recorded from all the receivers at the canyon walls, for all the topographies (from $H/L = 0$ to $H/L = 0.5$). The motions are more energetic in the X horizontal plane, parallel to the sinusoidal topography ($SH-$waves are polarized in the X horizontal plane). The normalized velocity time series at the X horizontal component as a function of their distance following the free surface from the source are illustrated in Figures 4.6, 4.7, 4.8, 4.9 and 4.10 for $H/L = 0$, $H/L = 0.1$, $H/L = 0.2$, $H/L = 0.33$ and $H/L = 0.5$ respectively. The superimposed velocity time histories for all canyon topographies, without normalization, are presented in Figure 4.11. Finally, the aligned time series are also given in Figure 4.12. The alignment is performed using the time lag that leads to the largest correlation of the two ground motions for all frequencies (Boissieres & Vanmarcke [1995a]) and is provided here for a better visual inspection of the motions.

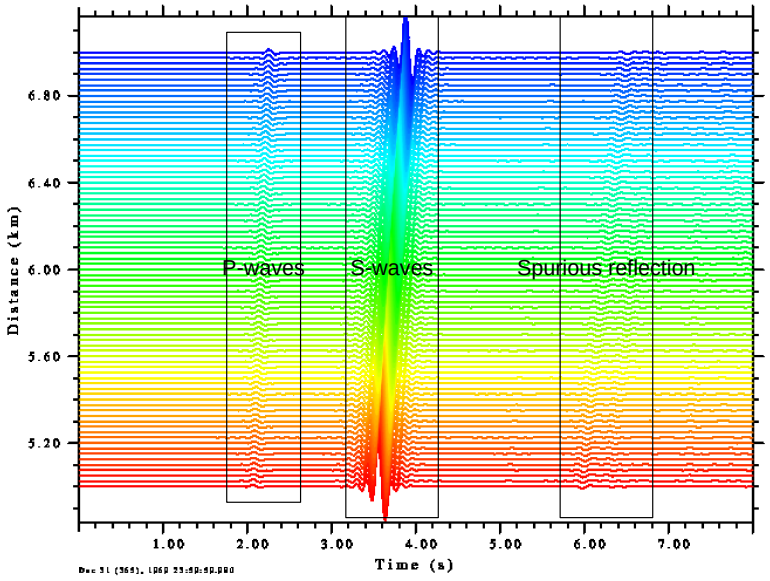

FIGURE 4.6: Normalized velocity time series of the X horizontal component as a function of the distance of the station from the source following the free surface; Plane topography $H/L = 0$. $P-$, $S-$ and spurious reflected waves are pointed.

Given that the V_S at the free surface is 1000 m/s (according to the model of Poggi et al. [2011]) and the frequency domain ranges from 2 to 10 Hz, the wavelength of the $S-$waves ranges from 100 to 500 m ($V_S = \lambda * f$). The canyon depth, for the parametric analysis performed herein, is 0, 200, 400, 660 and 1000 m for $H/L = 0$, $H/L = 0.1$, $H/L = 0.2$, $H/L = 0.33$ and $H/L = 0.5$ respectively. Hence, the wavelength values are of the same order as, or smaller than, the canyon width for almost all cases of canyon

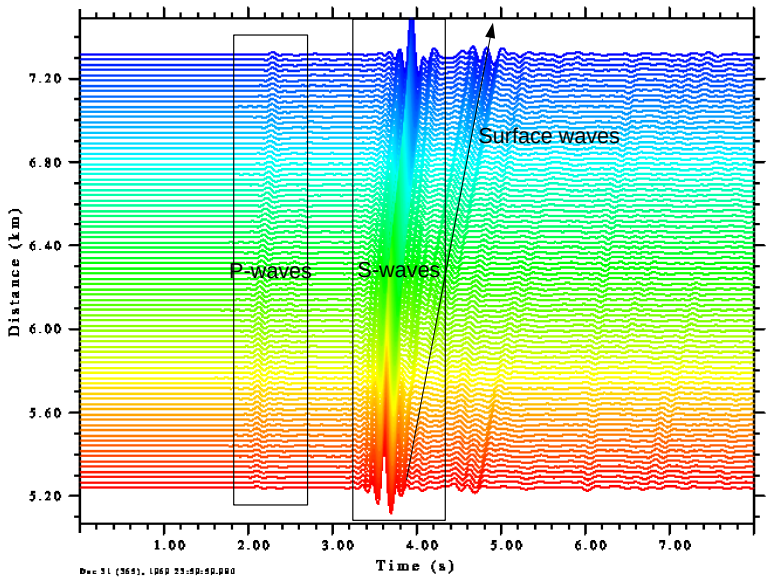

FIGURE 4.7: Normalized velocity time series of the X horizontal component as a function of the distance of the station from the source following the free surface; Sinusoidal topography $H/L = 0.1$. $P-$, $S-$ and surface waves are pointed.

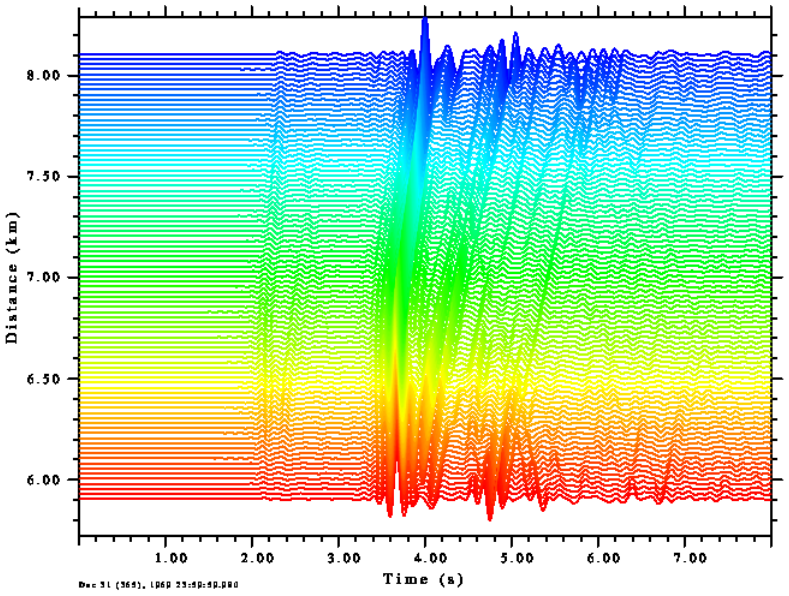

FIGURE 4.8: Normalized velocity time series of the X horizontal component as a function of the distance of the station from the source following the free surface; Sinusoidal topography $H/L = 0.2$.

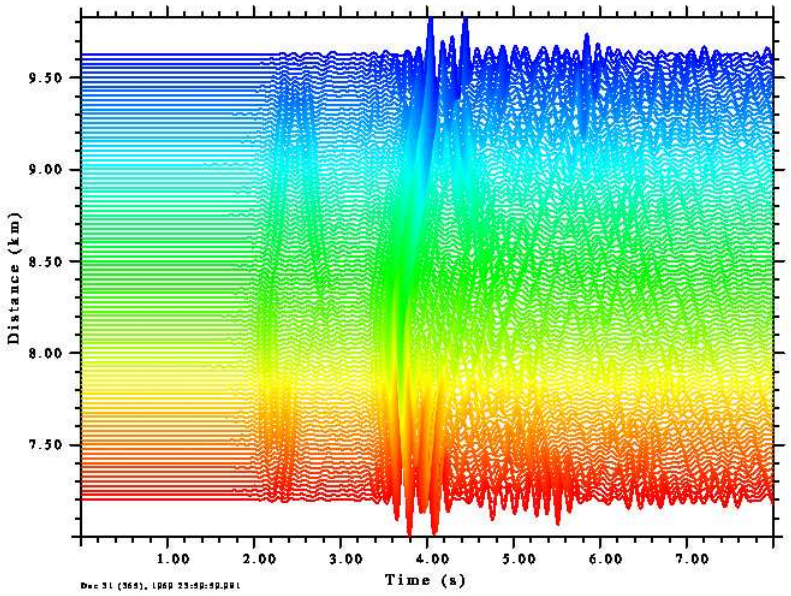

FIGURE 4.9: Normalized velocity time series of the X horizontal component as a function of the distance of the station from the source following the free surface; Sinusoidal topography $H/L = 0.33$.

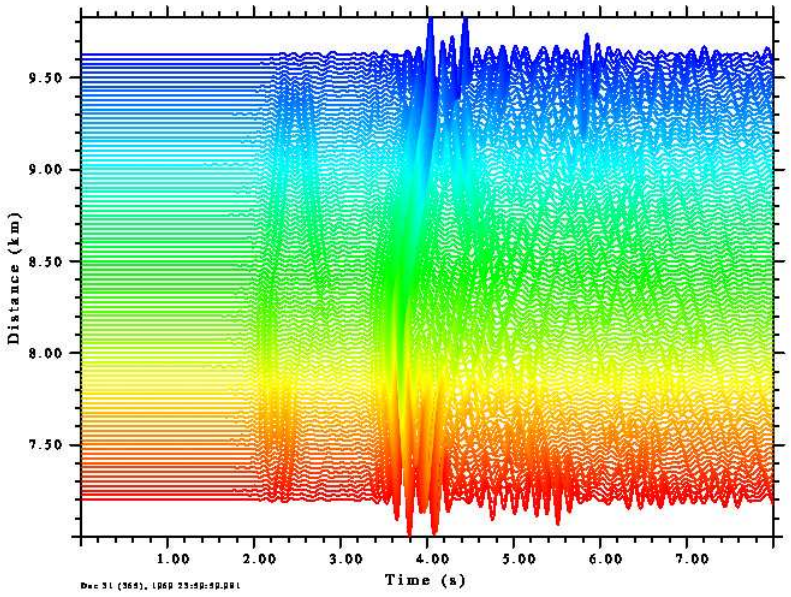

FIGURE 4.10: Normalized velocity time series of the X horizontal component as a function of the distance of the station from the source following the free surface; Sinusoidal topography $H/L = 0.5$.

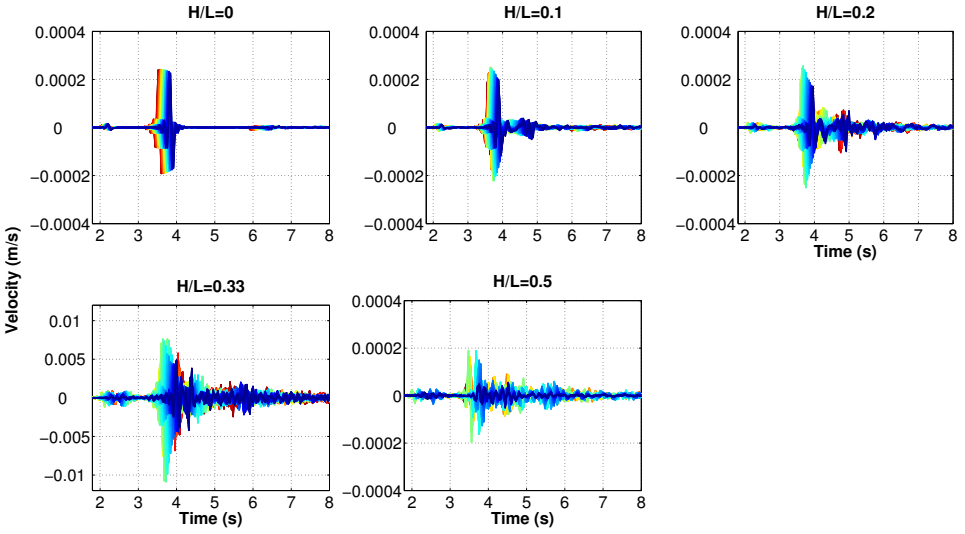

FIGURE 4.11: Velocity time series (m/s) (X horizontal component) of all receivers for all canyon topographies, i.e. $H/L = 0$, $H/L = 0.1$, $H/L = 0.2$, $H/L = 0.33$ and $H/L = 0.5$.

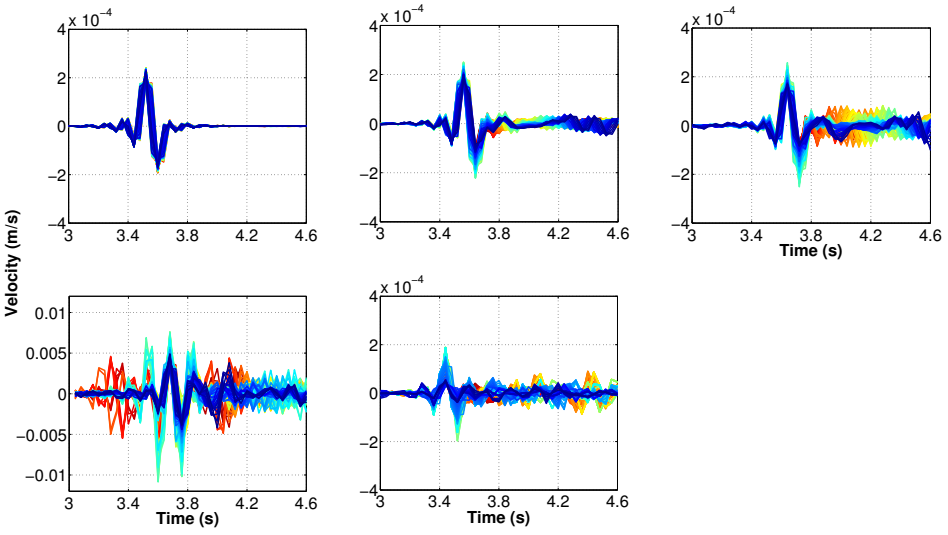

FIGURE 4.12: Aligned velocity time series (m/s) recorded from all receivers for all canyon topographies, i.e. $H/L = 0$, $H/L = 0.1$, $H/L = 0.2$, $H/L = 0.33$ and $H/L = 0.5$.

topographies. As shown from previous studies, when the wavelength is of the same order as or smaller than the canyon width then the effect of scattering becomes more significant leading to phase perturbations and either amplification or reduction of the motions at the canyon surface, depending on the location of the observation point. As observed from the time histories recorded along the array, the presence even of a smooth topography modifies the wave field significantly. In the case of a plane free surface, $H/L = 0$, only direct primary or pressure ($P-$) and secondary or shear ($S-$) waves are propagating along the array (Figure 4.6). The time shift, dt, of these primary arrivals identified in the time series recorded along the surface is due to the wave propagation. The waves arrive firstly in the closest station and propagate along the array; the dt and the incidence angle can be easily calculated knowing the velocity on the free surface and the receiver separation distance. Several seconds later, spurious waves can be seen in the recordings. Introducing steeper canyon walls, i.e. $H/L = 0.1$, results in modification of the wave field because of the generation of surface waves (Figure 4.7). The seismic wave field becomes more complex as the topography becomes more abrupt (steeper canyon walls), i.e. $H/L = 0.2$, $H/L = 0.33$ and $H/L = 0.5$. Additionally to the surface waves, diffracted and reflected waves on the walls of the sinusoidal topography are generated as well as model conversions are occurring (e.g. body-to-surface waves), making the wave field very complex. It can also be noticed that for steeper canyon walls the waves arrive firstly to the receivers at the bottom of the valley and then propagate along the two walls. The aligned time series reveal that the phase content is not very affected by the presence of topography while the impact on amplitude seems to be more important. The quantification of the averaged SVGM in amplitude and phase content along the canyon walls is necessary to conclude regarding the topographic effect on SVGM. In the next sections, the effect of the canyon topography on SVGM will be estimated by decomposing the variability in phase and amplitude differences of the ground motions.

4.1.5 Phase variability analysis

Our ultimate goal is to identify and quantify the phenomenon of wave-field perturbation related to local topography. The in-situ observations in Saint Guérin indicate a possible perturbation of the wave field (via the phase and amplitude variability analysis in Chapter 3) which, however, needs to be further confirmed and better understood. Herein, the influence of canyon topography on SVGM is investigated based on our numerical simulations, by estimating the same indicators as these of the Saint Guérin SVGM analysis. The spatial incoherence is quantified by lagged coherency curves that examine the relation between two signals in terms of phase content as function of frequency and station separation distance. The velocity time series are considered for the analysis. The time

step is 0.008 sec which is decimated to a time step of 0.04 sec to perform the coherency analysis in the frequency range of interest. The procedure followed for the evaluation of the lagged coherencies is the one described in Chapter 3. Briefly, an 11-point ($M = 5$) Hamming window is adopted. With the assumption of stationarity and ergodicity, the $S-$wave part of the seismograms is considered for the coherency function estimation. The chosen window is segmented from the original one by applying a 5% cosine bell window taper at each end (Figure 1.5). It can be observed in the recorded time series that the duration of the $S-$wave, is relatively short (around 1 sec). This is because of the simple, horizontally-layered, velocity profile and the point source located in the near field (few km away from the receivers), which limits the duration of the ground motion to values lower than those observed in Saint Guérin. Abrahamson [2007] proposes that the $S-$wave part may be identified as the time window where the normalized Arias Intensity (AI) of the time series remains within 10% and 75%; the initial time window is 10 sec before and 10 sec after the PGV. Because of the short length of the $S-$wave window of the simulations, the aforementioned 'rule of thumb' is modified according to visual inspection. As we verified in Chapter 3, section 3.4.1.1, as long as the time winodw of analysis contains the strong motion part, the lagged coherency results are robust. Firstly, the PGV is identified and then a window symmetrical from both sides of PGV, before and after, is considered. The length of the window before and after the PGV varies according to the energy content of the signals. For $H/L = 0$ and $H/L = 0.1$, 0.6 sec before and 0.6 sec after the PGV are considered providing a total length of 1.2 sec. For $H/L = 0.2$ and $H/L = 0.33$, 0.7 sec before and 0.7 sec after the PGV are considered providing a total length of 1.4 sec. For $H/L = 0.5$, 1 sec before and 1 sec after the PGV is considered providing a total length of 2 sec. The time window for each topography is chosen by visual inspection and for the steep canyon topographies it includes a small part of contaminated $S-$waves with other types of waves, since their discrimination becomes hard. This approach can be considered realistic, given that no such pure $S-$waves reproduced in simulations exist in reality; usually they are contaminated with other wave types. The chosen $S-$wave windows for all records in all canyon topographies are given in Figure 4.13. The final step before the lagged coherency estimation is the alignment of the two time histories of a station pair using the time lag that leads to the largest correlation of the two ground motions for all frequencies. Thus, the effect due to the wave-passage is removed.

Lagged coherency is estimated for all station pairs at the canyon walls. Equivalently to the analysis followed for Saint Guérin measurements in Chapter 3, the median estimates of lagged coherency of all the available pairs of receivers within a distance bin are computed. Given that the valley is about 2000 m long, five distance ranges are considered, i.e. [0 400] m, [400 800] m, [800 1200] m, [1200 1600] m and [1600 2000] m. The number of available station pairs considered in each distance bin is presented in Figure 4.14 for

the case of flat topography. For the sinusoidal topographies the total number of available pairs is higher, given the higher number of available receivers along the valley. There is a sufficient number of pairs in all distance bins for the conduction of a robust statistical analysis. The analysis is performed for the X component which is perpendicular to the stream (valley). The median lagged coherency estimates of all station pairs grouped per canyon topography are given in Figure 4.15 and grouped per distance bin in Figure 4.16.

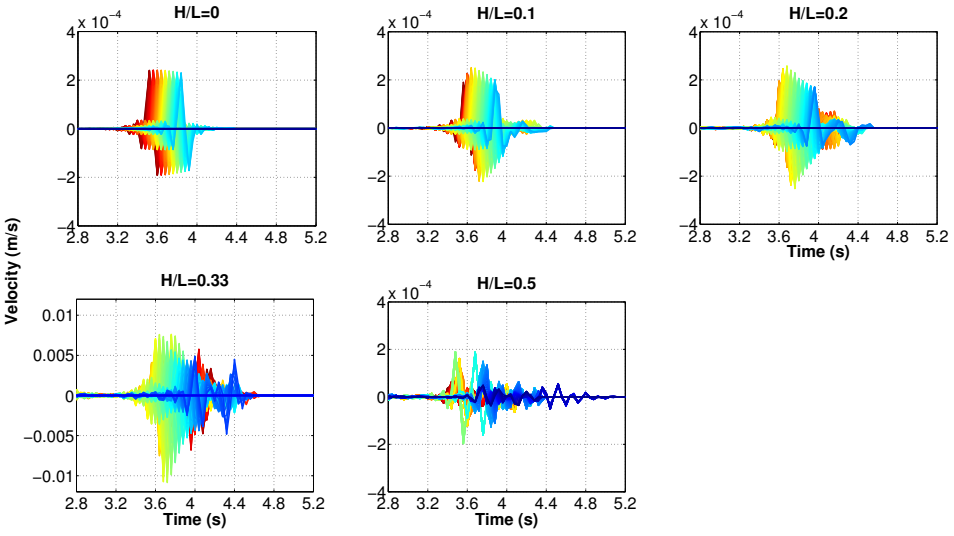

FIGURE 4.13: $S-$wave window selected for all receiver recordings and all canyon topographies, i.e. $H/L = 0$, $H/L = 0.1$, $H/L = 0.2$, $H/L = 0.33$ and $H/L = 0.5$.

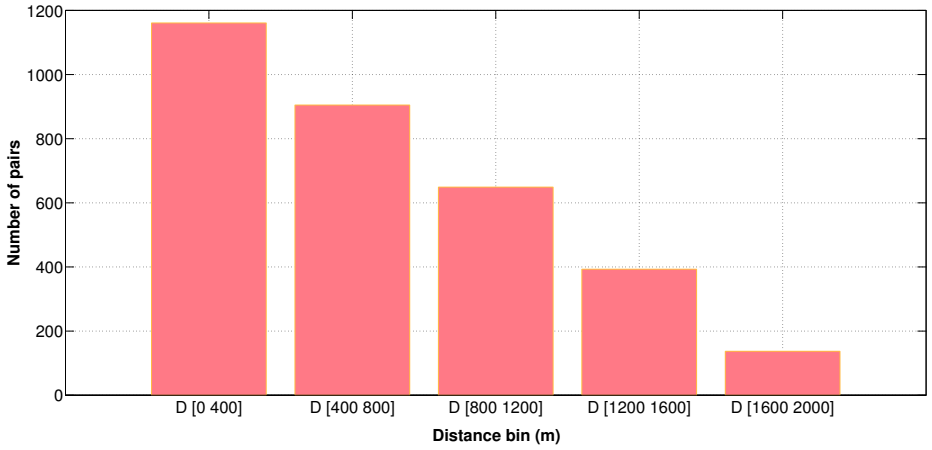

FIGURE 4.14: Total number of receiver pairs in each distance bin (m) at the canyon walls.

The estimated lagged coherency of the $S-$wave window appears to be little affected by the presence of a canyon topography. When no topography exists in the free surface, $H/L = 0$, the lagged coherency of the aligned time series for all receiver separation

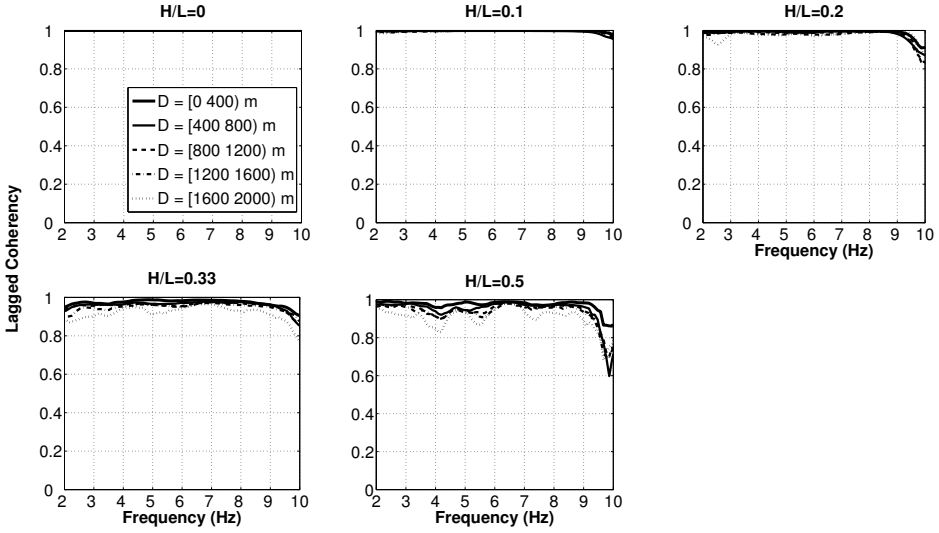

FIGURE 4.15: Median lagged coherency estimates for all distance bins along the valley, i.e. [0 400] m, [400 800] m, [800 1200] m, [1200 1600] m and [1600 2000] m, as a function of frequency for each canyon topography, i.e. $H/L = 0$, $H/L = 0.1$, $H/L = 0.2$, $H/L = 0.33$ and $H/L = 0.5$.

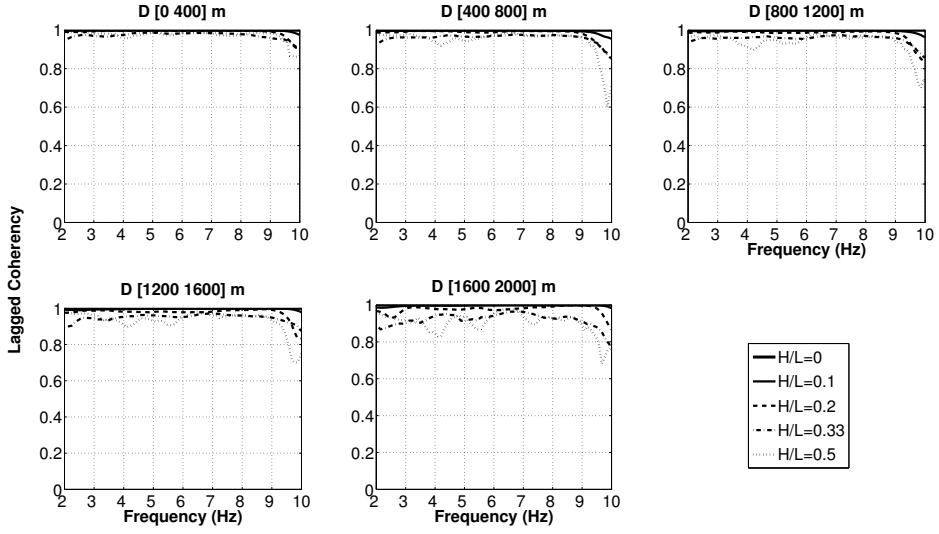

FIGURE 4.16: Median lagged coherency estimates within each distance bin along the valley, i.e. [0 400] m, [400 800] m, [800 1200] m, [1200 1600] m and [1600 2000] m, as a function of frequency for all canyon topographies, i.e. $H/L = 0$, $H/L = 0.1$, $H/L = 0.2$, $H/L = 0.33$ and $H/L = 0.5$.

distance bins is equal to 1, as expected (no causes of SVGM are included in the model). When the sinusoidal topographies of $H/L = 0.1$ and $H/L = 0.2$ are introduced in the free surface, despite the perturbation of the wave field due to the generation-conversion of waves, the phase content of the $S-$waves does not seem to be perturbated (Figures 4.7, 4.8 and 4.12). Therefore, the estimated lagged coherencies are again almost equal to 1. Small reduction of lagged coherency, however, with values that remain higher than 0.9, start to be identified when brutal canyon topographies are introduced to the model, i.e. $H/L = 0.33$ and $H/L = 0.5$. In these cases, although the wave field is very complex and the $S-$wave part is contaminated by other wave types, the lagged coherency is not reduced significantly. Already by visual inspection of the velocity time series, it is observed that topography enriches the wave field with different wave types but does not affect to a large extent the phase content of the most energetic part of the motions, i.e. $S-$waves. This explains the small influence of topography on lagged coherency. The slight loss of coherency for frequencies higher than 9.5 Hz can be explained by the limited resolution of the domain. Overall, lagged coherency is found to decrease with the increase of the H/L. Nevertheless, this parametric study for different canyon topographies points out that the effect of a canyon topography on the aleatory phase variability of the ground motions is very small.

Sensitivity analysis

To find the sensitivity on the duration of the time window of the results, a longer time window is used for analysis. The main influence of the presence of topography, as observed from the recorded time series, is the generation of different wave types which however do not seem to interfere significantly in the phase content of the strong motion part ($S-$wave); this is reflected in the lagged coherency estimates which are higher than 0.9 even for very steep canyon walls. It would be of interest to verify to what extent the coherency is affected if the chosen window includes the converted and generated waves due to topography, hence, the entire signal is chosen for comparison (Figure 4.11). In this case, the analyzed window consists of $P-$waves and $S-$waves for plane topography and $P-$waves, $S-$waves, surface waves, converted, reflected and diffracted waves, coda waves etc. for the canyon topographies. Comparison between the estimated lagged median values in different receiver separation distance bins for the $S-$wave windows and the entire signal is presented in Figure 4.17.

When no or smooth topography is present, i.e. H/L equal to 0 or 0.1, lagged coherency for all receiver separation distances is higher than 0.95. When H/L increases from 0.2 to 0.5, a more significant loss of lagged coherency is observed, reaching down to 0.8 and 0.5 respectively. According to the analysis, the time window selection for the estimation of lagged coherency is important, since only then the effect of topography is observed on the phase variability of the ground motions. This is because many different types of waves

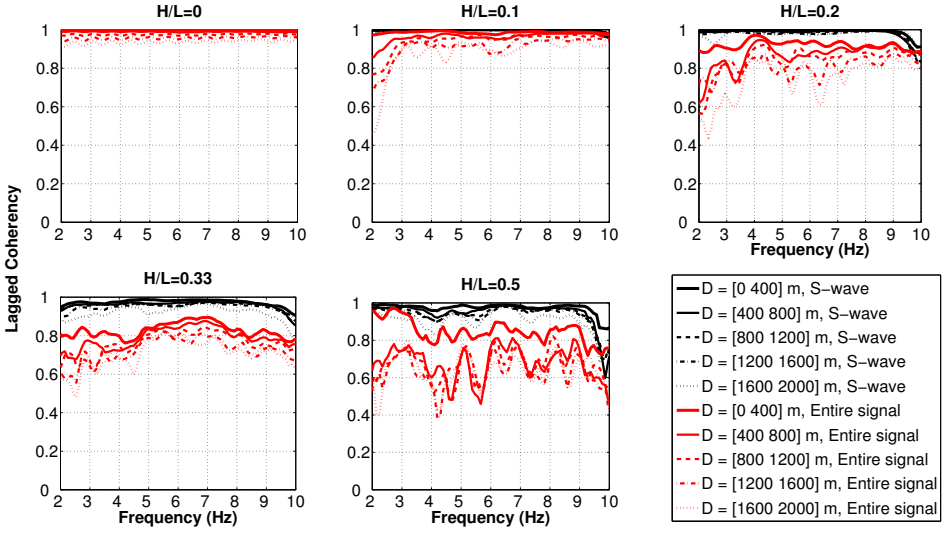

FIGURE 4.17: Comparison of lagged coherency estimates for $S-$wave time windows (black lines) and entire signal (red lines) for all canyon topographies, i.e. $H/L = 0$, $H/L = 0.1$, $H/L = 0.2$, $H/L = 0.33$ and $H/L = 0.5$.

with different phase contents are included in the lagged coherency estimation. As it was pointed out in Chapter 3, if the $S-$wave is predominant in the signal and included in the lagged coherency analysis, the results do not differ significantly (see sensitivity analysis in section 3.4.1.1). On the contrary, if different types of waves are considered for analysis (e.g. surface, scattered, coda waves or ambient noise), the lagged coherency functions appear to change (generally they appear to decrease); that is the case noted herein as well. Particularly in the case of topographical irregularities, the frequency content of the generated waves is not easily predicted so as to estimate its effect on coherency, e.g not only surface waves that are low frequency waves and for which the coherency model is already near unity (Abrahamson [2007]) are included. To be coherent among the analyses and make comparisons possible, we need to be careful on the choice of the time windows considered for SVGM. It is necessary to compare coherencies estimated using the same part of a seismic signal, e.g. $S-$wave part, $P-$wave part, coda part or combination of different types of waves. The $S-$wave part is usually recommended because it is considered as the most energetic and thus the most destructive from an engineering point of view.

4.1.6 Amplitude variability analysis

The quantification of the effect of spatial variability in terms of amplitude differences of the seismic ground motions is realized considering the variability of the Fourier spectra of the motion recorded at different positions along the surface. The unsmoothed Fourier amplitudes in terms of velocity of the $S-$wave window are considered for the analysis.

The difference of the natural logarithms of the Fourier velocities for a given frequency and receiver separation distance is estimated. The amplitude variability estimates are grouped in five separation distance bins, i.e. [0 400], [400 800], [800 1200], [1200 1600] and [1600 2000] m and the standard deviation within each distance bin is calculated. The standard deviation values within each bin at the canyon walls for each canyon topography are grouped and illustrated in Figure 4.18 for the X component. The results are also grouped by distance bin (Figure 4.19).

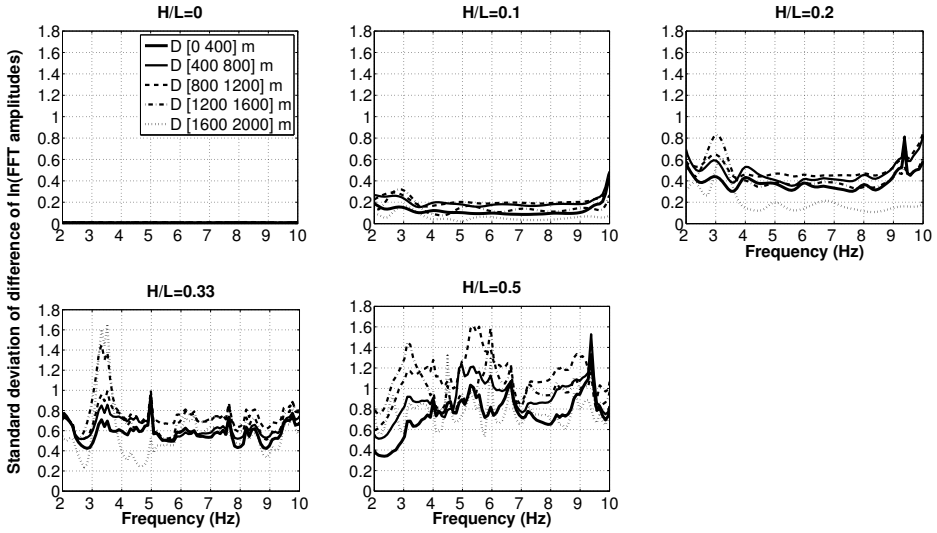

FIGURE 4.18: Standard deviation of the difference of natural logarithm of Fourier velocities of ground motion for all distance bins along the valley, i.e. [0 400] m, [400 800] m, [800 1200] m, [1200 1600] m and [1600 2000] m, as a function of frequency for each canyon topography, i.e. $H/L = 0$, $H/L = 0.1$, $H/L = 0.2$, $H/L = 0.33$ and $H/L = 0.5$.

The amplitude variability is found to increase with the increase of the H/L reaching values as high as 1.6; the steeper the canyon slopes the higher the amplitude variability. When the site is horizontal (flat) there is an almost zero variability; it is slightly higher than 0 for longer receiver separation distances due to the small attenuation included in the model (0.5% damping coefficient). The amplitude variability becomes very important when topography is introduced in the local site. The receiver separation distance dependency is evident with an interesting phenomenon to occur for longer distances, i.e. pairs of receivers consisting of receivers on the two 'mountains' that surround the valley. For all canyon topographies, the amplitude variability increases with receiver separation distance up to a certain distance (up to about 1200 m of inter-station distance) while pairs with longer separation distances show smaller variability. This phenomenon may be explained by the similar in amplitude, strong amplification of the motions at the two 'mountain peaks'. The distance bins [1200 1600] m and [1600 2000] m consist of receiver pairs that are located in the upper corner of the canyon walls where usually, as past studies have shown (e.g. Trifunac [1973], Wong & Trifunac [1974], Wong [1982]), there

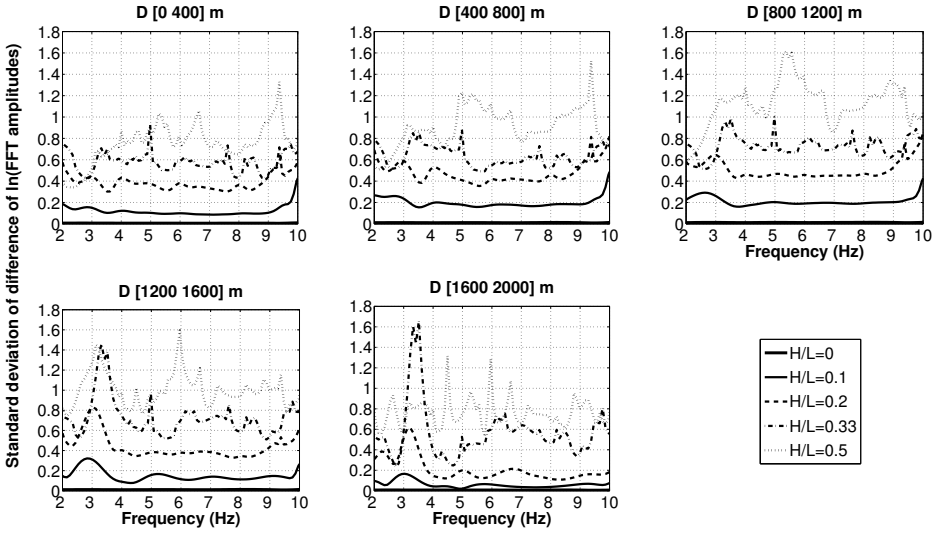

FIGURE 4.19: Standard deviation of the difference of natural logarithm of Fourier velocities of ground motion within each distance bin along the valley, e.g [0 400] m, [400 800] m, [800 1200] m, [1200 1600] m and [1600 2000] m, as a function of frequency for all canyon topographies, i.e. $H/L = 0$, $H/L = 0.1$, $H/L = 0.2$, $H/L = 0.33$ and $H/L = 0.5$.

is amplification of the motions. This may decrease the amplitude variability. Variability is not zero although the valley is symmetrical due to the positioning of the source which is not vertically below the valley but inclined (inclined incidence). On the contrary, pairs consisting of one receiver at the 'peak of the mountain' and one receiver at the bottom of the valley may show higher variability. This is due to amplification of the motions at the upper corner of the canyon and reduction at the bottom of the valley. Overall, the results underline the effect of a canyon topography on the amplitude variability of ground motions.

Sensitivity analysis

As performed for the phase variability, the entire signal is chosen for comparison (Figure 4.11). The analyzed window consists of $P-$waves and $S-$waves for plane topography, $H/L = 0$, and $P-$waves, $S-$waves, surface waves, converted, diffracted waves etc. for the canyon topographies. Comparison between the two cases in different receiver separation distance bins is presented in Figure 4.20. When no topography is present, amplitude variability for all receiver separation distances is around 0 (slightly higher due to the attenuation). The result is the same either the entire signal or just the $S-$wave part is used since in flat topography there is only the $P-$ and the $S-$wave propagating along the array. When H/L increases, amplitude variability becomes more important, reaching values as high as 1.8 for very steep canyon walls, i.e. $H/L = 0.5$. The overall trends of variability seem to be very similar for both cases of time windows, entire signal or $S-$wave window; however, when the entire signal is used the amplitude variability is

higher with a difference of about 0.2. This is possibly due to the strong contribution of different types of waves, as explained for the phase variability in the previous section. Contrarily to the phase content though, amplitude apparently is much more affected; this can easily be observed with visual inspection in the records presented in Figure 4.13. Generally, confirming the conclusions of phase SVGM of this parametric analysis and the conclusions in Chapter 3, when the stronger part of the motions is included in the window of analysis, i.e. the shear wave, the amplitude variability is robustly estimated as long as it is not significantly altered. In the last case that the $S-$wave is considerably changed from other types of waves, when the canyon topography becomes abrupt, the amplitude variability depends on the time window choice.

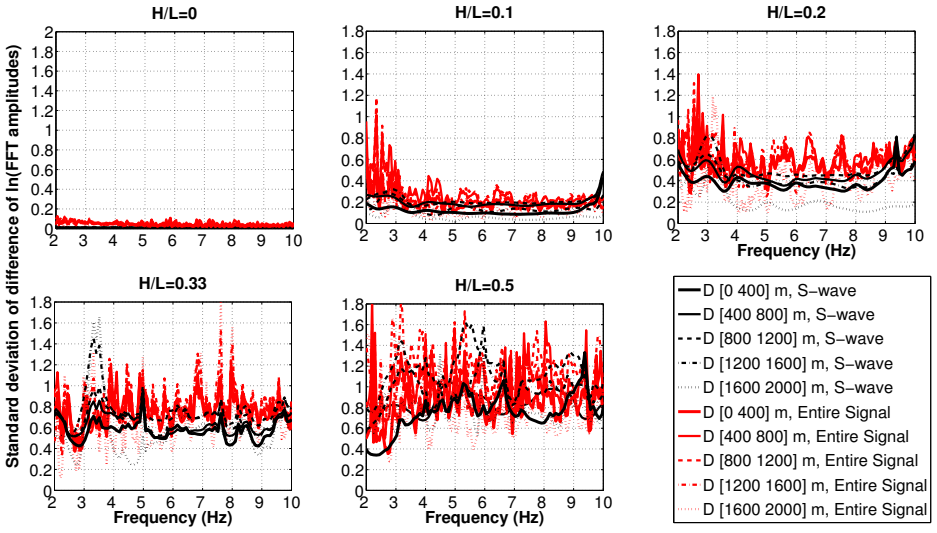

FIGURE 4.20: Comparison of lagged coherency estimates for $S-$wave time windows (black lines) and entire signal (red lines) for all canyon topographies, i.e. $H/L = 0$, $H/L = 0.1$, $H/L = 0.2$, $H/L = 0.33$ and $H/L = 0.5$.

4.2 Arch dam-foundation rock interaction effect on SVGM

Nonuniform ground motions may arise from the interaction between an engineered structure implemented in the complex topography and its foundation soil/rock. The interaction of arch dams constructed in canyon topographies is such an example that contributes to the perturbation of the incident wave field. The soil-structure interaction effect is due to the mass and rigidity of the foundation of the dam. This phenomenon is much less addressed in the literature with respect to the canyon topographic effect. The absence of very dense seismological instrumentations that could provide the necessary data for a deeper understanding and quantification of the effect of the interaction on SVGM, makes the task more difficult. Nevertheless, it is suggested that it may be significant

and it merits further and deeper research. The goal of the present chapter is to investigate the decoupled and then combined effects of the canyon topography and the arch dam-foundation rock interaction on SVGM. Ideally, in-situ seismic measurements before and after the construction of an arch dam on a canyon topography would be necessary. Initially, without the existence of the engineered structure, the effect of the presence of a canyon topography may be estimated by comparing the motions at the canyon walls and in the horizontal surface free field. This would provide the changes on SVGM because of the canyon topography with respect to SVGM in the plane free field. Thereafter, with the construction of the dam, the modification of the ground motions due to the presence both of the topography and of the structure could be deducted. However, decoupling the various causes of SVGM in-situ (site, path and source effects) is not an easy task. Numerical simulations of a site and of the dam is a useful tool to break down and investigate each phenomenon independently. The effect of the topography without and with the presence of an arch dam, excluding source and path effects (excluding complex effects such as rutpure kinematics on extended fault or scattering due to heterogeneities along the path), on SVGM is addressed using numerical simulations.

4.2.1 Numerical modeling of the site and the arch dam

Using the code SPECFEM3D (Peter et al. [2011]), which is based on the spectral element method (Komatitsch & Vilotte [1998]), the Saint Guérin arch dam and a simplified surrounding site are modeled with hexahedral elements. The dimensions of the domain are 20x30x15 km^3, the same as the domain used in the previous section. The resolution of the mesh enables seismic wave simulations with frequencies up to approximately 10 Hz; the size of the elements is around 300 m in depth. Near the surface ([0 1.8] km depth), the mesh employs a mesh tripling layer to increase resolution e.g the size of the elements is reduced to around 100 m or less. The canyon topography and the arch dam are accurate representations of the real arch dam and canyon topography in Saint Guérin while the surrounding alpine topography is not reproduced due to its complexity. The canyon is modeled with constant cross section till the edges of the domain up-stream and down-stream. The arch dam is implemented in the model in the middle of the domain, on the free surface, 10 and 15 km for X and Y coordinates respectively. The model follows the real dimensions of the arch dam, i.e. length of 200 m and height of 69 m. Given its small dimensions with respect to the rest of the site, the meshing of the dam is finer, with an average element size of 15 to 20 m. The numerical model of the entire site is illustrated in Figure 4.21 along with the local canyon topography, the location of the arch dam and a zoom in the arch dam. Additionally, in the same figure

is provided the name of nodes at the dam-foundation rock interface and on the crest for both up-stream and down-stream directions.

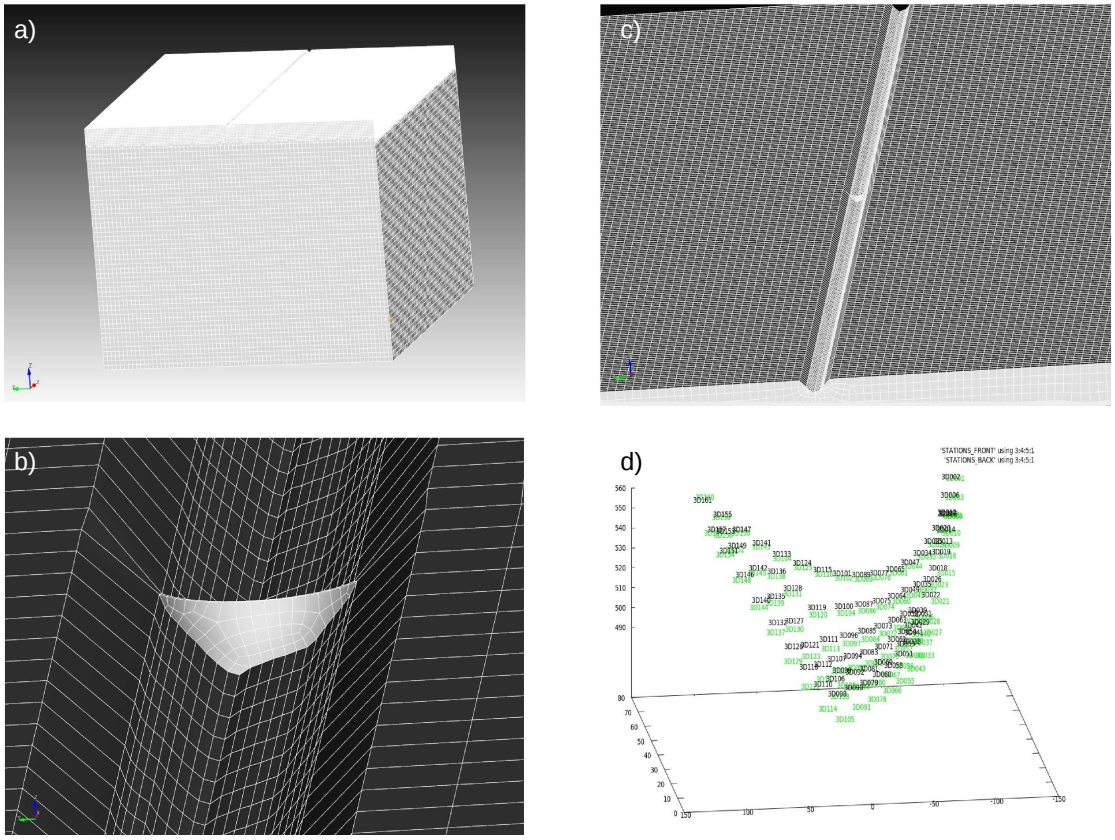

FIGURE 4.21: SPECFEM3D model of 20x30x15 km^3 site, Saint Guérin local canyon topography, arch dam and name of nodes at the dam-foundation rock interface and on the crest (up-stream nodes represented by black and down-stream nodes by green color).

4.2.2 Site and arch dam characteristics

The velocity model adopted is the reference bedrock velocity profile proposed by Poggi et al. [2011], described from Equation 4.1 and presented in Figure 4.3. The $S-$wave velocity, V_S, of the foundation rock varies between 1000 et 3200 m/s and the $P-$wave velocity, V_P, varies between 1730 m/s and 5540 m/s in the first 1.5 km below the free surface. In higher depths V_S and V_P remain constant, i.e. 3200 m/s and 5540 m/s respectively. The damping coefficient of the domain is 0.5%. The V_S of the concrete is considered to be constant and equal to 2600 m/s and the V_P equal to 4000 m/s. The density of concrete, rho, is considered equal to 2500 kg/m^3. Applying the Equations 4.4, 4.4 and 4.5, the Young's modulus, E, is calculated as 38.4 GPa. The damping coefficient of the arch dam was kept the same as for the rest of the domain, i.e. 0.5%. The effect of the reservoir has not been included in the model but it, undoubtedly, is a

very interesting prospect.

$$V_P = \sqrt{\frac{M}{rho}} \tag{4.3}$$

$$V_S = \sqrt{\frac{G}{rho}} \tag{4.4}$$

$$E = \frac{G(3M - 4G)}{(M - G)} \tag{4.5}$$

The seismic excitation corresponds to a double couple point source with step function time dependence (Figure 4.5) that is situated at 10 km depth below the arch dam (its horizontal coordinates, X and Y, are 10 and 15 km respectively). It represents a double couple with 45 ° strike, 90 ° dip and 0 ° rake angles of a magnitude 2.7 event. It generates several types of incident waves, i.e. $P-$waves, $SH-$waves and $SV-$waves. The location and the strike of the point source are different from the ones used for the sinusoidal topography simulations (location not below the array but inclined and strike equal to 22.5 °). The goal in this part of the analysis is to impinge the dam with a vertically incident strong motion wave with equal energy at the two horizontal components.

4.2.3 Ground motions

The time histories due to the seismic excitation are recorded in every node at the dam-foundation rock interface and, when the arch dam is included in the simulation, at all the corners of the hexahedral elements of the dam as well. The velocity time series at the interface without and with the presence of the arch dam are illustrated in Figure 4.22. A zoom in the first few seconds of recordings is also provided in the same figure. Similarly, the velocity time series on the crest of the dam are provided in Figure 4.23. Due to dam's rigidity, the recordings at the up-stream and down-stream face are identical, therefore only one of the two is presented herein, the down-stream direction.

Observing the time histories recorded along the canyon walls, without the presence of the dam, we notice an $S-$wave pulse propagating from the bottom of the valley (light blue corresponds to observation points/nodes at the bottom of the valley) towards the two mountain peaks (dark blue and red colour correspond to the two canyon edges). Comparing these records with the records when the surface topography is plane (Figure 4.11), the simple canyon topography hardly perturbates the wave field. The amplification of the motions at the two peaks with respect to the bottom of the valley is evident. When the arch dam is included in the model, the modification of the wave field is more significant, with several types of waves interfering and the duration of the seismic motion to last longer. On the dam's crest, the amplification of the motions on the middle of the

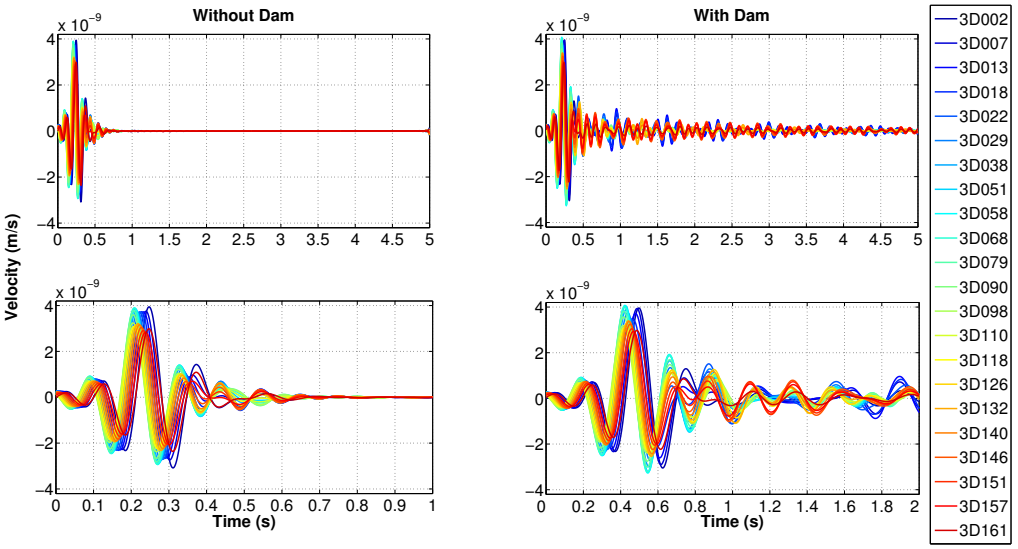

FIGURE 4.22: Velocity time series recorded from the array along the canyon without and with the arch dam; entire signal and zoom in of the records from 0 to 1 or 2 sec.

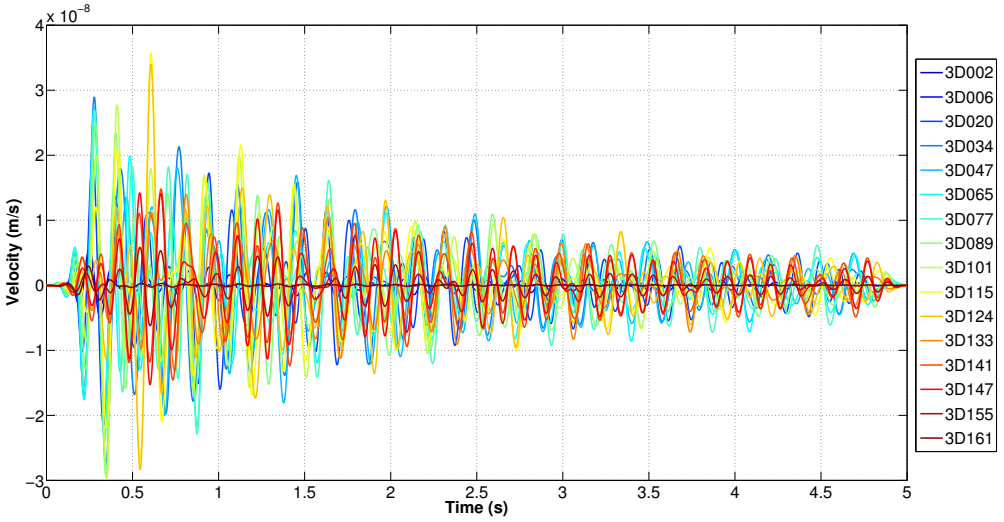

FIGURE 4.23: Velocity time series recorded from the array along the dam's crest.

dam with respect to the abutments and, evidently, its bottom can be easily identified (Figure 4.23).

4.2.4 Dynamic analysis of the arch dam

The resonant frequencies of the dam during the seismic event may be identified using the unsmoothed Fourier spectra of the time histories of the receivers located on the crest and at the dam-foundation rock interface. Contrary to the in-situ recordings where ambient noise data are available for identification of the vibration frequencies, in the numerical model no such data are available. However, given the broadband spectrum of the excitation (Figure 4.5), the identification of the vibrational frequencies using the motions during the seismic excitation are representative since no signature of the earthquake will perturbate the result. The velocity time series are decimated to have a time step of 0.02 sec, the same as the *dt* of the in-situ time series. As presented in Figure 4.24, the resonant frequencies of the structure, as identified from the crest receivers, in the frequency range that the resolution enables robust analysis, are about 4.1, 5.9, 7.3, 8.7 and 9.6 Hz. Obviously, depending on the position of the point of observation on the crest, some frequencies of vibration are better 'captured' (more amplified) at this point than others, which could give a rough idea of the corresponding modes. The first two values of frequencies of vibration are shifted ± 0.1 Hz according to the point of observation. The vibration frequencies are still clearly identified at the dam-foundation interface with an interesting phenomenon occurring around them. A sudden cut-off of the Fourier spectral amplitudes is occurring at the frequencies of vibration, as they are identified on the crest. This sudden cut-off could be explained by the destructive interference due to the impedance contrast between the foundation rock and the concrete medium constituting the dam. An interference may occur between two (or more) waves: herein, between the waves trapped in the dam (due to the impedance contrast with the foundation rock) and travelling either vertically or horizontally. These interferences create standing waves, i.e. the eigen modes of the dam. Constructive interferences form the maximum of the modes (i.e. peaks in the Fourier spectra), and destructive interferences form the nodes ('cut-off' in the Fourier spectra). Evidently, the 'cut-off' effect for a given frequency (mode) is occurring only close to the nodes of this mode thus the effect is observed in the corresponding Fourier spectra of the receivers at these locations (nodes) and not from all the receivers at the interface. This is the reason for which the median Fourier spectrum of all the spectra at the interface does not clearly show the frequency peaks.

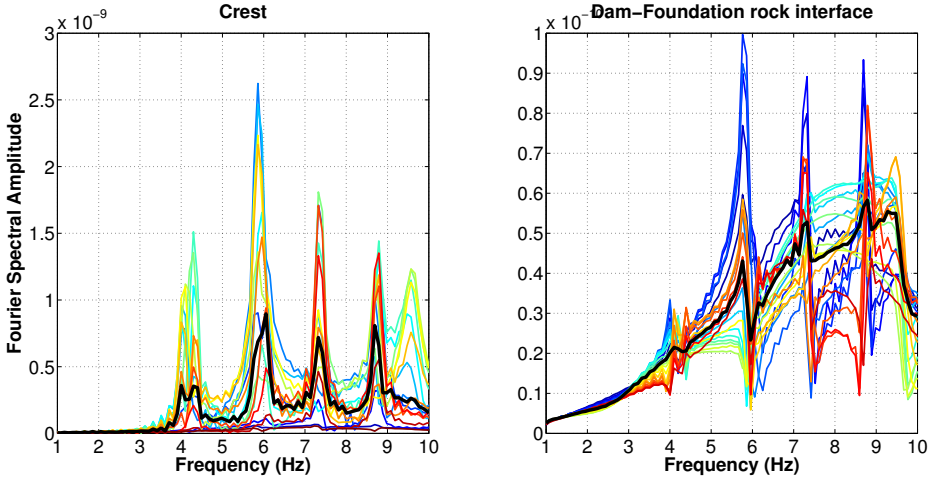

FIGURE 4.24: Eigen frequencies of the model of Saint Guérin arch dam estimated using a double couple point source; Fourier spectral velocities of the receivers on the crest and at the dam-foundation rock interface for the X component; black lines correspond to the median value of all spectra on the crest and at the dam-foundation rock interface.

4.2.5 Phase variability analysis

Lagged coherency between all receiver pairs is estimated at the dam-foundation interface of the model when the arch dam is present and at the same receivers along the canyon walls when the arch dam is not included in the model. The analysis is performed for the X component. An 11-point ($M = 5$) Hamming (spectral) window is adopted. The duration of the strong motion, i.e. $S-$wave, is very short (much less than 1 sec) not providing a sufficient number of points for the coherency estimation. Because of the short length of the $S-$wave window, we are obliged to use an elongated window. The first 2 sec of records are considered for the lagged coherency analysis which include a part of contaminated $S-$waves with other types of waves. This approach is considered realistic, given that in reality $S-$waves are usually contaminated with other wave types. As shown with the sensitivity analysis in Chapter 3, as long as the $S-$wave is included in the time window of analysis, the lagged coherency estimates are robustly estimated. The chosen window is segmented from the original one by applying a 5% cosine bell window taper at each end (Figure 1.5). The two time histories for each pair of receivers are aligned using the time lag that leads to the largest correlation of the two ground motions for all frequencies. Thus, the wave-passage effect is removed. The receiver pairs are grouped in the same receiver separation distance bins as for the case of Saint Guérin measurements, i.e. [0 40] m, [40 80] m, [80 120] m, [120 160] m and [160 200] m. The lagged coherency estimates when the dam is included in the model within each distance bin along canyon walls are calculated. Then the estimates are compared with the results without the presence of the arch dam. The median values of lagged coherency estimates in each distance bin for both cases are grouped in Figure 4.25.

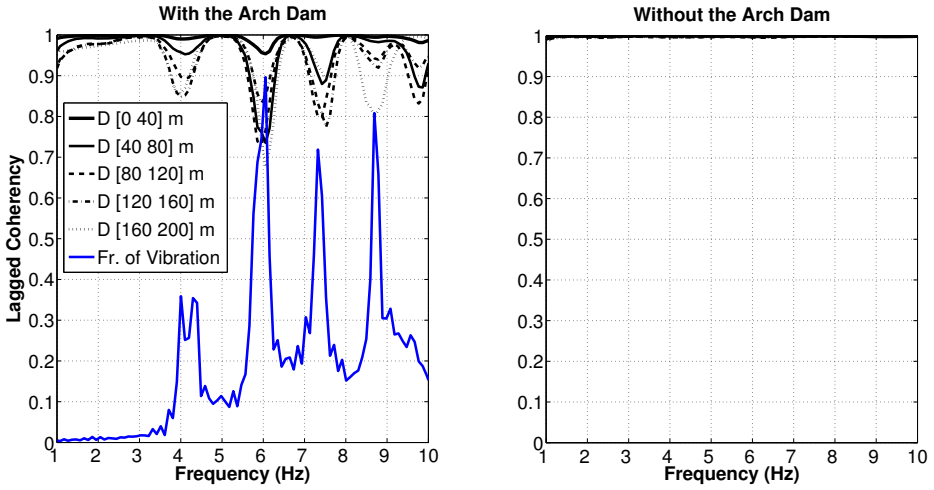

FIGURE 4.25: Comparison of median value of lagged coherency within each distance bin along canyon walls, i.e. [0 40] m, [40 80] m, [80 120] m, [120 160] m and [160 200] m without and with the presence of the dam (black lines); the blue line represents the frequencies of vibration at the dam-foundation rock interface as estimated on the crest.

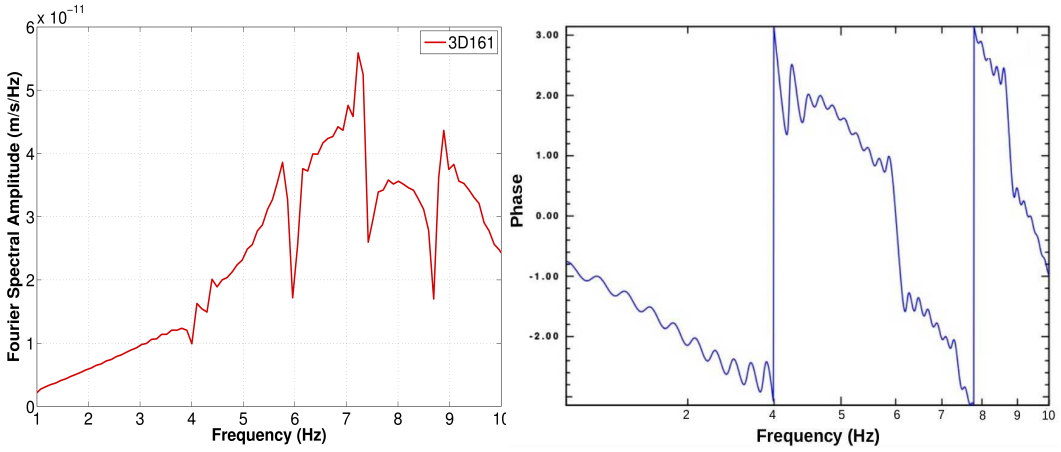

FIGURE 4.26: Fourier spectrum and phase as a function of frequency for receiver 3D161 at the dam-foundation rock interface (left abutment).

When the arch dam is included in the model, the overall loss of coherency with the increase of frequency is negligible; the receiver separation distance dependence is clearly identified. The non dependency on frequency is explained by the lack of other sources of incoherence in the medium, apart from the presence of the structure and the local topography. This explanation is confirmed from the model without the arch dam, where lagged coherency is equal to one for all distance bins in the frequency range of study. From the model without the arch dam, no loss of coherency is linked to the presence of the simple irregular topography. The simple canyon is not enough to create phase perturbations of the strong motion as it is seen already in the time histories. As shown in the previous section, phase perturbations are very limited even in the case of brutal topographies with several 'continuous mountains'. On the other hand, a clear loss of

coherency is observed around the five frequencies of vibration of the dam, as they are identified in Figure 4.24 and represented by the blue line in Figure 4.25 (median value). The brutal loss of coherency signifies a sudden change of the phase content; such an example is provided in Figure 4.26 for one of the receivers at the interface. Rapid phase change is occurring around 6, 7.5 and 8.8 Hz (note that the other two apparent changes around 4 and 7.8 Hz are fictitious, i.e. they are due to the fact that the phase is periodic between $-\pi$ and $+\pi$ and if we 'unwrap the phase', it would be continuous and smoothly varying around these frequencies. As the Fourier spectrum of this receiver shows, it is close to a node of the dam where resonant frequencies around 6, 7.5 and 8.8 Hz are identified and a 'cut-off' due to the destructive interference is occurring, as explained above. Thus the destructive interference that causes 'cut-offs' in the Fourier spectrum is also accompagned by brutal phase changes. The brutal phase change is responsible for the drop of lagged coherency around these frequencies. Based on this study, lagged coherency appears to be sensitive to the soil-dam interaction but not to the canyon topography. The last conclusion is in accordance to the parametric study performed earlier in this chapter (Figure 4.16). In Chapter 3, our observations based on the Saint Guérin seismic data suggested that around the frequencies of vibration the lagged coherency is lower, i.e. higher phase variability; however, the effect was not clearly identified and the reasoning of this hypothesis needed to be sufficiently supported by deeper understanding of the phenomenon. The numerical simulations confirmed our initial hypothesis and explained its physical reasons, i.e. destructive interference caused by the soil-structure interaction.

4.2.6 Amplitude variability analysis

The amplitude differences of the seismic ground motions is evaluated considering the variability of the Fourier spectra at the dam-foundation interface of the model when the arch dam is present and at the same nodes along the canyon walls when the arch dam is not included in the model. The unsmoothed Fourier amplitude spectral ordinates (in terms of velocity) of the 2 second strong motion window are considered for the analysis. The difference of the natural logarithms of the Fourier velocities for a given frequency and receiver separation distance (in the range of [0 200] m) is estimated. The standard deviation of difference of Fourier amplitude estimates of all pairs within the inter-station distance bins at the canyon walls are illustrated in Figures 4.27 for the X component which represents motions parallel to the valley (stream component).

Figure 4.27 demonstrates that, contrary to the lagged coherency, amplitude variability is more sensitive to the local canyon topography. For both models, without and with the arch dam, an increase of the amplitude variability of the motions is observed with

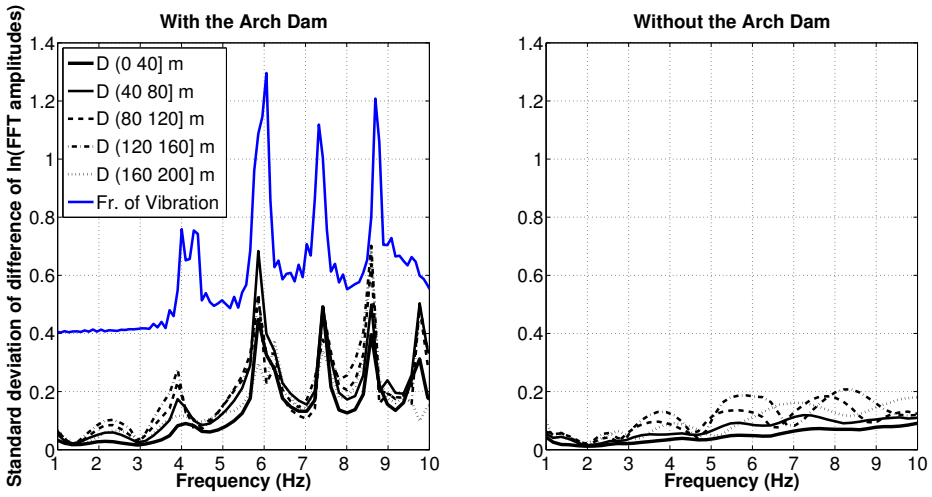

FIGURE 4.27: Comparison of median value of standard deviation of natural logarithm of Fourier amplitudes within each distance bin along canyon walls, i.e. [0 40] m, [40 80] m, [80 120] m, [120 160] m and [160 200] m without and with the presence of the dam (black lines); the blue line represents the frequencies of vibration at the dam-foundation rock interface as estimated on the crest.

frequency and receiver separation distance, with overall values varying from 0 to 0.15 and from 0 to 0.3 respectively. Additionally to the higher overall value of amplitude variability, the effect of the presence of the dam becomes evident due to the peaks of variability around the frequencies of its vibration. Based on these observations, both canyon topography and soil-dam interaction seem to influence amplitude variability.

4.2.7 Comparison of in-situ and numerical observations

The numerical model of the Saint Guérin arch dam and its canyon topography is a simplification of the reality. Due to the simplicity of the model, it can be argued that we can isolate only the effects of the canyon topography and the soil-structure interaction. The canyon walls are prolonged to the two edges of the numerical domain (Figure 4.21), not including neither the Saint Guérin reservoir (lake) nor its water volume. The surrounding complex alpine topography is not included in the model either. Aiming to keep the simulation time cost tolerable, the size of the domain, although it remains very big counting several km, cannot reproduce far field seismic events (more than 30 km), which are mainly the ones recorded from the Saint Guérin array. The seismic source is a point and not a fault that is located vertically below the dam. Finally, although the mechanical properties of the soil are equivalent to the in-situ ones (variable V_P and V_S with depth), no additional aleatory field (vertical/inclined changes of velocity, scattering points etc.) is modeled. Although no direct comparison can be made between the in-situ observations and the simulations because of the aforementioned neglected factors, several qualitative comparisons are allowed and could explain the physical phenomena

while quantitative comparisons are more delicate given the simplifications of the model with respect to reality. Firstly, the frequencies of vibration of the dam are compared followed by the crest amplification. Then, the comparison of the observed time lag, phase and amplitude variability are discussed.

Frequencies of vibration

The frequencies of vibration of the arch dam in Saint Guérin are identified using data of ambient noise before the occurrence of the seismic events, selected for analysis in Chapter 2; the median value of the three crest receivers are presented in Figure 2.24 for the two horizontal and the vertical components. The frequencies of vibration of the numerical model of the dam, for the stream component, are identified using a point source with flat spectrum; they are shown in Figure 4.24. The observed and the numerical frequencies in the stream direction are compared in Figure 4.28, at the dam-foundation rock interface and on the crest, in the frequency range [1 10] Hz (limitation imposed by the numerical modeling). The comparison is made for the NS comp. in-situ and its equivalent X comp. in the model. The simulation's Fourier amplitude spectra are scaled for easier visual inspection. The comparison reveals that the vibrational frequencies are overall captured from the model although they are relatively shifted. The observed differences are explained by the absence of the reservoir in the model that lead to shift of certain frequencies of vibration/mode shapes. As observed in Figure 4.24, at the dam-foundation rock interface due to destructive interference the median value of the Fourier spectra does not show the frequency peaks. Apparently the phenomenon is more evident in the numerical simulations with respect to the Saint Guérin observations, since there we can easily identify the frequency peaks even at median value of the spectra at the interface. An additional reason may be the location of the 9 stations in Saint Guérin interface with respect to the exhaustively covered with 22 receivers of the numerical model.

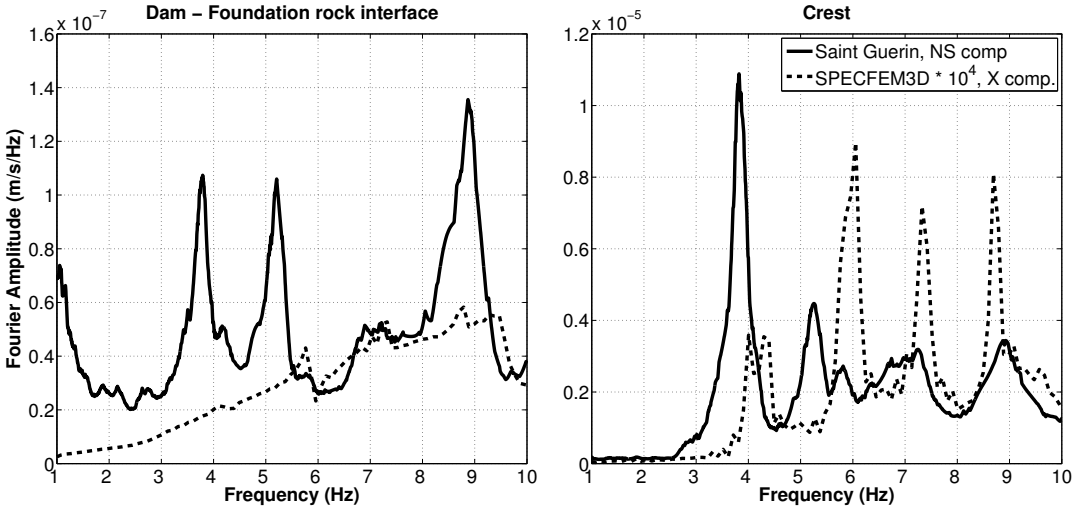

FIGURE 4.28: Comparison of frequencies of vibration of the arch dam between the Saint Guérin NS comp. (black solid lines) and the numerical model of the arch dam X comp. (black dashed lines).

Amplification of the motions on the dam crest due to the seismic excitation

The comparison of the crest amplification from the observations in Saint Guérin site and the numerical model is possible because most of the material properties of the dam are properly introduced in the model. Moreover, the comparison is allowed since the point source which is the seismic excitation in the model corresponds to a magnitude 2.7 event, that is in the range of magnitude of the recorded earthquakes in Saint Guérin. The amplification of the crest motions of the dam in Saint Guérin (median value of SG02, SG03 and SG04) with respect to the dam-foundation rock interface (median value of receivers SG05, SG06, SG07, SG08, SG09, SG10, SG11 and SG12) based on seismic events' recordings for the three components are presented in Figure 2.28. Similarly, the crest amplification of the modeled dam because of the seismic excitation of the point source for the stream component, X, is estimated. The ratio of the median value of unsmoothed Fourier amplitude spectra of all the receivers in the crest to the median value of the receivers at the interface is calculated. Additionally to the Fourier amplitudes, the analysis is performed using the Response spectral amplitudes with 1% damping coefficient (in accordance to the damping estimations in-situ in Chapter 3). The results for both cases are compared in Figure 4.29. The crest amplification is found to be of comparable values with the peaks of amplification around the frequencies of vibration to be well captured from the model. This indicates that the contrast of the two media, rock and concrete, is reasonably accurate proving representative boundary conditions at the dam's base and correct linear behavior of the dam's body during the earthquake, linked to proper representation of mass and rigidity. The differences, as explained when comparing the Fourier spectra in the previous section, are explained by the several simplifications made in the model.

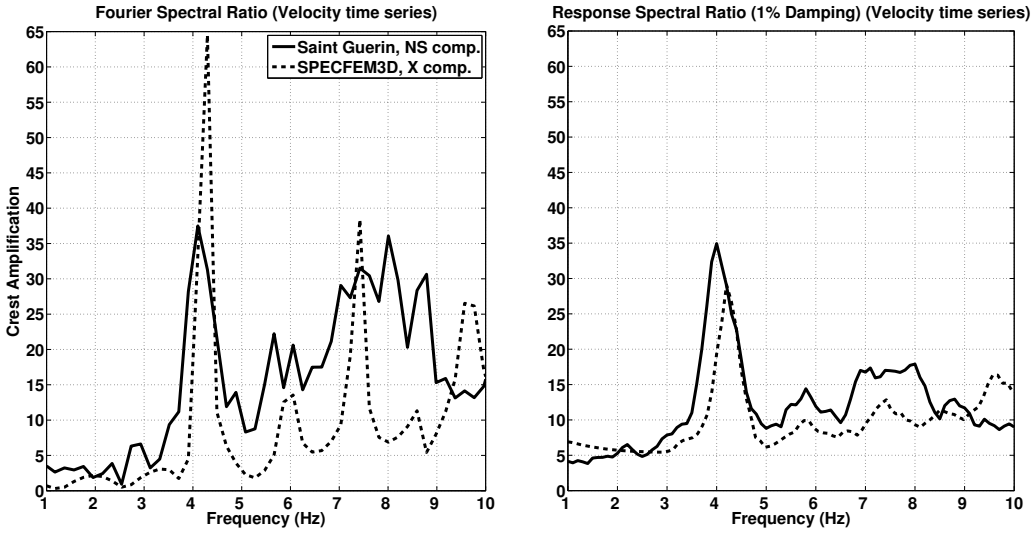

FIGURE 4.29: Ratio between the spectra at the crest and at the interface : Fourier spectra (left) and Response spectra (right) of velocity time series. The median spectrum of the crest receivers with respect to the median spectrum of the receivers at the dam-foundation rock interface are presented for the Saint Guérin NS comp. (black solid lines) and numerical model of the arch dam X comp. (black dashed lines).

Time lag

The time lag, dt, between the strong motion part of the two receivers ($S-$wave) is determined by estimating the cross-correlation function between the receivers and evaluating the positive maximum correlation coefficients. Comparison between observations and model is allowed under the condition that the velocity model that was implemented in the numerical model (Figure 4.1) approaches the real velocity structure in Saint Guérin. Because of the limited geological knowledge on the site of Saint Guérin which provides as only information the range of V_S and V_P (Chapter 2), we make the aforementioned hypothesis. The comparison of the time lags as a function of receiver separation distance (m) at the interface for all the recordings of the subset of events in Saint Guérin (NS comp.) and the simulated event in the model (X comp.) is presented in Figure 4.30. The time lags are of the same order of magnitude in in-situ observations and the numerical simulation. In Saint Guérin, the calculated time lag of receiver pairs at the interface ranges from 0 to 0.06 sec with an average value of 0.03 sec (Figure 3.5) and in the model ranges from 0 to 0.02 sec. The values are reasonable and expected, considering the distance of the point source from the points of recording (10 km) and the velocity profile (constant value of V_S 3200 m/s that degrades to 1000 m/s in the last 1.8 km below the surface), the dt can be approximately calculated as $dt = dx/V_S$ and thus $dt[00.025]$ sec. The dt increases with receiver separation distance up to a point where it starts decreasing again till it gets to 0 again for distances equal to $\sim$ 210 m. This is explained as following : The position of the source in the model is located below the middle of the dam, this explains that the signals arrive simultaneously at the two abutments of the

dam (receiver separation distance between them equal to ~ 210 m), i.e. $dt = 0$ sec. This is not the case for the in-situ measurements due to different different/various angles of incidence of the wave field.

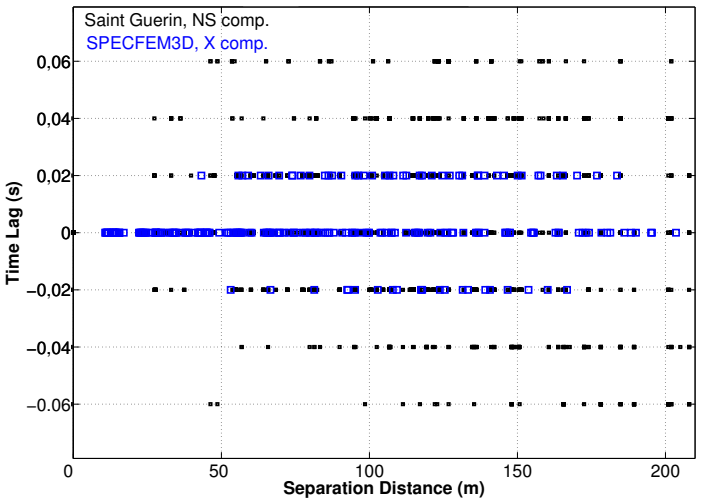

FIGURE 4.30: Comparison of the time lag between each pair of receivers at the dam-foundation rock interface as a function of their receiver separation distance (m) between the Saint Guérin observations, NS comp., (black squares) and the SPECFEM3D model of the arch dam, X comp. (blue squares).

Phase and amplitude variability

The main causes of SVGM are the extended source effect, the scattering effect and the diverse regional and local site effects. The lack of other sources of incoherence in the medium of the numerical model, apart from the presence of the arch dam and the local topography, does not allow a direct phase and amplitude spatial variability comparison. Anyhow, the comparison was not the aim of the model, as explained. However, the comparison is provided in Figures 4.31 and 4.32 for lagged coherency and amplitude variability respectively for the X component. As demonstrated in the figures, the order of magnitude of variability of the model is much lower than the observed in Saint Guérin, which is explained by the lack of other causes of SVGM apart from the local site effects due to the canyon topography and the soil-dam interaction. It needs to be mentioned also that, as shown by previous studies, amplitude variability increases as the wavelength decreases (frequency increases) and as the direction of incidence tends toward the horizontal (here is vertical). So in our study, since only a vertical incidence is considered, low amplitude variability is expected with respect to the real records where various incidence angles are occurring (which, additionally, are not predominantly vertical as shown in the wave passage analysis of Chapter 3). Nevertheless, overall, the higher variability due to the vibration of the structure confirms the observations made

from the Saint Guérin measurements. This confirmation was the desired goal of the modeling which offered the possibility to better understand the phenomenon.

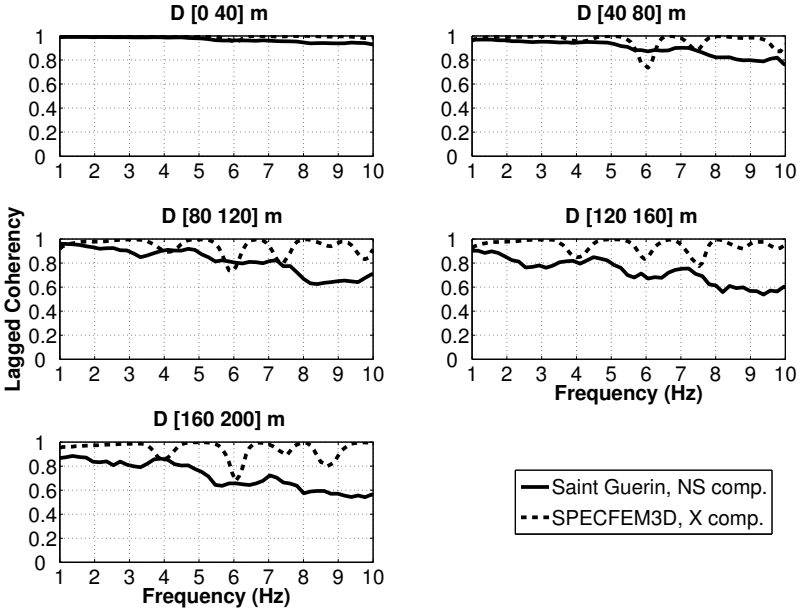

FIGURE 4.31: Comparison of the lagged coherency estimates of the pair of receivers at the dam-foundation rock interface between the Saint Guérin NS comp. (black solid lines) and the SPECFEM3D model of the arch dam X comp. (black dashed lines).

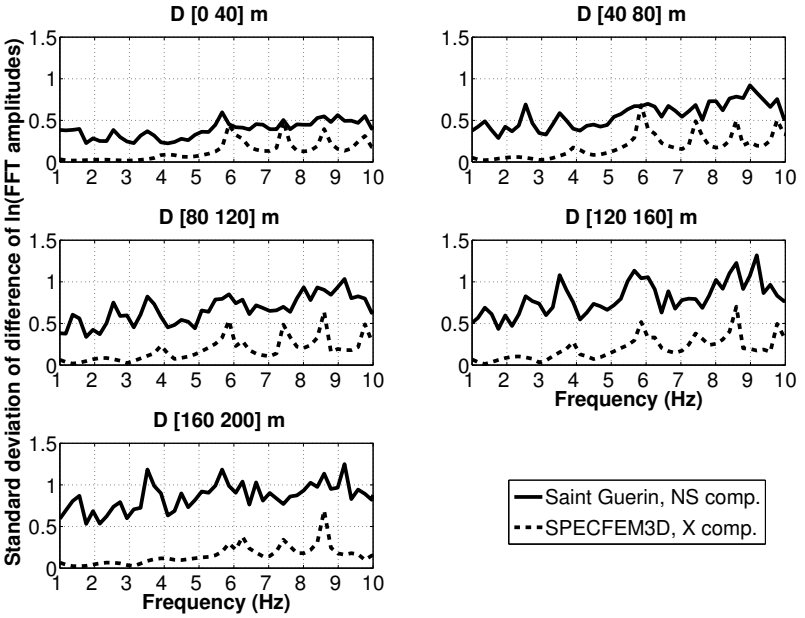

FIGURE 4.32: Comparison of the standard deviation of difference of natural logarithm of Fourier amplitudes of the pair of receivers at the dam-foundation rock interface between the Saint Guérin NS comp. (black solid lines) and the SPECFEM3D model of the arch dam X comp. (black dashed lines).

4.3 Discussion

A parametric study using a sinusoidal topography is conducted aiming to identify the effect of canyon topography on SVGM. The sinusoidal topography can be considered as a simplified representative canyon topography in the broader alpine area. A double-couple point source in several kilometres depth generates the incident wave field. The wave field at the canyon walls is very complex due to the local topography that leads to wave conversion and wave generation. A parametric study of different width to length ratios is performed and the spatial variability in terms of amplitude and phase is estimated. The lagged coherency of the $S-$wave window appears to be little affected by the presence of the canyon topography, with values that remain higher than 0.9 even in the case of brutal topographies. Nevertheless, the steeper the canyon slopes the higher the phase variability is. Contrary to the phase variability, the amplitude variability becomes very important when topography is introduced. Generally, the steeper the canyon slopes, the higher the estimated amplitude variability. It is found to increase with both frequency and station separation distance. However, for longer separation distances, i.e. receiver pairs consisting of receivers approaching the two 'summits' that surround the valley, the amplitude variability starts to decrease. This could be explained by the similar in amplitude, strong amplification of the motions at the two upper corners of the canyon facing the incident wave. On the other hand, the amplitude of the motions near the bottom of the canyon are reduced with the reduction to be greater when the slopes are steeper. This leads to higher variability for pairs consisting of one receiver at the upper corner and one at the bottom of the valley. Thus, the variability depends on the observation points but it can and it should be averaged over the canyon walls to perform further analysis.

A better insight into the effect of the dam-foundation rock interaction on SVGM is attempted by modeling the canyon topography and the arch dam of Saint Guérin. The canyon topography is prolonged along the X direction of the domain (continuous up-stream and down-stream flow) while the reservoir and the surrounding alpine topography are not modeled. The lack of other sources of incoherence in the medium of the numerical model allows us to make conclusions regarding strictly the presence of the arch dam and the local topography on SVGM. Despite the simplicity of the model, the frequencies of vibration of the modeled dam, identified from the crest motions, are approaching the observed frequencies in Saint Guérin. The numerical simulations confirm the in-situ observations regarding the higher variability around the frequencies of vibration of the structure. The physical explanation for this phenomenon is that at the dam-foundation rock interface destructive interference is occurring, i.e. the impedance contrast between the foundation rock and the concrete medium causes a cut-off at the Fourier spectra and a brutal change of phase around the vibration frequencies which is reflected on the

estimation of variability. The crest amplification of the model is also similar to the observations, with stronger amplification to occur around the frequencies of vibration. The order of magnitude of the variability in the model is lower than the observed in Saint Guérin, which is explained by the lack of other causes of SVGM apart from the local site effects due to the canyon topography and the soil-dam interaction.

The use of simplified numerical models was chosen, aiming to decouple the several, complicated effects that contribute to SVGM on a dam site. When the phenomena are studied independently, the contribution of each one on SVGM is more evident. Generally, the findings of this numerical study suggest that the presence of the structure along with the local canyon topography increase phase and amplitude variability. Our conclusions, drawn from a simplified model, set the base for further research on the topic enriching/completing our model with the dam's reservoir and the realistic surface topography of the alpine area.

Conclusions and perspectives

Truth is a remarkable thing. We cannot miss knowing some of it.
But we cannot know it entirely.
Aristotle

This study presents a measure and a profound investigation of the spatial variability of the ground motions at the dam-foundation rock interface of an arch dam. In-situ measurements are used to quantify SVGM and numerical simulations to deeper understand the particular physical phenomena that contribute to SVGM at the interface, i.e. local canyon topography and rock-structure interaction. The data comes from an original seismological experimental campaign that has taken place on and around Saint Guérin arch dam over the period of six months. The subset of events consists of low to moderate magnitude local and regional earthquakes. Thus, analysis is allowed in the linear range. Numerical simulations in the SPECFEM3D code based on the spectral element method are used to enlighten several particular observations made in-situ.

Dynamic analysis of the arch dam in Saint Guérin is conducted, taking advantage of the continuous ambient noise data and a subset of seismic records. The data allows us to identify the frequencies of vibration along with the damping coefficient and the crest amplification. The damping ratio of the first identified vibrational frequency ranges between 1 and 2 %, for the three components of motion. It is consistent with values found in the literature, ranging from 1% for smaller to 4% for stronger shaking. The amplification in terms of the Fourier ratio on the crest to the interface of the dam ranges from 5 to 35 with an average value of 10 along the frequency range. It is higher than the currently considered design values ($\sim$ 7), but justified due to small shaking, i.e. lower damping coefficient. The observed damping and crest amplification should not be extrapolated to strong shaking where the material component of damping is expected to be higher thus the amplification of the crest reduced. Non linear behaviour of materials (rock and concrete) during strong shaking may significantly effect the results. From a statistical point of view, the amplification analysis is robust but maybe not sufficiently, since few good quality records on the crest are available. This restriction was imposed by the limited time that the stations at the interface were installed due to difficulties in access during the winter period but also due to the difference of the type of seismological stations used. To enrich our analysis, we could complete the database with events recorded during the second semester of the instrumentation. However, due to absence of some of the stations at the dam-foundation interface during the second half of the campaign, the amplification should be estimated using only the remaining interface stations.

The wave passage analysis, conducted using the Saint Guérin data, indicates a preferential backazimuth of the seismic waves from the East which could be explained by the composition of the subset mainly of events occurring in the North-East, East and South-East. The wave field at the dam-foundation rock is complex, with non negligible time delays between different locations that reach up to 0.06 sec. A single wave direction (azimuth) and one apparent velocity (incidence) along the dam-foundation rock interface cannot be easily identified given the irregular topography and the soil-structure

interaction. It does not resemble to a vertical incidence which is the current, widely used approach in engineering applications. According to our observations, the simplification of vertical input motion at the base of an arch dam needs to be replaced by analyses that include incidence with various angles.

The phase and amplitude variabilities of the ground motions are estimated using the $S-$wave part of the seismograms after removing the wave passage effect. Lagged and unlagged coherency estimates are used for phase variability quantification and the standard deviation of the difference of natural logarithm of Fourier velocities evaluates the amplitude variability of the motions. At the dam-foundation rock interface, high variability is observed both in phase and amplitude for the three components of motion (NS, EW, Z). Higher phase and amplitude variability is noticed in certain narrow frequency bands; these bands seem to correspond to the frequencies of vibration of the arch dam and this hypothesis will be confirmed by the numerical modeling analysis that follows. The ground motions in the free field appear to be slightly less variable than at the interface. Sensitivity analyses show no dependency of the variability estimates on source (magnitude, source to site distance, azimuth) or site (canyon topography) features. Sensitivity analyses on the time window (length of the strong phase $S-$ wave window as well as different type of waves) and the smoothing parameter (used for the Fourier spectra calculation) show that attention must be paid when choosing them, since their impact may be significant on the variability estimates. Our analyses show that when the $S-$wave is included in the time window, even including other wave types in the window, the analysis yields to the same trends of coherency. Use of coda waves yields to lower coherencies, but with less than 20% of difference. Another possibility, instead of using seismic data, is to consider ambient noise recordings to estimate the variability at the interface of the dam with the foundation rock. The first attempts to do so are not promising though. According to our preliminary analysis, the lagged coherency estimates based on ambient noise are not comparable with the observations based on earthquakes. Inevitably, the governing effects on ambient noise measurements are very different from the seismic events, making the comparison hard. Thus, at this stage, use of noise recordings to study the phase variability is not justified. More detailed studies have to be carried out to confirm this conclusion and the existing dataset could be of great use for this research.

Once the estimators of phase and amplitude variability are obtained from the seismic data, existing parametric models are fitted to them. Generally, we can conclude that, although no irregular topography or engineered structure are present in the location of the arrays used for the derivation of these models, they fit in an overall satisfactory way the observations in Saint Guérin. Because of the difficulty faced in identifying a single plane wave and velocity of propagation, plane wave coherency is not calculated. However the lagged coherencies measured in Saint Guérin are compared with an existing plane-wave

coherency model, following the logic that if one plane wave dominates the motions, plane and lagged coherency should be identical. Indeed, it is found that at lower frequencies that the motions are dominated by one plane wave, the lagged coherencies observed and the plane-wave model are essentially identical for the short station separation distances. However, as frequency increases, the lagged coherency, which incorporates also the scattered energy, tends to the median value of noise, whereas the plane-wave coherency tends to zero. Based on this study, we could argue that lagged, unlagged and amplitude variability models calibrated in plane free field seismological arrays may be used for the estimation of variability of input motions in case of arch dams located in canyon topographies. To justify this argument, proof is needed that in the case of arch dams' location, the particular local phenomena can be neglected.

Based on the in-situ measurements, focus is given on two observations : 1) the ground motions in the free field appear to be slightly less variable with respect to the motions at the dam-foundation rock interface and 2) at the dam-foundation rock interface, there is an abrupt higher variability around the frequencies of vibration of the dam. These observations suggest that the presence of the structure along with the canyon topography increase SVGM. This increase though seems to be small given that the observations are satisfactory fitted by models based on data coming from flat seismic arrays. Decoupling the various causes of SVGM and evaluating the impact of each one in-situ is not an easy task. To this end, numerical simulations are used to break down and investigate the two phenomena independently.

An extended parametric study using a simplified sinusoidal canyon topography showed that phase variability is hardly affected by the presence of canyon walls. On the other hand, the impact on amplitude variability becomes very important when topography is introduced in the local site. Generally, the steeper the canyon slopes, the higher the phase and amplitude variability is found to be. An interesting, although intuitively expected, point of the analysis is that, for longer separation distances, i.e. station pairs consisting of stations that are located in the upper corner of the canyon walls, the amplitude variability starts to decrease. This is most probably due to the similar amplification of the stations at these points. Contrarily, pairs consisting of one station at the 'summit of the mountain' and one at the bottom of the valley show higher variability due to amplification of the motions at the upper corner of the canyon and reduction at the bottom of the valley. Overall, the variability depends on the observation points but it can and it should be averaged over the canyon walls to perform further analysis.

A geometrically accurate model of the Saint Guérin arch dam and its canyon topography, with absence of other 'site effects' such as dam-reservoir interaction, local or regional scatterers in the earth's medium etc., gives us a better insight on the dam-foundation rock interaction effect on SVGM. The numerical simulations confirm the in-situ observations regarding the higher variability around the frequencies of vibration of the

structure. The physical explanation for this phenomenon is that at the dam-foundation rock interface there is destructive interference occurring, i.e. the impedance contrast between the foundation rock and the concrete medium causes a cut-off at the Fourier spectra and a brutal change of phase around the vibration frequencies which is reflected on the estimation of variability.

Although our in-situ and numerical observations suggest that the presence of the structure along with the irregular local topography influence the loss of coherency and increase amplitude variability, the two features seem to have only a secondary effect on SVGM. This conclusion needs to be supported by further research on the topic. Our results from SVGM analysis at the dam-foundation rock interface open up new insights and possibilities for future studies. It would be of great interest to perform similar analysis for seismic array data obtained from other hard-rock canyon sites that arch dams are or could eventually be constructed. Instrumenting with a dense seismological network the canyon topography and its surrounding area, before and after the dam's construction could enhance our understanding. The SVGM analysis at the canyon walls before the dam's addition and comparison with the free field data would show the variability solely related to the canyon topography. The comparison of SVGM analysis performed before and after the construction of the dam would reveal the dam-foundation interaction effect. Furthermore, we could compare the coherency and amplitude variability tendencies with the Saint Guérin curves and the available parametric models. In case of agreement among the results, we could boost our argument that lagged coherency and amplitude variability models calibrated by flat free field seismological arrays are suitable for the estimation of variability of input motions in case of arch dams located in canyon topographies.

The source characteristics' ranges of our subset limit us to small shaking and linear material behaviors. Extended sensitivity analyses show that variability in observations does not depend on source characteristics. Fitting our curves with models calibrated on high magnitude and short distance earthquakes further confirm non dependency of ground motion variability when subjected to near-field strong shaking. Nevertheless, larger magnitude local events can rupture the fault segment causing non-linear material behavior of the soil and of the structure. Instrumenting a site near a large active fault with dense array and then performing similar analyses to ours would give the desired answers. Such a seismological experimental campaign, either permanent or temporary but of relatively long duration, would also provide with a large and complete dataset covering the necessary magnitude and distance ranges leading to a robust statistical analysis. Geophysical studies are also necessary aiming to complete the comprehension of physical phenomena. Limitations in understanding may be imposed by lack of sufficiently detailed geological/geomorphological studies of the broader area of study.

An alternative to in-situ instrumentations, which are evidently costly and time consuming, is numerical simulations of ground motion. As proved by the numerical study presented herein, this tool is very powerful. It gives the liberty to simulate any type of representative site with a wide range of earthquake source characteristics, 'instrumented' with a limitless in number network of stations. In particular, the source code SPECFEM3D, based on the spectral element method, which was used for the present work, gives the possibility to simulate complex sites, several kilometres long, and different seismic sources, either point sources or faults, representative of far or near field events respectively. The current work on the canyon topographic effect on spatial variability would naturally be followed up firstly by multiplying the number as well as the positioning of the point sources. This would validate our conclusions based on one point source. An interesting second step would be to replace the point source with a fault which would correspond to near-field strong magnitude event. Additionally, altering the simplified one-directional sinusoidal canyon topography with a more realistic model of, for example, the alpine region would be of great importance. The digital terrain model (DTM), which represents the topography of the broader area around the Saint Guérin region, is available and could eventually be implemented on the free surface of the site that we created in SPECFEM3D. Another step could be to introduce aleatory variability in the earth's medium. Therefore, the final model would include the variability due to the source effect, the scattering and the local site effects. This way, a realistic representation of SVGM could be achieved.

Our model with the simplified canyon topography and the Saint Guérin's arch dam enhanced our comprehension regarding the foundation rock-dam interaction effect on SVGM. Although our goal was not to compare the numerical variability analysis with the observations in Saint Guérin, the results showed that such a comparison would be of great interest, if the necessary additions would be made in the model. Adding the mentioned above causes of SVGM in the model, i.e. source and path effects in addition to the local site effects of topography and presence of the structure, could make the comparison possible. A final touch to this simulation would be the representation of the dam's reservoir; fluids can be represented in the model as acoustic waves. The options that numerical simulations give are limitless and when combined with in-situ measurements, the outcome can have the desired robustness and quality.

A lot is still needed to be learn regarding the variable seismic input motions at the base of an arch dam. The contribution of the present study enlightens several physical phenomena occurring at the dam-foundation rock interface and defines parametric models that are able to reproduce variable seismic ground motions. These parametric models may be used directly in random vibration analyses of the dams and in Monte Carlo simulations for the generation of spatially variable motions to be applied as input excitations at the supports of the structure. A comparison of the response of the dam

under homogeneous and variable ground motions would respond to the final and most important question on the subject that the engineering community is asking itself : Does the spatial variability of seismic ground motions have a significant effect on the dam's seismic response?

Bibliography

Abdel Ghaffar, A. & Nazmy, A., 1991. 3d nonlinear seismic behavior of cable stayed bridges, *Journal of Structural Engineering, ASCE*, **117**, 3456–3476.

Abdel Ghaffar, A. & Rubin, L., 1982. Suspension bridge response to multiple support excitations, *Journal of the Engineering Mechanics Division, ASCE*, **108**, 419–435.

Abdel Ghaffar, A. & Rubin, L., 1983. Lateral earthquake response of suspension bridges, *Journal of Structural Engineering, ASCE*, **109**, 665–675.

Abrahamson, N., 1993. Spatial variation of multiple support inputs, in *Proceedings of the 1st U.S. Seminar on Seismic Evaluation and Retrofit of Steel Bridges. A Caltrans and University of California at Berkeley Seminar, San Francisco, CA.*

Abrahamson, N., 2006. Program on technology innovation: Spatial coherency models for soil structure interaction, *EPRI, Palo Alto, CA and the US Department of Energy, Germantown, MD, Report*, (1014101).

Abrahamson, N., 2007. Program on technology innovation: Effects of spatial incoherence on seismic ground motions, *EPRI, Palo Alto, CA.*

Abrahamson, N. & Bolt, B., 1987. Array analysis and synthesis mapping of strong seismic motion, *Seismic Strong Motion Synthetics, B.A. Bolt editor, Academic Press Inc., New York, NY*.

Abrahamson, N., Schneider, J., & Stepp, J., 1990. Spatial variation of strong ground motion for use in soil structure interaction analyses, in *Proceedings of the Fourth U.S. National Conference on Earthquake Engineering, Palm Springs, CA.*

Abrahamson, N., Schneider, J., & Stepp, J., 1991. Empirical spatial coherency functions for applications to soil structure interaction analyses, *Earthquake Spectra*, **7**, 1–27.

Abrahamson, N. A., 1988. Statistical properties of peak ground accelerations recorded by the smart 1 array, *Bulletin of the Seismological Society of America*, **78**(1), 26–41.

Abrahamson, N. A., 1992a. Spatial variation of earthquake ground motion for application to soil-structure interaction, Tech. rep., Electrical Power Research Institute, Rpt. No. EPRI TR-100463, Tier 1.

Abrahamson, N. A., 1992b. Spatial variation of earthquake ground motion for application to soil-structure interaction, Tech. rep., Electrical Power Research Institute, Rpt. No. EPRI TR-100463, Tier 2.

Abrahamson, N. A., 1992c. Generation of spatially incoherent strong motion time histories, in *Proceedings of the Tenth World Conference on Earthquake Engineering, Madrid, Spain*.

Abrahamson, N. A. & Bolt, B. A., 1985. *Estimation of seismic wave coherency and rupture velocity using the SMART 1 strong-motion array recordings*, Ph.D. thesis, University of California, Berkeley.

Aki, K. & Richards, P. G., 2002. *Quantitative seismology*, vol. 1.

Alarcon, P. N., 1975. Dynamic behavior of concrete gravity dams during earthquakes, Tech. rep., Individual Studies, International Institute of Seismology and Earthquake Engineering, Tokyo.

Alves, S. & Hall, J., 2006a. System identification of a concrete arch dam and calibration of its finite element model, *Earthquake engineering and structural dynamics*, **35**(11), 1321–1337.

Alves, S. & Hall, J., 2006b. Generation of spatially nonuniform ground motion for nonlinear analysis of a concrete arch dam, *Earthquake Engineering and Structural Dynamics*, **35**, 1339–1357.

Ancheta, T., Stewart, J., & Abrahamson, N., 2011. Engineering characterization of earthquake ground motion coherency and amplitude variability, in *Proc. 4th IASPEI / IAEE Int. Sym. on Effects of Surface Geology on Seismic Motion*, pp. 23–26.

ASCE, 2000. Seismic analysis of safety related nuclear structures and commentary, Tech. rep., American Society of Civil Engineers (ASCE Standard), 4-98, Reston, VA.

Baize, S., Cushing, E., & Jomard, H., 2013. Updated seismotectonic zoning scheme of Metropolitan France, with reference to geologic and seismotectonic data, *Bulletin de la Societe Geologique de France*.

Barrages-Séismes, 2014. Risque sismique et sécurité des ouvrages hydrauliques, Tech. rep., Rapport rédigé à la demande du MEDDE – DGPR.

Bayraktar, A. & Dumanoğlu, A., 1998. The effect of the asynchronous ground motion on hydrodynamic pressures, *Computers and structures*, **68**(1), 271–282.

Behnamfar, F. & Sugimura, Y., 1999. Dynamic response of adjacent structures under spatially variable seismic waves, *Probabilistic Engineering Mechanics*, **14**, 33–44.

Bi, K. & Hao, H., 2009. Analysis of influences of an irregular site with uncertain soil properties on spatial seismic ground motion coherency, in *AEES 2009 Conference. Newcastle Australia*.

Blacker, T. D., Bohnhoff, W. J., & Edwards, T. L., 1994. Cubit mesh generation environment. volume 1: Users manual, Tech. rep., Sandia National Labs., Albuquerque, NM (United States).

Bogdanoff, J., Goldberg, J., & Schiff, A., 1965. The effect of ground transmission time on the response of long structures, *Bulletin of the Seismological Society of America*, **55**, 627–640.

Boissieres, H. & Vanmarcke, E., 1995a. Estimation of lags for a seismograph array: wave propagation and composite correlation, *Soil Dynamics and Earthquake Engineering*, **14**, 5–22.

Bolt, B., Loh, C., Penzien, J., Tsai, Y., & Yeh, Y., 1982. Preliminary report on the smart 1 strong motion array in taiwan, Tech. rep., Earthquake Engineering Research Center Report No. UCB/EERC 82/13, University of California, Berkeley, CA.

Boore, D., 1972. A note on the effect of simple topography on seismic sh waves', *Bull. seismological society of America*, **62**, 275–284.

Bycroft, G., 1980a. El centro, california differential ground motion array, Tech. rep., USGS Open File Report, U.S. Geological Survey, Denver, CO.

Bycroft, G., 1980b. Soil foundation interaction and differential ground motions, *Earthquake Engineering and Structural Dynamics*, **8**, 397–404.

Camara, R., 2000. A method for coupled arch dam foundation reservoir seismic behaviour analysis, *Earthquake Engineering and Structural Dynamics*, **29**, 441–460.

Capon, J., 1969. High-resolution frequency-wavenumber spectrum analysis, *Proceedings of the IEEE*, **57**(8), 1408–1418.

Casarotti, E., Stupazzini, M., Lee, S. J., Komatitsch, D., Piersanti, A., & Tromp, J., 2008. Cubit and seismic wave propagation based upon the spectral-element method: An advanced unstructured mesher for complex 3d geological media, in *Proceedings of the 16th International Meshing Roundtable*, pp. 579–597, Springer.

Castoldi, A., 1978. Contribution of surveillance to the evaluation of the seismic efficiency of dams, example of the Ambiesta dam, in *Seminar on Constructions in Seismic Zones, Bergamo*, pp. 107–118.

CEN, 2005. Eurocode 8: Design of structures for earthquake resistance part 2: Bridges, Tech. rep., EN 1998 2:2005, Brussels, Belgium.

Chaljub, E., 2015. Numerical methods for ground motion estimation : An overview, ftp://ist-ftp.ujf-grenoble.fr/users/chaljube/MEEES/LECTURES/Lecture_notes.pdf.

Chaljub, E., Komatitsch, D., Vilotte, J.-P., Capdeville, Y., Valette, B., & Festa, G., 2007. Spectral-element analysis in seismology, *Advances in Geophysics*, **48**, 365–419.

Chamot-Rooke, N. & Rabaute, A., 2006. Plate tectonics from space, *Map of the CGMW, Paris*.

Chang, S., Tsai, I., Yeh, C., Chem, C., Dzong, D., & Hwang, Y., 1987. A study on seismic response of the Techi arch dam, Tech. rep., CEER Report R76-14, National Taiwan University.

Chen, M. & Harichandran, R., 2001. Response of an earth dam to spatially varying earthquake ground motion, *Journal of Engineering Mechanics, ASCE*, **127**, 932–939.

Chopra, A. K., 2012. Earthquake analysis of arch dams: factors to be considered, *Journal of Structural Engineering*, **138**(2), 205–214.

Clough, R., Stephen, R., & Kuo, J., 1982. Dynamic response analysis of techi dam, Tech. rep., Report No. UCB/EERC 82/11 Earthquake Engineering Research Center, University of California, Berkeley.

Cole, H. A., 1973. On-line failure detection and damping measurements of aerospace structures by random decrement signature, Tech. rep., NASA CR-2205.

Conte, J., Elgamal, A., Yang, Z., Zhang, Y., Acero, G., & Seible, F., 2002. Nonlinear seismic analysis of a bridge ground system, in *Proceedings of the 15th ASCE Engineering Mechanics Conference, New York, NY*.

Council, N. R. et al., 1991. *Earthquake engineering for concrete dams: design, performance, and research needs*, National Academy Press.

Darbre, G., 1995. Strong-motion instrumentation of dams, *Earthquake Engineering and Structural Dynamics*, **24**, 1101–1111.

Datta, T. & Mashaly, E., 1990. Transverse response of offshore pipelines to random ground motion, *Earthquake Engineering and Structural Dynamics*, **19**, 217–228.

Deodatis, G., Saxena, V., & Shinozuka, M., 2000. Effect of spatial variability of ground motion on bridge fragility curves, in *Proceedings of the Eighth ASCE Specialty Confer ence on Probabilistic Mechanics and Structural Reliability, University of Notre Dame, Notre Dame, IN*.

Der Kiureghian, A., Keshishian, P., & Hakobian, A., 1997. Multiple support response spectrum analysis of bridges including the site response effect and the msrs code, Tech. rep., Earthquake Engineering Research Center Report No. UCB/EERC 97/02, University of California, Berkeley, CA.

Enochson, L. D. & Goodman, N. R., 1965. Gaussian approximations to the distributions of sample coherence, Tech. rep., AFFDL-TR-65-57, Wright- Patterson Air Force Base.

Faccioli, E., 1991. Seismic amplification in the presence of geological and topographic irregularities.

Faccioli, E., Vanini, M., & Frassine, L., 2002. Complex site effects in earthquake ground motion, including topography, in *12th European Conference on Earthquake Engineering*, vol. 844.

Fujii, T., Egawa, K., & Katayama, I., 1987. Seismic response of Nagawado arch dam, in *China - U.S. Workshop on Earthquake Behavior of Arch Dams, Beijing, People's Republic of China*.

Ghaemian, M. & Sohrabi-Gilani, M., 2012. Seismic responses of arch dams due to non-uniform ground motions, *Scientia Iranica*, **19**(6), 1431–1436.

Goda, K. & Atkinson, G. M., 2010. Intraevent spatial correlation of ground-motion parameters using sk-net data, *Bulletin of the Seismological Society of America*, **100**(6), 3055–3067.

Goldstein, P. & Archuleta, R. J., 1991a. Deterministic frequency-wavenumber methods and direct measurements of rupture propagation during earthquakes using a dense array: theory and methods, *J. geophys. Res*, **96**(B4), 6173–6185.

Goldstein, P. & Archuleta, R. J., 1991b. Deterministic frequency-wavenumber methods and direct measurements of rupture propagation during earthquakes using a dense array: theory and methods, *J. geophys. Res*, **96**(B4), 6187–6198.

Graves, R. W., 1993. Modeling three-dimensional site response effects in the marina district basin, San Francisco, California, *Bulletin of the Seismological Society of America*, **83**(4), 1042–1063.

Hahn, G. & Liu, X., 1993. Torsional response of unsymmetric buildings to incoherent ground motions, *Journal of Structural Engineering, ASCE*, **120**, 1158–1181.

Hahn, G. & Liu, X., 1994. Torsional response of unsymmetric buildings to incoherent ground motions and erratum, *Journal of Structural Engineering, ASCE*, **120**, 1158–1181 and 3101–3104.

Hao, H., 1991. Response of multiply supported rigid plate to spatially correlated seismic excitations, *Earthquake Engineering and Structural Dynamics*, **20**, 821–838.

Hao, H., 1997. Stability of simple beam subjected to multiple seismic excitations, *Journal of Engineering Mechanics, ASCE*, **123**, 739–742.

Hao, H. & Duan, X., 1995. Seismic response of asymmetric structures to multiple ground motions, *Journal of Structural Engineering, ASCE*, **121**, 1557–1564.

Hao, H. & Gong, L., 2005. Analysis of coupled lateral torsional pounding responses of one storey asymmetric adjacent structures subjected to bi directional ground motions part ii: Spatially varying ground motion input, *Advances in Structural Engineering*, **8**, 481–496.

Hao, H., Oliveira, C., & Penzien, J., 1989. Multiple station ground motion processing and simulation based on smart 1 array data, *Nuclear Engineering and Design*, **111**, 293–310.

Harada, T., 1984. Probabilistic modeling of spatial variation of strong earthquake ground displacement, in *Proceedings of the Eighth World Conference on Earthquake Engineering, San Francisco, CA*.

Harichandran, R., 1987. Stochastic analysis of rigid foundation filtering, *Earthquake Engineering and Structural Dynamics*, **15**, 889–899.

Harichandran, R., 1991. Estimating the spatial variation of earthquake ground motion from dense array recordings, *Structural Safety*, **10**, 219–233.

Harichandran, R. & Vanmarcke, E., 1986. Stochastic variation of earthquake ground motion in space and time, *Journal of Engineering Mechanics, ASCE*, **112**, 154–174.

Harichandran, R. & Vanmarcke, E., 1987. "Discussion" by M. Novak and "Closure" by authors, *Journal of Engineering Mechanics, ASCE*, **113**, 1267–1270.

Harichandran, R. & Wang, W., 1988. Response of simple beam to spatially varying earthquake excitation, *Journal of Engineering Mechanics, ASCE*, **114**, 1526–1541.

Harichandran, R. & Wang, W., 1990. Response of indeterminate two span beam to spatially varying earthquake excitation, *Earthquake Engineering and Structural Dynamics*, **19**, 173–187.

Harichandran, R. S., 1999. Spatial variation of earthquake ground motion, what is it, how do we model it, and what are its engineering implications, in *Manuscript corresponding to seminars presented at the University of New South Wales, Sydney, Australia (04/1994), Universidad Nacional Autónoma de México (03/1998), University of Puerto Rico, Mayaguez (11/1999), University of Canterbury, New Zealand (02/2000)*.

Hashash, Y., Hook, J., Schmidt, B., & Yao, J. C., 2001. Seismic design and analysis of underground structures, *Tunneling and Underground Space Technology*, **16**, 247–293.

Heredia Zavoni, E. & Barranco, F., 1996. Torsion in symmetric buildings due to ground motion spatial variation, *Journal of Engineering Mechanics, ASCE*, **121**, 834–843.

Hindy, A. & Novak, M., 1980. Pipeline response to random ground motion, *Journal of the Engineering Mechanics Division, ASCE*, **106**, 339–360.

Hoshiya, M. & Ishii, K., 1983. Soil dynamics and earthquake engineering, *Earthquake Engineering and Structural Dynamics*, **2**, 128–134.

Iida, R., Matsumoto, N., & Kondo, S., 1983. Comparison of the measured and computed responses of the Yuda dam during the July 6, 1976 and June 12, 1978 earthquakes, in *Proceedings of the 11th Joint U.S.-Japan Panel Conference on Wind and Seismic Effects. National Bureau of Standards. Washington, D.C.*.

Imtiaz, A., 2015a. *Seismic wave field, spatial variability and coherency of ground 370 motion over short distances: near source and alluvial valley effects*, Ph.D. thesis, 371 Université de Grenoble, France.

Iwan, W. D., 1979. The deployment of strong-motion earthquake instrument arrays, *Earthquake Engineering & Structural Dynamics*, **7**(5), 413–426.

Jenatton, L., Guiguet, R., Thouvenot, F., & Daix, N., 2007. The 16,000-event 2003–2004 earthquake swarm in Ubaye (French Alps), *Journal of Geophysical Research*, **112**(B11304).

Jenkins, G. & Watts, D., 1969. Spectral analysis and its applications, in *Holden Day, San Francisco, CA*.

Johnson, N. & Galletly, R., 1972. The comparison of the response of a highway bridge to uniform ground shock and moving ground excitation, *The Shock and Vibration Bulletin*, **42**, 75–85.

Kahan, M., Gibert, R., & Bard, P., 1996. Influence of seismic waves spatial variability on bridges: A sensitivity analysis, *Earthquake Engineering and Structural Dynamics*, **25**, 795–814.

Katayama, I. & Tsuzuki, T., 1987. Dynamic modeling experience in simulating earthquake response of an arch dam, in *China-U.S. Workshop on Earthquake Behavior of Arch Dams, Beijing, People's Republic of China*.

Kato, K., Takemura, T., Uchiyama, S., Iizuka, S., & Nigbor, R., 1998. Borrego valley downhole array in southern california: Instrumentation and preliminary site effect study, in *Proc. 2nd Int. Sym. on the Effects of Surface Geology on Seismic Motion, Yokohama, Japan*.

Kausel, E. & Pais, A., 1987. Stochastic deconvolution of earthquake motions, *Journal of Engineering Mechanics, ASCE*, **113**, 266–277.

Kim, S. & Feng, M., 2003. Fragility analysis of bridges under ground motion with spatial variation, *International Journal of Non Linear Mechanics*, **38**, 705–721.

Kim, S. & Stewart, J., 2003. Kinematic soil structure interaction from strong motion recordings, *Journal of Geotechnical and Geoenvironmental Engineering, ASCE*, **129**, 323–335.

Kojic, S. & Trifunac, M., 1991. Earthquake stresses in arch dams. i: Theory and an tiplane excitation, *Journal of Engineering Mechanics, ASCE*, **117**, 532–552.

Kojić, S. B. & Trifunac, M. D., 1991. Earthquake stresses in arch dams. ii: Excitation by sv-, p-, and rayleigh waves, *Journal of Engineering Mechanics*, **117**(3), 553–574.

Komatitsch, D. & Tromp, J., 1999. Introduction to the spectral element method for three-dimensional seismic wave propagation, *Geophysical journal international*, **139**(3), 806–822.

Komatitsch, D. & Vilotte, J.-P., 1998. The spectral element method: An efficient tool to simulate the seismic response of 2d and 3d geological structures, *Bulletin of the Seismological Society of America*, **88**(2), 368–392.

Komatitsch, D., Liu, Q., Tromp, J., Süss, P., Stidham, C., & Shaw, J. H., 2004. Simulations of ground motion in the Los Angeles basin based upon the spectral-element method, *Bulletin of the Seismological Society of America*, **94**(1), 187–206.

Komatitsch, D., Tsuboi, S., & Tromp, J., 2005. The spectral-element method in seismology, *Seismic earth: Array analysis of broadband seismograms*, pp. 205–227.

Konno, K. & Ohmachi, T., 1998. Ground-motion characteristics estimated from spectral ratio between horizontal and vertical components of microtremor, *Bulletin of the Seismological Society of America*, **88**(1), 228–241.

Kramer, S. L., 1996. Geotechnical earthquake engineering.

Kuroda, S. & Baba, K., 1985. Seismic observations and lessons learnt from characteristics of rock motion and responses of dams during earthquakes, in *Proceedings of the 15th International Congress on Large Dams, Question 56, Lausanne, Switzerland*.

Lee, S.-J., Chan, Y.-C., Komatitsch, D., Huang, B.-S., & Tromp, J., 2009. Effects of realistic surface topography on seismic ground motion in the Yangminshan region of Taiwan based upon the spectral-element method and LiDAR DTM, *Bulletin of the Seismological Society of America*, **99**(2A), 681–693.

Lee, W. H., Jennings, P., Kisslinger, C., & Kanamori, H., 2002. *International handbook of earthquake & engineering seismology*, Academic Press.

Léger, P., Idé, I., & Paultre, P., 1990. Multiple support seismic analysis of large structures, *Computers and Structures*, **36**, 1153–1158.

Liao, S., 2006. *Physical characterization of seismic ground motion spatial variation and conditional simulation for performance-based design*, Ph.D. thesis, Drexel University, Philadelphia, USA.

Liao, S. & Li, J., 2002. A stochastic approach to site-response component in seismic ground motion coherency model, *Soil Dynamics and Earthquake Engineering*, **22**, 813–820.

Lin, J. & Wang, J., 1996. Seismic response of arch dams to wave scattering and spatial variation of ground motions, in *Proceeding of the 11th World Conference on Earthquake Engineering*.

Lin, J. & Zhang, Y., 2005. Seismic random vibration of long span structures, *in Vibration and Shock Handbook, C.W. de Silva editor, CRC Press, Boca Raton, FL.*

Lin, J., Zhang, Y., Li, Q., & Williams, F., 2004. Seismic spatial effects for long span bridges using the pseudo excitation method, *Engineering Structures*, **26**, 1207–1216.

Loh, C. & Ku, B., 1995. An efficient analysis of structural response for multiple support seismic excitations, *Engineering Structures*, **17**, 15–26.

Lott, F. F., 2017. *Wind Systems in the Dead Sea and Footprints in Seismic Records*, vol. 70, KIT Scientific Publishing.

Lou, L., 2006. *Effect of the spatial variability of ground motions on the seismic response of reinforced concrete highway bridges*, Ph.D. thesis, Department of Civil, Architectural and Environmental Engineering, Drexel University, Philadelphia, PA.

Lou, L. & Zerva, A., 2005. Influence of spatial variation of ground motions on the nonlinear response of a multi span bridge, in *Proceedings of the Fourth European Workshop on the Seismic Behaviour of Irregular and Complex Structures, Thessaloniki, Greece*.

Lou, L. & Zerva, A., 2005a. Effects of spatially variable ground motions on the seismic response of a skewed, multi span bridge, *Soil Dynamics and Earthquake Engineering*, **25**, 729–740.

Luco, J. & Mita, A., 1987. Response of circular foundation to spatially random ground motion, *Journal of Engineering Mechanics, ASCE*, **113**, 1–15.

Luco, J. & Wong, H., 1986. Response of a rigid foundation to a spatially random ground motion, *Earthquake Engineering and Structural Dynamics*, **14**, 891–908.

Lupoi, A., Franchin, P., Pinto, P., & Monti, G., 2005. Seismic design of bridges account ing for spatial variability of ground motion, *Earthquake Engineering and Structural Dynamics*, **34**, 327–348.

MacDonald, R. & Viksne, A., 1980. *Strong Motion Instrumentation in Bureau of Reclamation Programs*, Bureau of Reclamation.

Maeso, O., Aznarez, J., & Domınguez, J., 2002. Effects of space distribution of excitation on seismic response of arch dams, *Journal of Engineering Mechanics, ASCE*, **128**, 759–768.

Maeso, O., Aznarez, J., & Domınguez, J., 2004. Three dimensional models of reservoir sediment and effects on the seismic response of arch dams, *Earthquake Engineering and Structural Dynamics*, **33**, 1103–1123.

Masri, S., 1976. Response of beams to propagating boundary excitation, *Earthquake Engineering and Structural Dynamics*, **4**, 497–507.

Matsushima, Y., 1977. Stochastic response of structure due to spatially variant earthquake excitations, in *Proceedings of the Sixth World Conference on Earthquake Engineering, New Delhi, India*.

Menke, W., Lerner-Lam, A., Dubendorff, B., & Pacheco, J., 1990. Polarization and coherence of 5 to 30 hz seismic wave fields at a hard rock site and their relevance to velocity heterogeneities in the crust, *Bulletin of the Seismological Society of America*, **80**, 430–449.

Mita, A. & Luco, J., 1986. Response of structures to a spatially random ground motion, in *Proceedings of the Third U.S. National Conference on Earthquake Engineering, Charleston, SC*.

Mitchell, S. A., 1996. A characterization of the quadrilateral meshes of a surface which admit a compatible hexahedral mesh of the enclosed volume, in *Annual Symposium on Theoretical Aspects of Computer Science*, pp. 465–476, Springer.

Monti, G. & Pinto, P., 1998. Effects of multi support excitation on isolated bridges, Tech. rep., Technical Report MCEER 98/0015, Multidisciplinary Center for Earthquake Engineering Research (MCEER), University at Buffalo, State University of New York, Buffalo, NY.

Monti, G., Nuti, C., & Pinto, P., 1996. Nonlinear response of bridges under multi support excitation, *Journal of Structural Engineering, ASCE*, **122**, 1147–1159.

Mylonakis, G., Simeonov, V., Reinhorn, A., & Buckle, I., 1999. Implications of spatial variation of ground motion on the collapse of sr14/i5 southbound separation and overhead bridge in the northridge earthquake, *ACI International Special Publication SP 187*, **34**, 299–327.

Mylonakis, G., Papastamatiou, D., Psycharis, J., & Mahmoud, K., 2001. Simplified modeling of bridge response on soft soil to nonuniform seismic excitation, *Journal of Bridge Engineering*, **6**, 587–597.

Nadim, F. & Gudmestad, O., 1994. Reliability of an engineering system under a strong earthquake with application to offshore platforms, *Structural Safety*, **14**, 203–217.

Nadim, F., Vanmarcke, E., Gudmestad, O., & Hetland, S., 1991. Influence of spatial variation of earthquake motion on response of gravity base platforms, *Structural Safety*, **10**, 113–128.

Nazmy, A. & Abdel Ghaffar, A., 1992. Effect of ground motion spatial variability on the response of cable stayed bridges, *Earthquake Engineering and Structural Dynamics*, **21**, 1–20.

Newland, D., 1984. An introduction to random vibrations and spectral analysis, *Longman Inc., New York*.

Newmark, N., 1967. Problems in wave propagation in soil and rocks, in *Proceedings of the International Symposium on Wave Propagation and Dynamic roperties of Earth Materials, University of New Mexico Press, Albuquerque, NM*.

Newmark, N., 1969. Torsion in symmetrical buildings, in *Proceedings of the Fourth World Conference on Earthquake Engineering, Santiago, Chile*.

Newmark, N., Hall, W., & Morgan, J., 1977. Building response and free field motion in earthquakes, in *Proceedings of the Sixth World Conference on Earthquake Engineering, New Delhi, India*.

Nose, M., 1970. Observation and measurement of dynamic behavior of the Kurobe dam, in *Tenth Congress, ICOLD, Montreal, C4. [Note: C is a standard ICOLD designation for Reports. It is a standard part of reference identification for ICOLD]*, pp. 461–479.

Nowak, P. & Hall, J., 1990. Arch dam response to nonuniform seismic input, *Journal of Engineering Mechanics, ASCE*, **116**, 125–139.

Nuti, C. & Vanzi, I., 2005. Influence of earthquake spatial variability on differential soil displacements and sdf system response, *Earthquake Engineering and Structural Dynamics*, **34**, 1353–1374.

NYCDOT, 1998. Seismic criteria guide lines, New York, NY, Tech. rep., New York City Department of Transportation (NYCDOT).

Okamoto, S. & Takahashi, T., 1960. On behaviors of an arch dam during earthquakes, in *Proceedings of the 2nd World Conference on Earthquake Engineering, Vol. 2, Tokyo, Japan*.

Okamoto, S., Yoshida, M., Kato, K., & Hakuno, M., 1964a. Dynamic behavior of an arch dam during earthquakes, Tech. rep., Report of the Institute of Industrial Science, The University of Tokyo.

Okamoto, S., Yoshida, M., Kato, K., & Hakuno, M., 1964b. Dynamic behavior of an arch dam during earthquakes, Tech. rep., Report of the Institute of Industrial Science, The University of Tokyo.

Oliveira, C., Hao, H., & Penzien, J., 1991. Ground motion modeling for multiple input structural analysis, *Structural Safety*, **10**, 79–93.

Oliveira, S., Espada, M., & Câmara, R., 2012. Long-term dynamic monitoring of arch dams. the case of Cabril dam, Portugal, in *15th World Conference On Earthquake Engineering*.

Olson, K., Nigbor, R., & Konno, T., 2000. 3d viscoelastic wave propagation in the Upper Borrego valley, California, constrained by borehole and surface data, *Bulletin of Seismological Society of America*, **90 No. 1**, 134–150.

Pais, A. & Kausel, E., 1990. Stochastic response of rigid foundations, *Earthquake En gineering and Structural Dynamics*, **19**, 611–622.

Park, S., Ghasemi, H., Shen, J., Somerville, P., Yen, W., & Yashinsky, M., 2004. Simulation of the seismic performance of the Bolu Viaduct subjected to near fault ground motions, *Earthquake Engineering and Structural Dynamics*, **33**, 1249–1270.

Perotti, F., 1990. Structural response to non stationary multiple support random excitation, *Earthquake Engineering and Structural Dynamics*, **19**, 513–527.

Peter, D., Komatitsch, D., Luo, Y., Martin, R., Le Goff, N., Casarotti, E., Le Loher, P., Magnoni, F., Liu, Q., Blitz, C., et al., 2011. Forward and adjoint simulations

of seismic wave propagation on fully unstructured hexahedral meshes, *Geophysical Journal International*, **186**(2), 721–739.

Poggi, V., Edwards, B., & Fäh, D., 2011. Derivation of a reference shear-wave velocity model from empirical site amplification, *Bulletin of the Seismological Society of America*, **101**(1), 258–274.

Price, T. & Eberhard, M., 1998. Effects of varying ground motions on short bridges, *Journal of Structural Engineering, ASCE*, **124**, 948–955.

Proulx, J. & Darbre, G., 2008. Earthquake response of large arch dams observational evidence and numerical modelling, in *14th World Conference On Earthquake Engineering, Beijing, China*.

Rautian, T. & Khalturin, V., 1978. The use of the coda for determination of the earthquake source spectrum, *Bulletin of the Seismological Society of America*, **68**(4), 923–948.

Riepl, J., Oliveira, C. S., & Bard, P.-Y., 1997. Spatial coherence of seismic wave fields across an alluvial valley (weak motion), *Journal of Seismology*, **1**(3), 253–268.

Rodrigues, J. & Brincker, R., 2005. Application of random decrement technique in operational modal analysis, in *Proceedings of the 1st International Operational Modal Analysis Conference (IOMAC), Copenhagen, Denmark*.

Sanchez-Sesma, F. & Rosenbleuth, E., 1979. Ground motion at canyons of arbitrary shape under incident sh waves, *Earthquake Engineering and Structural Dynamics*, **7**, 441–450.

Sanchez-Sesma, F., Faccioli, E., & Fregonese, R., 1986. An index for measuring the effects of topography on seismic ground motion intensity, *Earthquake Engineering and Structural Dynamics*, **14**, 719–734.

Sánchez-Sesma, F. J. & Campillo, M., 1993. Topographic effects for incident p, sv and rayleigh waves, *Tectonophysics*, **218**(1-3), 113–125.

Sawada, T. & Kamada, H., 1988, August 2-9. Modeling of nonstationary cross spectrum for multivariate earthquake motions by multifilter technique, in *Proceedings of the Nineth World Conference on Earthquake Engineering, II Tokyo, Japan*, vol. 795-800.

Saxena, V., 2000a. *Spatial variation of earthquake ground motion and development of bridge fragility curves*, Ph.D. thesis, Department of Civil Engineering and Operations Research, Princeton University, Princeton, NJ.

Saxena, V., Deodatis, G., Shinozuka, M., & Feng, M., 2000b. Development of fragility curves for multi span reinforced concrete bridges, in *Monte Carlo Simulation: Proceedings of the International Conference on Monte Carlo Simulation, MCS 2000, G.I. Schueller and P.D. Spanos Editors, Monte Carlo, Monaco*.

Scanlan, R., 1976. Seismic wave effects on soil structure interaction, *Earthquake Engineering and Structural Dynamics*, **4**, 379–388.

Schlupp, A., Avouac, J., & Clauzon, G., 2001. Post-messinian activity of the nimes fault, *Bulletin de la Société géologique de France*, **172**, 697–711.

Schneider, J., Abrahamson, N. S., & Stepp, J., 1990. Spatial variation of ground motion from EPRI's dense accelerograph array at Parkfield, California, in *Proceeding of Fourth U.S. National Conference on Earthquake Engineering, EERI, Palm Springs*, pp. 375–384.

Schneider, J., Stepp, J., & Abrahamson, N., 1992. The spatial variation of earthquake ground motion and effects of local site onditions, in *Proceedings of 10th World Conf on Earthquake Engineering, Madrid, Spain*.

Sdnchez-Sesma, F., 1983. Diffraction of elastic waves by three-dimensional surface irregularities, *Bull. seismological society of America*, **73**, 1621–1636.

Sextos, A. & Kappos, A., 2005. Evaluation of the new eurocode 8 part 2 provisions regarding asynchronous excitation of irregular bridges, in *Proceedings of the Fourth European Workshop on the Seismic Behaviour of Irregular and Complex Structures, Thessaloniki, Greece*.

Sextos, A., Pitilakis, K., & Kappos, A., 2003a. Inelastic dynamic analysis of rc bridges accounting for spatial variability of ground motion, site effects and soil structure inter action phenomena. part 1: Methodology and analytical tools, *Earthquake Engineering and Structural Dynamics*, **32**, 607–627.

Sextos, A., Kappos, A., & Pitilakis, K., 2003b. Inelastic dynamic analysis of rc bridges accounting for spatial variability of ground motion, site effects and soil structure inter action phenomena. part 2: Parametric study, *Earthquake Engineering and Structural Dynamics*, **32**, 629–652.

Sextos, A., Kappos, A., & Mergos, P., 2004. Effect of soil structure interaction and spatial variability of ground motion on irregular bridges: The case of the Krystallopigi bridge, in *Proceedings of the 13th World Conference on Earthquake Engineering, Van couver, Canada*.

Shinozuka, M., Saxena, V., & Deodatis, G., 2000. Effect of spatial variation of ground motion on highway structures, Tech. rep., Technical Report MCEER 00 0013, Multidisciplinary Center for Earthquake Engineering Research (MCEER), University at Buffalo, State University of New York, Buffalo, NY.

Skorik, L., 1981. Analysis of the earthquake records in the region of the Chirkey hydroelectric station, *Translated from Gidrotekhnicheskoe Stroitel'stvo No. 2*, **24**, 25–28.

Smith, S., Ehrenberg, J., & Hernandez, E., 1982. Analysis of the El Centro differential array for the 1979 Imperial Valley earthquake, *Bulletin of the Seismological Society of America*, **72**, 237–258.

Somerville, P., McLaren, J., Sen, M., & Helmberger, D., 1991. The influence of site conditions on the spatial incoherence of ground motions, *Structural Safety*, **10**, 1–13.

Somerville, P. G., McLaren, J. P., & Saikia, C. K., 1988. Site-specific estimation of spatial incoherence of strong ground motion, *Earthquake Engineering and Soil Dynamics II, Recent advances in ground motion evaluation., Geotechnical Special Publication, ASCE, New York*, **20**.

Soyluk, K. & Dumanoglu, A., 2004. Spatial variability effects of ground motions on cable stayed bridges, *Soil Dynamics and Earthquake Engineering*, **24**, 241–250.

Spudich, P., 1994. Recent seismological insights into the spatial variation of earthquake ground motions, *New Developments in Earthquake Ground Motion Estimation and Implications for Engineering Design Practice, ATC*, pp. 35–1.

Spudich, P. & Oppenheimer, D., 1986. Dense seismograph array observations of earthquake rupture dynamics, *Earthquake Source Mechanics*.

Sue, C. & Tricart, P., 2003. Neogene to ongoing normal faulting in the inner western alps: a major evolution of the alpine tectonics, *Tectonics*, **22**, 1–25.

Svay, A., Perron, V., Imtiaz, A., Zentner, I., Cottereau, R., Clouteau, D., Bard, P.-Y., Hollender, F., & Lopez-Caballero, F., 2017. Spatial coherency analysis of seismic ground motions from a rock site dense array implemented during the kefalonia 2014 aftershock sequence, *Earthquake Engineering & Structural Dynamics*.

Szczesiak, T., Weber, B., & Bachmann, H., 1999. Nonuniform earthquake input for arch dam foundation interaction, *Soil Dynamics and Earthquake Engineering*, **18**, 487–493.

Tamura, C., Noguchi, T., & Kato, K., 1977. Earthquake observation along measuring lines on the surface of alluvial soft ground, in *Proceedings of the Sixth World Conference on Earthquake Engineering, New Delhi, India*.

Thouvenot, F., Frechet, J., Jenatton, L., & Gamond, J., 2003. The belledonne border fault: identification of an active seismic strike-slip fault in the western alps, *Geophysical Journal International*, **155**, 174–192.

Toksoz, M. & Johnston, D., 1981. Seismic wave attenuation: Society of exploration geophysicists, *Geophysics reprint series*.

Trifunac, M., 1973. Scattering of plane sh waves by a semi-cylindrical canyon, *Earthquake Engineering and Structural Dynamics*, **1**, 267–281.

Trifunac, M. & Gicev, V., 2006. Response spectra for differential motion of columns paper ii: Out of plane response, *Soil Dynamics and Earthquake Engineering*, **26**, 1149–1160.

Trifunac, M. & Todorovska, M., 1997. Response spectra for differential motion of columns, *Earthquake Engineering and Structural Dynamics*, **26**, 251–268.

Tsung-Ho, H., Hsueh-hai, L., Tu-hsin, H., & Cheng-jung, Y., 1976. Strong-motion observation of water-induced earthquakes at Hsinfengkiang reservoir in China, *Engineering Geology*, **10**(2-4), 315–330.

Tzanetos, N., Elnashai, A., Hamdan, F., & Antoniou, S., 2000. Inelastic dynamic response of rc bridges subjected to spatially non synchronous earthquake motion, *Advances in Structural Engineering*, **3**, 191–214.

U.S. Army, C. o. E., 1958. Gravity dam design, Tech. rep., Design Manual EM 1110-2-2200. Washington, D.C.

Vanmarcke, E., 2010. *Random fields: analysis and synthesis*, World Scientific Publishing Co Inc.

Veletsos, A. & Prasad, A., 1989. Seismic interaction of structures and soils: Stochastic approach, *Journal of Structural Engineering, ASCE*, **115**, 935–956.

Veletsos, A., Prasad, A., & Wu, W., 1997. Transfer functions for rigid rectangular foundations, *Earthquake Engineering and Structural Dynamics*, **26**, 5–17.

Vigny, C., Chery, J., Duquesnoy, T., Jouanne, F., Ammann, J., Anzidei, M., Avouac, J.-P., Barlier, F., Bayer, R., Briole, P., et al., 2002. Gps network monitors the western alps' deformation over a five-year period: 1993–1998, *Journal of Geodesy*, **76**(2), 63–76.

Walpersdorf, A., Sue, C., Baize, S., Cotte, N., Bascou, P., Beauval, C., Collard, P., Daniel, G., Dyer, H., Grasso, J.-R., Hautecoeur, O., Helmstetter, A., Hok, S., Langlais, M., Menard, G., Mousavi, Z., F., P., Rizza, M., Rolland, L., Souami, D.,

Thirard, L., Vaudey, P., Voisin, C., & Martinod, J., 2015. Coherence between geodetic and seismic deformation in a context of slow tectonic activity (SW Alps, France), *Journal of Geodynamics*, **85**, 58–65.

Werner, S. & Lee, L., 1979. The three dimensional response of structures subjected to traveling wave excitation, in *Proceedings of the Second U.S. National Conference on Earthquake Engineering, Stanford, CA*.

Werner, S., Lee, L., Wong, H., & Trifunac, M., 1979. Structural response to traveling seismic waves, *Journal of the Structural Division, ASCE*, **105**, 2547–2564.

White, D. R., Mingwu, L., Benzley, S. E., & Sjaardema, G. D., 1995. Automated hexahedral mesh generation by virtual decomposition, in *Proceedings of the 4th International Meshing Roundtable, Sandia National Laboratories, Albuquerque, USA*, pp. 165–176.

Wong, H., 1982. Effect of surface topography on the diffraction of p, sv, and rayleigh waves, *Bulletin of the Seismological Society of America*, **72**(4), 1167–1183.

Wong, H. & Jennings, P., 1975. Effects of canyon topography on strong ground motion, *Bulletin of the Seismological Society of America*, **65**, 1239–1257.

Wong, H. & Trifunac, M., 1974. Scattering of plane sh waves by a semi-elliptical canyon, *Earthquake Engineering and Structural Dynamics*, **3**, 157–169.

Yamahara, H., 1970. Ground motion during earthquakes and the input loss of earthquake power to excitation of buildings, *Journal of Soils and Foundations*, **10**, 145–161.

Yamamura, N. & Tanaka, H., 1990. Response analysis of flexible mdf systems for multiple support seismic excitations, *Earthquake Engineering and Structural Dy namics*, **19**, 345–357.

Yamazaki, F. & Shimizu, Y., 2000. Super dense real-time monitoring of earthquakes for a city gas network in Japan, in *Proceedings of the 17th International Symposium on Automation and Robotics in Construction*, pp. 581–586.

Yang, Z., He, L., Bielak, J., Zhang, Y., Elgamal, A., & Conte, J., 2003. Nonlinear seismic response of a bridge site subject to spatially varying ground otion, in *Proceedings of the 16th Engineering Mechanics Conference, ASCE, Seattle, WA*.

Zembaty, Z. & Krenk, S., 1993. Spatial seismic excitations and response spectra, *Journal of Engineering Mechanics, ASCE*, **119**, 2449–2460.

Zembaty, Z. & Rutenberg, A., 2002. Spatial response spectra and site amplification effects, *Engineering Structures*, **24**, 1484–1496.

Zerva, A., 1990. Response of multi span beams to spatially incoherent seismic ground mo tions, *Earthquake Engineering and Structural Dynamics*, **19**, 819–832.

Zerva, A., 1991. Effect of spatial variability and propagation of seismic ground motions on the response of multiply supported structures, *Probabilistic Engineering Mechanics*, **6**, 212–221.

Zerva, A., 1993. Pipeline response to directionally and spatially correlated seismic ground motions, *Journal of Pressure Vessel Technology, ASME*, **115**, 53–58.

Zerva, A., 2009. *Spatial variation of seismic ground motions. Modeling and engineering applications*, CRC Press.

Zerva, A. & Harada, T., 1997. Effect of surface layer stochasticity on seismic ground motion coherence and strain estimates, *Soil Dynamics and Earthquake Engineering*, **16**, 445–457.

Zerva, A. & Zervas, V., 2002. Spatial variation of seismic ground motions: an overview, *Applied Mechanics Review, ASME*, **55(3)**, 271–297.

Zerva, A. & Zhang, O., 1997. Correlation patterns in characteristics of spatially variable seismic ground motions, *Earthquake Engineering and Structural Dynamics*, **26**, 19–39.

Zerva, A., Ang, A., & Wen, Y., 1988. Lifeline response to spatially variable ground motions, *Earthquake Engineering and Structural Dynamics*, **16**, 361–379.

Zhang, L. & Chopra, A., 1991a. Three dimensional analysis of spatially varying ground motions around a uniform canyon in a homogeneous half space, *Earthquake Engineering and Structural Dynamics*, **20**, 911–926.

Zhang, L. & Chopra, A. K., 1991b. Impedance functions for three-dimensional foundations supported on an infinitely-long canyon of uniform cross-section in a homogeneous half-space, *Earthquake engineering & structural dynamics*, **20**(11), 1011–1027.

Appendix A

Appendix A: Array stations in Saint Guérin

A.1 Coordinates of the array stations

TABLE A.1: Coordinates of the array stations

Index	Station Name	Latitude (deg)	Longitude (deg)	Easting (m)	Northing (m)	Elevation (m)
1	**SG01**	45.6507	6.5805	311479.7946	5058089.4700	1559
2	**SG02**	45.6503	6.5801	311441.7292	5058047.2441	1559
3	**SG03**	45.6501	6.5793	311387.5522	5058027.1685	1559
4	**SG04**	45.6502	6.5786	311330.0347	5058036.6808	1559
5	**SG05**	45.6506	6.5779	311277.9282	5058082.7460	1559.049
6	**SG06**	45.6504	6.5782	311298.1364	5058062.7688	1538.123
7	**SG07**	45.6503	6.5784	311315.2544	5058050.3727	1524.945
8	**SG08**	45.6503	6.5787	311333.2014	5058042.2540	1513.351
9	**SG09**	45.6502	6.5794	311388.2690	5058029.0827	1510.598
10	**SG10**	45.6502	6.5797	311414.4638	5058037.4085	1514.012
11	**SG11**	45.6504	6.5800	311437.0546	5058049.6344	1523.442
12	**SG12**	45.6505	6.5803	311461.6425	5058068.8345	1544.12
13	**SG13**	45.6508	6.5793	311383.1002	5058083.4655	1499.78
14	**SG14**	45.6512	6.5796	311409.7611	5058145.8459	1510.598
15	**SG15**	45.6517	6.5793	311386.8311	5058196.9956	1503
17	**SG17**	45.6512	6.5808	311503.5795	5058143.0660	1578.32
18	**SG18**	45.6521	6.5810	311521.5348	5058238.6936	1622.82
19	**SG19**	45.6464	6.5830	311658.7000	5057602.7000	1610
20	**SG20**	45.6427	6.5767	311155.3500	5057206.4700	1612

A.2 Station separation distances

TABLE A.2: Station separation distances (m)

	SG01	**SG02**	**SG03**	**SG04**	**SG05**	**SG06**	**SG07**	**SG08**	**SG09**	**SG10**	**SG11**	**SG12**	**SG13**	**SG14**	**SG15**	**SG17**	**SG18**	**SG19**	**SG20**
SG01	0,000	56,851	111,311	158,791	201,978	184,793	172,516	160,632	119,860	94,881	68,396	31,253	113,547	102,106	152,774	61,737	167,580	521,108	942,211
SG02	56,851	0,000	57,777	112,193	167,604	145,931	131,017	117,843	74,368	53,517	35,944	32,926	90,865	114,399	169,042	115,674	217,013	497,289	889,788
SG03	111,311	57,777	0,000	58,299	122,908	98,481	83,217	72,563	48,445	53,414	64,958	86,295	81,830	130,078	178,823	165,130	258,393	506,256	854,560
SG04	158,791	112,193	58,299	0,000	69,549	46,195	39,569	46,097	76,103	95,670	113,514	136,293	92,259	143,583	179,061	204,472	285,577	546,773	850,043
SG05	201,978	167,604	122,908	69,549	0,000	35,290	60,036	82,359	131,918	150,751	166,389	184,844	120,725	153,977	167,494	234,368	296,193	614,839	886,391
SG06	184,793	145,931	98,481	46,195	35,290	0,000	24,907	47,582	100,081	121,477	140,308	163,728	95,485	141,843	164,673	224,210	296,698	588,928	871,260
SG07	172,516	131,017	83,217	39,569	60,036	24,907	0,000	22,857	77,397	100,648	121,812	148,788	79,570	135,102	164,630	216,581	295,966	570,614	863,319
SG08	160,632	117,843	72,563	46,097	82,359	47,582	22,857	0,000	56,688	81,409	104,603	134,723	66,125	128,842	164,098	208,357	293,328	555,426	860,173
SG09	119,860	74,368	48,445	76,103	131,918	100,081	77,397	56,688	0,000	27,697	54,474	89,931	55,689	118,725	168,091	175,713	272,562	514,603	860,944
SG10	94,881	53,517	53,414	95,670	150,751	121,477	100,648	81,409	27,697	0,000	27,363	64,187	57,511	108,593	162,336	152,449	252,624	507,776	875,900
SG11	68,396	35,944	64,958	113,514	166,389	140,308	121,812	104,603	54,474	27,363	0,000	37,427	67,938	100,829	157,021	127,148	229,687	506,329	893,379
SG12	31,253	32,926	86,295	136,293	184,844	163,728	148,788	134,723	89,931	64,187	37,427	0,000	91,373	98,723	153,990	91,862	196,553	510,346	917,658
SG13	113,547	90,865	81,830	92,259	120,725	95,485	79,570	66,125	55,689	57,511	67,938	91,373	0,000	68,696	113,637	155,679	241,658	565,013	913,009
SG14	102,106	114,399	130,078	143,583	153,977	141,843	135,102	128,842	118,725	108,593	100,829	98,723	68,696	0,000	56,567	115,741	183,597	605,689	978,486
SG15	152,774	169,042	178,823	179,061	167,494	164,673	164,630	164,098	168,091	162,336	157,021	153,990	113,637	56,567	0,000	149,036	185,042	662,230	1023,037
SG17	61,737	115,674	165,130	204,472	234,368	224,210	216,581	208,357	175,713	152,449	127,148	91,862	155,679	115,741	149,036	0,000	106,992	563,082	999,805
SG18	167,580	217,013	258,393	285,577	296,193	296,698	295,966	293,328	272,562	252,624	229,687	196,553	241,658	183,597	185,042	106,992	0,000	650,743	1095,305
SG19	521,108	497,289	506,256	546,773	614,839	588,928	570,614	555,426	514,603	507,776	506,329	510,346	565,013	605,689	662,230	563,082	650,743	0,000	640,596
SG20	942,211	889,788	854,560	850,043	886,391	871,260	863,319	860,173	860,944	875,900	893,379	917,658	913,009	978,486	1023,037	999,805	1095,305	640,596	0,000

A.3 Data availability

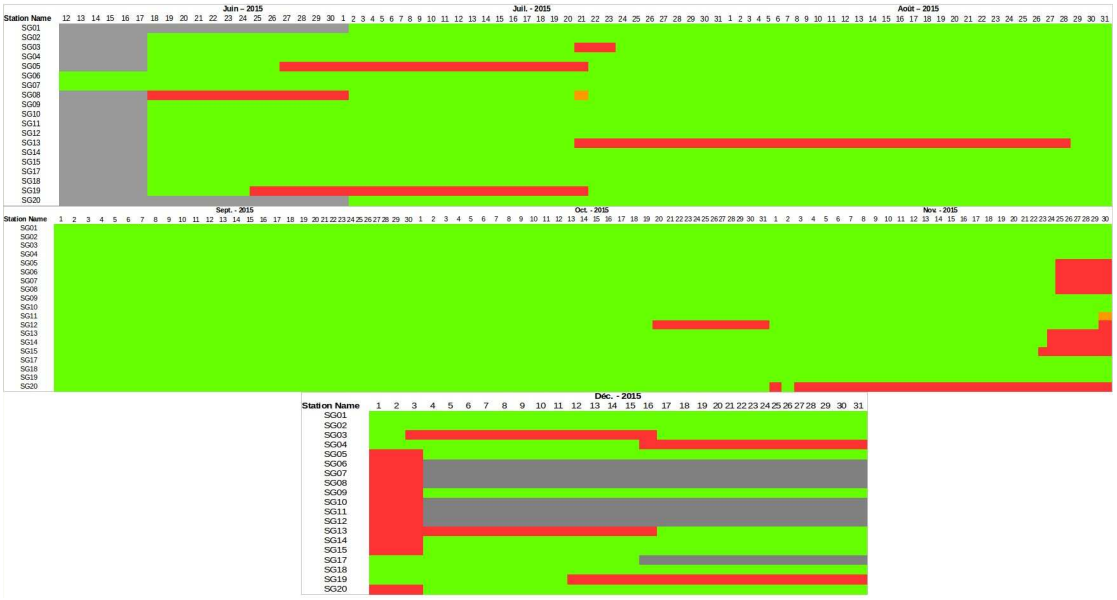

FIGURE A.1: Data availability recorded from the 19 stations. The left cologne indicates the period between two visits. Green rectangles indicate $95 - 100\%$ of data availability, red rectangles $\leq 50\%$ and orange $\geq 87.5\%$ of data availability. The gray zones correspond to absence of data due to removal of a station.

Appendix B

Appendix B: Seismological catalog of Saint Guérin events

B.1 Seismological catalog of Saint Guérin events

TABLE B.1: Seismological catalog of events recorded from the Saint Guérin network from June 2015 till December 2015 (metadata provided by Renass catalog)

	YYYY – MM – DD UTC	**Latitude(deg)**	**Longitude(deg)**	**Magnitude(M_L)**	**Depth(km)**	**R_{epi}(km)**
1	2015-07-19T04:10:48.302000+00:00	44.468	6.612	2.4	2	108,11
2	2015-07-11T09:40:47.561000+00:00	46.849	7.218	1.9	9	177,92
3	2015-07-17T17:38:30.456000+00:00	46.093	7.421	1.7	11	120,06
4	2015-06-20T13:22:38.532000+00:00	44.416	6.765	2.7	7	117,43
5	2015-06-20T10:30:22.749000+00:00	46.224	7.366	3.0	16	126,79
6	2015-09-14T21:36:29.575000+00:00	44.129	7.181	2.7	7	160,18
7	2015-07-19T04:12:48.411000+00:00	44.513	6.688	1.7	8	105,19
8	2015-07-19T04:15:42.069000+00:00	44.524	6.702	2.8	10	104,43
9	2015-07-30T05:52:03.228000+00:00	44.507	6.73	2.6	9	106,99
10	2015-08-05T07:20:06.290000+00:00	46.746	7.492	1.9	4	178,26
11	2015-08-05T03:24:41.124000+00:00	44.476	6.966	1.6	4	118,10
12	2015-08-22T09:55:14.067000+00:00	45.995	7.27	2.0	2	104,14
13	2015-09-10T07:32:08.332000+00:00	44.816	7.205	3.3	1	100,41
14	2015-09-12T09:27:00.001000+00:00	44.445	7.311	2.3	6	136,19
16	2015-09-21T12:10:01.441000+00:00	44.593	6.369	1.9	17	90,63
17	2015-08-07T02:23:10.233000+00:00	47.327	6.488	1.9	10	214,92
18	2015-08-15T18:34:15.818000+00:00	46.647	7.596	2.6	23	173,93
20	2015-08-18T07:10:10.589000+00:00	46.824	8.088	2.1	18	213,23
21	2015-09-24T09:58:16.642000+00:00	42.871	6.404	2.4	0	281,80
22	2015-09-24T12:53:41.557000+00:00	44.482	6.729	2.8	10	109,55
23	2015-09-28T12:40:15.443000+00:00	46.669	4.571	2.0	7	190,47
24	2015-09-30T14:14:50.674000+00:00	44.551	6.787	1.9	8	104,24
25	2015-10-06T06:03:10.280000+00:00	45.4	6.277	1.7	8	3,53
26	2015-10-10T00:16:36.032000+00:00	45.17	4.071	1.9	9	171,01
27	2015-10-10T20:18:04.870000+00:00	44.532	8.833	3.3	0	226,36
28	2015-10-14T14:46:01.489000+00:00	46.329	7.618	2.2	14	148,79
29	2015-10-15T17:02:10.407000+00:00	46.273	7.456	2.1	11	135,53
30	2015-11-06T03:03:03.926000+00:00	44.491	6.739	4.1	12	108,90
31	2015-11-16T21:06:41.556000+00:00	44.744	7.772	3.4	14	141,37
32	2015-10-30T15:16:49.905000+00:00	44.616	7.334	2.7	3	123,09
33	2015-11-08T21:03:42.959000+00:00	45.67	7.032	2.7	8	69,07
34	2015-11-06T10:50:53.274000+00:00	45.024	6.848	2.6	0	64,02
35	2015-10-30T11:16:11.006000+00:00	43.952	7.745	2.5	0	200,80
36	2015-10-31T00:20:17.468000+00:00	43.971	7.753	2.5	2	199,47
37	2015-10-31T04:54:31.875000+00:00	45.43	6.32	2.3	4	7,54
38	2015-10-26T04:26:45.413000+00:00	47.648	8.898	2.3	16	322,44
39	2015-10-26T21:15:36.684000+00:00	44.96	5.393	2.2	10	82,10
40	2015-12-05T08:11:43.936000+00:00	44.547	6.732	2.2	10	102,92
41	2015-11-06T19:43:06.661000+00:00	44.488	6.731	2.1	9	108,99
42	2015-11-13T15:09:04.363000+00:00	46.238	7.431	2.1	6	131,42
44	2015-11-06T03:32:58.451000+00:00	44.48	6.769	2.0	0	110,92
45	2015-10-21T18:36:14.854000+00:00	44.952	5.41	2.0	9	81,59
46	2015-11-07T11:42:46.965000+00:00	45.956	6.753	1.9	8	73,69
47	2015-10-24T03:19:05.079000+00:00	45.678	6.856	1.9	4	57,47
48	2015-11-27T19:06:26.954000+00:00	46.004	6.889	1.9	5	84,15
49	2015-11-08T14:18:25.507000+00:00	45.992	6.894	1.9	0	83,34
50	2015-11-02T11:43:52.503000+00:00	46.199	5.257	1.9	5	116,45
51	2015-12-06T10:04:59.105000+00:00	44.564	6.733	1.8	5	101,20
52	2015-11-03T18:25:11.507000+00:00	44.94	6.624	1.8	5	59,89
53	2015-11-12T17:27:06.918000+00:00	45.994	6.893	1.7	9	83,46
54	2015-12-06T17:13:05.191000+00:00	45.074	7.263	1.7	10	88,60
55	2015-11-10T22:43:14.094000+00:00	45.987	6.896	1.6	9	83,00
56	2015-11-18T08:10:41.083000+00:00	46.372	7.604	2.6	9	151,35
57	2015-10-30T13:35:53.571000+00:00	45.413	6.331	1.5	6	7,83
58	2015-12-09T03:58:53.179000+00:00	45.109	7.261	1.5	1	86,91

B.2 Signal-to-noise ratio (SNR) of the velocity time series

NS component

	SG01	SG02	SG03	SG04	SG05	SG06	SG07	SG08	SG09	SG10	SG11	SG12	SG13	SG14	SG15	SG17	SG18	SG19	SG20
Event 1	0,00	0,00	0,00	0,00	0,00	13,96	13,56	12,93	11,58	12,48	0,00	13,58	14,28	13,32	13,58	13,39	14,54		14,82
Event 2	0,00	0,00	0,00	0,00	0,00	0,00	0,00	0,00	0,00	0,00	0,00	0,00	0,00	0,00	0,00	4,64	0,00		8,01
Event 3	12,30	0,00	0,00	0,00	0,00	9,80	7,47	0,00	0,00	0,00	0,00	0,00	11,44	0,00	0,00	11,99	0,00		12,69
Event 4	0,00	0,00	0,00	0,00	0,00	12,84	0,00	0,00	0,00	0,00	0,00	13,15	13,88	12,51	12,89	13,37	13,80	12,06	0,00
Event 5	0,00	10,55	0,00	0,00	14,49	13,31	12,44	0,00	12,68	12,40	8,91	13,28	14,63	14,73	15,28	15,69	16,41	15,42	0,00
Event 6	0,00	0,00	0,00	0,00	0,00	12,69	12,50	11,89	0,00	0,00	0,00	12,73	13,32	12,09	12,79	12,16	0,00	14,17	13,34
Event 7	0,00	0,00	0,00	0,00		10,04	9,26	7,89	6,42	6,25	0,00	9,15	10,69	0,00	0,00	8,94	0,00		10,97
Event 8	14,68	0,00	0,00	0,00		14,82	14,52	14,02	13,07	13,59	7,13	14,42	15,10	0,00	0,00	0,00	0,00		0,00
Event 9	0,00	0,00	0,00	0,00	13,87	12,17	10,47	8,76	7,81	7,98	0,00	0,00		11,62	12,98	13,46	14,71	14,70	0,00
Event 10	0,00	0,00	0,00	0,00	0,00	0,00	0,00	0,00	0,00	0,00	0,00	0,00		9,44	9,81	0,00	0,00	11,41	0,00
Event 11	15,54	0,00	0,00	0,00	14,97	14,39	14,02	13,89	13,34	13,83	0,00	14,65		15,52	16,00	14,82	15,93	15,74	0,00
Event 12	15,22	11,27	0,00	11,47	14,50	13,80	12,99	12,27	12,73	12,81	0,00	13,47		14,43	14,89	14,45	15,77	13,88	0,00
Event 13	16,27	14,96	0,00	15,14	16,48	15,99	15,69	15,38	15,26	15,28	11,19	15,59	16,08	15,72	15,87	15,67	16,32	16,93	16,24
Event 14	12,94	0,00	0,00	0,00	13,25	0,00	0,00	0,00	0,00	0,00	0,00	0,00	12,36	11,12	11,39	11,44	12,91	12,74	12,74
Event 16	10,99	0,00	0,00	0,00	12,10	10,78	9,54	0,00	0,00	0,00	0,00	0,00	11,31	9,63	0,00	10,35	12,20	12,16	12,31
Event 17	0,00	0,00	0,00	0,00	10,67	8,29	7,18	5,31	0,00	0,00	0,00	0,00		11,45	11,64	10,60	0,00	13,16	0,00
Event 18	0,00	10,41	0,00	10,70	13,69	12,85	11,87	10,89	11,40	11,83	0,00	12,79		13,20	14,29	14,09	15,47	15,27	0,00
Event 20	10,75	0,00	0,00	0,00	0,00	0,00	0,00	0,00	0,00	0,00	0,00	0,00		0,00	0,00	0,00	0,00	8,77	0,00
Event 21	0,00	0,00	0,00	0,00	10,49	0,00	9,02	6,61	0,00	9,68	0,00	0,00	10,54	0,00	0,00	0,00	0,00	0,00	11,22
Event 22	0,00	11,14	11,52	0,00	14,73	14,26	13,80	13,11	13,29	13,75	4,37	13,61	14,16	13,38	14,09	13,48	14,54	12,70	14,58
Event 23	11,18	0,00	0,00	0,00	0,00	0,00	0,00	0,00	0,00	0,00	0,00	0,00	11,03	0,00	11,24	0,00	0,00	0,00	12,85
Event 24	0,00	0,00	9,45	0,00	10,80	0,00	9,87	0,00	8,77	0,00	9,73	0,00	0,00	0,00	8,50	0,00	9,72	0,00	10,39
Event 25	13,98	7,87	0,00	6,18	14,32	12,63	11,68	11,03	10,43	0,00	10,94	11,47	13,94	14,55	14,99	14,20	15,06	15,22	15,24
Event 26	0,00	0,00	0,00	0,00	11,97	9,67	8,16	0,00	0,00	0,00	0,00	0,00	10,73	10,23	11,73	10,58	12,64	0,00	12,83
Event 27	0,00	13,47	14,08	12,95	15,63	15,36	14,93	14,26	14,54	0,00	15,37	14,98	15,33	14,85	15,10	14,77	16,04	16,33	15,64
Event 28	0,00	0,00	0,00	0,00	12,26	0,00	0,00	0,00	0,00	0,00	9,51	10,23	12,27	11,94	12,19	12,70	12,45	14,23	13,75
Event 29	0,00	0,00	0,00	0,00	12,00	9,59	7,41	0,00	0,00	0,00	8,11	9,13	11,93	12,45	13,42	12,85	14,41	13,98	14,05
Event 30	17,21	0,00	0,00	0,00	17,46	16,79	16,35	16,25	15,94	16,03	16,15	16,02	17,09	16,87	16,84	16,62	17,76	17,28	
Event 31	16,24	14,08	14,56	14,05	16,24	15,62	15,34	15,19	15,49	15,46	15,75	15,61	16,23	15,83	15,97	15,36	16,77	16,45	
Event 32	12,62	0,00	0,00	0,00	13,32	11,37	10,08	9,31	0,00	0,00	9,12		12,40	11,48	12,13	12,35	14,32	13,21	13,93
Event 33	17,01	14,72	14,42	14,43	16,66	16,12	15,71	15,68	15,84	15,92	16,13	16,17	16,76	17,02	16,98	16,23	17,38	16,94	
Event 34	14,51	0,00	0,00	0,00	14,69	13,65	12,81	12,68	12,47	12,32	12,96	12,81	14,32	13,48	13,90	13,62	15,35	14,56	
Event 35	0,00	0,00	0,00	0,00	0,00	0,00	0,00	0,00	0,00	0,00	0,00		0,00	0,00	9,85	10,12	13,15	11,96	13,10
Event 36	10,05	0,00	0,00	0,00	0,00	0,00	0,00	0,00	0,00	0,00	0,00		0,00	7,91	8,98	0,00	12,31	11,19	10,72
Event 37	15,92	13,34	13,28	12,80	16,14	15,20	14,69	14,52	14,21	14,23	14,39		15,91	15,94	16,27	15,60	16,79	16,67	16,05
Event 38	12,17	0,00	0,00	0,00	0,00	0,00	0,00	0,00	0,00	0,00	0,00		10,88	9,52	0,00	0,00	12,63	12,68	12,03
Event 39	14,06	0,00	0,00	0,00	14,33	13,52	12,81	11,96	11,48	11,86	12,80		13,68	12,58	13,30	13,12	14,80	15,23	14,43
Event 40	0,00	0,00		0,00	12,75	0,00	0,00	0,00	7,22	0,00	0,00	0,00		0,00	12,67	10,12	0,00	11,79	13,13
Event 41	12,21	0,00	0,00	0,00	12,46	10,53	8,87	8,25	0,00	0,00	9,01	0,00	11,57	10,82	11,40	9,82	13,02	12,79	
Event 42	12,87	0,00	0,00	0,00	0,00	0,00	0,00	0,00	0,00	9,58	10,47	0,00	12,27	12,72	13,13	10,72	0,00	12,88	
Event 44	17,13	14,68	14,58	14,58	17,39	16,74	16,29	16,22	16,01	15,99	16,15	16,07	17,08	16,80	16,86	16,71	17,76	17,31	
Event 45	12,56	9,09	0,00	8,64	13,07	12,70	12,37	11,35	11,27	12,18	12,84		12,61	11,56	12,10	11,48	13,22	14,17	13,29
Event 46	13,80	0,00	0,00	0,00	13,13	11,43	9,38	8,68	9,38	9,46	10,21	9,92	13,15	13,55	14,30	13,48	15,31	4,12	
Event 47	15,26	10,22	0,00	0,00	15,06	13,80	12,87	12,26	12,29	12,50	12,80		14,82	15,13	15,54	14,95	16,30	16,03	16,00
Event 48	0,00	11,05	0,00	0,00	0,00	0,00	0,00	0,00	12,61	12,69	12,66	13,29				14,37	15,78	14,65	
Event 49	14,29	0,00	0,00	0,00	13,83	12,59	0,00	0,00	0,00	0,00	12,85	12,44	14,03	14,08	14,51	13,38	15,00	11,82	
Event 50	10,65	0,00	0,00	0,00	10,26	0,00	0,00	0,00	0,00	0,00	0,00	0,00	9,84	0,00	10,28	11,36	13,67	12,34	13,75
Event 51	0,00	0,00		0,00	11,66	0,00	0,00	0,00	0,00	0,00	0,00	0,00		0,00	9,82	0,00	0,00	10,67	11,69
Event 52	11,38	0,00	0,00	0,00	12,04	0,00	0,00	0,00	0,00	0,00	0,00	0,00	11,13	11,01	11,97	0,00	13,03	0,00	
Event 53	14,64	0,00	0,00	0,00	0,00	12,79	11,87	11,56	12,38	12,00	12,40	0,00	14,17	15,00	14,99	13,31	0,00	14,22	
Event 54	0,00	0,00		0,00	0,00	0,00	0,00	0,00	0,00	0,00	0,00	0,00		0,00	12,44	0,00	0,00	9,92	12,25
Event 55	13,97	0,00	0,00	0,00	0,00	11,97	10,67	10,02	11,65	11,09	11,94	0,00	13,45	13,97	14,36	12,20	0,00	13,64	
Event 56	0,00	12,85	12,15	12,06	14,54	13,80	13,15	12,93	13,76	13,70	14,21	14,09	15,08	14,86	15,17	14,47	15,78	15,32	
Event 57	13,37	0,00	0,00	0,00	0,00	0,00	0,00	0,00	0,00	0,00	0,00		13,52	13,91	14,44	13,38	14,59	12,96	14,67
Event 58	0,00	0,00		0,00	0,00	0,00	0,00	0,00	0,00	0,00	0,00	0,00		0,00	13,88	0,00	0,00	0,00	12,75

FIGURE B.1: Signal-to-noise ratio (SNR) of the velocity time series of the NS component of all stations for the 55 selected seismic events; gray squares correspond to absence of the station, red squares to missing data due to malfunctioning of the station and red 0 values to $SNR \leq 3$.

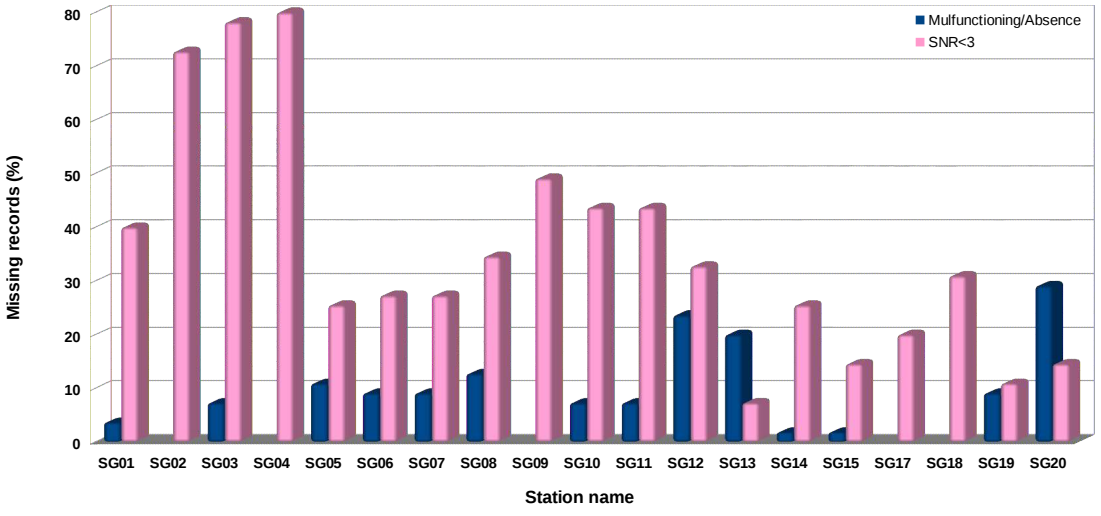

FIGURE B.2: Percentage (%) of missing records because of malfunctioning/absence of a station (blue bars) and because of $SNR \leq 3$ (pink bars).

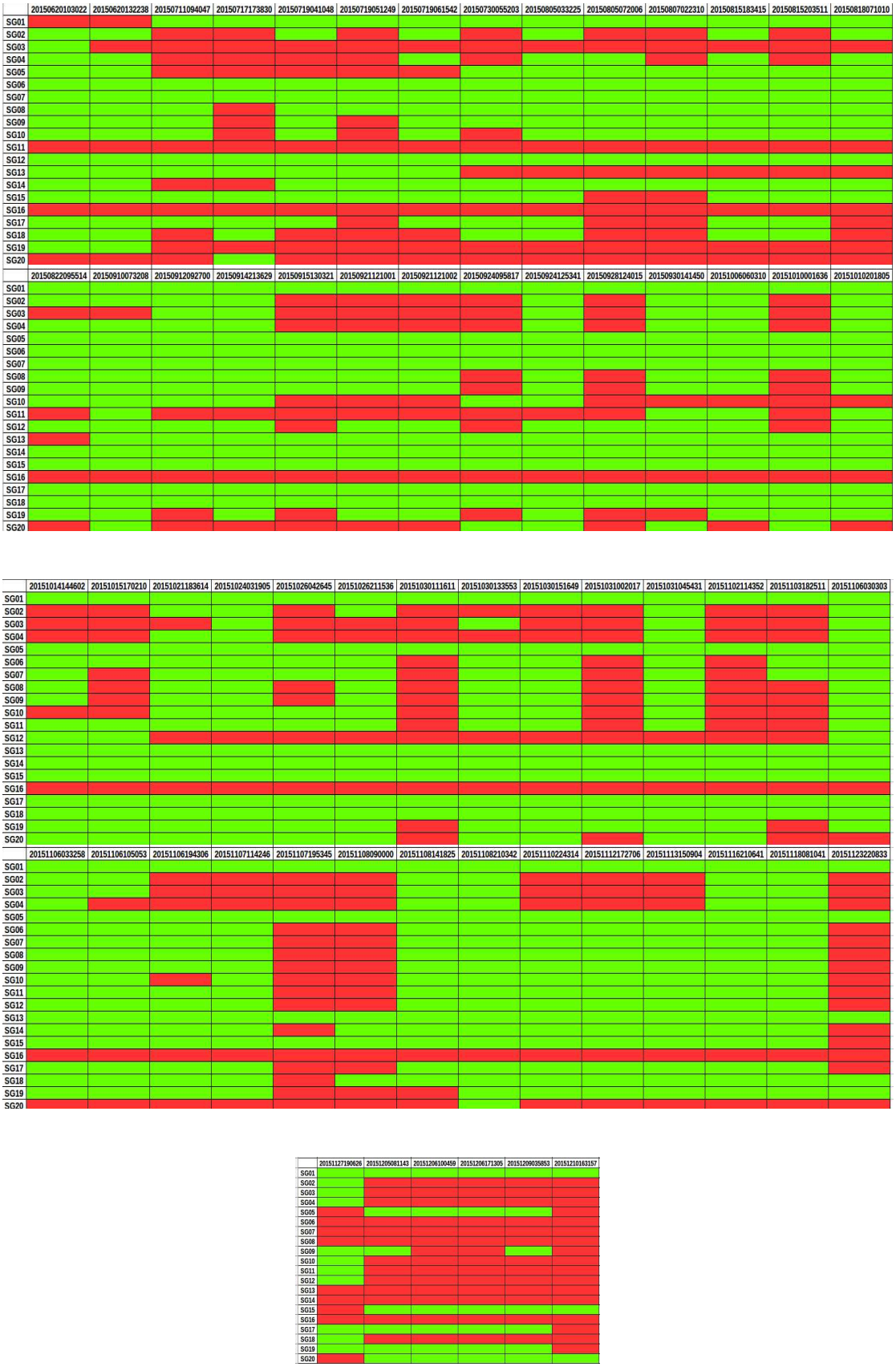

FIGURE B.3: Data availability recorded from the 19 stations for each of the 55 events. Green rectangles indicate available record, red rectangles indicate absense either due to mulfunctioning or because of low SNR.

B.3 Peak Ground Velocity values

TABLE B.2: Peak Ground Velocity values (PGV) for the NS component of all the available recordings for the subset of events.

	NS component																	
	SG01	**SG02**	**SG03**	**SG04**	**SG05**	**SG06**	**SG07**	**SG08**	**SG09**	**SG10**	**SG11**	**SG12**	**SG13**	**SG14**	**SG15**	**SG17**	**SG18**	**SG19**	**SG20**
Event 1	0	0	0	0	0	6,64E-007	5,99E-007	5,77E-007	5,13E-007	5,27E-007	0	5,42E-007	4,83E-007	5,21E-007	5,45E-007	5,45E-007	7,78E-007	0	4,50E-007
Event 2	7,60E-008	0	0	0	0	0	0	0	6,60E-008	4,54E-008	0	0	0	0	0	6,03E-008	0	0	8,56E-008
Event 3	3,65E-007	0	0	0	0	2,28E-007	2,73E-007	0	0	0	0	0	3,54E-007	0	0	4,00E-007	0	0	2,34E-007
Event 4	0	0	0	0	0	1,02E-006	0	0	0	0	0	7,61E-007	7,42E-007	8,19E-007	8,27E-007	7,50E-007	1,19E-006	4,76E-006	0
Event 5	0	5,07E-005	0	0	2,84E-006	2,64E-006	2,41E-006	0	3,68E-006	3,77E-006	3,92E-006	4,79E-006	3,74E-006	5,46E-006	5,59E-006	5,17E-006	5,84E-006	2,09E-005	0
Event 6	0	0	0	0	0	5,87E-007	5,75E-007	5,24E-007	0	0	0	6,04E-007	5,16E-007	4,69E-007	5,83E-007	5,51E-007	0	2,51E-006	5,95E-007
Event 7	0	0	0	0	0	1,58E-007	1,47E-007	1,31E-007	1,31E-007	9,79E-008	0	1,11E-007	9,76E-008	0	0	1,03E-007	0	0	9,52E-008
Event 8	8,99E-007	0	0	0	0	1,07E-006	9,69E-007	9,37E-007	8,26E-007	8,49E-007	9,37E-007	9,32E-007	8,54E-007	0	0	0	0	0	0
Event 9	0	0	0	0	8,70E-007	7,99E-007	7,98E-007	7,39E-007	7,05E-007	6,65E-007	0	0	0	5,66E-007	5,84E-007	6,59E-007	9,60E-007	4,36E-006	0
Event 10	0	0	0	0	0	0	0	0	0	0	0	0	0	1,76E-007	1,81E-007	0	0	6,82E-007	0
Event 11	3,22E-006	0	0	0	1,56E-006	1,54E-006	1,55E-006	1,71E-006	2,96E-006	3,37E-006	0	3,69E-006	0	3,04E-006	3,85E-006	2,89E-006	2,67E-006	5,96E-006	0
Event 12	2,59E-006	1,57E-005	0	2,20E-005	1,50E-006	1,11E-006	1,24E-006	1,17E-006	1,62E-006	1,85E-006	0	2,22E-006	0	3,29E-006	3,89E-006	2,10E-006	3,09E-006	9,61E-006	0
Event 13	5,07E-006	5,46E-005	0	1,01E-004	7,57E-006	6,27E-006	5,61E-006	4,76E-006	4,89E-006	0	4,22E-006	5,27E-006	5,31E-006	5,32E-006	4,66E-006	4,45E-006	6,65E-006	3,57E-005	3,55E-006
Event 14	2,52E-007	0	0	0	4,41E-007	0	0	0	0	0	0	0	2,22E-007	3,01E-007	2,39E-007	2,38E-007	3,31E-007	1,69E-006	2,13E-007
Event 16	3,48E-007	0	0	0	4,38E-007	3,31E-007	2,92E-007	0	0	0	0	0	2,63E-007	3,44E-007	0	3,46E-007	3,82E-007	2,06E-006	4,22E-007
Event 17	0	0	0	0	1,47E-007	1,28E-007	1,18E-007	1,32E-007	0	0	0	0	0	2,34E-007	2,06E-007	1,92E-007	0	1,16E-006	0
Event 18	0	1,20E-005	0	2,12E-005	6,93E-007	8,20E-007	8,60E-007	8,38E-007	1,37E-006	1,41E-006	0	1,65E-006	0	1,06E-006	1,16E-006	1,43E-006	1,47E-006	4,48E-006	0
Event 20	1,23E-007	0	0	0	0	0	0	0	0	0	0	0	0	0	0	0	0	5,63E-007	0
Event 21	2,08E-006	0	0	0	1,26E-007	0	1,25E-007	1,21E-007	0	1,09E-007	0	0	1,22E-007	0	0	0	0	0	9,91E-008
Event 22	1,81E-006	1,31E-005	1,67E-005	0	1,58E-006	1,38E-006	1,15E-006	1,24E-006	1,23E-006	9,89E-007	1,08E-006	1,09E-006	1,17E-006	1,47E-006	1,34E-006	1,27E-006	1,44E-006	9,38E-006	1,03E-006
Event 23	3,14E-007	0	0	0	0	0	0	0	0	0	0	0	2,72E-007	0	4,63E-007	0	0	0	3,62E-007
Event 24	0	0	2,40E-006	0	1,19E-007	0	1,14E-007	0	1,06E-007	0	9,33E-008	0	0	0	3,66E-007	0	1,40E-007	0	9,47E-008
Event 25	2,14E-006	2,06E-005	0	2,90E-005	2,49E-006	1,99E-006	1,96E-006	2,03E-006	2,20E-006	0	2,03E-006	2,42E-006	2,77E-006	3,47E-006	4,72E-006	1,88E-006	3,01E-006	1,84E-005	1,94E-006
Event 26	0	0	0	0	4,87E-007	3,65E-007	3,11E-007	0	0	0	0	0	2,37E-007	2,67E-007	3,03E-007	3,21E-007	3,39E-007	0	1,85E-007
Event 27	0	1,60E-005	3,07E-005	2,50E-005	1,61E-006	1,76E-006	1,75E-006	1,73E-006	2,06E-006	0	1,91E-006	1,99E-006	1,82E-006	2,22E-006	1,98E-006	2,27E-006	3,08E-006	1,14E-005	1,66E-006
Event 28	2,41E-006	0	0	0	5,69E-007	0	0	0	0	0	7,07E-007	8,19E-007	6,48E-007	1,18E-006	1,54E-006	1,03E-006	1,22E-006	4,29E-006	7,12E-007
Event 29	3,34E-006	0	0	0	4,65E-007	3,91E-007	5,17E-007	0	0	0	6,11E-007	6,63E-007	4,92E-007	1,39E-006	1,21E-006	7,43E-007	1,09E-006	3,02E-006	5,79E-007
Event 30	1,66E-005	0	0	0	2,64E-005	2,15E-005	1,89E-005	1,91E-005	1,50E-005	1,31E-005	1,26E-005	1,39E-005	1,40E-005	1,69E-005	1,35E-005	1,45E-005	2,02E-005	6,90E-005	0
Event 31	4,21E-006	3,10E-005	5,96E-005	6,34E-005	3,59E-006	3,17E-006	2,94E-006	3,20E-006	3,82E-006	3,33E-006	3,22E-006	3,80E-006	3,21E-006	4,09E-006	3,64E-006	4,76E-006	5,38E-006	2,24E-005	0
Event 32	4,87E-007	0	0	0	4,68E-007	4,23E-007	3,93E-007	4,22E-007	0	0	3,90E-007	0	3,84E-007	4,31E-007	4,34E-007	5,38E-007	7,62E-007	3,03E-006	3,87E-007
Event 33	2,14E-005	9,04E-005	1,68E-004	1,15E-004	9,40E-006	1,07E-005	8,01E-006	9,12E-006	1,43E-005	1,77E-005	1,85E-005	2,31E-005	1,42E-005	3,26E-005	3,91E-005	1,45E-005	1,94E-005	4,66E-005	0
Event 34	7,62E-007	0	0	0	1,30E-006	1,11E-006	1,01E-006	9,63E-007	7,03E-007	6,33E-007	7,43E-007	7,39E-007	6,44E-007	6,28E-007	6,82E-007	7,63E-007	1,23E-006	4,82E-006	0
Event 35	1,40E-006	0	0	0	0	0	0	0	0	0	0	0	0	0	2,13E-007	1,81E-007	1,93E-007	9,65E-007	1,78E-007
Event 36	9,87E-008	0	0	0	0	0	0	0	0	0	0	0	0	1,18E-007	1,20E-007	0	1,36E-007	6,70E-007	1,01E-007
Event 37	7,55E-006	9,26E-005	1,75E-004	1,48E-004	9,14E-006	7,39E-006	8,38E-006	8,06E-006	8,58E-006	7,87E-006	8,38E-006	0	8,63E-006	1,04E-005	1,27E-005	7,85E-006	1,28E-005	8,53E-005	6,50E-006
Event 38	1,76E-007	0	0	0	0	0	0	0	0	0	0	0	1,59E-007	1,71E-007	0	0	2,26E-007	6,72E-007	1,13E-007
Event 39	7,57E-007	0	0	0	9,12E-007	8,39E-007	8,66E-007	7,92E-007	8,95E-007	9,13E-007	1,03E-006	0	8,62E-007	7,49E-007	1,01E-006	9,92E-007	1,10E-006	6,25E-006	9,20E-007
Event 40	3,54E-006	0	0	0	5,34E-007	0	0	0	3,31E-007	0	0	0	0	0	3,92E-007	2,79E-007	0	2,17E-006	2,86E-007
Event 41	2,61E-007	0	0	0	5,75E-007	4,32E-007	3,96E-007	3,57E-007	0	0	2,36E-007	0	2,66E-007	2,98E-007	3,15E-007	2,54E-007	3,75E-007	1,83E-006	0
Event 42	2,89E-007	0	0	0	0	0	0	0	0	2,67E-007	2,58E-007	0	2,49E-007	5,00E-007	6,08E-007	2,90E-007	0	1,77E-006	0
Event 44	1,67E-005	1,11E-004	1,22E-004	0,0001792211	2,64E-005	2,13E-005	1,89E-005	1,90E-005	1,50E-005	1,31E-005	1,26E-005	1,39E-005	1,41E-005	1,70E-005	1,36E-005	1,44E-005	2,01E-005	6,90E-005	0
Event 45	3,25E-007	2,31E-006	0	3,29E-006	3,98E-007	3,88E-007	3,92E-007	3,37E-007	3,53E-007	3,54E-007	4,18E-007	0	3,93E-007	3,30E-007	4,49E-007	4,23E-007	5,08E-007	2,84E-006	4,19E-007
Event 46	1,65E-006	0	0	0	1,02E-006	1,16E-006	9,33E-007	9,95E-007	1,28E-006	1,54E-006	1,85E-006	1,56E-006	1,60E-006	2,11E-006	2,52E-006	1,33E-006	1,98E-006	1,06E-005	0
Event 47	4,23E-006	2,39E-005	0	0	3,73E-006	3,40E-006	3,41E-006	3,43E-006	5,41E-006	4,12E-006	3,51E-006	0	4,72E-006	6,81E-006	8,61E-006	3,64E-006	9,02E-006	1,87E-005	2,90E-006
Event 48	7,92E-006	2,75E-005	0	0	0	0	0	0	2,81E-006	3,18E-006	3,64E-006	4,05E-006	0	0	0	4,13E-006	4,18E-006	1,53E-005	0
Event 49	1,67E-006	0	0	0	1,06E-006	7,55E-007	0	0	0	0	1,37E-006	1,40E-006	1,25E-006	2,12E-006	2,35E-006	1,49E-006	1,74E-006	9,55E-006	0
Event 50	3,92E-007	0	0	0	3,42E-007	0	0	0	0	0	0	0	3,89E-007	0	4,12E-007	4,77E-007	6,77E-007	1,66E-006	5,75E-007
Event 51	3,61E-006	0	0	0	2,28E-007	0	0	0	0	0	0	0	0	0	1,24E-007	0	0	9,30E-007	1,32E-007
Event 52	2,36E-007	0	0	0	2,79E-007	0	0	0	0	0	0	0	1,67E-007	3,07E-007	3,81E-007	0	2,89E-007	0	0
Event 53	1,61E-006	0	0	0	0	8,84E-007	9,91E-007	1,13E-006	1,03E-006	8,78E-007	1,16E-006	0	9,54E-007	2,89E-006	2,44E-006	1,41E-006	0	4,41E-006	0
Event 54	1,70E-006	0	0	0	0	0	0	0	0	0	0	0	0	0	2,85E-007	0	0	9,19E-007	1,18E-007
Event 55	9,07E-007	0	0	0	0	7,67E-007	6,64E-007	5,14E-007	6,68E-007	5,73E-007	7,16E-007	0	6,62E-007	1,28E-006	1,32E-006	7,31E-007	0	3,56E-006	0
Event 56	2,98E-006	2,89E-005	2,38E-005	3,11E-005	1,24E-006	1,18E-006	1,21E-006	1,26E-006	1,88E-006	1,92E-006	2,13E-006	2,54E-006	1,79E-006	2,12E-006	2,45E-006	2,37E-006	2,70E-006	1,00E-005	0
Event 57	1,66E-006	0	0	0	0	0	0	0	0	0	0	0	1,82E-006	2,08E-006	2,66E-006	1,51E-006	2,23E-006	1,56E-005	1,21E-006
Event 58	3,52E-006	0	0	0	0	0	0	0	0	0	0	0	0	0	6,36E-007	0	0	0	2,73E-007

TABLE B.3: Peak Ground Velocity values (PGV) for the EW component of all the available recordings for the subset of events.

	EW component																		
	SG01	**SG02**	**SG03**	**SG04**	**SG05**	**SG06**	**SG07**	**SG08**	**SG09**	**SG10**	**SG11**	**SG12**	**SG13**	**SG14**	**SG15**	**SG17**	**SG18**	**SG19**	**SG20**
Event 1	0	0	0	0	0	4,93E-007	4,53E-007	3,89E-007	4,31E-007	5,19E-007	0	7,69E-007	6,09E-007	5,82E-007	6,97E-007	8,16E-007	8,01E-007	0	5,40E-007
Event 2	1,02E-007	0	0	0	0	0	0	0	4,45E-008	3,95E-008	0	0	0	0	0	5,46E-008	0	0	4,42E-008
Event 3	3,53E-007	0	0	0	0	2,38E-007	2,32E-007	0	0	0	0	0	2,57E-007	0	0	2,96E-007	0	0	2,00E-007
Event 4	0	0	0	0	0	7,58E-007	0	0	0	0	0	1,37E-006	1,04E-006	9,94E-007	9,79E-007	1,28E-006	1,44E-006	5,82E-006	0
Event 5	0	3,92E-005	0	0	3,58E-006	3,62E-006	3,28E-006	0	3,97E-006	4,66E-006	4,01E-006	5,83E-006	3,81E-006	5,89E-006	9,53E-006	5,46E-006	6,61E-006	1,17E-005	0
Event 6	0	0	0	0	0	4,51E-007	4,83E-007	4,29E-007	0	0	0	6,94E-007	5,50E-007	5,45E-007	5,20E-007	6,20E-007	0	3,75E-006	3,50E-007
Event 7	0	0	0	0	0	1,01E-007	1,01E-007	8,96E-008	9,85E-008	1,19E-007	0	2,60E-007	1,32E-007	0	0	1,92E-007	0	0	1,25E-007
Event 8	1,05E-006	0	0	0	0	6,77E-007	6,70E-007	6,28E-007	7,48E-007	8,91E-007	1,08E-006	1,10E-006	9,21E-007	0	0	0	0	0	0
Event 9	0	0	0	0	8,02E-007	7,92E-007	8,26E-007	7,94E-007	9,25E-007	1,08E-006	0	0	0	1,06E-006	8,58E-007	1,37E-006	1,72E-006	5,05E-006	0
Event 10	0	0	0	0	0	0	0	0	0	0	0	0	0	2,03E-007	2,17E-007	0	0	6,90E-007	0
Event 11	2,04E-006	0	0	0	1,99E-006	1,84E-006	1,75E-006	1,63E-006	1,44E-006	1,43E-006	0	2,05E-006	0	2,66E-006	3,61E-006	1,62E-006	1,86E-006	4,87E-006	0
Event 12	1,56E-006	9,73E-006	0	1,80E-005	1,36E-006	1,12E-006	1,24E-006	1,22E-006	1,36E-006	1,34E-006	0	1,58E-006	0	3,71E-006	3,42E-006	1,28E-006	2,06E-006	5,22E-006	0
Event 13	5,67E-006	4,24E-005	0	6,72E-005	3,49E-006	3,79E-006	4,44E-006	4,25E-006	4,72E-006	0	5,31E-006	6,60E-006	6,58E-006	6,05E-006	6,64E-006	6,15E-006	7,68E-006	2,10E-005	4,12E-006
Event 14	3,15E-007	0	0	0	2,30E-007	0	0	0	0	0	0	0	3,56E-007	2,95E-007	3,70E-007	3,75E-007	3,90E-007	1,06E-006	3,01E-007
Event 16	2,30E-007	0	0	0	2,12E-007	2,31E-007	2,25E-007	0	0	0	0	0	2,50E-007	2,76E-007	0	2,48E-007	3,93E-007	2,12E-006	2,86E-007
Event 17	0	0	0	0	2,03E-007	1,74E-007	1,77E-007	1,55E-007	0	0	0	0	0	1,67E-007	2,02E-007	2,25E-007	0	1,01E-006	0
Event 18	0	7,69E-006	0	1,47E-005	7,26E-007	7,62E-007	7,62E-007	6,72E-007	6,70E-007	8,27E-007	0	1,02E-006	0	9,76E-007	9,78E-007	1,11E-006	1,74E-006	5,14E-006	0
Event 20	1,05E-007	0	0	0	0	0	0	0	0	0	0	0	0	0	0	0	0	3,02E-007	0
Event 21	0	0	0	0	1,06E-007	0	1,08E-007	9,57E-008	0	1,07E-007	0	0	1,11E-007	0	0	0	0	0	9,83E-008
Event 22	1,66E-006	1,06E-005	5,98E-006	0	1,08E-006	1,01E-006	9,64E-007	8,73E-007	1,11E-006	1,28E-006	1,44E-006	1,53E-006	1,39E-006	1,30E-006	1,29E-006	1,85E-006	2,05E-006	8,24E-006	1,40E-006
Event 23	2,48E-007	0	0	0	0	0	0	0	0	0	0	0	2,08E-007	0	3,81E-007	0	0	0	3,50E-007
Event 24	0	0	8,04E-007	0	1,17E-007	0	1,23E-007	0	1,17E-007	0	1,50E-007	0	0	0	7,77E-007	0	3,18E-007	0	1,03E-007
Event 25	3,23E-006	1,58E-005	0	1,98E-005	3,33E-006	3,11E-006	2,82E-006	2,50E-006	2,08E-006	0	2,26E-006	3,01E-006	1,94E-006	3,89E-006	3,94E-006	3,54E-006	4,55E-006	1,08E-005	3,95E-006
Event 26	0	0	0	0	3,43E-007	3,17E-007	3,03E-007	0	0	0	0	0	1,73E-007	2,49E-007	2,52E-007	3,32E-007	2,89E-007	0	2,07E-007
Event 27	0	1,23E-005	6,39E-006	1,28E-005	1,45E-006	1,14E-006	1,06E-006	1,01E-006	1,32E-006	0	1,94E-006	2,23E-006	1,81E-006	1,94E-006	2,21E-006	2,75E-006	3,77E-006	8,68E-006	1,27E-006
Event 28	7,18E-007	0	0	0	6,12E-007	0	0	0	0	0	6,86E-007	6,86E-007	7,19E-007	9,40E-007	1,72E-006	7,53E-007	1,17E-006	3,05E-006	4,48E-007
Event 29	0	0	0	0	5,46E-007	5,02E-007	4,57E-007	0	0	0	7,64E-007	9,68E-007	6,38E-007	1,05E-006	2,29E-006	6,44E-007	8,13E-007	1,87E-006	4,68E-007
Event 30	2,27E-005	0	0	0	1,93E-005	1,98E-005	2,00E-005	1,73E-005	1,85E-005	2,08E-005	2,27E-005	2,42E-005	2,10E-005	1,94E-005	2,00E-005	2,47E-005	3,29E-005	6,61E-005	0
Event 31	4,40E-006	2,08E-005	1,71E-005	4,03E-005	2,36E-006	2,08E-006	2,08E-006	1,89E-006	2,42E-006	3,09E-006	3,58E-006	4,05E-006	3,42E-006	3,53E-006	3,60E-006	4,60E-006	5,48E-006	1,35E-005	0
Event 32	4,28E-007	0	0	0	4,71E-007	4,10E-007	3,71E-007	3,43E-007	0	0	4,05E-007	0	4,01E-007	4,52E-007	4,39E-007	4,75E-007	6,54E-007	1,93E-006	4,17E-007
Event 33	1,60E-005	7,59E-005	3,47E-005	9,77E-005	1,26E-005	7,93E-006	9,17E-006	6,32E-006	1,10E-005	1,05E-005	9,86E-006	1,07E-005	1,64E-005	2,98E-005	2,62E-005	1,18E-005	1,88E-005	4,53E-005	0
Event 34	9,24E-007	0	0	0	8,95E-007	8,26E-007	7,97E-007	7,78E-007	9,39E-007	9,62E-007	9,89E-007	9,56E-007	1,01E-006	9,31E-007	9,40E-007	1,01E-006	1,28E-006	2,60E-006	0
Event 35	1,95E-007	0	0	0	0	0	0	0	0	0	0	0	0	0	1,89E-007	2,10E-007	3,01E-007	9,00E-007	2,02E-007
Event 36	1,11E-007	0	0	0	0	0	0	0	0	0	0	0	0	1,31E-007	1,24E-007	0	1,89E-007	4,51E-007	9,54E-008
Event 37	1,00E-005	6,88E-005	3,78E-005	9,83E-005	1,80E-005	1,39E-005	1,25E-005	1,07E-005	7,57E-006	7,33E-006	8,58E-006	0	8,25E-006	1,36E-005	9,20E-006	1,18E-005	1,45E-005	4,20E-005	1,21E-005
Event 38	1,80E-007	0	0	0	0	0	0	0	0	0	0	0	1,42E-007	1,66E-007	0	0	2,19E-007	5,38E-007	1,10E-007
Event 39	1,06E-006	0	0	0	1,37E-006	1,14E-006	1,03E-006	1,01E-006	8,69E-007	8,95E-007	8,24E-007	0	8,54E-007	9,72E-007	6,65E-007	1,14E-006	1,61E-006	3,38E-006	8,90E-007
Event 40	0	0	0	0	3,23E-007	0	0	0	3,35E-007	0	0	0	0	0	3,47E-007	3,87E-007	0	1,72E-006	3,71E-007
Event 41	4,59E-007	0	0	0	3,30E-007	3,12E-007	3,16E-007	2,92E-007	0	0	4,38E-007	0	3,81E-007	3,76E-007	3,73E-007	5,06E-007	6,46E-007	1,71E-006	0
Event 42	4,40E-007	0	0	0	0	0	0	0	0	3,78E-007	3,79E-007	0	3,16E-007	5,89E-007	1,15E-006	3,43E-007	0	1,33E-006	0
Event 44	2,27E-005	7,23E-005	6,39E-005	0,0001404118	1,92E-005	1,99E-005	1,99E-005	1,73E-005	1,85E-005	2,08E-005	2,27E-005	2,42E-005	2,09E-005	1,94E-005	2,02E-005	2,47E-005	3,28E-005	6,60E-005	0
Event 45	4,74E-007	1,51E-006	0	2,60E-006	5,93E-007	4,84E-007	4,46E-007	4,65E-007	3,95E-007	4,20E-007	3,74E-007	0	4,17E-007	4,50E-007	3,52E-007	4,46E-007	6,67E-007	1,60E-006	4,40E-007
Event 46	1,44E-006	0	0	0	9,25E-007	1,12E-006	1,17E-006	1,10E-006	1,38E-006	1,27E-006	1,18E-006	1,58E-006	1,18E-006	2,34E-006	2,92E-006	1,19E-006	1,74E-006	1,35E-005	0
Event 47	4,22E-006	2,46E-005	0	0	4,05E-006	2,81E-006	2,44E-006	2,39E-006	3,30E-006	3,55E-006	3,89E-006	0	4,99E-006	6,48E-006	9,40E-006	4,94E-006	7,24E-006	1,05E-005	2,51E-006
Event 48	0	2,37E-005	0	0	0	0	0	0	2,63E-006	2,49E-006	2,32E-006	2,60E-006	0	0	0	1,80E-006	3,02E-006	7,57E-006	0
Event 49	1,38E-006	0	0	0	9,36E-007	9,97E-007	0	0	0	0	1,46E-006	1,33E-006	1,12E-006	1,92E-006	2,12E-006	9,58E-007	1,56E-006	4,34E-006	0
Event 50	4,77E-007	0	0	0	4,55E-007	0	0	0	0	0	0	0	3,08E-007	0	3,12E-007	4,20E-007	6,38E-007	1,46E-006	5,96E-007
Event 51	1,71E-007	0	0	0	1,50E-007	0	0	0	0	0	0	0	0	0	1,47E-007	0	0	8,58E-007	1,60E-007
Event 52	2,03E-007	0	0	0	3,27E-007	0	0	0	0	0	0	0	2,19E-007	2,63E-007	2,84E-007	0	2,48E-007	0	0
Event 53	1,32E-006	0	0	0	0	1,05E-006	9,70E-007	8,86E-007	1,23E-006	1,44E-006	1,77E-006	0	1,35E-006	2,60E-006	2,71E-006	9,45E-007	0	3,70E-006	0
Event 54	0	0	0	0	0	0	0	0	0	0	0	0	0	0	2,48E-007	0	0	7,09E-007	1,03E-007
Event 55	7,83E-007	0	0	0	0	4,46E-007	5,11E-007	6,01E-007	6,49E-007	5,83E-007	7,63E-007	0	6,51E-007	1,61E-006	1,61E-006	5,92E-007	0	2,22E-006	0
Event 56	0	2,21E-005	6,92E-006	1,82E-005	1,07E-006	9,60E-007	1,14E-006	1,15E-006	1,39E-006	1,40E-006	1,41E-006	1,61E-006	1,56E-006	2,23E-006	2,33E-006	2,00E-006	3,16E-006	6,46E-006	0
Event 57	1,87E-006	0	0	0	0	0	0	0	0	0	0	0	1,54E-006	2,31E-006	2,05E-006	2,34E-006	2,62E-006	7,54E-006	2,32E-006
Event 58	0	0	0	0	0	0	0	0	0	0	0	0	0	0	9,35E-007	0	0	0	1,76E-007

B.4 Reference stations

TABLE B.4: Reference station for $S-$wave window selection for each of the 55 selected events.

No of Event	**Reference Station**
1	17
2	17
3	17
4	17
5	17
6	17
7	17
8	13
9	17
10	15
11	17
12	17
13	17
14	17
16	17
17	17
18	17
20	19
21	13
22	17
23	15
24	15
25	17
26	17
27	17
28	17
29	17
30	17
31	17
32	17
33	17
34	17
35	17
36	18
37	17
38	18
39	17
40	17
41	17
42	17
44	17
45	17
46	17
47	17
48	17
49	17
50	17
51	15
52	18
53	17
54	15
55	17
56	17
57	17
58	15

Appendix C

Appendix C: Dynamic analysis of Saint Guérin arch dam

C.1 Frequencies of vibration

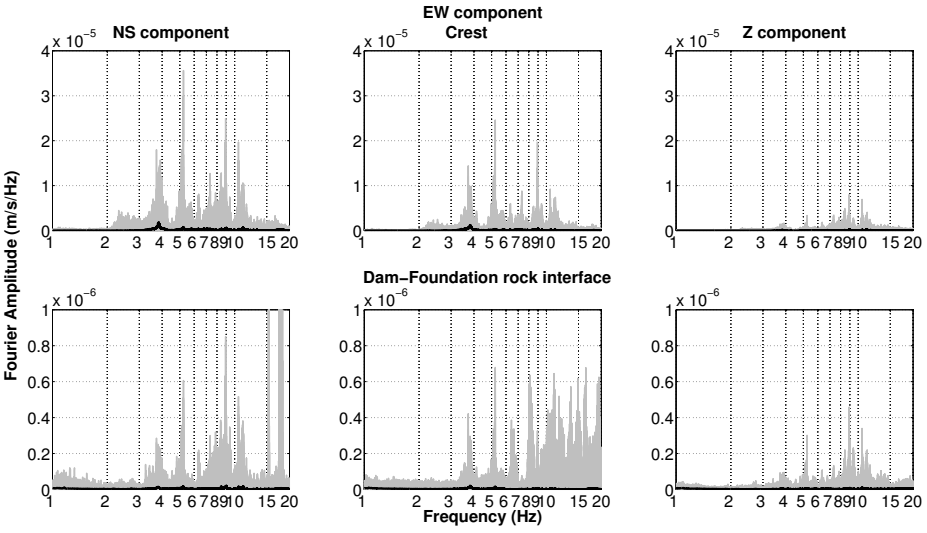

FIGURE C.1: Unsmoothed Fourier velocity spectral amplitudes of individual ambient noise records (grey lines) on the crest and at the dam foundation rock interface (20 minutes-long records two hours before each of the 55 events of Figure 2.15) and median value (black lines) of the three stations on the crest and the nine stations at the dam-foundation rock interface for the two horizontal and the vertical components (NS, EW and Z).

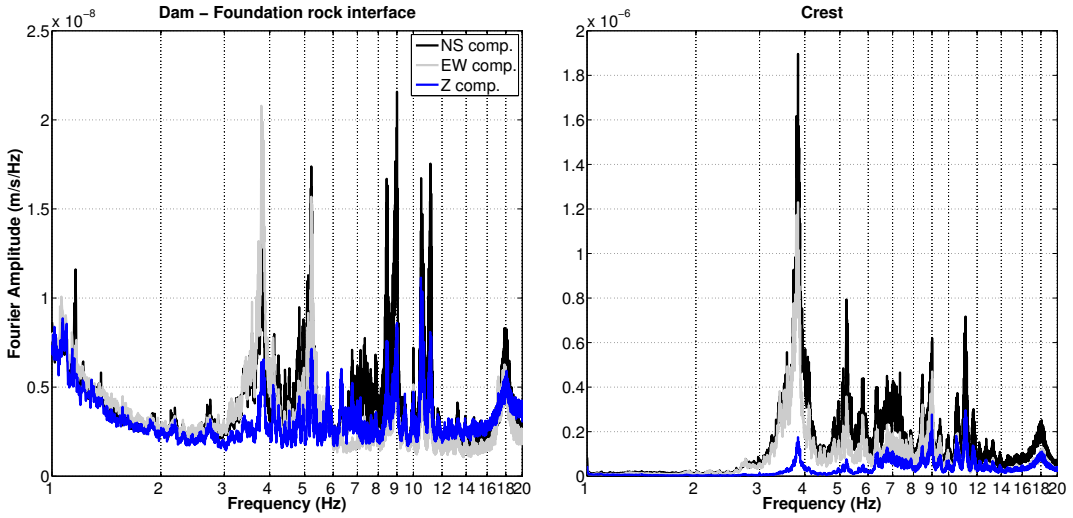

FIGURE C.2: Median value of frequencies of vibration of the Saint Guérin arch dam estimated using 20 minutes-long records of ambient noise two hours before each of the 55 events of Figure 2.15; median value of unsmoothed Fourier velocity spectral amplitudes of the nine stations at the dam-foundation rock interface (right) and median value of unsmoothed Fourier amplitudes of the three stations on the crest (left) for the two horizontal and the vertical components (NS, EW and Z) is presented.

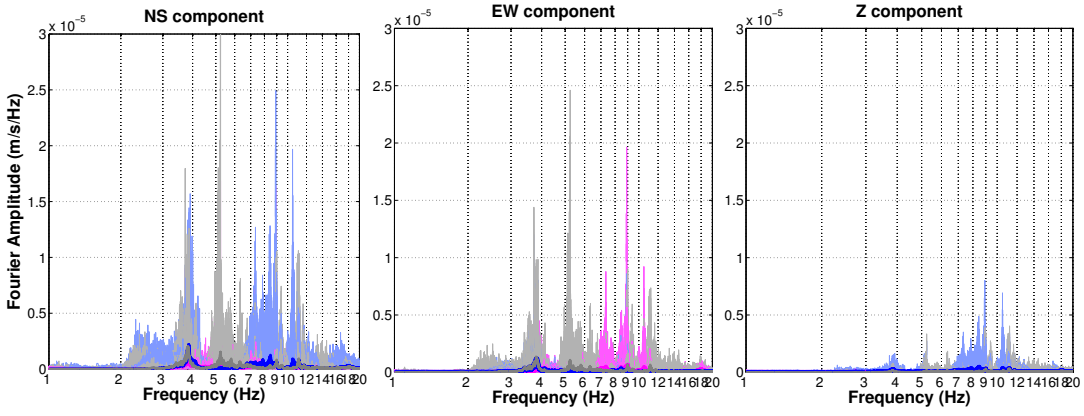

FIGURE C.3: Frequencies of vibration of the Saint Guérin arch dam estimated using 20 minutes-long records of ambient noise two hours before each of the 55 events of Figure 2.15; individual unsmoothed Fourier velocity spectral amplitudes and median value of unsmoothed Fourier amplitudes of the three stations on the crest (left) for the two horizontal and the vertical components (NS, EW and Z) is presented.

C.2 Damping ratio

TABLE C.1: Damping ratio, ξ (%), of station SG02

SG02			
Event	ξ (%)		
	NS	**EW**	**Z**
5	2,4361	1,537	2,0747
12	2,6491	1,8329	12
13	2,667	1,4721	13
18	1,2612	2,6965	18
22	1,6744	0,8608	22
25	3,6982	1,711	25
27	0,8529	0,7403	27
31	1,6971	0,7991	31
33	2,3697	0,9693	33
37	2,6713	2,2633	37
44	3,3928	1,5063	44
45	1,6121	0,956	45
47	2,7273	1,1435	47
48	2,4016	2,7344	48
56	5,9339	1,787	56
Mean	**2.54**	**1.53**	**1.16**

TABLE C.2: Damping ratio, ξ (%), of station SG03

SG03			
Event	ξ (%)		
	NS	**EW**	**Z**
22	0,5166	2,1138	0,6799
24	0,9013	1,9868	1,1129
27	0,8956	1,7668	1,1171
31	2,0577	0,2998	1,5463
33	2,9826	0,3372	1,954
37	1,0947	0,8893	1,4564
44	3,0625	0,4001	2,7135
56	2,161	0,3209	1,2266
Mean	**1,71**	**1,01**	**1,48**

TABLE C.3: Damping ratio, ξ (%), of station SG04

SG04			
Event	ξ (%)		
	NS	**EW**	**Z**
12	2,3414	1,5085	2,5031
13	1,257	0,9187	1,40258
18	1,1298	0,679	1,5494
25	2,8033	4,6852	1,0175
27	1,079	1,56925	0,9868
31	1,9627	0,7803	2,4461
33	3,7918	0,9712	2,1143
37	1,6982	1,3102	1,6095
44	2,1252	0,7156	6,3664
45	2,0048	2,5091	1,2629
56	0,9319	0,3943	2,3774
Mean	**1,92**	**1,46**	**2,15**

C.3 Crest amplification

Sensitivity analysis on PGV and source parameters

Crest amplification during earthquakes depends on the amplitude of the incident signal. The dependency of the crest amplification on PGV, at the first two frequencies of vibration as they were identified in a previous section, i.e. around 3.8 and 5.2 Hz, is examined. The Fourier spectral ratio of each of the three crest stations, i.e SG02, SG03 and SG04, to the median Fourier spectrum of the stations at the interface at 3.8 and 5.2 Hz is plotted against the PGV of each event in Figure C.4 for the two horizontal components. The results reveal no clear trend of the ratio on PGV for all three crest stations for either of the two components.

Although the crest amplification is not directly linked to the source parameters, i.e. magnitude and epicentral distance, a deeper investigation is held which could help to identify possible dependencies. The residuals of each 'individual median' value of crest amplification of each of the three crest stations, i.e SG02, SG03 and SG04, from the 'global median' value of all the events and all the crest stations are estimated. The subset of events is divided into two epicentral distance groups, local events with epicentral distance R_{epi} of [0 100] km and regional events with epicentral distance R_{epi} of [100 350] km. Figures C.5, C.6 and C.7 show the residual plots of the amplification estimations of the NS, EW and Z component respectively as a function of magnitude, for the 3 crest stations and different frequency ranges. Similarly, the events are grouped into two magnitude ranges, M_L [1.5 2.5] and M_L [2.5 4.1] to examine the epicentral distance dependence. Residuals of amplification values (NS, EW and Z components) of the two magnitude groups of events are presented in Figures C.8, C.9 and C.10 as a function of

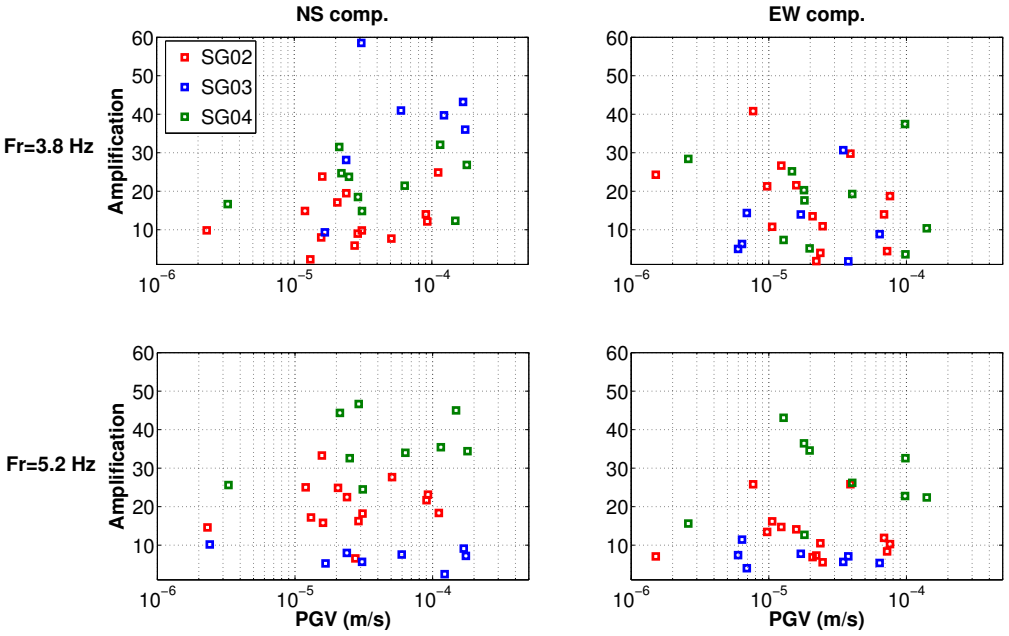

FIGURE C.4: Amplification of individual median estimates for the three crest stations, SG02, SG03 and SG04 for each event as a function of PGV, NS and EW comp.

the corresponding epicentral distances for different frequency ranges.

There is no observed dependency of the crest amplification on either magnitude or epicentral distance for all three crest stations and for the three components of motion. Generally, a reduction of the residuals is observed for the two horizontal components for higher frequencies, i.e. [10 20] Hz, where the amplification stabilizes to a constant value. However, the number of available data is relatively small for a robust statistical analysis and conclusions should be driven with caution. Additionally, the amplifications are estimated based on a number of measurements during small shaking (distant and low magnitude earthquakes) in which case a small damping is expected (about 1% as estimated earlier in Chapter 2). The amplification conclusions should not be extrapolated to strong motions because the material component of the damping is expected to be higher.

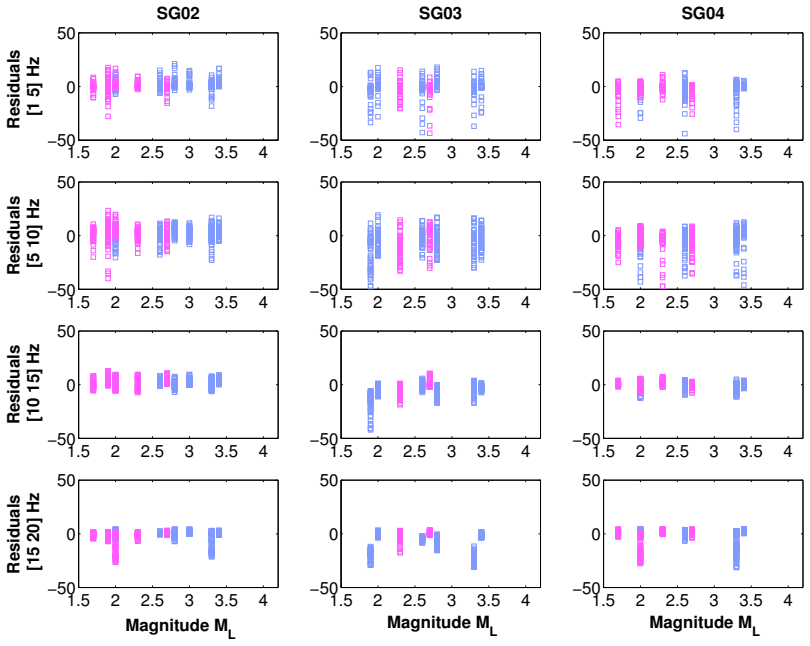

FIGURE C.5: Amplification residuals of individual median estimates for the three crest stations, SG02, SG03 and SG04 for each event with respect to the global median of all the events of the three stations as a function of magnitude, M_L, of the NS component for epicentral distance bins of R_{epi} [0 100] km (magenta) and R_{epi} [100 350] km (blue).

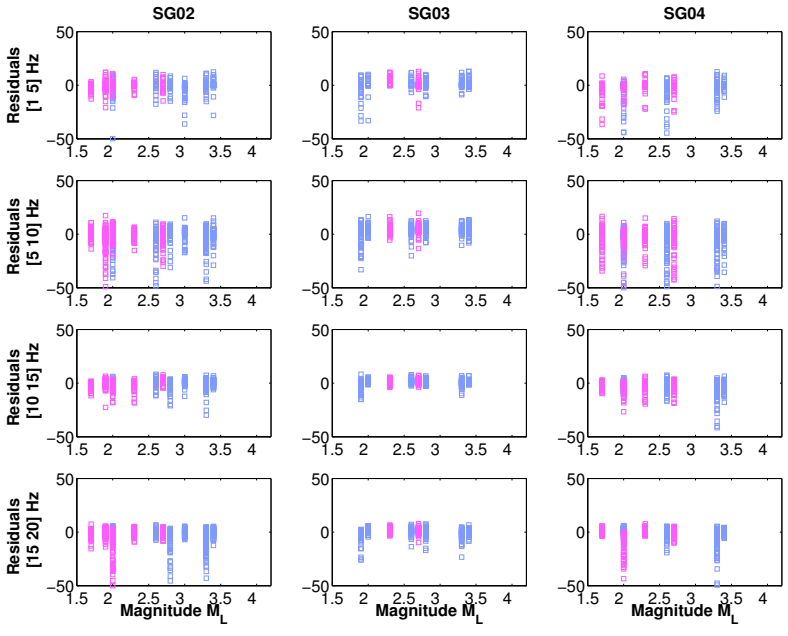

FIGURE C.6: Amplification residuals of individual median estimates for the three crest stations, SG02, SG03 and SG04 for each event with respect to the global median of all the events of the three stations as a function of magnitude, M_L, of the EW component for epicentral distance bins of R_{epi} [0 100] km (magenta) and R_{epi} [100 350] km (blue).

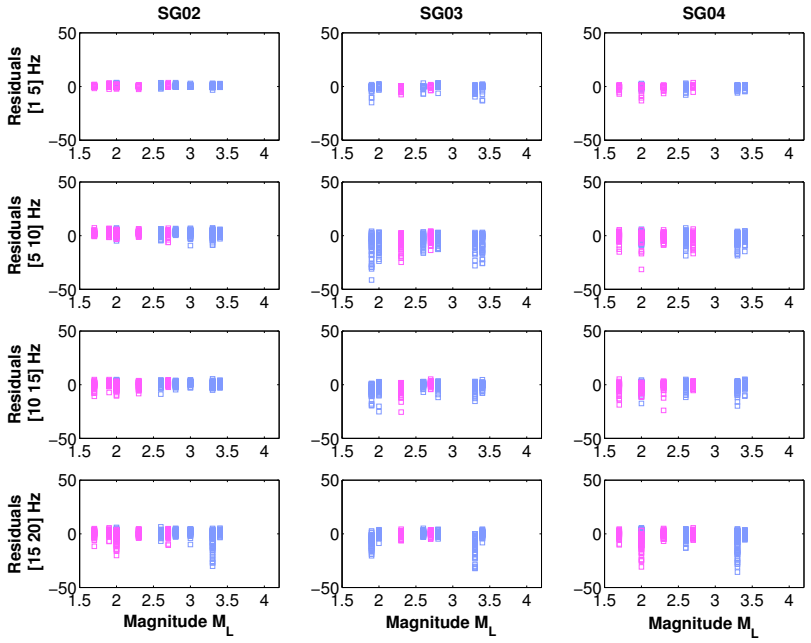

FIGURE C.7: Amplification residuals of individual median estimates for the three crest stations, SG02, SG03 and SG04 for each event with respect to the global median of all the events of the three stations as a function of magnitude, M_L, of the Z component for epicentral distance bins of R_{epi} [0 100] km (magenta) and R_{epi} [100 350] km (blue).

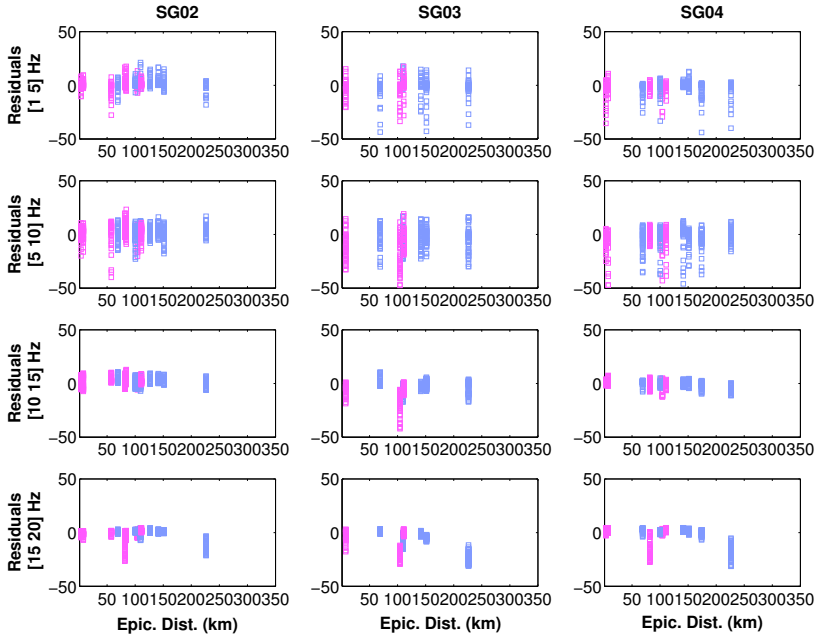

FIGURE C.8: Amplification residuals of individual median estimates for the three crest stations, SG02, SG03 and SG04 for each event with respect to the global median of all the events of the three stations as a function of epicentral distance of the NS component for magnitude bins of M_L [1.5 2.5] (magenta) and M_L [2.5 4.1] (blue).

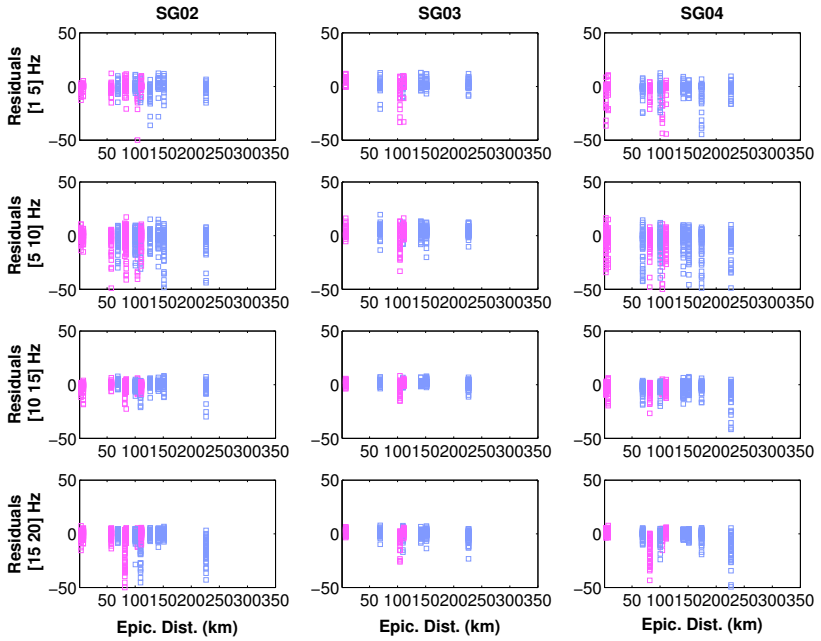

FIGURE C.9: Amplification residuals of individual median estimates for the three crest stations, SG02, SG03 and SG04 for each event with respect to the global median of all the events of the three stations as a function of epicentral distance of the EW component for magnitude bins of M_L [1.5 2.5] (magenta) and M_L [2.5 4.1] (blue).

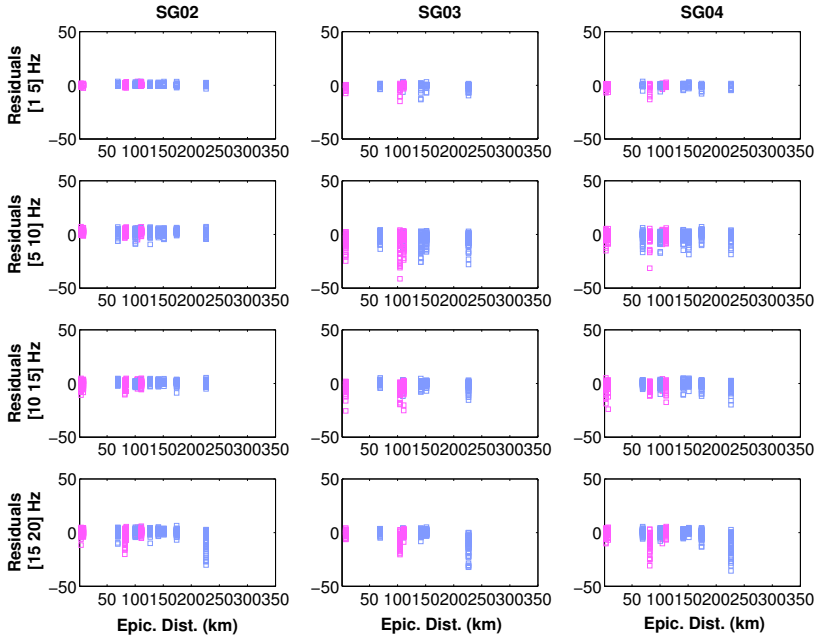

FIGURE C.10: Amplification residuals of individual median estimates for the three crest stations, SG02, SG03 and SG04 for each event with respect to the global median of all the events of the three stations as a function of epicentral distance of the Z component for magnitude bins of M_L [1.5 2.5] (magenta) and M_L [2.5 4.1] (blue).

Crest amplification during ambient noise

The ratio of the Fourier spectra at the position of the 3 stations on the crest of the dam, with respect to the median value of motions at the position of the stations at the base are calculated for the two horizontal and the vertical components of ambient noise recordings. 20 minute-long records, 2 hours before the occurrence of each seismic event, are used for the analysis (same data as for the identification of the frequencies of vibration). The analysis is performed for each station location on the crest independently and thereafter the median value of the amplification of the three stations is found. The ratio of the unsmoothed Fourier amplitudes of the recordings on the crest to the base are presented in Figure C.11 for the frequency range of interest (from 1 to 20 Hz).

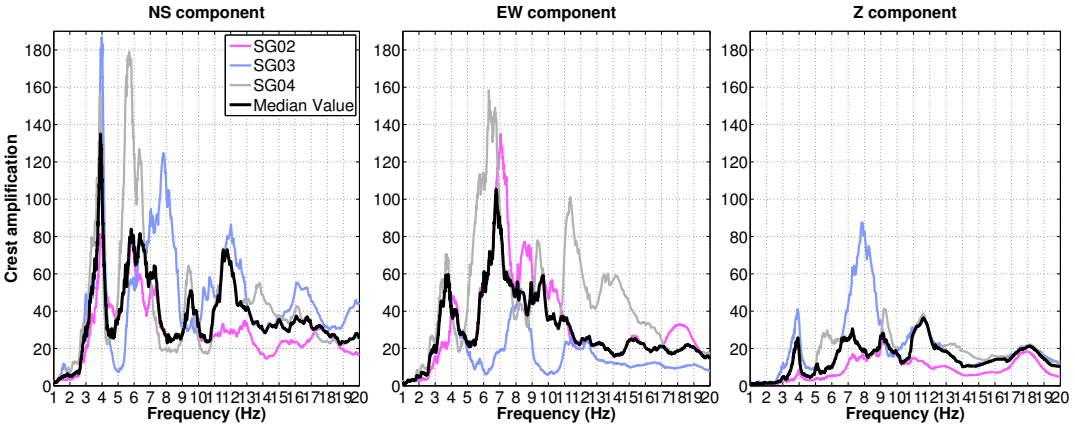

FIGURE C.11: Amplification of the crest of the dam (SG02, SG03, SG04 and median value of the motions at the three stations) with respect to the dam - foundation rock interface (median value of stations SG05, SG06, SG07, SG08, SG09, SG10, SG11 and SG12) based on ambient noise recordings for the two horizontal and the vertial (NS, EW and Z) components.

Appendix D

Appendix D: Sensitivity analysis of lagged coherency on source characteristics

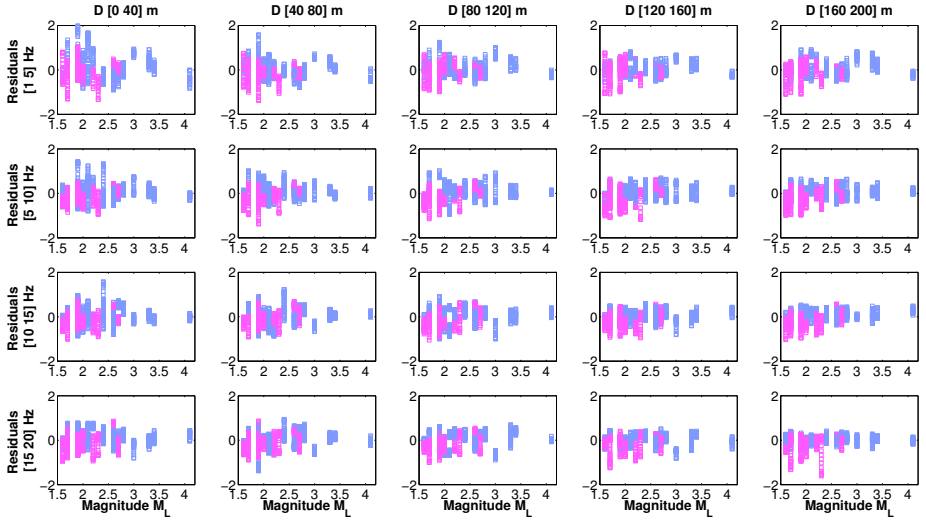

FIGURE D.1: Coherency residuals of individual median estimates of ATANH(lagged coherency) for each event with respect to the global median (ATANH units) of all the events as a function of magnitude of the EW component for epicentral distance bins of R_{epi} [0 100] km (magenta) and R_{epi} [100 350] km (blue).

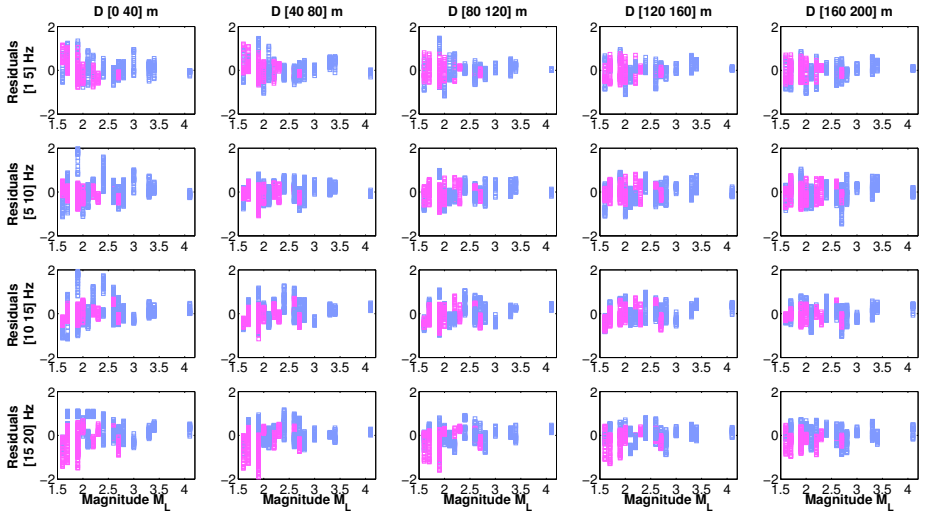

FIGURE D.2: Coherency residuals of individual median estimates of ATANH(lagged coherency) for each event with respect to the global median (ATANH units) of all the events as a function of magnitude of the Z component for epicentral distance bins of R_{epi} [0 100] km (magenta) and R_{epi} [100 350] km (blue).

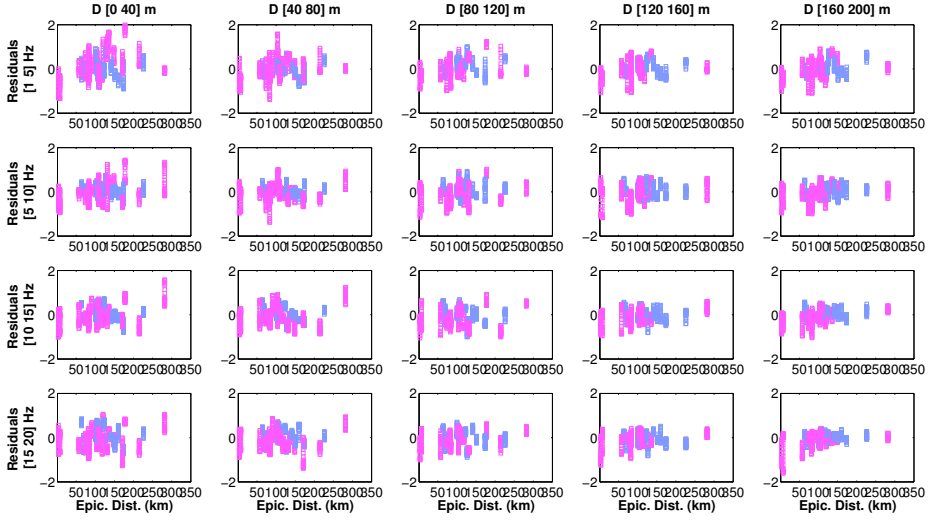

FIGURE D.3: Coherency residuals of individual median estimates of ATANH(lagged coherency) for each event with respect to the global median (ATANH units) of all the events as a function of epicentral distance of the EW component for magnitude bins of M_L [1.5 2.5] (magenta) and M_L [2.5 4.1] (blue).

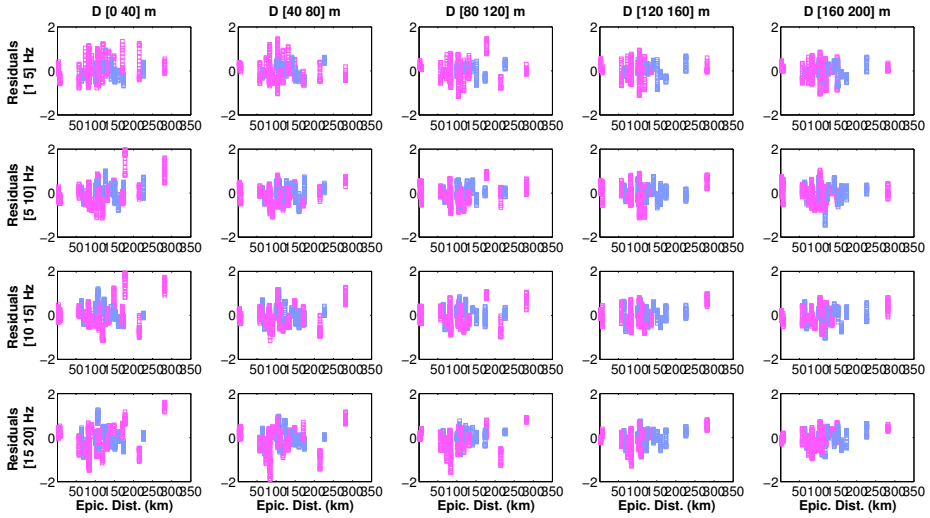

FIGURE D.4: Coherency residuals of individual median estimates of ATANH(lagged coherency) for each event with respect to the global median (ATANH units) of all the events as a function of epicentral distance of the Z component for magnitude bins of M_L [1.5 2.5] (magenta) and M_L [2.5 4.1] (blue).

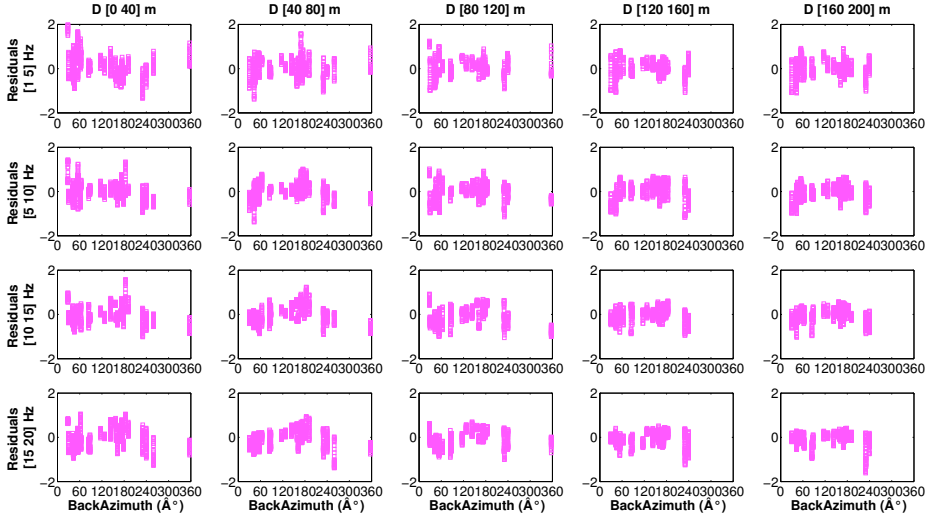

FIGURE D.5: Coherency residuals of individual median estimates of ATANH(lagged coherency) for each event with respect to the global median (ATANH units) of all the events as a function of back azimuth of the EW component.

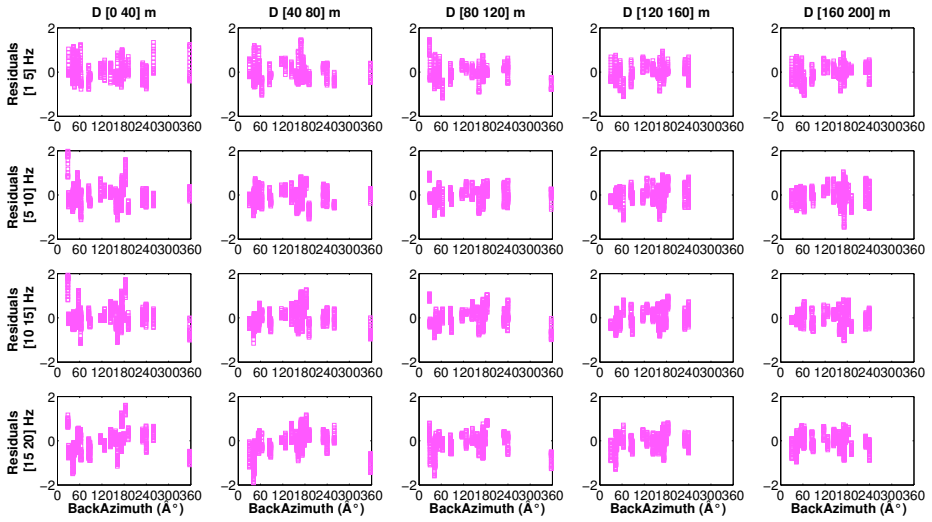

FIGURE D.6: Coherency residuals of individual median estimates of ATANH(lagged coherency) for each event with respect to the global median (ATANH units) of all the events as a function of back azimuth of the Z component.

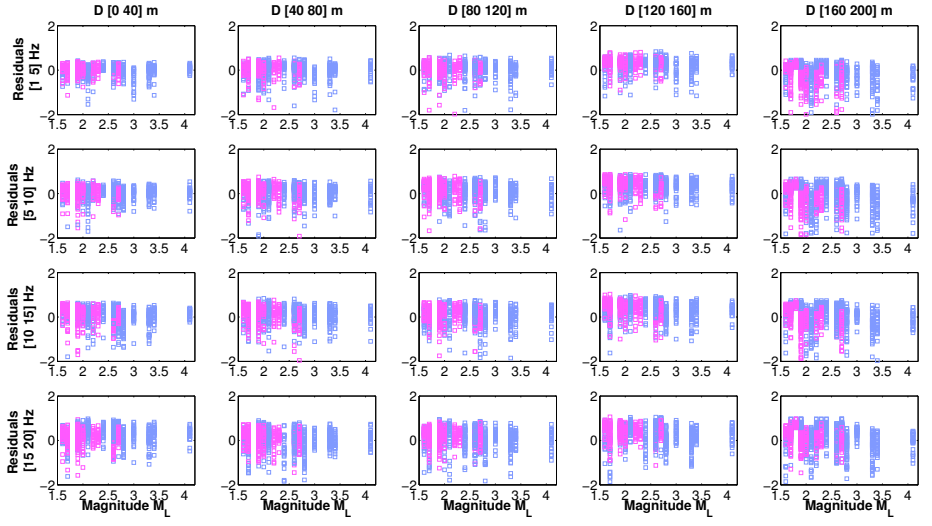

FIGURE D.7: Amplitude variability residuals of individual estimates of standard deviation of difference of natural logarithm of Fourier spectral velocities for each event with respect to the global median of all the events as a function of magnitude, M_L of the EW component for epicentral distance bins of D [0 100] km and D [100 350] km.

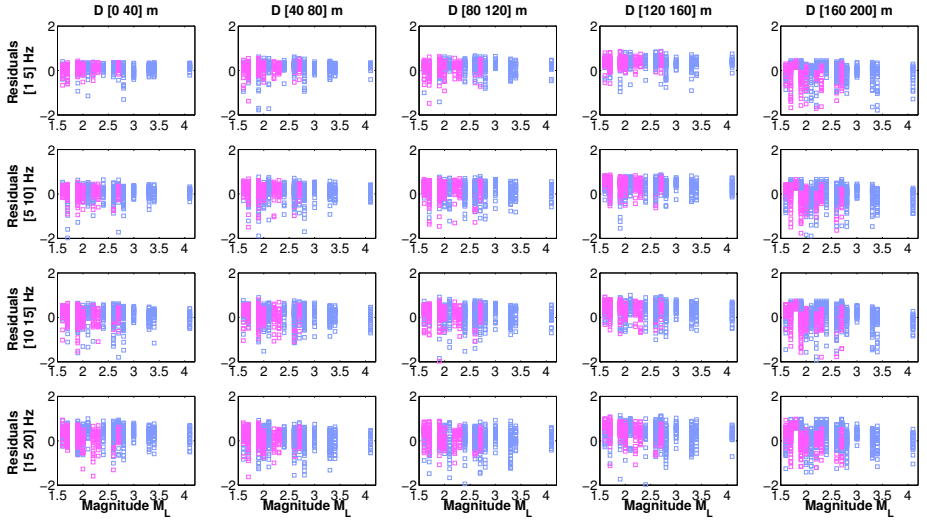

FIGURE D.8: Amplitude variability residuals of individual estimates of standard deviation of difference of natural logarithm of Fourier spectral velocities for each event with respect to the global median of all the events as a function of magnitude, M_L of the Z component for epicentral distance bins of D [0 100] km and D [100 350] km.

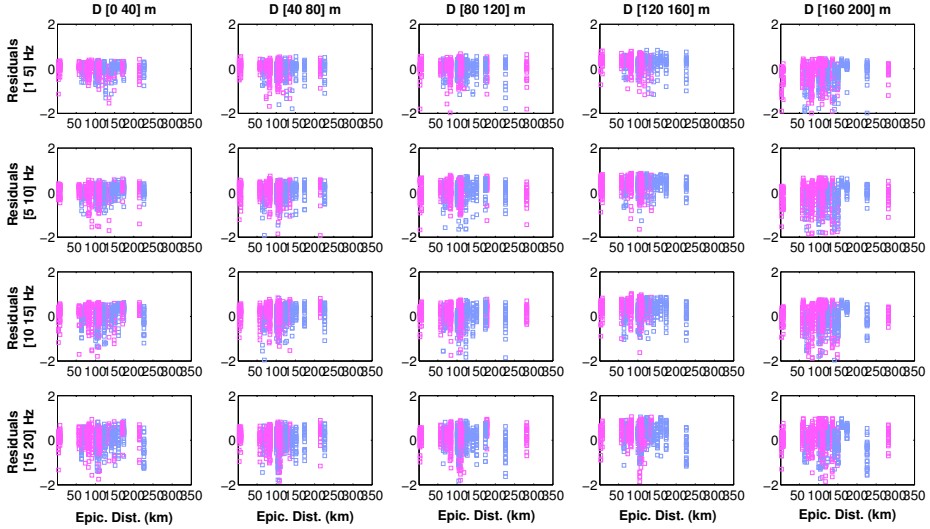

FIGURE D.9: Amplitude variability residuals of individual estimates of standard deviation of difference of natural logarithm of Fourier spectral velocities for each event with respect to the global median of all the events as a function of epicentral distance of the EW component for magnitude bins of M [1.5 2.5] and M [2.5 4.1].

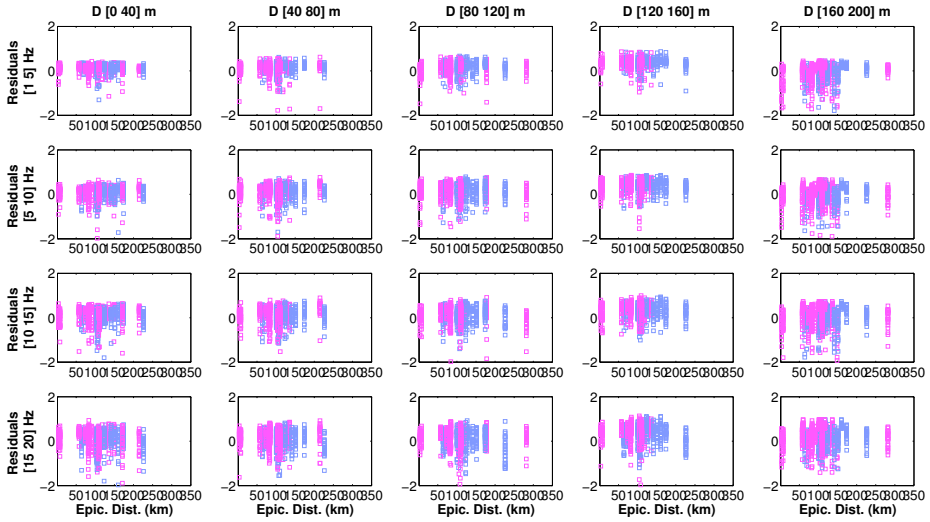

FIGURE D.10: Amplitude variability residuals of individual estimates of standard deviation of difference of natural logarithm of Fourier spectral velocities for each event with respect to the global median of all the events as a function of epicentral distance of the Z component for magnitude bins of M [1.5 2.5] and M [2.5 4.1].

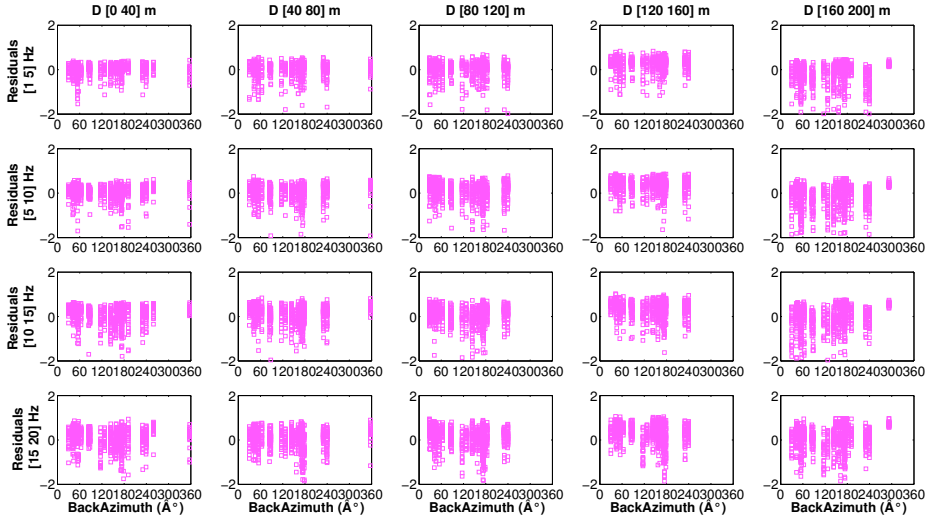

FIGURE D.11: Amplitude variability residuals of individual estimates of standard deviation of difference of natural logarithm of Fourier spectral velocities for each event with respect to the global median of all the events as a function of back azimuth of the EW component.

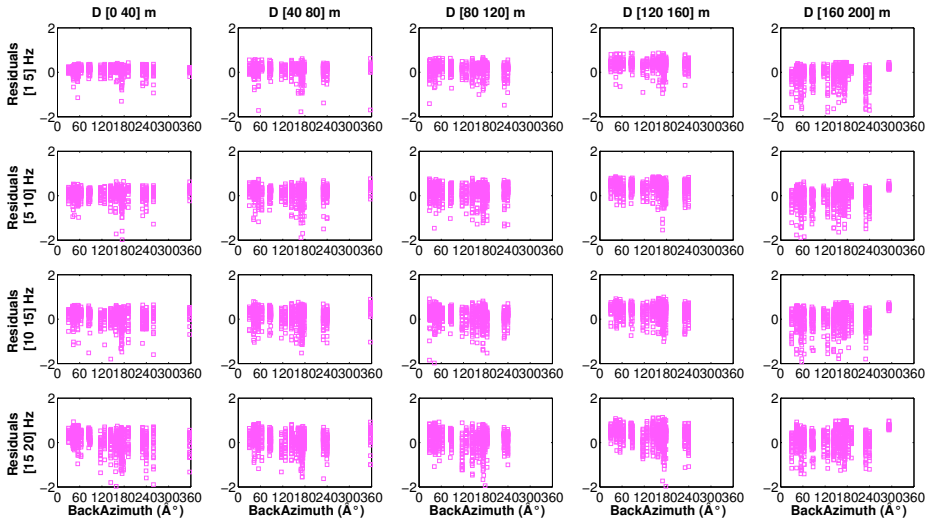

FIGURE D.12: Amplitude variability residuals of individual estimates of standard deviation of difference of natural logarithm of Fourier spectral velocities for each event with respect to the global median of all the events as a function of back azimuth of the Z component.

Appendix E

Appendix E: Numerical analysis in SPECFEM3D

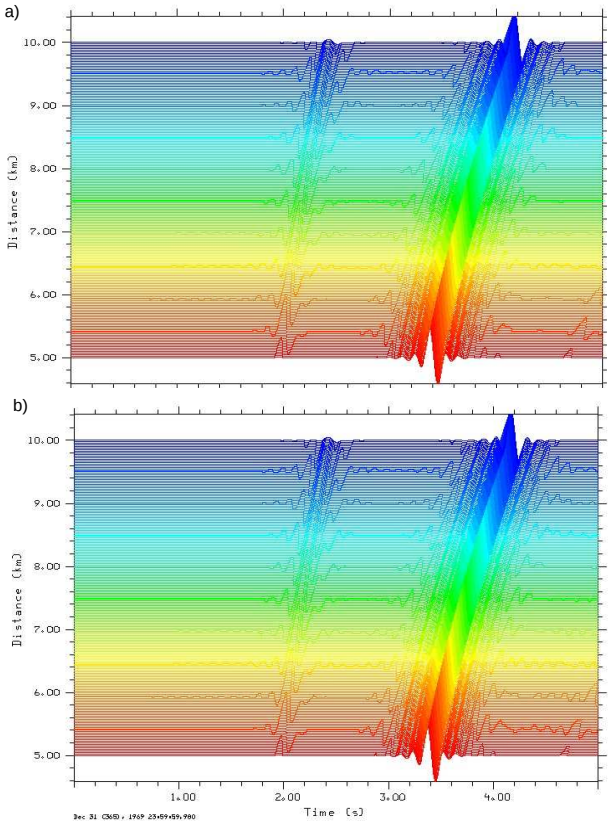

FIGURE E.1: Comparison of the recorded velocity time histories at a site with $H/L = 0$ modeled in SPECFEM3D with mesh hexaedral element in depth 200 (a) and 300 (b) m with mesh tripling refinement at 1.8 km below the free surface.

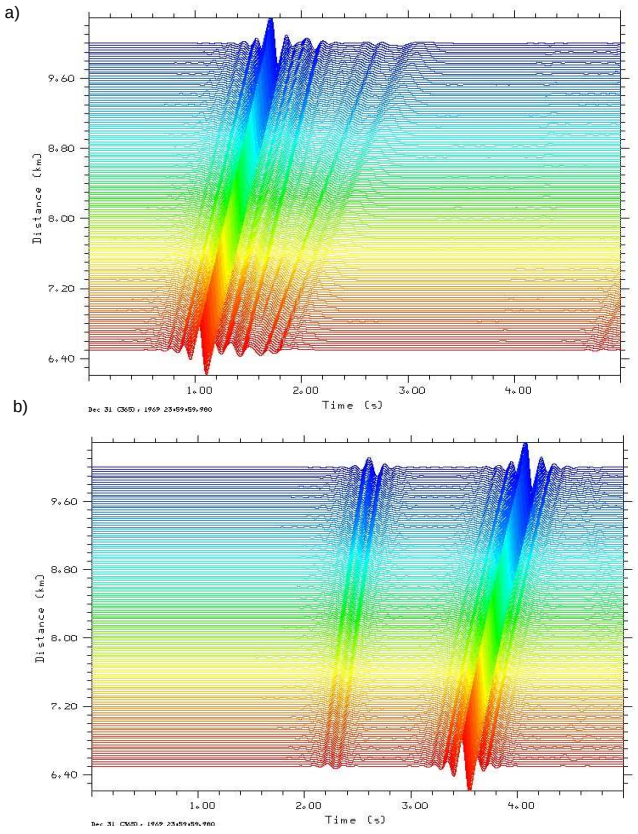

FIGURE E.2: Comparison of the recorded velocity time histories due to a double-couple point source located at a) 1.5 km and b) 10 km below the free surface at a site with with $H/L = 0$ modeled in SPECFEM3D.